

New Metal Oxides from Syntheses under Extreme Conditions

Inaugural-Dissertation

zur

Erlangung des Doktorgrades
der Mathematisch-Naturwissenschaftlichen Fakultät
der Universität zu Köln

vorgelegt von

Désirée Badea

aus Köln

April 2025

First reviewer and examiner: PD Dr. Jörn Bruns

Second reviewer and examiner: Prof. Dr. Uwe Ruschewitz

Chair of the thesis defense committee: Prof. Dr. Klas Lindfors

Dein Leben ist deine Chance.

Köln, 28.11.2019

Johann Vasile Bader

Abstract

This PhD dissertation explores fundamental research on oxygen-containing compounds formed under extreme conditions, including highly alkaline environments, high pressures in the multi anvil press and high O₂ pressures in autoclaves. As part of a collaboration with BASF, the study also focused on the synthesis and characterization of novel compounds relevant to ethylene oxide catalyst production.

Ba[TcO₃N] was synthesized by reacting ammonium pertechnetate with Ba(OH)₂ · 8 H₂O under highly alkaline conditions. Structural characterization revealed isolated [TcO₃N]²⁻ tetrahedra, providing insights into technetium behavior in alkaline environments, crucial for nuclear waste management. *Raman* spectroscopy, X-ray absorption near edge structure spectroscopy and density functional theory calculations confirmed the Tc +VII oxidation state and clarified its bonding.

In similar approaches, mixed anionic nitridotrioxometallates, specifically K₃[ReO₄][ReO₃N] and K₃[TcO₄][TcO₃N], were synthesized by reacting ammonium pertechnetate and perrhenate in KOH hydrofluxes. Structural analysis using X-ray diffraction, *Raman* spectroscopy, X-ray photoelectron spectroscopy and quantum chemical calculations confirm the presence of Re-N and Tc-N bonds, which are key to the unique structure of these compounds. Additional syntheses of single crystals of A₃[ReO₄][ReO₃N] (A = Rb, Cs) and A'₂[ReO₃N] (A' = K, Cs) were carried out, with further characterization by *Raman* spectroscopy and quantum chemical calculations.

The work also explores the synthesis of new iridium compounds, including Ba₂[Ir(OH)₆](OH)₂, of which the crystal structure has been elucidated. Similar attempts led to the synthesis of Ba_{2.4}Sr_{1.6}[Ir(OH)₆](OH)₆, also analyzed by single crystal X-ray diffraction.

By using a *Walker*-type multi anvil press, a new ternary silver-lead oxide, Ag₂PbO₃, was obtained from Ag₂O and PbO₂. The structure and composition were confirmed by single crystal X-ray diffraction, powder X-ray diffraction and X-ray photoelectron spectroscopy, showing silver and lead coordination in a rock-salt type structure.

In addition to fundamental research on compounds from extreme conditions, the ethylene oxide catalysis was addressed in collaboration with BASF. Therefore, in the last part of this work powder X-ray diffraction and energy-dispersive X-ray spectroscopy data were obtained of fresh and spent catalyst samples provided during the collaboration with BASF.

Furthermore, promoter solutions which are typically used for the production of the catalyst were combined resulting in the compounds $[\text{Ag}(\mu\text{-en})][\text{ReO}_4]$ and $[\text{Ag}_2(\text{DHPP})](\text{C}_2\text{O}_4)$. Structural analyses were conducted for both compounds using single crystal X-ray diffraction. The thermal analysis of $[\text{Ag}(\mu\text{-en})][\text{ReO}_4]$ revealed that it decomposes to elemental Ag, in analogy with industrial processes.

In ethylene oxide catalysis, Ag serves as the primary catalyst for selective oxidation, while Re and Cs enhance activity and selectivity, and Cl optimizes surface properties. Therefore, additional experiments aimed to identify new intermediates, focusing on Ag, Re, Cs and Cl under various extreme conditions.

Contents

Abbreviations.....	v
List of Figures	vi
List of Tables.....	viii
1 Introduction	1
2 State of Knowledge	3
2.1 Hydroflux Technique.....	3
2.2 Multi Anvil Press	6
2.3 High Pressure O₂ Autoclave	8
2.4 Industrial Ethylene Epoxidation Catalysis.....	10
3 Objective.....	13
4 Results and Discussion	15
4.1 Work with Technetium	15
4.1.1 Technetium Review (Publication 1)	17
4.2 Hydroflux Syntheses	37
4.2.1 Ba[TcO ₃ N] from Highly Alkaline Ba(OH) ₂ Medium (Publication 2).....	38
4.2.2 K ₃ [MO ₄][MO ₃ N] with <i>M</i> = Tc, Re from KOH Hydroflux (Publication 3) .	46
4.2.3 A ₃ [ReO ₄][ReO ₃ N] and A' ₂ [ReO ₃ N] with <i>A</i> = Rb, Cs and <i>A'</i> = K, Cs from Alkali Metal Hydroxide (Publication 4).....	55
4.2.4 Ba ₂ [Ir(OH) ₆](OH) ₂ from Alkaline Earth Metal Hydroxide (Publication 5)	64
4.2.5 Ba _{2.4} Sr _{1.6} [Ir(OH) ₆](OH) ₆ from Alkaline Earth Metal Hydroxides	68
4.3 Syntheses in the Multi Anvil Press	71
4.3.1 Ag ₂ PbO ₃ from High Pressure and High Temperature Experiments.....	71
4.3.2 Further Synthesis Attempts in the Multi Anvil Press.....	75
4.4 Intermediates During Ethylene Oxide Catalysis	79
4.4.1 Characterization of Laboratory Model EO Catalytic Samples and Intermediates	80
4.4.2 [Ag(μ- <i>en</i>)] [ReO ₄] Intermediate During Catalysis (Publication 6).....	84
4.4.3 [Ag ₂ (DHPP)](C ₂ O ₄) Possible Side Phase During Catalysis.....	91
5 Conclusion and Outlook	94
6 Experimental.....	98
6.1 General Procedures and Analytic Methods	98
6.1.1 Hydroflux Technique	98

6.1.2	Multi Anvil Press.....	98
6.1.3	High Pressure O ₂ Autoclave.....	98
6.1.4	Chemicals	99
6.1.5	X-ray Single Crystal Diffraction	99
6.1.6	X-ray Powder Diffraction and <i>Rietveld</i> Refinement	99
6.1.7	IR Spectroscopy	100
6.1.8	<i>Raman</i> Spectroscopy	100
6.1.9	X-ray Photoelectron Spectroscopy.....	100
6.1.10	Energy-dispersive X-ray Spectroscopy	100
6.1.11	<i>Polynator</i>	100
6.1.12	<i>CHARDI</i>	101
6.2	Experimental Procedures.....	102
6.2.1	Ba _{2.4} Sr _{1.6} [Ir(OH) ₆](OH) ₆	102
6.2.2	Ag ₂ PbO ₃	102
6.2.3	Further Synthesis Attempts in the Multi Anvil Press.....	102
6.2.4	Characterization of the EO Catalyst.....	103
6.2.5	[Ag ₂ (DHPP)](C ₂ O ₄)	104
7	Appendix	105
7.1	Ba[TcO ₃ N]	105
7.2	K ₃ [MO ₄][MO ₃ N] (<i>M</i> = Tc, Re)	112
7.3	A ₃ [ReO ₄][ReO ₃ N] and A' ₂ [ReO ₃ N] (<i>A</i> = Rb, Cs; <i>A'</i> = K, Cs).....	121
7.4	Ba ₂ [Ir(OH) ₆](OH) ₂	138
7.5	Ba _{2.4} Sr _{1.6} [Ir(OH) ₆](OH) ₆	139
7.6	Ag ₂ PbO ₃	145
7.7	Further Synthesis Attempts in the Multi Anvil Press	149
7.8	Characterization of the EO Catalyst.....	151
7.9	[Ag(μ- <i>en</i>)] [ReO ₄].....	155
7.10	[Ag ₂ (DHPP)](C ₂ O ₄).....	162
8	References	165

Abbreviations

B.E.	- binding energy
cif	- crystallographic information file
DFT	- density functional theory
DHPP	- decahydropyrazino[2,3- <i>b</i>]pyrazine
EDX	- energy-dispersive X-ray spectroscopy
EO	- ethylene oxide
<i>en</i>	- ethane-1,2-diamine
eq	- equivalent/s
et al.	- et alii (and others)
e.g.	- exempli gratia (for example)
<i>goof</i>	- goodness of fit
i.e.	- id est (that is)
min	- minute/s
No.	- number
PTFE	- polytetrafluoroethylene
P-XRD	- powder X-ray diffraction
SC-XRD	- single crystal X-ray diffraction
UV	- ultraviolet
vis	- visible
XAFS	- X-ray absorption fine structure
XANES	- X-ray absorption near edge structure
XPS	- X-ray photoelectron spectroscopy
3D	- three dimensional

List of Figures

Figure 1. Possible parameters of extreme conditions.....	1
Figure 2. Dependency within the temperature of the flux, hydroflux and hydrothermal techniques in relation to the water content.....	3
Figure 3. KOH-H ₂ O phase diagram	4
Figure 4. Setup of a <i>Walker</i> type multi anvil press	6
Figure 5. Schematic drawing of the O ₂ autoclave and filling system	8
Figure 6. Key developments in EO catalysis.....	11
Figure 7. Four techniques using extreme conditions that are key aspects of this work	13
Figure 8. Flask with NH ₄ [TcO ₄] solution and section of table of nuclides.....	15
Figure 9. Overview over the compounds which were obtained using ultra alkaline conditions with exemplary crystal structures.....	37
Figure 10. Microscopic image of yellow single crystals of Ba _{2.4} Sr _{1.6} [Ir(OH) ₆](OH) ₆	68
Figure 11. Unit cell of the crystal structure of Ba _{2.4} Sr _{1.6} [Ir(OH) ₆](OH) ₆	68
Figure 12. Arrangement of the Ir(OH) ₆ polyhedra with view along the <i>c</i> -axis and extended asymmetric unit of Ba _{2.4} Sr _{1.6} [Ir(OH) ₆](OH) ₆	69
Figure 13. Arrangement of the Ba-O polyhedra and of the Sr/Ba-O polyhedra	70
Figure 14. Microscopic image of black metallic single crystals of Ag ₂ PbO ₃	72
Figure 15. Unit cell of the crystal structure of Ag ₂ PbO ₃	73
Figure 16. Visualization of the distorted rock-salt structure type in Ag ₂ PbO ₃	73
Figure 17. Powder X-ray data and <i>Rietveld</i> refinement patterns of Ag ₂ PbO ₂	74
Figure 18. XPS survey spectrum of Ag ₂ PbO ₃	75
Figure 19. Pb 4f, Ag 3d and O 1s XPS core level spectra of Ag ₂ PbO ₃	75
Figure 20. Powder X-ray data of the experiment of heating ReO ₃ and Ag ₂ O in the multi anvil press.....	76
Figure 21. Powder X-ray data of the experiment of heating Re ₂ O ₇ , Ag ₂ O and AgCl in the multi anvil press	77
Figure 22. Powder X-ray data and <i>Rietveld</i> refinement pattern of the product mixture from the multi anvil experiment with H ₃ BO ₃ and K ₂ S ₂ O ₇	78
Figure 23. Powder X-ray data of the O ₂ high pressure experiment of combining ReO ₃ with Ag ₂ O.....	82
Figure 24. Extended asymmetric unit of [Ag ₂ (DHPP)](C ₂ O ₄).....	91
Figure 25. Crystal structure of [Ag ₂ (DHPP)](C ₂ O ₄).....	93

Figure 26. Summary of the compounds containing the $[MO_3N]^{2-}$ anion ($M = \text{Tc}, \text{Re}$) obtained in this work	94
Figure 27. Extended asymmetric unit of Ag_2PbO_3	96
Figure 28. Schematic of an autoclave and a PTFE inlay.....	98
Figure 29. Microscopic image of brown single crystals of $\text{Ba}_2[\text{Ir}(\text{OH})_6](\text{OH})_2$	138
Figure 30. Unit cell of the crystal structure of $\text{Ba}_2[\text{Ir}(\text{OH})_6](\text{OH})_2$	138
Figure 31. 3D stacking of layers with $\text{Ba}(\text{OH})_9$ polyhedra and extended asymmetric unit of $\text{Ba}_2[\text{Ir}(\text{OH})_6](\text{OH})_2$	138
Figure 32. Powder X-ray data of the experiment of heating $\text{Ag}[\text{ReO}_4]$ in the multi anvil press	149
Figure 33. Powder X-ray data of the experiment of heating $\text{Ag}[\text{ReO}_4]$ and Ag_2O in the multi anvil press.....	149
Figure 34. Powder X-ray data of the experiment of heating Ag_2O and SnO_2 in the multi anvil press	150
Figure 35. Powder X-ray data of the O_2 high pressure experiment of combining elemental Re with Ag_2O	151
Figure 36. Powder X-ray data of the O_2 high pressure experiment of combining ReO_3 with Ag_2O	151
Figure 37. Powder X-ray data of the O_2 high pressure experiment of combining ReO_3 with AgCl	152
Figure 38. Powder X-ray data of the O_2 high pressure experiment combining $\text{Ag}[\text{ReO}_4]$ with elemental Ag	152
Figure 39. Powder X-ray data of the O_2 high pressure experiment of combining $\text{Ag}[\text{ReO}_4]$ with Ag_2O	153
Figure 40. Powder X-ray data of the experiment of combining Cs complex solution with $\text{NH}_4[\text{ReO}_4]$	153
Figure 41. Powder X-ray data of the experiment of combining Cs complex solution with $\text{Cs}[\text{ReO}_4]$	154

List of Tables

Table 1. Selected compounds which were obtained from hydroxide hydrofluxes and characterized via SC-XRD	5
Table 2. Selected crystallographic data of $\text{Ba}_{2.4}\text{Sr}_{1.6}[\text{Ir}(\text{OH})_6](\text{OH})_6$	69
Table 3. Selected crystallographic data of Ag_2PbO_3	72
Table 4. <i>Polynator</i> δ -values for the polyhedra in Ag_2PbO_3	73
Table 5. Conducted multi anvil press experiments	77
Table 6. Selected O_2 high pressure experiments	80
Table 7. Selected crystallographic data of $[\text{Ag}_2(\text{DHPP})](\text{C}_2\text{O}_4)$	91
Table 8. Selected bond lengths of $[\text{Ag}_2(\text{DHPP})](\text{C}_2\text{O}_4)$ and literature data of DHPP and $\text{Ag}_2\text{C}_2\text{O}_4$	92
Table 9. List of used chemicals with information about supply source, form and purity. .	99
Table 10. Starting materials and conditions of experiments in the multi anvil press	103
Table 11. Starting materials and temperature program of experiments in O_2 autoclaves.	103
Table 12. Starting materials and products of experiments in O_2 autoclaves	103
Table 13. Crystallographic data of $\text{Ba}_{2.4}\text{Sr}_{1.6}[\text{Ir}(\text{OH})_6](\text{OH})_6$	139
Table 14. Atomic coordinates and equivalent isotropic displacement parameters for $\text{Ba}_{2.4}\text{Sr}_{1.6}[\text{Ir}(\text{OH})_6](\text{OH})_6$	139
Table 15. Anisotropic displacement parameters for $\text{Ba}_{2.4}\text{Sr}_{1.6}[\text{Ir}(\text{OH})_6](\text{OH})_6$	140
Table 16. Bond lengths for $\text{Ba}_{2.4}\text{Sr}_{1.6}[\text{Ir}(\text{OH})_6](\text{OH})_6$	140
Table 17. Bond angles for $\text{Ba}_{2.4}\text{Sr}_{1.6}[\text{Ir}(\text{OH})_6](\text{OH})_6$	140
Table 18. Hydrogen atom coordinates and equivalent isotropic displacement parameters for $\text{Ba}_{2.4}\text{Sr}_{1.6}[\text{Ir}(\text{OH})_6](\text{OH})_6$	144
Table 19. Atomic occupancy for $\text{Ba}_{2.4}\text{Sr}_{1.6}[\text{Ir}(\text{OH})_6](\text{OH})_6$	144
Table 20. Crystallographic data of Ag_2PbO_3	145
Table 21. Atomic coordinates and equivalent isotropic displacement parameters for Ag_2PbO_3	145
Table 22. Anisotropic displacement parameters for Ag_2PbO_3	146
Table 23. Bond lengths for Ag_2PbO_3	146
Table 24. Bond angles for Ag_2PbO_3	146
Table 25. Lattice parameters and refinement factors for the <i>Rietveld</i> fit of the powder diffraction pattern of Ag_2PbO_3	149

Table 26. Lattice parameters and refinement factors for the <i>Rietveld</i> fit of the powder diffraction pattern of the product mixture from the multi anvil experiment with H_3BO_3 and $\text{K}_2\text{S}_2\text{O}_7$	150
Table 27. Crystallographic data of $[\text{Ag}_2(\text{DHPP})](\text{C}_2\text{O}_4)$	162
Table 28. Atomic coordinates and equivalent isotropic displacement parameters for $[\text{Ag}_2(\text{DHPP})](\text{C}_2\text{O}_4)$	163
Table 29. Anisotropic displacement parameters for $[\text{Ag}_2(\text{DHPP})](\text{C}_2\text{O}_4)$	163
Table 30. Bond lengths for $[\text{Ag}_2(\text{DHPP})](\text{C}_2\text{O}_4)$	163
Table 31. Bond angles for $[\text{Ag}_2(\text{DHPP})](\text{C}_2\text{O}_4)$	164
Table 32. Hydrogen atom coordinates and equivalent isotropic displacement parameters for $[\text{Ag}_2(\text{DHPP})](\text{C}_2\text{O}_4)$	164

1 Introduction

Extreme conditions in chemical reactions refer to the use of highly unusual parameters, such as very high pressures, extreme temperatures, acidic or alkaline conditions, to drive or influence chemical reactions, see Figure 1 for selected examples. These factors enable pathways to novel compounds and reactions that would not be possible under standard laboratory conditions.

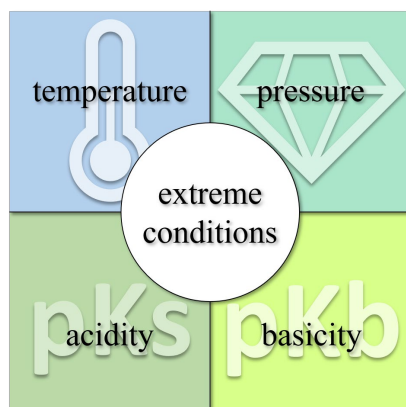


Figure 1. Possible parameters of extreme conditions.

For example, high pressure syntheses are widely employed to create compounds with unique properties that are inaccessible at atmospheric pressure.^[1] Extreme pressures and often high temperatures allow for new crystalline structures, unusual valence states and increased coordination numbers. This method has proven invaluable in synthesizing compounds like stishovite, a high pressure polymorph of SiO_2 , and intercalation compounds, such as $\text{Ag}_3\text{Ni}_2\text{O}_4$ which require pressures of up to 130 MPa in O_2 high pressure autoclaves.^[2-3]

High pressure techniques can be also used to synthesize superconducting materials at unusual conditions. For example, hydrogen sulfide becomes superconducting at 203 K when exposed to pressures around 150 GPa, while LaH_{10} exhibits a superconducting transition temperature near 250 K at pressures of 170 GPa.^[4-5]

Furthermore, the application of pressure in the chemical industry has played and still plays a significant role in the synthesis of chemicals. Notable examples include the *Haber-Bosch* process from 1906, where ammonia is catalytically obtained under high pressure at approximately 20 MPa and temperatures of 700°C .^[6] This process is still fundamental for the chemical industry. Another important example is the *Fischer-Tropsch* process, which is

used to synthesize hydrocarbons from CO and H₂ at pressures of 20-40 bar. The reaction is catalyzed by iron or cobalt at temperatures of about 340°C.^[7]

While temperature and pressure can be parameters of extreme conditions, two other examples are highly acidic or alkaline conditions. Chemical syntheses under strongly acidic conditions can be applied for the formation of complex metal oxides and coordination compounds. These reactions often contain strong acids, e.g. sulfuric acid or trifluoromethanesulfonic acid. The Wickleder group has already made significant contributions to this research field and has published several important findings.^[8-9]

When using sulfuric acid without and with addition of SO₃, unique actinide species, e.g. UO₂(S₂O₇) and U(SO₄)₂, can be stabilized.^[8] Additionally, the synthesis of trichloromethanesulfonates, employs the trichloromethanesulfonic acid to generate species such as (H₅O₂)[Cl₃CSO₃], which exhibit interesting structural properties and have potential in various chemical applications.^[9]

Alkaline conditions can help to dissolve metal oxides and hydroxides, enabling the formation of single crystals. In a flux synthesis for example, starting materials can be dissolved in a molten salt at high temperatures, allowing the formation of compounds that are difficult to crystallize under other conditions, e.g. products like SrPd₃O₄ and CaPd₃O₄.^[10] The hydroflux synthesis adapts this method by additionally using small amounts of water at elevated temperatures.^[11-12] This approach is especially useful for growing crystals of complex oxides and hydroxides.

The *zur Loye* group demonstrated the successful use of molten hydroxides in the crystallization of new compounds. The group synthesized platinum group metal hydroxides from several alkaline metal hydroxides.^[13] More recently, the *Ruck* group synthesized new compounds with the composition Sr₃[M(OH)₆]₂ (*M* = Sc, Y, Ho - Lu), using hydroflux conditions to stabilize hydroxides.^[14]

Both high pressure techniques and hydroflux syntheses will be described in more detail in the following chapters 2.1, 2.2 and 2.3. A brief insight into the use of catalysis processes in the chemical industry, which can also involve high pressures and high temperatures, is provided in chapter 2.4.

2 State of Knowledge

2.1 Hydroflux Technique

As previously described, the hydroflux technique can be seen as a method utilizing extreme conditions, e.g. basicity. In general, the simple flux growth involves the use of a high temperature melt of an inorganic compound as a medium for crystallization.^[12] These high temperature melts typically consist of basic inorganic compounds such as oxides, hydroxides or carbonates, which have relatively low melting points. Often a mixture of these compounds is used to create a eutectic melt with an even lower melting point. In addition, the use of small amounts of water significantly lower the melting point of certain fluxes, such as hydroxides. In general, the term "hydroflux" has been introduced by *Scheel* and *Ewell* in 1975 to describe this combination of the flux and the hydrothermal techniques where water modifies the solution properties of the melt.^[12] Figure 2 shows the dependency within the temperature of the different methods in relation to the water content.^[11] While flux syntheses need to be performed in suitable reaction vessels such as corundum crucibles, silver ampoules or silver crucibles, hydroflux syntheses can be carried out in stainless steel autoclaves with PTFE inlays. Therefore, the hydroflux technique provides a promising alternative to the traditional hydrothermal and flux syntheses by utilizing a highly concentrated water-soluble metal salt at moderate temperatures.

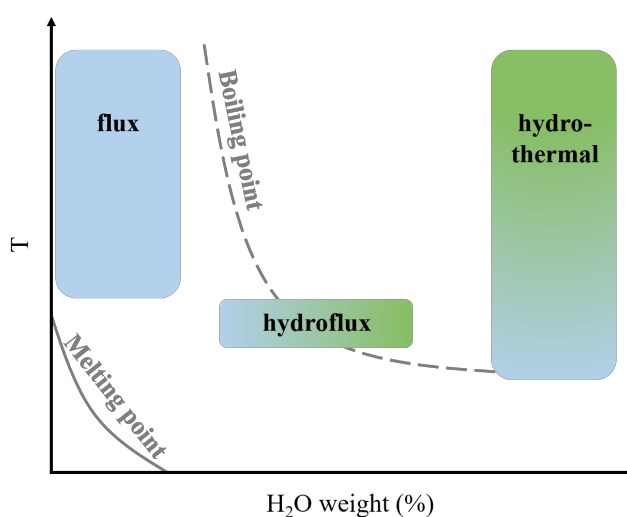


Figure 2. Dependency within the temperature of the flux, hydroflux and hydrothermal techniques in relation to the water content. The color defines the pressure: green shows high pressure and blue low pressure. The figure is adapted from *zur Loye et al.*^[11]

Alkali metal hydroxides have proven to be particularly suitable hydroflux media, as they can be easily washed out and are readily available. In addition, single crystals can be

obtained easily from alkali metal hydroxides. In hydroxide melts, the acid-base chemistry is conceptualized by the *Lux-Flood* concept of oxoacidity.^[15] The *Brønsted* theory, introduced in 1923, describes acid-base reactions as proton transfers, where acids act as proton donors and bases as proton acceptors.^[16] In contrast, the *Lux-Flood* theory centers on the oxide anion O^{2-} , defining acids as oxide anion acceptors and bases as donors, a model especially useful for aprotic systems.^[15]

Although the acid-base chemistry of fluxes is well-explained, the underlying processes that influence crystal growth are still not fully understood.^[17] Due to the limited understanding of the mechanisms involved in structure formation during growth, researchers need to perform exploratory experiments to determine the best conditions for each unique system. The variety of available fluxes allows nearly limitless combinations of melts. As previously mentioned, a commonly used hydroflux is KOH, as hydroxide melts can dissolve almost all elements except for some noble metals.^[18] Hydroxides such as KOH and NaOH have relatively low melting points, which can be further reduced by eutectic mixtures and by using water.^[19] Hydroflux syntheses using KOH with 10% H_2O lower the reaction temperature from approximately 400°C to around 200°C, see Figure 3.^[19-20]

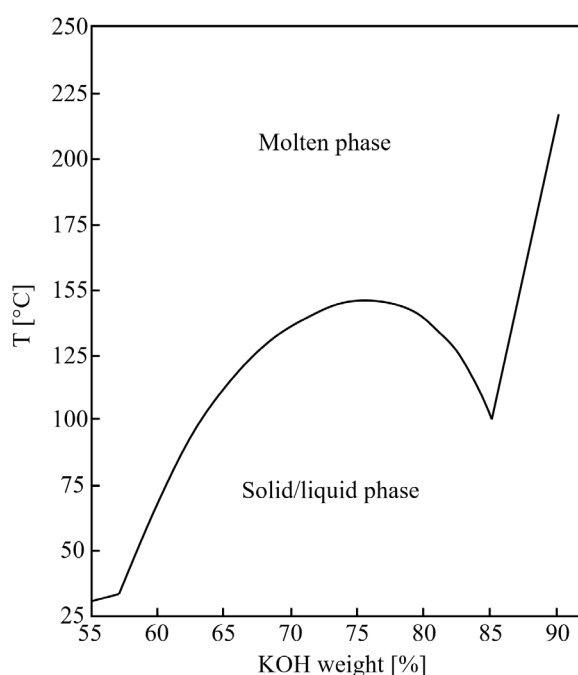
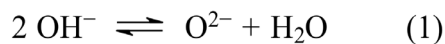


Figure 3. KOH-H₂O phase diagram adapted from the literature.^[20]

The temperature, the heating/cooling rate and the water content have a major influence on the reaction.^[18] A temperature between 200-230°C seems to be sufficient for KOH hydrofluxes, while a cooling rate of 0.3°C or less per minute has been found to promote single crystal growth. Most reactions can be heated with a heating rate of 5°C per minute.^[18]

By varying the water content and thus the oxoacidity, it is possible to control the solubility of the product and the product itself, see equation 1. Therefore, the auto-dissociation of the hydroxide can influence the product by forming oxides or hydroxides.^[21]



The first reported use of a hydroflux melt was done in 1986 by *Harms and Gunßer*.^[22] The synthesis and characterization of the crystal structures of metastable gallium compounds using conventional methods proved not to be possible. However, the use of the hydroflux method based on sodium and potassium nitrate allowed the synthesis of various gallium oxides and hydroxides, such as α -Ga₂O₃ and α -GaOOH starting from γ -Ga₂O₃.^[22]

In the early 2010s, the *zur Loye* Group took up the method again and synthesized new hydroxometallates.^[11, 13] Table 1 shows selected compounds, which were obtained single crystalline by the hydroflux method and characterized via SC-XRD.

Table 1. Selected compounds which were obtained from hydroxide hydrofluxes and characterized via SC-XRD.

Compound	Hydroflux	Literature
Sr ₃ [M(OH) ₆] ₂ (<i>M</i> = Sc, Y, Ho-Lu)	KOH	[14]
BaNa[Rh(OH) ₆]	NaOH	[23]
AE ₂ [Pt(OH) ₆](OH) ₂ (<i>AE</i> = Sr, Ba)	NaOH	[13]
Ba ₂ [M(OH) ₆] (<i>M</i> = Mn, Co, Cu)	NaOH and KOH	[11]
K ₂ Ba[MO ₄] ₂ (<i>M</i> = Cr, Mo, W)	KOH	[24]
K ₈ [Rh(IO ₆) ₂]OH · 3 H ₂ O	KOH	[25]
K ₂ Se ₃ , K ₂ Te ₃ and K ₂ Se ₂ Te	KOH	[26]

2.2 Multi Anvil Press

Over the past eight decades, high pressure techniques have improved the range of pressure and volume conditions that can be achieved. High pressure experiments, spanning from 0.1 GPa to 500 GPa, are performed using different experimental setups.^[27] These can be divided into two types: dynamic methods, which produce high pressure for short periods, typically lasting microseconds, and static methods, where pressure is applied continuously for a longer and adjustable time.^[27] In order to realize high pressures and temperatures in combination with a large volume at acceptable costs, the static multi anvil press developed 1990 by *Walker* et al. can be used.^[28] Figure 4 shows the parts for the sample preparation within the octahedron, the tungsten cubes, an octahedron before and after the compression and the a *Walker* type multi anvil press.^[28]

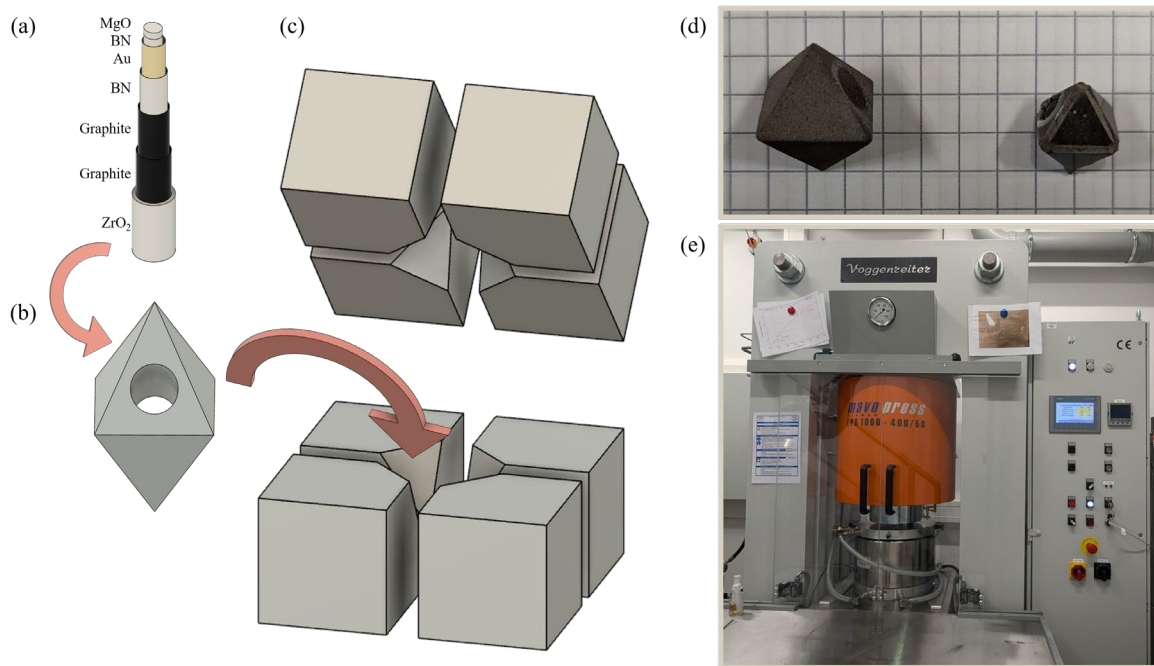


Figure 4. (a) Cross section of the pressure cell with specification of the respective used material, (b) empty octahedron, (c) eight truncated tungsten carbide cubes for the compression of the octahedron, (d) octahedron before and after the compression and (e) a *Walker* type multi anvil press.^[28]

To perform an experiment, the cube with the octahedron is placed in the press with three wedges below and three wedges above the cube. When pressure is applied, the wedges are pressed together, simultaneously compressing the cube and the octahedron with the sample. In general, pressures of up to 25 GPa can be generated while temperatures of up to $\sim 2700^\circ\text{C}$ can be applied.^[27]

High pressure and high temperature synthesis has its roots in the development of artificial diamond production, which dates back to the 19th century.^[29] Since then, the interest in the

synthesis of compounds under high pressures and at high temperatures has steadily increased.

For example, the high pressure modification of Co_3TeO_6 was recently obtained using a multi anvil experiment.^[30] This modification exhibits exceptional thermal stability up to 1070 K and crystallizes in a acentric trigonal structure, which contrasts with its monoclinic modification at normal pressure. The transition temperatures for magnetic and magnetoelectric phases were determined through specific heat measurements and show a non-hysteretic behavior of the magnetoelectric coupling.^[30]

Furthermore, *Huppertz et al.* are working on synthesizing new borates from high pressure/high temperature experiments.^[31-33] One highlight is the bismuth triborate BiB_3O_6 exhibiting nonlinear optical properties, which have garnered significant attention.^[34] The discovery of new polymorphs of BiB_3O_6 under high pressure conditions showcases the potential for developing optical materials.^[31, 35]

Different rare earth borates are known from syntheses under ambient pressures. However, the structural motifs and phase behavior of $\text{RE}(\text{BO}_2)_3$ with $\text{RE} = \text{Ho-Lu}$ could only be formed with different structural types under high pressure conditions.^[32] This variability opens up opportunities to explore new compounds that would not be accessible without the application of high pressures.

Furthermore, there is a general influence of high pressure on the structure of new oxoborates, as it can lead to the stabilization of unusual coordination environments and structural motifs, such as edge-sharing BO_4 tetrahedra in form of $[\text{B}_2\text{O}_6]^{6-}$ units, which were previously unobserved.^[33] These motifs were first observed in $\text{Dy}_4\text{B}_6\text{O}_{15}$ and $\text{Ho}_4\text{B}_6\text{O}_{15}$ through a high pressure synthesis.^[33] Another distinctive characteristic of the high pressure compound NiB_2O_4 is that, unlike the first two compounds, all tetrahedra are interconnected through one shared edge and two shared corners.^[36]

2.3 High Pressure O₂ Autoclave

Besides the multi anvil press, O₂ high pressure autoclaves can be used for solid state chemistry to carry out reactions under controlled O₂ high pressure and high temperature conditions. In addition, reaction involving mineralizer solutions are also possible.

The autoclaves are made of a nickel-chromium-cobalt alloy, i.e. *Niomic 90*, to ensure the handling of the extreme conditions, namely high pressures, high temperatures and corrosive chemicals. Figure 5 shows a schematic drawing of the O₂ autoclave and the apparatus for filling the autoclave with O₂. These autoclaves can operate at pressures up to 6000 bar and temperatures up to 600°C.^[37] They are self-sealing according to the *Bridgman* principle and are ideal for reactions involving corrosive substances like concentrated potassium hydroxide.^[37]

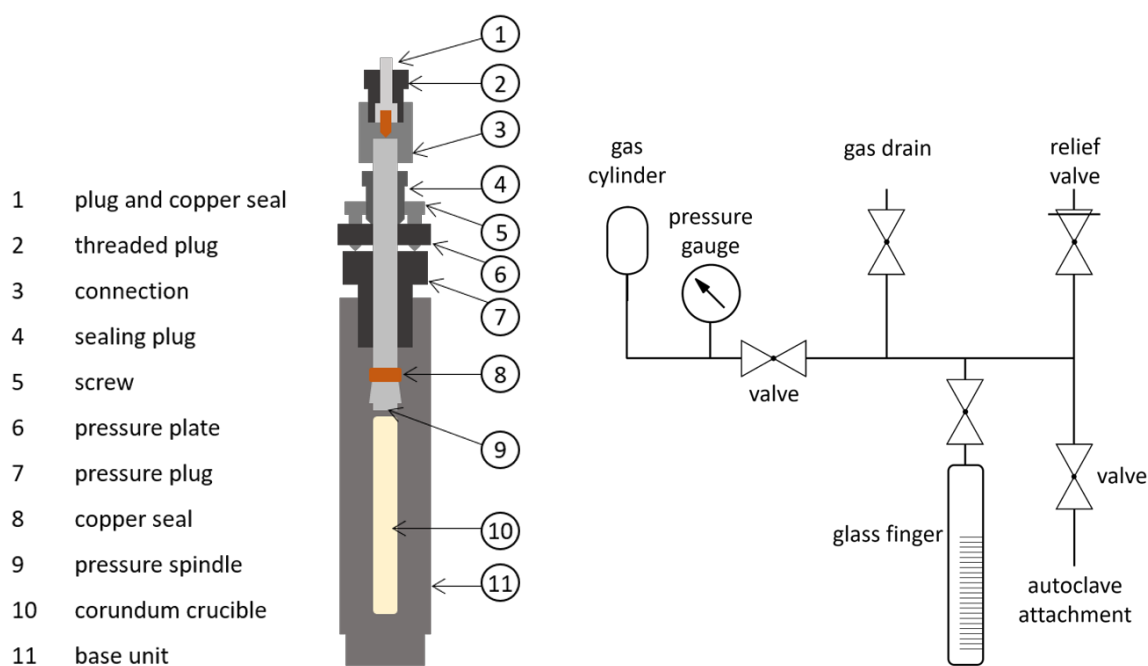


Figure 5. Schematic drawing of the O₂ autoclave (left) and O₂ connection for filling the autoclave (right).^[37]

For the preparation, the sample is placed into a non-reactive container, such as gold or corundum crucibles, to avoid unwanted reactions with the autoclave. O₂ is added as the reaction medium by first condensing a defined volume into the glass finger using liquid nitrogen, see Figure 5 right, and then by condensing the afore measured O₂ volume into the autoclave. The amount of O₂ is carefully measured to create the desired pressure, which can be calculated using the van der Waals equation. Once the autoclave is sealed, it is heated in a furnace to the target temperature with a specific heating and cooling rate. After the reaction, the O₂ is released carefully and the products removed from the crucible.

This method is highly effective as it allows precise control of pressure and temperature, making it possible to obtain novel compounds formed under extreme conditions. Using the O₂ autoclave is especially useful for synthesizing compounds like transition metal oxides, which can have unique properties and applications.^[2, 37-40] To provide a brief overview of the products that can be obtained under high O₂ pressures in autoclaves, a few examples are presented below. Over the past decades, *Jansen et al.* have successfully synthesized several unusual transition metal oxides.^[2, 37-40]

One of the first results from O₂ high pressure syntheses is the first silver stannate Ag₂SnO₃.^[37] Bright red crystals of this compound can be obtained through a solid state reaction of Ag₂O and freshly prepared K₂Sn(OH)₆ at 430°C under an oxygen pressure of 350 bar. The EDX analysis confirmed the proposed ratio of silver to tin. The thermal analysis revealed that Ag₂SnO₃ decomposes with the release of oxygen starting at 600°C, resulting in the formation of silver, tin oxide and oxygen.^[37]

Silver scandium oxide, i.e. AgScO₂, is a compound which can be synthesized from Ag₂O and Sc₂O₃ through a solid state reaction at 450°C and an O₂ pressure of 750 bar.^[38] The compound crystallizes in the space group $R\bar{3}m$ and shows a high thermal stability, decomposing at approximately 740°C into elemental silver and Sc₂O₃ while releasing oxygen. Conductivity measurements reveal that AgScO₂ exhibits ionic conductivity that increases with temperature.^[38]

Another example is the ternary silver platinum oxide Ag₈PtO₆ which crystallizes in the space group $P\bar{1}$.^[40] The compound is synthesized from Ag₂O and PtO₂ in an alkaline medium at 300°C with 2500 bar O₂ pressure. Notably, its structure consists of ideal PtO₆ octahedra connected by O-Ag-O dumbbells, forming a three-dimensional network. This compound features the electronic configuration 5d⁶ 6s⁰ of the Pt atoms, indicating a non-magnetic state that aligns with its observed diamagnetism. Additionally, Ag₈PtO₆ exhibits semiconducting properties with a band gap of approximately 0.9 eV, making it a promising candidate for various electronic applications.^[40]

2.4 Industrial Ethylene Epoxidation Catalysis

The use of the ethylene oxide catalyst can also generally be classified as operating under extreme conditions, including not only the large-scale production of ethylene oxide but also the need of elevated temperatures and pressures in the process. Accordingly, in addition to the hydroflux method, syntheses in the multi anvil press and the use of O₂ high pressure autoclaves, the ethylene oxide (EO) catalysis process can also be examined under extreme conditions in this context.

In general, catalysis is the process of accelerating a chemical reaction by using a substance called a catalyst, which itself remains unchanged after the reaction. The concept of catalysis was first introduced in 1835 by *Berzelius*, who observed that certain substances could increase the rate of reactions without being consumed.^[41] This discovery played an important role in industrial research, especially in processes like the *Haber-Bosch* process which is conducted at high temperatures and high pressures.^[6] Catalysts can lead to faster reaction rates, greater selectivity and milder reaction conditions, resulting in more efficient use of raw materials, fewer unwanted byproducts and reduced costs.^[42] The oxidation of ethylene to ethylene oxide using silver as a catalyst is an important example of an industrial process with a significant production capacity.^[43]

When examining the timeline of the development of the EO catalysis process, the increasing complexity of this catalytic process becomes evident. Figure 6 shows the timeline of key developments in EO catalysis. Before 1931, the production of ethylene oxide primarily relied on stoichiometric synthesis methods, i.e. the chlorohydrin process first industrialized by BASF.^[44] A major advancement was achieved in 1931 when the first catalytic method for ethylene epoxidation using air was introduced and enabled the production of EO.^[45] In 1937, the first catalysts only consisting of elemental silver were developed.^[46] A selectivity of ~50% for ethylene oxide was achieved. Another key advancement was introduced in 1938 with the introduction of gas-phase chloride moderation, which improved selectivity to ~70%.^[46-47] A milestone was the transition from oxidation with air to pure O₂, which enabled the process to be conducted in a loop gas system, thereby reducing throughput and simultaneously increasing selectivity.^[48] In 1970 advancements in high dispersion techniques further improved the performance of silver-only catalysts and during the same period, the introduction of alkali-metal promoters increased the selectivity to ~80%.^[49-50]

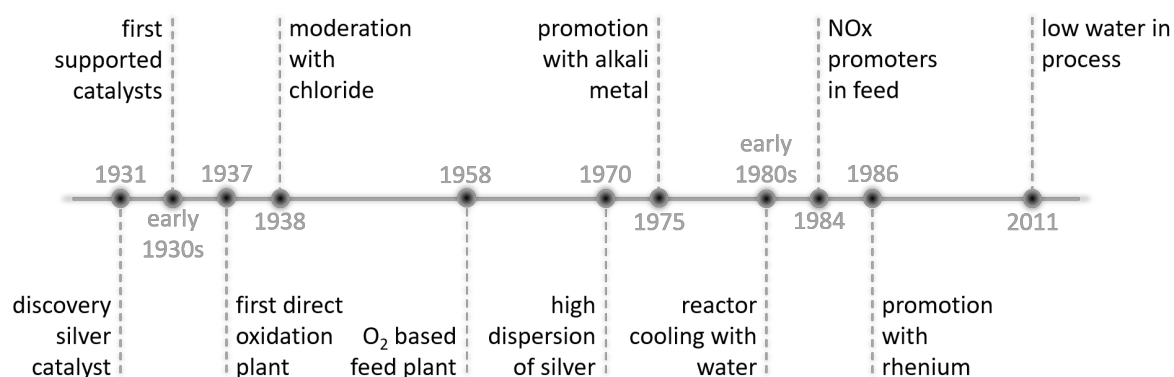
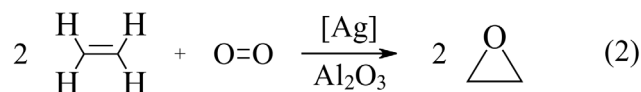


Figure 6. Key developments in EO catalysis.

See literature: 1931^[45], early 1930s^[51-52], 1937^[46], 1938^[46-47], 1958^[48], 1970^[49], 1975^[50], early 1980s^[48], 1984^[53], 1986^[54] and 2011^[55-56].

With the help of rhenium promoters a selectivity >85.7% could be achieved.^[54] Advancements during the 1990s and 2000s, along with improvements in process conditions, ultimately allowed selectivities above 90%.^[57]

As shown above, there has been significant progress in understanding the chemistry behind highly selective catalysis over the past few decades. In general, the reaction to EO is described as a heterogeneous catalytic process at temperatures up to 300°C and pressures up to 30 bar.^[58] The solid phase consists of silver particles on an Al₂O₃ support and both O₂ and C₂H₄ are present in the gas phase, see equation 2. While the exact reason for the importance of silver in contrast to e.g. Pd, Pt, or Ni is not fully understood, its interaction with oxygen is essential to achieve high selectivity.^[43] Silver exhibits ideal selectivity for both the dissociation of the O₂ molecule and the provision of reactive atomic oxygen species necessary for the epoxidation process.^[43] This capability allows to selectively convert ethylene to ethylene oxide while reducing the quantities of by-products.^[59] In industrial application, certain promoters like cesium and rhenium, along with additives such as chlorine, are added to the silver catalyst to enhance the selectivity.^[58, 60-61]



Today's research focusses on the nature of silver as a catalyst. *Linic* and *Christopher* stated that an Ag nanowire surface should be more selective to EO than finely dispersed Ag particles.^[62] The experiments aimed to explore the influence of surface structure on the catalytic performance. The use of nanowires showed a higher selectivity, which was attributed to a higher concentration of the Ag surface facets in the nanowire catalysts compared to the particle catalysts.^[62]

Another example of current research is the study of kinetics of ethylene epoxidation. *Bhan* et al. studied the kinetics of ethylene epoxidation using a promoted $\text{Ag}/\text{Al}_2\text{O}_3$ catalyst and examined the influence of organic chlorides acting as promoters.^[63]

Additionally, not only the use of the EO catalyst and the processes related to the catalysis are investigated, but also the preparation of the catalyst and the occurrence of intermediates during the preparation are researched.^[64-65] *Karpov, Jansen* et al. investigated the aqueous silver ethylene diamine oxalate complex solution which is used for impregnating the Al_2O_3 support.^[65] The study revealed that crystal formation from the mixture leads to the intermediate $[\text{Ag}(\mu\text{-en})]_2(\text{C}_2\text{O}_4) \cdot 2 \text{H}_2\text{O}$, providing insights into the catalyst preparation process.^[65]

3 Objective

One aim of this work was the synthesis and characterization of ternary and quaternary oxygen containing compounds from unusual and extreme conditions. The focus was on the synthesis via the hydroflux method, the multi anvil press and O₂ high pressure autoclaves. Although syntheses using hydrofluxes and high pressure techniques are already established, these methods are not widely used and demonstrate considerable potential. Notably, they have been advanced by the groups of *Ruck*^[14, 25-26, 66], *zur Loye*^[11, 13, 24, 67-68], *Jansen*^[2, 37-40] and *Huppertz*^[27, 36, 69-70]. Figure 7 illustrates the four principal objectives of this work. Using the multi anvil press, O₂ high pressure autoclaves and the hydroflux method, the objective was to synthesize new oxidic compounds. Building on the results of the master's thesis, the primary focus was on obtaining novel ternary and quaternary rhenium oxides from extreme conditions. Since rhenium is often used as an analogue in experiments involving technetium, collaborative efforts with the Nuclear Chemistry group at the University of Cologne aimed to conduct corresponding experiments with radioactive ⁹⁹Tc to expand on its chemistry, which is less covered in the literature than other elements.

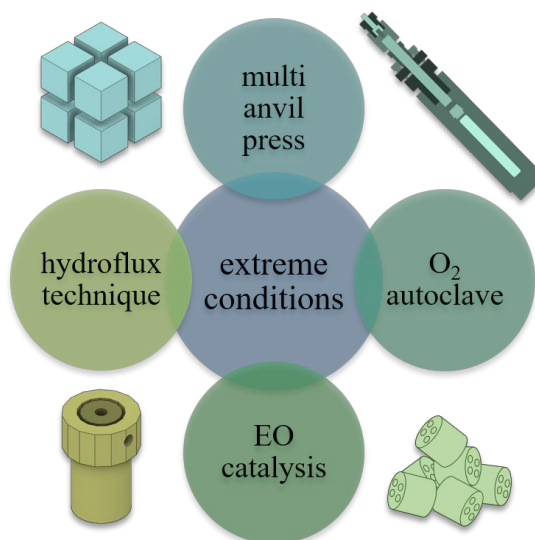


Figure 7. Four techniques using extreme conditions that are key aspects of this work.

The application of the EO catalyst can be considered under extreme conditions in a broad sense. Not only is a large volume of ethylene oxide produced, but the process also involves the use of elevated temperatures and pressures. Another aim of this work was to characterize the model EO catalyst, which was supplied by BASF as part of the collaboration. Furthermore, the research of this collaboration aimed to identify new intermediates that form during the production of the EO catalyst and to investigate EO catalyst phases of known compounds. For this, a systematic approach should be employed, combining various

promoter solutions and compounds under different pH values, temperatures, pressures and concentrations. The work primarily focused on compounds containing Ag, Re, Cs and W. Furthermore, solid phase reactions were intended to be performed using O₂ autoclaves at high temperatures in combination with high pressures to identify possible side phases of the catalyst.

4 Results and Discussion

4.1 Work with Technetium

As this work includes the use of technetium and its handling requires special safety precautions, this chapter outlines the experimental procedures involving technetium and its chemistry, which is also summarized in the first publication of this work in chapter 4.1.1.

Working with technetium and its compounds requires careful preparation. Since technetium is a radioactive element that undergoes β^- decay, strict safety measures must be followed. Figure 8 shows an aqueous $\text{NH}_4[\text{TcO}_4]$ solution and the section of table of nuclides with the respective technetium isotopes. It is essential to follow the radiation protection guidelines outlined in the StrlSchV (Strahlenschutzverordnung) before handling radioactive isotopes. Additionally, training from a radiation protection officer is required for working in controlled areas.^[71]

Benches are typically covered with waterproof plastic and a layer of paper to prevent irreversible contamination. Solutions are handled in plastic trays lined with paper and pipettes are used only with suction devices to avoid direct contact. Equipment and glassware must stay within the controlled area and decisions about storing or using radioactive materials are made on a case-by-case basis. All containers and equipment that have been in contact with radioactive substances must be labeled appropriately.

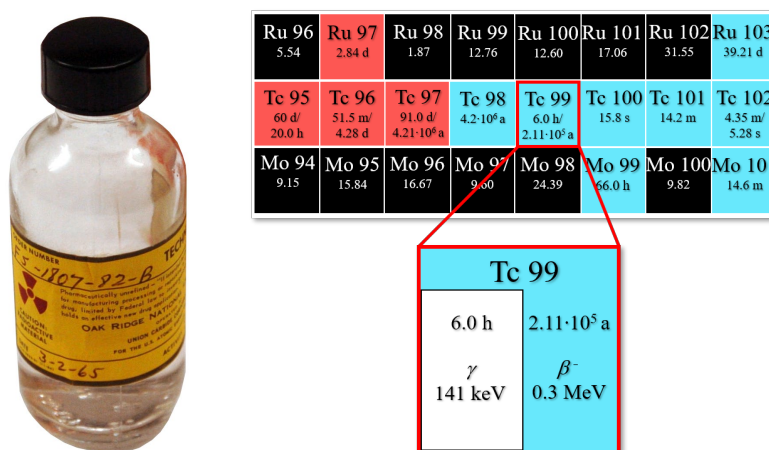


Figure 8. Flask with $\text{NH}_4[\text{TcO}_4]$ solution (left) and section of table of nuclides (right). Blue symbolizes β^- decay, red represents β^+ decay, white shows metastable and black stable isotopes. For $^{99\text{m}}\text{Tc}$ and ^{99}Tc , the corresponding decay energies and half-lives are presented.

Radioactive liquids and solutions are collected separately in containers for either short-lived or long-lived waste, categorized further into organic and inorganic types. ^{99}Tc compounds are disposed in containers for long-lived waste. Solid waste disposal containers are also

available. Radioactive materials must always be kept secure and only used as long and in such activities as the work requires. If contamination occurs, the radiation protection officer must be informed immediately.^[71]

4.1.1 Technetium Review (Publication 1)

^{99m}Tc is a widely used radioisotope in medical imaging.^[72] In addition, ^{99}Tc compounds are of interest in various fields, including nuclear energy and environmental studies.^[73] Despite its extensive use in medicine, many aspects of technetium's chemistry, as well as the properties of both ^{99}Tc and ^{99m}Tc , remain insufficiently explored. Since most review articles on technetium are either outdated or focused on radiopharmaceuticals and geochemistry, the creation of a new article incorporating recent research findings across other areas of technetium chemistry is essential.^[74-76] A comprehensive review can help to improve existing knowledge and provide valuable insights for research in this area.

Publication 1

Technetium – The Unknown Center of the Periodic Table

E. Strub, D. Badea, J. Bruns, A. Frontera, N. Mayordomo Herranz, A. Sakhonenkova,
M. Roca Jungfer, M. S. Wickleder, C. Yong and M. Zegke

Eur. J. Inorg. Chem. **2025**, e202400780.

doi.org/10.1002/ejic.202400780

Explanation of the personal contribution to the previously mentioned publication:

The entire review was written by all authors. Désirée Badea conducted an extensive literature search on binary, ternary and quaternary technetium compounds, with particular focus on oxides and oxyhalides. The relevant compounds were summarized by Désirée Badea in a specific section. The remaining sections were written by the other authors. The entire manuscript was reviewed and refined by Désirée Badea and all the other authors.

Technetium - The Unknown Center of the Periodic Table

Erik Strub,^{*,[a]} Désirée Badea,^[b] Jörn Bruns,^[b] Antonio Frontera,^[c] Natalia Mayordomo,^[d] Anna Sakhonenkova,^[e] Maximilian Roca Jungfer,^[f] Mathias Wickleder,^[b] Clarence Yong,^[a] and Markus Zegke^[a]

It took 78 years from Mendeleev's proposal of an existence of "eka-manganese" (1869) until it was finally named as technetium (Tc) in 1947. Another 78 years have passed since then. This provides a good occasion to pinpoint what we know and what we still do not know of this radioelement. Technetium is placed near the center of the Periodic Table, in the center of the groups 6, 7, and 8. Some chemical properties of the elements surrounding technetium show trends within the columns or along the rows of the Periodic Table, but a consistent interpretation of these trends is lacking as long as the knowl-

edge on technetium remains incomplete. This is especially remarkable as, on the other hand, the isotope ^{99m}Tc is applied on a daily basis in nuclear medicine. The aim of this paper is to review the fundamental understanding of technetium chemistry, mostly focusing on the research of the last decade, its implications, and its future perspectives. These developments show a picture of growing connections between physicochemical data, fundamental inorganic chemistry, organometallic and coordination chemistry, computational chemistry, and geochemistry.

Introduction

A Brief History of Technetium

The existence of an element below manganese (eka-manganese) was proposed as early as 1869 by Mendeleev.^[1] The story of its final discovery has been told often, e.g. by Zingales.^[2] It was finally discovered^[3] and named as technetium,^[4] 78 years after Mendeleev's proposal.

Tc turned out to be a radioelement, with isotopes ranging from ^{85}Tc to ^{120}Tc , and varied half-lives from ns to My. There is an extremely low natural abundance of Tc on Earth as a consequence of spontaneous fission of primordial ^{238}U , however, the isotope ^{99}Tc (half-life 211,000 years) is mostly anthropogenic since it is one of the major fission products of nuclear fission of ^{235}U and ^{239}Pu , with a fission yield of around 6%.^[5] A typical nuclear power reactor today produces around 20 kg of

^{99}Tc annually. So it is to no surprise that especially in the earlier days, when radiation safety measures were less strict, a lot of studies have been performed to characterize technetium physically and chemically. A good overview of these works is given in Schwachau - Technetium: Chemistry and Radiopharmaceutical Applications.^[6]

Since the naming of technetium, nearly another 78 years have passed, and today, its short-lived isomer ^{99m}Tc (half-life 6 hours) is the most applied radioisotope in medicine with roughly 25 million applications per year (that is, almost one every second), mostly for SPECT (single photon emission computer tomography), for which the 140 keV gamma is very convenient.^[7] For this purpose, roughly 1 g of ^{99}Mo are produced annually by reprocessing neutron-irradiated highly enriched ^{235}U .^[8] ^{99}Mo is fixated on commercial alumina columns (generators) from which Tc is eluted as pertechnetate $[\text{TcO}_4]^-$ in physiological NaCl solution. For this reason, Tc has a great significance for humanity despite its artificial origin.

Even though ^{99m}Tc is such an important nuclide for radiopharmacy, radiation protection rules have become more restrictive, and research, particularly on ^{99}Tc , has been stagnating in the last decades (see Figure 1). However, apart from general regulatory and safety measures, ^{99}Tc is chemically easy to handle even in gram amounts. It emits mostly low energy beta radiation (297 keV), which can be easily shielded.

General Differences in the Chemistry Between ^{99}Tc and ^{99m}Tc

Contrary to ^{99}Tc , the chemistry of ^{99m}Tc is mostly performed with nanomolar amounts due to its higher specific radioactivity. This strongly influences reaction kinetics and therefore might open different reaction pathways. ^{99m}Tc chemistry has been focused around medical applications, establishing certified "kits" that allow the easy preparation of different ^{99m}Tc

[a] E. Strub, C. Yong, M. Zegke
University of Cologne, Division of Nuclear Chemistry, Zùlpicher Str 45, 50674
Köln, Germany
E-mail: erik.strub@uni-koeln.de

[b] D. Badea, J. Bruns, M. Wickleder
University of Cologne, Department of Chemistry, Germany

[c] A. Frontera
University of the Balearic Islands, Chemisty, Spain

[d] N. Mayordomo
Helmholtz-Zentrum Dresden-Rossendorf, Institute of Resource Ecology,
Germany

[e] A. Sakhonenkova
St Petersburg State University, Khlopin radium institute, Russian Federation

[f] M. Roca Jungfer
University of Heidelberg, Organic Chemistry Institute, Germany

© 2025 The Author(s). European Journal of Inorganic Chemistry published by Wiley-VCH GmbH. This is an open access article under the terms of the Creative Commons Attribution License, which permits use, distribution and reproduction in any medium, provided the original work is properly cited.

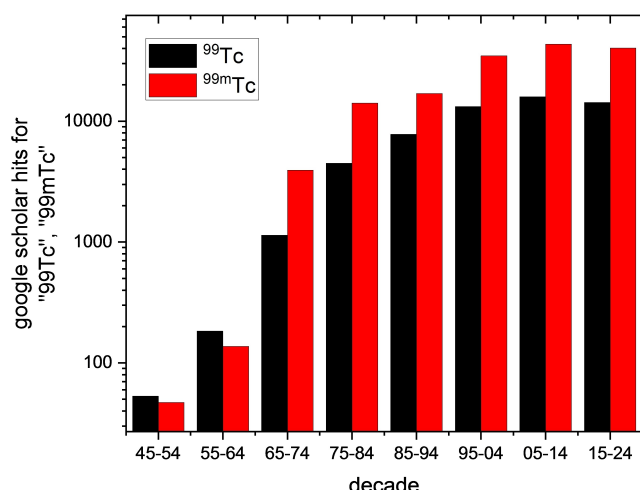


Figure 1. Number of publications referring to searches on google scholar for ⁹⁹Tc and ^{99m}Tc per decade.^[9]

compounds. Because the final preparations will always have to be performed with nanomolar amounts, also characterization of the final products is very challenging, while trying to use the more stable ⁹⁹Tc may yield different results due to kinetic differences, as the synthesis of ⁹⁹Tc complexes is carried out at much higher concentrations than that of ^{99m}Tc complexes.^[10] Consequently, such differences turn out to be interesting from the viewpoint of fundamental chemistry. For example, macroscopic amounts of [⁹⁹TcO₄]⁻ do not form arene sandwich complexes while ^{99m}Tc (in imperatively low concentration) leads to a yield of 90% under otherwise similar conditions.^[10] This is a common concern in radiopharmacy: because the comparison of nanomolar and micromolar amounts of products might fail and X-ray diffraction (XRD) is not available for nanomolar amounts, the structure of some ^{99m}Tc pharmaceuticals must be considered unknown, presenting a challenge for licensing processes. But even if the structures of ^{99m}Tc compounds might not be replicated with ⁹⁹Tc due to kinetics - the existing database of ⁹⁹Tc still lists far fewer compounds than that of the surrounding

elements of the Periodic Table (Figure 2). The geochemistry of Tc in the context of a final disposal of nuclear waste might face similar problems, e.g., when leaching of nanomolar amounts might still lead to considerable dissolution of material over a time span of several days, years or even millennia.

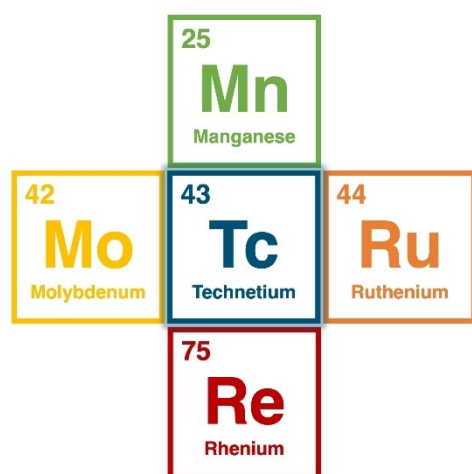
Other Isotopes of Technetium

Recently, further Tc isotopes have attracted interest: The short-lived ¹⁰¹Tc (half-life 14 min) has been suggested for possible theragnostic applications,^[12,13] and can be produced using neutron generators^[13] or secondary neutrons of the ¹⁸O(*p*, *n*)¹⁸F reaction in a cyclotron.^[12] This simultaneous production provides a possible alternative route to isotopes of Tc suitable for use in radiopharmacy. The isotopes ⁹⁶Tc (half-life 4,28 d) and ⁹⁷Tc (half-life 4.2 My) have been considered as a tracer/spike pair in ultra-trace analysis of ⁹⁹Tc with AMS (Accelerator Mass Spectrometry).^[14] In addition, ^{94m}Tc (half-life 52 min) has been used in the past and might be a possible nuclide for positron emission tomography.^[15,16] All these possible applications are subject to the same restrictions comparing nanomolar and micromolar amounts described above. Thus, in all these cases, a deep understanding of fundamental Tc inorganic chemistry is a prerequisite for a successful utilization of these isotopes.

Scope of this Work

Recent findings and scientific surprises, which are detailed below, have inspired a small but very diverse and lively community to continue ⁹⁹Tc research. The aim of this concept paper is to set a focus on these important developments of the last decade and their implications and future perspectives. Consequently, the sections of this are devoted to different aspects of technetium chemistry, dealing with

- physicochemical data
- fundamental inorganic chemistry
- organometallic and coordination chemistry



Number of Crystallographic Data

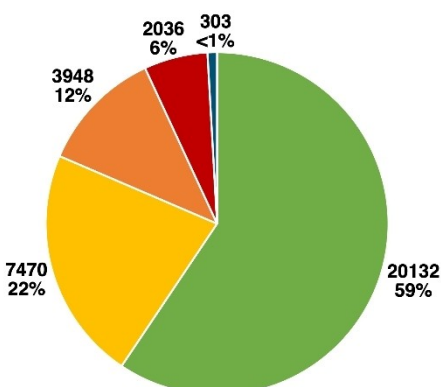


Figure 2. Number of structures in the Inorganic Crystal Structure Database (ICSD) database for Tc and its neighbors in the Periodic Table.^[11]

- IV) computational chemistry
- V) geochemistry

We will not focus on radiopharmaceutical applications in detail, and only touch on these where they provide relevant material as a starting point for ^{99}Tc chemistry. Extensive coverage has been provided by others elsewhere, e.g., the recent review of Duatti and references therein.^[17]

I Physicochemical Data

Many measurements of classical physicochemical data of Tc compounds or alloys (like melting points, thermodynamic data, critical temperatures, etc.) require macroscopic amounts of Tc, i.e., more than just a few mg that are sufficient for XRD (X-ray Diffraction) or X-ray absorption spectroscopy (XAS) methods. Therefore, most of these data originate from earlier times in which fewer lab restrictions have been in place, see Schwochau - Technetium: Chemistry and Radiopharmaceutical Applications.^[6] Nevertheless, there are some recent results, namely heat capacity measurements,^[18] and a book on electrochemistry.^[19]

From our point of view, there are two important developments in the field of physicochemical data in a wider sense, which are important for the characterization of Tc compounds using instrumental analytics: The first development concerns DFT (Density Functional Theory) calculations of chemical shifts in ^{99}Tc nuclear magnetic resonance (NMR). This work, e.g. Chatterjee et al., Bühl, or Hall et al. is generally ambitious because the number of experimental chemical shift data for Tc comprises about only 500 data points (not corrected for doubles).^[20–23] However, recent developments show that if solvation is taken into account and multi-step calculations are being used, Tc shifts in radiopharmaceuticals can be satisfactorily determined^[24] and Kuznetsov *et al.* have recently pointed out the “pivotal role of ^{99}Tc in solid-state and molecular chemistry”.^[25] Secondly, the measurement of XAS at the L_3 edge using synchrotron radiation has proven suitable for the characterization of Tc oxidation states.^[26,27] XANES (X-ray Absorption Near Edge Spectroscopy) can determine oxidation states and can give clues to electronic structure and geometry while EXAFS (Extended X-Ray Absorption Fine Structure) can be used to probe the Tc neighboring atoms and give accurate inter-atomic distances.”; both techniques work very well with mg or even μg amounts. Besides these recent developments it is worth to mention that already Schwochau^[6] reported on IR (infrared), Raman or UV-visible as well as EPR (electromagnetic paramagnetic resonance) spectroscopy, LPAS (laser induced photoacoustic spectroscopy) or mass spectrometry. All these methods are utilized to characterize Tc compounds whenever the necessary amounts are available, but we are not aware of significant recent method developments. The only exception here might be the detection of Tc with liquid electrode plasma optical emission spectrometry.^[28]

II Fundamental Inorganic Chemistry

Despite the fact that Tc has been known for over 80 years now, less is known about its systematics within the Periodic Table, compared to most other transition elements. Recent developments concerning fundamental inorganic technetium chemistry consider the binary, ternary and quaternary technetium complexes with simple ligands, like halides or oxyhalides as well as pertechnetate chemistry in water, in super acidic and in super basics conditions. Especially, Tc polyoxometallate structures have been identified; several of these developments are strongly influenced by redox processes which often mitigate the easy transfer of rhenium chemistry to Tc.

Binary, Ternary and Quaternary Technetium Complexes with Simple Ligands

When examining crystallographically characterized technetium compounds in the inorganic database,^[11] it seems reasonable to begin by comparing binary technetium salts. Although relatively few technetium compounds are known compared to those of other d-block elements, a selected range of important technetium salts can be discussed. Besides the few characterized technetium hydrides and borides, such as TcH , Tc_3B , Tc_7B_3 , and TcB_2 , salts of the group 14 elements remain scarcely studied by XRD.^[29,30]

Hydrides are potential starting materials for Tc chemistry with acidic ligands that serve as a source for various anions. The recent reinvestigation of $[\text{TcH}_3(\text{PPh}_3)_4]$ and its reaction product with CO, *mer-trans*- $[\text{TcH}(\text{CO})_3(\text{PPh}_3)_2]$, made a hydride complex of Tc available in sufficient quantity. *Mer-trans*- $[\text{TcH}(\text{CO})_3(\text{PPh}_3)_2]$ reacts with HX to give corresponding di- or tricarbonyl complexes. The parallel oxidation of the two *trans*- PPh_3 ligands leads to an isomerization under formation of the *fac*- $\text{Tc}[\text{CO}]_3^+$ core. The reactions are easily monitored by ^{99}Tc NMR.^[31]

However, the crystal structures of technetium's pentel and chalcogen compounds are better explored. The structure chemistry of certain binary halides has also been known since 1966.^[32] Four halogen compounds have been elucidated through X-ray crystallography, with TcBr_3 , TcBr_4 , TcCl_3 , and TcCl_4 featuring technetium in the +3 and +4 oxidation states.^[32–35]

The discovery of new binary halides of technetium is important to understand the potential speciation of technetium in halide-containing media, but also offers an intriguing possibility for the study of coordination chemistry. Like for other elements of the Periodic Table, binary halides in some cases represent self-adducted dimers of coordinatively unsaturated species that may govern the reactivity of such compounds, making them ideal starting materials. Additionally, such compounds shed light on the intrinsic differences of manganese, technetium and rhenium within group 7 as well as differences to group 6 and 8,^[36–38] e.g., for Tc and Fe, only 2 fluorides (TcF_5 and TcF_6) are known. Fe is the only other element within these nine elements for which only 2 fluorides are known. Several similarities between elements are observed across their group boundaries, as exemplarily illustrated in Figure 3. In this light,

Similarity due to isoelectronic anions [MO ₄] ⁻ [MO ₄] ²⁻ vs. RuO ₄ / OsO ₄			
Cr d ⁵ s ¹	Mn d ⁵ s ²	Fe d ⁶ s ²	Steric influence on maximum number of F atoms in fluorides s1 configuration
Mo d ⁵ s ¹	Tc d ⁶ s ¹	Ru d ⁷ s ¹	
W d ⁴ s ²	Re d ⁵ s ²	Os d ⁶ s ²	

Figure 3. Groups 6 and 7 show a similarity to their isoelectronic oxoanions. While there is a general similarity of the ionic radii of period 5 and 6 due to the lanthanoid contraction, e.g. the formation of ReF₇ is observed, but not of TcF₇. The “odd” ground state electron configurations of d⁶s¹ (Tc), d⁷s¹ (Ru) and d⁴s² (W) occur only once and are distributed apparently randomly across groups and periods.

understanding the chemistry of Tc which is in the center of this “block-of-nine” will lead to a deeper understanding of trends of chemistry of these elements.

Among the most important class of inorganic compounds are technetium oxyfluorides and fluorides, due to their role in the nuclear fuel cycle. Relatively few of these have been prepared. Some relevant contributions in recent years include [TcO₃F], [TcOF₅], [Tc₂O₂F₉]⁺ and [TcOF₄]⁺.^[39–41] Adsorption enthalpies of oxychlorides and oxyfluorides of group 7 elements (inter alia) have been correlated with their respective boiling points.^[42] Earlier results of this work were used for the characterization of bohrium (element 107) as the 4th member of the group 7 elements.^[43] After the development of a new synthesis for [TcF₆]²⁻ a number of nitrosyl-containing technetium fluoride complexes in low oxidation states have been prepared. There is a remarkable range of oxidation states in these compounds (I, II, III, IV and VI).^[39,44–50]

Of the pnictogens, in addition to the nitrogen compound Tc₄N₃,^[51] three phosphorus-containing compounds with technetium in oxidation states +1, +2, and +3 (TcP₃, TcP₄, Tc₂P₃, Tc₃P) have long been synthesized,^[52–54] occurring as phosphides or polyphosphides. In contrast, only two technetium oxides have been thoroughly characterized via X-ray techniques. Tc₂O₇ and TcO₂, which can be obtained by heating Tc₂O₇.^[55,56]

When expanding the focus from binary to ternary and quaternary technetium compounds, the number of crystallographically characterized structures increases significantly. Beginning with halogen oxides, four single-crystal structures have been identified. In addition to the oxyfluorides mentioned above there are TcOF₄, TcO₂F₃, and TcO₂F₃·TcO₃F, which crystallize with technetium in high oxidation states of +6 and +7.^[39–41] Via fluoride ion donation of TcO₂F₃ even a xenon compound with the formula TcO₂F₃·XeO₂F₂ as well as the antimony species TcO₂F₃·SbF₅ has been crystallized.^[44] In 2008, Bi₂Tc₂O₆ was synthesized from Bi₂O₃ and TcO₂ at 700 °C, with

Bi₃TcO₈ subsequently obtained through further reaction with Bi₂O₃.^[57] Additionally, a spinel-type compound with the composition TcCo₂O₄ has been structurally characterized in detail.^[58,59]

Moreover, compounds such as TcA₂O₄ (A = Mg, Mn, Sr), with technetium in the +4 oxidation state, have also been synthesized. The perovskite structure SrTcO₃ is a compound that has been extensively investigated, including temperature-dependent measurements and investigations of its magnetic behavior. Apart from the aforementioned perovskite, related compounds with the formula A'TcO₃ (A' = Ba, Ca, Cd, Pb) have also been structurally elucidated.^[58,60] Compounds containing higher oxygen content are A''₂Tc₂O₇ (A'' = Cd, Dy, Er, Nd, Sm).^[58–63]

Recent Developments in Pertechetate Chemistry

Many technetium compounds were synthesized starting from pertechetates, because the pertechetate anion [TcO₄]⁻ is the typical chemical form of Tc when separated from the fission product cocktail. Therefore, it is essential to consider both earlier findings and the most recent developments regarding pertechetates.

Pertechetates in Water

Up until recently, only six pertechetate salts have been known, while for its neighbors (chromate, molybdate, tungstate) several species are known already as mineralogical samples, and even more from chemical research.^[11] Extending the library of known pertechetate salts across the Periodic Table showed, for instance, the unexpected formation of a yellow manganese pertechetate complex.^[64] In the presence of mercury, both the formation of a mercury(I) pertechetate and a mercury(II)

pertechnetate could be observed, which may open the path to mixed oxidation state complexes, allowing to study the redox properties of such compounds in more detail. In lanthanoid complexes it could be shown that these may form with varying degrees of hydration, indicating that water plays indeed a pivotal role in Tc coordination chemistry, and that the removal of water may not just alter the solid-state structure, but also its redox chemistry. It is remarkable that, with exceptions, many compounds of Re and Tc of the s, p and d block were observed to be isostructural, while significant differences occur between the lanthanoid pertechnetates and the lanthanoid perrhenates, see Strub et al.^[64] The library of pertechnetate salts was also further extended with the synthesis of tetravalent zirconium, hafnium, and thorium pertechnetates.^[65,66] Investigations by small-angle X-ray scattering (SAXS) suggested that the $M^{IV}-TcO_4^-$ ($M = Zr, Hf$ and Th) bonding persists in solution, and pertechnetate shows more extensive binding to $Zr/Hf/Th^{IV}$ than perrhenate in solution.^[65,66] Simulating nuclear fuel reprocessing, $Zr-XO_4$ solvent extraction studies showed that pertechnetate can enhance extraction of Zr^{IV} .^[65]

Pertechnetate in Super Acidic Conditions

Likewise, as the solubility of Tc in water has been the most useful aspect of its chemistry in terms of biological applications, little is known about the edges of the pH scale and how pertechnetate reacts in super acidic or super basic solutions. Remarkable progress in the detection of Tc species in solution of sulfuric acid (H_2SO_4), perchloric acid ($HClO_4$), nitric acid (HNO_3), and triflic acid (CF_3SO_3H) has been made over the last years. Investigations by XAS and UV-VIS spectroscopy revealed, that the dominating species contain the metal in the oxidation states VII, V, and even VI.^[67–69] In order to understand the redox chemistry of Tc in these acids it is necessary to investigate the formed compounds in the solid state.

Pertechnetate is auto-reduced in triflic acid solutions, that is without the addition of a reducing agent. This is one indicator that reduction to lower valent species may occur given the right conditions, potentially even in the environment. Given different cations, more complex systems and solid-state networks could be synthesized,^[70,71] see Figure 4. Structurally, $TcO_3[CF_3SO_3]$ is very similar to the fluorosulfate $TcO_3[FSO_3]$, one of the few known oxoanionic technetium compounds.^[72]

The formation of polyoxometallates (POMs) of Tc from pertechnetate is another mystery that slowly gets solved,^[73] see Zegke et al.^[70] In solutions of pertechnetic acid these may form upon concentrating the stock solution, forming dark red materials that are highly oxygen- and moisture-sensitive. These Tc POMs contain Tc in different oxidation states (+V and +VII), and emerge from auto-reduction processes that depend on the Tc redox potentials and have not been observed by homolog Re compounds.

Synthetically, it will be challenging to transfer the chemistry of pertechnetic acid into non-aqueous systems. However, excluding water as a competing ligand, it may allow the isolation of systems that are too hygroscopic at ambient

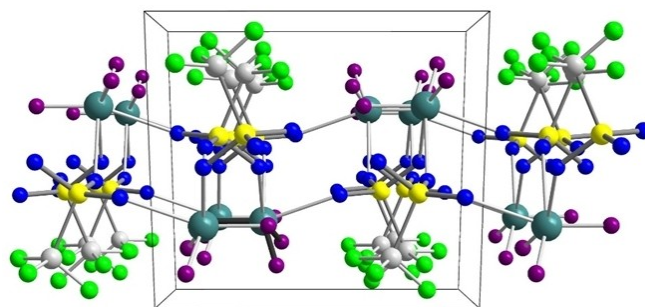


Figure 4. Crystal structure of $TcO_3[CF_3SO_3]$.^[69] The distances to the oxide ligands (violet) are by about 0.5 Å shorter than the respective distances to the triflate oxygens (blue), justifying the description of the compound as pertechnetyl triflate.

conditions, such as chromium pertechnetate. Further including redox-active cations in this system may help to analyze how strong the oxidation capacity of Tc is in the solid state, and whether reduced Tc(VI) species could be formed.

It has also not yet been achieved to synthesize pertechnetates with cations with a charge of +4 or higher, or for oxocations. More importantly though, the redox chemistry of technetium itself needs to be ultimately advanced to the chemistry of lower valent technetium. In particular, the chemistry of Tc(II), Tc(III) and Tc(VI) is very poorly understood, and these species may very likely play a key role in the reduction of Tc(VII) to Tc(I).^[21,74]

Pertechnetate in Super Basic Conditions

Contrary to this, in super basic conditions, pertechnetate shows the activation of the NH_4^+ ion, resulting in the formation of a nitridospecies.^[75,76]

The number of published studies on reactions of pertechnetates with strongly basic media is even smaller than that of reactions in super acidic media, especially when focusing on results validated with single crystal X-ray results. One major focus is on the radiolysis of pertechnetates in radioactive wastewater.^[77,78] A result of these studies is, for example, the reductive formation of $TcO_2 \cdot n H_2O$. If ammonium pertechnetate is used in hydroflux reactions the incorporation of nitrogen in form of $[TcO_3N]^{2-}$ anions can be observed, see also recent work.^[75,76] Accordingly, the oxidation state of +VII remains unchanged and seems to be the most dominant one besides +IV even under extremely alkaline conditions. However, in an electrochemical cell relatively stable compounds with the +V oxidation state can also be obtained. However, the latter disproportionate also to +IV and +VII species.^[79]

III Organometallic and Coordination Chemistry

The overall picture in organometallic chemistry of Tc is that there are several “islands” of knowledge developing around stable core structures that are partly originating from an

interest in radiopharmaceuticals. Despite the general motivation to develop stable, polydentate ligands which allow a tailoring of their coordinating properties and robust anchoring for the conjugation of technetium to biovectors, also the development of new, reasonably stable small fundamental structural motifs containing ligands that do not usually undergo further reactions (such motifs are referred to as „cores“; e.g. $fac\{-Tc(CO)_3\}^+$, $\{TcO\}^{3+}$, $\{TcN\}^{2+}$, $\{TcO_3\}^+$) are on-going. These allow for the systematic study of the coordination chemistry of Tc as has been exemplified in a number of different ways in recent years as will be outlined in this section. One major challenge for Tc chemistry is still to understand the fundamental binding properties and differences of and between ligands or ligand classes as well as their influence on the reactivity of Tc. Some compound classes, such as side-on bonded alkyne complexes, are completely missing, while others such as carboxylates or thioureas are rare while having implications for the geochemical context as they can stabilize intermediate oxidation states and modify the redox and solubility properties of Tc.^[80]

Advances Towards Radiopharmacy

Given their well-known tendency to provide systematic insights into the chemistry of transition metals, carbonyl complexes were among the first well-defined technetium coordination compounds.^[81–83] Despite a few long-known compounds, however, technetium carbonyls have received more attention in recent years not only due to their potential application in radiopharmaceuticals,^[84,85] but also as they may be relevant to the nuclear waste problem. Compounds containing the $fac\{-Tc(CO)_3\}^+$ core are stable *in vivo* and readily available for the medicinally relevant nuclear isomer ^{99m}Tc by one-pot reduction of $^{99m}TcO_4^-$.^[86] The water ligands of the intermediate $fac\{-^{99m}Tc(CO)_3(H_2O)_3\}^+$ readily exchange for a variety of ligands. In the radiopharmaceutical context the most relevant are potentially chelating three-dentate ligands that can be linked to biological markers examples include chelators based on iminodiacetate,^[87,88] pyridine, imidazole,^[89–92] or cyclopentadienyl (Cp),^[85,93,94] while also exotic ligands such as coated gold

nanoparticles have been used.^[95] The lipophilicity can be adjusted by both the technetium core structure as well as the ligand motifs. Exemplarily, $^{99m}Tc(CO)_3\text{-mebrofenin}$ is more lipophilic compared to compounds with a different ^{99m}Tc core structure.^[96] Similarly and remarkably, the small size of the $[^{99m}Tc(CO)_3(\eta^5\text{-C}_5\text{H}_4\text{R})]$ (R = bioactive moiety) unit makes it biologically equivalent to the attachment of a phenyl group, indicating that it shows little influence on the biological activity of a conjugated biomarker compared to the unconjugated biomarker.^[97] An orthogonal approach to three-dentate chelators is the use of bidentate chelators e.g. bipyridines or picolinic amides together with an additional capping ligand e.g. isocyanides or imidazoles in a “1 + 2” approach that offers the possibility for two orthogonal ways of bioconjugation and tailoring of the complex properties.^[98–102] Some examples for these radiopharmaceutical principles with illustrative examples for the $fac\{-Tc(CO)_3\}^+$ core are given in Figure 5.

Advances in Fundamental Carbonyl Chemistry

Beyond potential radiopharmaceutical applications, Tc carbonyl species were identified in liquid nuclear waste supernatants at the Hanford Site by X-ray absorption spectroscopy and ^{99}Tc NMR spectroscopy.^[20,74,103] The formation of $fac\{-Tc(CO)_3\}^+$ such as $[^{99}Tc(CO)_3(\text{gluconate})]^{2-}$ or $fac\{-Tc(CO)_2(NO)\}^{2+}$ is possibly the result of Tc(VII) reduction by the radiolysis products of nitrate, water and organic components.^[104] The classic starting materials for group 7 carbonyl chemistry are $[M_2(CO)_{10}]$ and $[MX(CO)_5]$ (M = Mn, Tc, Re; X = Cl, Br, I). The high-pressure syntheses for the volatile $[Tc_2(CO)_{10}]$ and its equally volatile halogenation products $[TcX(CO)_5]$ (X = Cl, Br, I) are unfortunately mostly incompatible with radiation protection requirements, making them essentially inaccessible. Therefore, considerable efforts for legislation-compliant low-pressure alternatives have been made in recent years and even the ^{99m}Tc analogs have been studied.^[102,105–111] In a related line of research, work on the iconic, but elusive higher carbonyl compounds $[Tc(CO)_6]^{+}$, $[TcH(CO)_5]$ and $[TcF(CO)_5]$ provided a plethora of Tc carbonyl chemistry and a variety of decomposition pathways. Decarbonylation

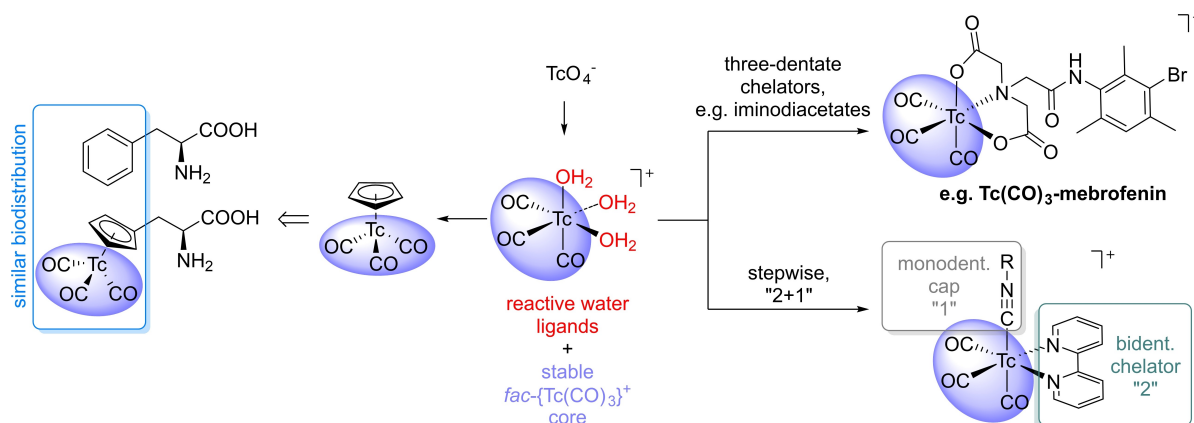


Figure 5. Examples for the functionalization of the $fac\{-Tc(CO)_3\}^+$ core.

followed by aggregation to multi-nuclear clusters is the “normal” decomposition pathway. Particularly ligands with either a large *trans*-influence or those exerting a strong *cis*-effect (i.e., strong π -donors) facilitate decarbonylation of the CO ligands in *trans*- or *cis*-position respectively. Both effects play a role in stabilizing the *fac*- $\{\text{Tc}(\text{CO})_3\}^+$ core over the isomeric *mer*- $\{\text{Tc}(\text{CO})_3\}^+$. Similarly, they make molecules such as $[\text{Tc}(\text{CO})_6]^+$ and $[\text{TcF}(\text{CO})_5]$ relatively unstable with respect to decarbonylation. Very recently, the extremely volatile and sensitive $[\text{TcH}(\text{CO})_5]$ was finally authenticated by NMR and vibrational spectroscopy. It is surprisingly more inert towards CO-displacement reactions than previously thought, especially in comparison to its group neighbors. That being said, the quest for $[\text{TcF}(\text{CO})_5]$ and related mixed carbonyl fluoride complexes has not yet been settled as only one clustered decomposition product has been identified in this line of research so far.^[84,105–112]

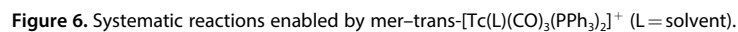
A sterically shielded series of isocyanide analogs of the archetypical $[\text{TcH}(\text{CO})_5]$, $[\text{Tc}(\text{CO})_5]$ and $[\text{Tc}(\text{CO})_5]^-$ was developed to study the fundamental properties of technetium complexes with more exotic co-ligands. $[\text{TcH}(\text{CO})(\text{CNp}-\text{F}-\text{Ar}^{\text{DarF2}})_4]$, $[\text{Tc}(\text{CO})(\text{CNp}-\text{F}-\text{Ar}^{\text{DarF2}})_4]$ and $[\text{Tc}(\text{CO})(\text{CNp}-\text{F}-\text{Ar}^{\text{DarF2}})_4]^-$ represent rare examples of an unambiguously confirmed technetium hydride, a molecular, monomeric technetium(0) species and the first authenticated and structurally characterized technetium complex with the central metal in a formally negative oxidation state of -I.^[113–115] Consistent with the formally negative oxidation state and providing a proof of concept for the envisioned reactivity, the technetium atom in $[\text{Tc}(\text{CO})(\text{CNp}-\text{F}-\text{Ar}^{\text{DarF2}})_4]^-$ is nucleophilic undergoing nucleophilic substitution at ClSnMe_3 to give the first compound with a technetium-tin bond: $[\text{Tc}(\text{SnMe}_3)(\text{CO})(\text{CNp}-\text{F}-\text{Ar}^{\text{DarF2}})_4]$. A reaction with HCl first leads to $[\text{TcH}(\text{CO})(\text{CNp}-\text{F}-\text{Ar}^{\text{DarF2}})_4]$, which is protonated under H_2 loss to give the original starting material $[\text{TcCl}(\text{CO})(\text{CNp}-\text{F}-\text{Ar}^{\text{DarF2}})_4]$. Such protonation reactions under coordination of the corresponding acid anion have in the meantime also been reported for $[\text{TcH}(\text{CO})_5]$.

The underlying reactivity seems to be general as the phosphine analog *mer-trans*- $[\text{TcH}(\text{CO})_3(\text{PPh}_3)_2]$ reacts similarly. The retention of the stereochemistry in the phosphine complexes indicates that the loss of H_2 and coordination of the anion are very quick. Reactions of *mer-trans*- $[\text{TcH}(\text{CO})_3(\text{PPh}_3)_2]$ with protic acids of weakly coordinating anions instead enable the stabilization and preparation of highly reactive solvent complexes *mer-trans*- $[\text{Tc}(\text{L})(\text{CO})_3(\text{PPh}_3)_2]^+$ (L=solvent). These complexes can be prepared at the gram scale and act as synthons for the coordinatively unsaturated $16e^-$ species $[\text{Tc}(\text{CO})_3(\text{PPh}_3)_2]^+$. Therefore, they represent a convenient platform for the study of technetium complexes with a large variety of ligands largely retaining the parent compound's structure. The reaction products retain the *mer*- $\{\text{Tc}(\text{CO})_3\}^+$ core or decarbonylate once to yield *cis*- $\{\text{Tc}(\text{CO})_2\}^+$ for bidentate or sufficiently π -donating ligands (see below). In this way technetium(I) complexes of MO_4^- (M=Tc, Re), ER_2 (E=S, Se, Te), BH_4^- , NO_2^- , NO_3^- , *cyclo*-oxycarbenes, organyl and other previously elusive ligands could be synthesized (some examples are shown in Figure 6).

Alkynyl complexes in particular were prepared from lithium alkynyls and envisioned as promising intermediates having in mind the on-going challenge of preparing technetium complexes with a side-on bonded alkyne ligand. A different strategy that has often been successful for the isolation of transition metal complexes with elusive ligands such as N_2 , H_2 , alkenes or alkynes is the use of pincer-type ligands with a *P,N,P* donor set. Such complexes have only recently been reevaluated and studied somewhat systematically. The complexes show *fac-mer*-isomerism, decarbonylation reactions and HX activation. The latter is thought to be enabled by internal deprotonation with an amido-type aromatization/dearomatization metal-ligand cooperativity pathway providing another route to Tc alkynyl complexes. Such reactions are postulated to proceed via transiently coordinated alkyne ligands, but no experimental evidence for such complexes was observed.^[116–118] Contrastingly, the protonation of the alkynyl ligands in *mer-trans*- $[\text{Tc}(\text{CCR})(\text{CO})_3(\text{PPh}_3)_2]$ indeed led to new ^{99}Tc NMR resonances potentially consistent with a side-on bonded alkyne ligand or its isomeric vinylidene carbene analog, one carbonyl ligand is lost in the process resulting in an inseparable 1:1 mixture of *cis,trans*- $[\text{Tc}(\text{L})(\text{CO})_2(\text{PPh}_3)_2]^+$ and *trans*- $[\text{Tc}(\text{CO})_4(\text{PPh}_3)_2]^+$. The synthesis of the first technetium alkynyl complexes and their methyl and phenyl analogs emphasizes the marked importance of the choice of organometallic reagents in organotechnetium chemistry. Grignard reagents that work well for the preparation of high-valent organotechnetium chemistry, lead to halide transfer instead of aryl or alkyl transfer, while organolithium reagents lead to the desired organotechnetium species. The strategy has also been extended to the replacement of chlorido complexes with the $\{\text{Tc}^{\text{V}}\text{N}\}^{2+}$ core.^[119–122]

Advances in transmetalation reactions

In similar reactions, the treatment of both the Tc^{IV} starting material $[\text{TcCl}_4(\text{PR}_3)_2]$ ($\text{PR}_3 = \text{PPh}_3$ and PET_2Ph), and the Tc^{III} starting materials $[\text{TcCl}_3(\text{PR}_3)_3]$ ($\text{PR}_3 = \text{PMe}_2\text{Ph}$, PMePh_2 , and PET_2Ph) and $[\text{TcCl}_3(\text{PPh}_3)_2(\text{CH}_3\text{CN})]$ with arylmagnesium bromides in benzene yields deep blue η^1 -aryl Tc^{III} complexes of the composition $[\text{Tc}(\eta^1\text{-aryl})_3(\text{PR}_3)_2]$. These are only moderately stable depending on the phosphine used ($\text{PMe}_2\text{Ph} < \text{PET}_2\text{Ph} < \text{PMePh}_2 < \text{PPh}_3$), and they decompose by forming oily brown products. Interestingly, while the triphenylphosphine complex $[\text{Tc}(\text{Ph})_3(\text{PPh}_3)_2]$ is stable on air. As its rhenium analog, the latter product is not soluble in any common solvents preventing an unambiguous structural elucidation and ongoing reactions. This problem was overcome by preparation of an analogous complex containing trifluoromethylated aryl ligands: the well-soluble complex $[\text{Tc}\{\text{Ph}(\text{CF}_3)_2\}_3(\text{PPh}_3)_2]$. While Grignard reagents readily led to displacement of the chlorido and acetonitrile ligands from $[\text{TcCl}_3(\text{PPh}_3)_2(\text{CH}_3\text{CN})]$, the corresponding aryl lithium reagent attacks the coordinated acetonitrile forming the first azavinylidene complex of technetium: $[\text{Tc}\{\text{NC}(\text{CH}_3)\text{Ph}(\text{CF}_3)_2\}_3\{\text{Ph}(\text{CF}_3)_2\}_2(\text{PPh}_3)_2]$.^[123] Contrastingly, $[\text{TcCl}_3(\text{PPh}_3)_2(\text{CH}_3\text{CN})]$ reacts with lithium aryl tellurolates and selenolates under selective halide replacement to give the corresponding $[\text{Tc}^{\text{III}}(\text{ArE})_3]$



(PPh₃)(CH₃CN)] (E = Se, Te; Ar = phenyl, 2,6-Me₂phenyl, mesityl) retaining one acetonitrile and one PPh₃ ligand, while reactions of the technetium(V) starting material [TcOCl₄][−] give [Tc^{VO}(ArE)₄][−] (E = Se, Te; Ar = phenyl).^[124] Although similar complexes with other simple ligands such as technetium(III) carboxylates have rarely been reported despite their obvious importance in geocological systems, the recent development of potential Tc carboxylate starting materials is encouraging.^[125–127]

Another interesting class of compounds are the water- and air-stable organometallic phenyl complexes with a nitridotechnetium(V) core. A transmetalation from PhLi to Starting from [TcNCl₂(PPh₃)₂] yields [TcNPh₂(PPh₃)₂]. Moreover, when starting with (NBu₄)[TcNCl₄] and the N-heterocyclic carbene (NHC) 1,3,4-triphenyl-1,2,4-triazol-5-ylidene (HL^{Ph} or its methoxy-protected form), the chlorido compound [TcNCl₂(HL^{Ph})₂] is formed, while no reaction was observed between the NHC and [TcNPh₂(PPh₃)₂]. The desired mixed NHC/aryl complex [TcNPh₂(HL^{Ph})₂] had to be accessed by transmetalation from PhLi to [TcNCl₂(HL^{Ph})₂] instead. Interestingly, the chemistry of the NHC is entirely different from its Re analog, in which CH activation and orthometalation are dominating reactions.^[128] In addition to this, Braband and co-workers have been successful in synthesizing water-stable organometallic ⁹⁹Tc-NHC complexes. Starting from the ethylene glycolato complex [Tc^{VO}(glyc)₂][−] the authors have characterized three different ⁹⁹Tc^{VO}₂-NHC complexes (with NHC = 1,3-dimethylimidazole-2-ylidene (L1), 1,1'-methylene-3,3'-dimethyl-4,4'-diimidazole-2,2'-diylidene (L2), and 1,1'-methylene-3,3'-diethyl-4,4'-diimidazole-2,2'-diylidene (L3)). It was shown that monodentate NHC complexes are hydrolytically unstable, while bidentate complexes are water-stable over a broad pH range, allowing the interconversion of the [Tc^{VO}O₂(NHC)₂]⁺ into [Tc^{VO}OCI(NHC)₂]²⁺ in the presence of aqueous HCl. While these ⁹⁹Tc^{VO}₂-NHC complexes can also be made *via in situ* deprotonation of imidazolium salts (avoiding the use of free NHCs), the remarkable stability and pH-dependent reactivity may serve as a steppingstone towards ^{99m}Tc-NHC complexes.^[129] Of similar medicinal interest are the surprisingly robust bis(arene) cations [Tc(arene)₂]⁺ that were recently reinvestigated and developed towards bioconjugates. Interestingly, they were found to be much more easily and reliably formed at the low concentrations governing the chemistry of ^{99m}Tc compared to their ⁹⁹Tc analogs.^[130]

Advances in Isocyanide Chemistry

While NHC and arene complexes may be promising radiopharmaceuticals, the Tc isocyanide complex under the trade-name cardiolite® is one of the most frequently applied radiopharmaceuticals to date. The fundamental study of transition metal isocyanide chemistry was governed by the long standing believe that isocyanides are a homogeneous compound class with little electronic variability behaving equivalently to the commercialized small alkyl isocyanides CN^tBu or CNCy and were usually considered as tailorable electronic equivalents of CO. The disparity between seemingly random but sometimes

strongly reducing behavior with an often nearly non-existent π -acceptor behavior in these alkyl isocyanides was largely ignored. This believe was recently challenged for technetium using the sterically demanding terphenyl isocyanides CNAr^{Dipp2} (CN(C₆H₃(*o,o*-bis(2,6-diisopropylphenyl))) and CNAr^{Mes2} (CN(C₆H₃(*o,o*-bis(2,4,6-trimethylphenyl))))). In contrast to the previous believe-set, not only low-valent, i.e. Tc(I) and Tc(III) complexes with additional carbonyl, nitrosyl and chlorido co-ligands, could be isolated, but surprisingly stable Tc^V complexes with complementary nitrido- and aryl imido ligands have been prepared. Particularly the *cis-trans* configuration of the isocyanide ligands to the PPh₃ co-ligands in the Tc^V complexes was surprising and can be fine-tuned by careful choice of the ligand, with the CNAr^{Dipp2} supporting the *trans* arrangement, while the CNAr^{Mes2} allows for the *cis* geometry.^[131] A common rationale that enabled the prediction of the coordination behavior of isocyanide ligands as well as the stability of the high-valent complexes was developed: the Surface-Averaged-Donor-Acceptor-Potential (SADAP) combining steric and electronic effects in the uncoordinated ligands. The SADAP concept was originally designed, however, to understand the marked differences in isocyanide reactivity towards Tc^I carbonyl starting materials and the potential of different isocyanides to replace carbonyl ligands. Treatment of *fac*-[Tc(CO)₃(CNR)₂Cl] (CNR = CNⁿBu or CN^tBu) with the sterically demanding isocyanide CNp-FAr^{DarF2} [DarF = 3,5-(CF₃)₂C₆H₃] results in the loss of the CO groups forming *mer,trans*-[Tc(CNp-FAr^{DarF2})₃(CNR)₂Cl], which in turn can be substituted in a halide exchange reaction, culminating in a Tc complex with three different isocyanide groups when the initial material contains CNⁿBu and the last step is performed with CN^tBu. Using *p*-fluorophenyl isocyanide, CNPh^{PF} leads to the hexakis(isocyanide)technetium(I) cation through an exchange of all ligands in both [Tc₂(CO)₆(μ -Cl)₃][−] or *fac*-[Tc(CO)₃(CNR)₂Cl].^[132] The hexakis(isocyanide)technetium(I) cation can also be made with *p*-isocyanoethynylbenzene CNPh^{PC≡CH} as the ligand.^[133]

Advances in the Chemistry with Face-Capping Ligands

Another remarkable example of a single ligand forming stable complexes with the seven most common oxidation states of technetium is the „Kläui ligand“, η^5 -(cyclopentadienyl)tris(dimethyl phosphito-*P*)cobaltate(III) (L^{OMe}, Figure 7).^[134] Tc is coordinated via the oxo group on the P atoms of the ligand, while the coordination sphere is complemented by strongly bound nitrosyl, oxido or nitrido ligands, or less tightly binding halido and phosphine co-ligands. Interestingly, all members of this series ([Tc^I(NO)Cl(PPh₃)(L^{OMe})], [Tc^{II}(NO)Cl₂(L^{OMe})], [Tc^{III}Cl₂(PPh₃)(L^{OMe})], [Tc^{IV}Cl₃(L^{OMe})], [Tc^VOCI₂(L^{OMe})], [Tc^VNCl(PPh₃)(L^{OMe})], [Tc^{VI}NCl₂(L^{OMe})], and [Tc^{VII}O₃(L^{OMe})] are stable in water and on air. They thus provide unique starting materials, particularly for the study of technetium chemistry with the metal in rarer oxidation states +2 and +6, where few examples of suitable starting material platforms have been reported and the corresponding chemistry seen little advancement in recent times. Unfortunately the replacement of the chlorido ligand in

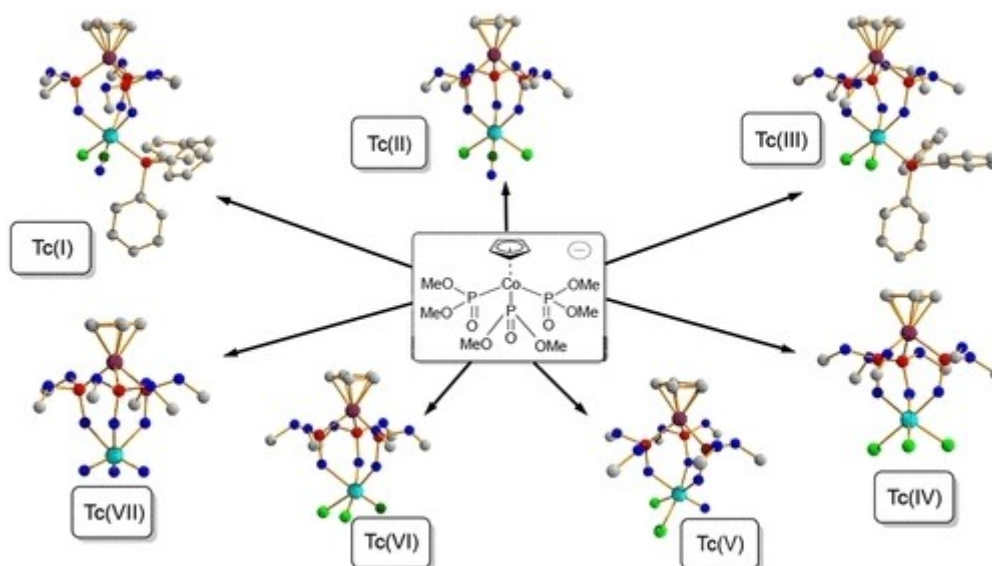


Figure 7. The “Kläui ligand” and its complexes with Tc from oxidation states +1 to +7. Figure taken from Grunwald.^[134]

$[\text{Tc}^{\text{I}}(\text{NO})\text{Cl}(\text{PPh}_3)(\text{L}^{\text{OMe}})]$ by Ag^+ as halide scavenger in hopes to isolate reactive solvent complexes for on-going ligand exchange reactions led to the formation of a complex mixture of redox-pairs between $[\text{Tc}^{\text{I}}(\text{NO})\text{Cl}(\text{PPh}_3)(\text{L}^{\text{OMe}})] + \text{Ag}^+$ and the crystallographically and spectroscopically characterized adduct $[\{\text{Tc}^{\text{I}}(\text{NO})(\text{PPh}_3)(\text{L}^{\text{OMe}})\mu\text{-Cl}\}\text{Ag}\{\mu\text{-ClTc}^{\text{I}}(\text{NO})(\text{PPh}_3)(\text{L}^{\text{OMe}})\}]^+$ and the oxidation/reduction products.^[135]

The “Kläui ligand” is often considered a structural and electronic equivalent to cyclopentadienyl (Cp). In contrast to several hundred structurally characterized rhenium cyclopentadienyl complexes, little is known about the chemistry of Cp complexes with Tc beyond complexes of the type $[\text{Tc}(\text{CO})_3(\text{Cp}^R)]$. A platform for the systematic study of technetium Cp chemistry was identified by Abram and co-workers. The relatively robust $\{\text{Tc}(\text{NO})(\text{Cp})(\text{PPh}_3)\}^+$ core was prepared by a much simpler route than its rhenium analog: KCp and $[\text{Tc}^{\text{I}}(\text{NO})\text{-X}_2(\text{PPh}_3)_2(\text{CH}_3\text{CN})]$ ($\text{X} = \text{Cl}, \text{Br}$) react to the air-stable starting materials $[\text{Tc}^{\text{I}}(\text{NO})(\text{Cp})(\text{PPh}_3)\text{X}]$.^[136] Stable complexes under exchange of the coordinated halide anions can be prepared by direct ligand exchange using the protic acids or halide scavenging salts of ligands such as I^- , I_3^- , F_3CSO_3^- , CF_3COO^- , or SCN^- as well as suitable neutral donor ligands such as phosphine chalcogenides. In contrast to the difficulties outlined for the “Kläui”-analog above, the halido ligands can also easily be scavenged in the presence of suitable solvent ligands such as acetonitrile or pyridine and at least the acetonitrile compound shows promise as a starting material for ligand exchange reactions.^[137] One prerequisite is, however, that the incoming ligands binds stronger to the $\{\text{Tc}(\text{NO})(\text{Cp})(\text{PPh}_3)\}^+$ fragment than the chlorido moiety in the starting material, since a self-quenching process otherwise leads to the brick-stable, unreactive chloride-bridged dimer $[\{\text{Tc}^{\text{I}}(\text{NO})(\text{Cp})(\text{PPh}_3)\}\mu\text{-Cl}\{\text{Tc}^{\text{I}}(\text{NO})(\text{Cp})(\text{PPh}_3)\}]^+$. This is for example the case in reactions aimed at the coordination of alkynes. Nevertheless, multifaceted decomposition reactions take place when such reac-

tions are performed in the presence of both alcohols and alkynes leading to rare examples of phosphonium stabilized Fischer-type carbene complexes.^[138]

The Connection of Organometallic Chemistry to Applied Fields

Overall, the fundamental coordination chemistry of technetium and the influence of different ligands on the spectroscopic signatures remain underdeveloped. The focus of fundamental studies needs to aim at providing comprehensive insights about the coordination properties of the element with various ligands. Organometallic chemistry interconnects applied fields such as radiopharmacy, geoecology and nuclear waste. Recently, radiopharmaceutical compounds have been proposed for the use in environmental remediation.^[139] In the latter fields this may include the identification of potential coordination modes and the development of model systems that could lead to less ambiguous interpretation of speciation data obtained by powerful and specialized techniques such as XAS and ^{99}Tc NMR but also to understand the electrochemical behavior of the element. In terms of radiopharmacy and although the synthetic chemistry of ^{99}Tc usually not directly translatable to the chemistry of $^{99\text{m}}\text{Tc}$, where entirely different protocols have to be developed due to the different kinetic regimes, knowledge about the interaction of technetium with simple and complex ligands can help to understand issues regarding surprising biodistribution or stability and finally guide the optimization of ligand systems and linkers for bioconjugation. Some distinct differences between technetium and rhenium may add an additional layer of fog to the understanding of $^{99\text{m}}\text{Tc}$ chemistry, when comparing its chemistry to a rhenium surrogate instead of actual technetium given redox, reactional and structural differences between the elements.

IV Computational Chemistry

The role of “applied” DFT calculations for the understanding of Tc chemical shifts in NMR has already been emphasized above (section I). This part deals with the more fundamental approach understanding the Tc bonding behavior in certain pertechnetate and related compounds.

Utilization of Pertechnetate and Related Compounds in Crystal Engineering: A Focus on Matere Bonds

The role of technetium compounds, particularly pertechnetate in crystal engineering has gained significant attention due to their ability to participate in non-covalent interactions.^[140] These interactions often involve technetium acting as an electron acceptor, facilitating the formation of so called matere bonds - a recently recognized type of interaction specific to the group 7 elements manganese, technetium and rhenium, equivalent to the well known halogen bonds in group 17.^[141] Matere bonds (MaBs) are characterized by the attractive interaction between an electron-rich atom, such as oxygen, and the metal center, in most cases belonging to a permetalate anion, such as $[\text{TcO}_4]^-$, $[\text{ReO}_4]^-$, or $[\text{MnO}_4]^-$.^[140–145] This section highlights the significance of these bonds in crystal engineering focusing on technetium, underpinned by specific examples drawn from the Cambridge Structural Database (CSD) and recent theoretical studies.

Matere Bonds in Pertechnetate and Perrhenate Compounds

Recent research has highlighted the distinctive behavior of pertechnetate and perrhenate anions in forming anion-anion interactions. These anions serve, despite their negative charge, as relatively strong electron acceptors, with technetium and rhenium participating in highly directional and often linear non-covalent interactions. These interactions are driven by σ -holes—regions of reduced electron density—located on the metal centers of the anions. For instance, a study by Daolio *et al.* provided both experimental and theoretical evidence for the

presence of anion...anion interactions in crystalline perrhenate and pertechnetate salts.^[141] This concept was first described for halogens (“halogen bonds”) and has been established in most groups of the Periodic Table since. In these structures, the oxygen atom of one anion interacts with the metal center (Tc or Re) of another anion, leading to the formation of well-defined supramolecular structures such as anionic dimers or extended polymeric chains. These supramolecular motifs significantly influence the overall architecture and stability of the crystal structures, making matere bonds a critical element in the design of functional materials.

Two specific examples illustrate the significance of these interactions. The first example, corresponding to CSD refcode AMOGIS,^[146] shows pertechnetate anions forming infinite zig-zag 1D chains through directional matere bonds ($\text{O}\cdots\text{Tc}-\text{O}$, 172.9°) flanked by 3,4,6,7,8,9-Hexahydro-2H-pyrimidino(1,2-a)pyridinium cations (Figure 8). The second example, represented by refcode NAPVUZ,^[141] involves melaminium perrhenate (2,4,6-triamino-1,3,5-triazin-1-ium perrhenate). In the solid state (Figure 8b), this compound exhibits anion...anion interactions where the oxygen of one anion approaches the rhenium atom of another along the extension of a $\text{Re}-\text{O}$ covalent bond, forming linear infinite chains. The strong directionality of these interactions (177.7°) aligns with the small size of the σ -hole and helps to minimize repulsion with the O-atoms of the adjacent anion.

Selected examples from the Cambridge Structural Database (CSD)

A comprehensive analysis of the Cambridge Structural Database (CSD) reveals numerous instances where pertechnetate and perrhenate anions engage in matere bonds. Previous studies have shown that approximately 19% of structures containing $[\text{ReO}_4]^-$ anions exhibit these interactions, with a significant proportion (around 75%) involving anion...anion contacts.^[141] These interactions are characterized by highly directional geometries, with distances shorter than the sum of van der Waals radii, indicating strong, close-range interactions between the involved atoms. Such directional interactions frequently lead to

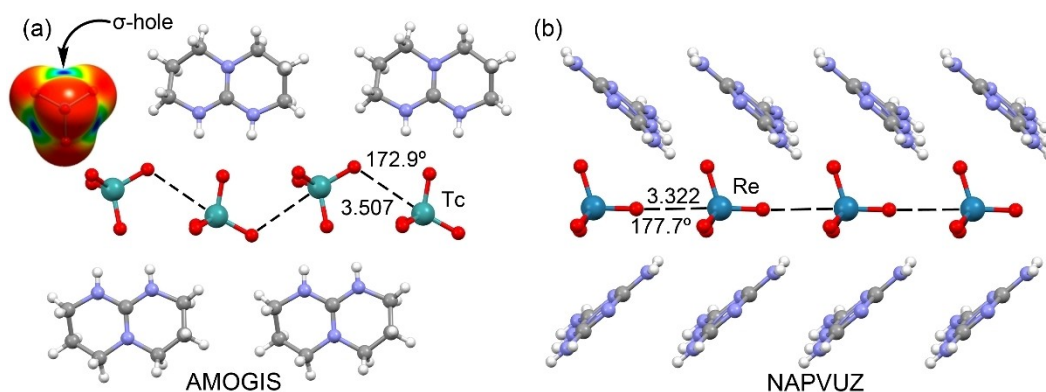


Figure 8. Ball and stick representation of the X-ray structures AMOGIS (a) and AZEMUO (b). Distances in Å. Color code: Carbon grey, Oxygen red, Nitrogen blue, Technetium teal, Hydrogen light grey.

the formation of linear chains, as depicted in Figure 8, infinite anionic networks, or other extended supramolecular assemblies, highlighting the potential of $[\text{TcO}_4]^-$ and $[\text{ReO}_4]^-$ as versatile building blocks in crystal engineering.^[140–142]

However, matere bonds are not confined to oxoanionic species alone. An intriguing example is illustrated in Figure 9, where anion...anion MaBs drive the formation of an infinite 1D assembly.^[147] In this structure, the lone pair on the nitrogen atom of one chlorido-nitrido-technetate(VI) anion is directed towards the Tc atom of the adjacent $[\text{TcNCl}_4]^-$ anion, opposite to the Tc–N bond (at the σ -hole location, see Figure 9, right). This 1D assembly is flanked by catena-((μ 2–18-crown-6)-cesium) counterions, creating an “infinite sandwich” structure with Cs^+ cations intercalated between crown ether molecules.

In addition to anion...anion interactions shown in Figures 8 and 9a, the CSD also documents cases where $[\text{TcO}_4]^-$ and $[\text{ReO}_4]^-$ anions participate in interactions with atoms that can donate electrons from non-bonding orbitals, such as nitrogen or chlorine.^[140] These interactions further expand the utility of these anions in constructing diverse supramolecular architectures. Although the number of structures containing $[\text{TcO}_4]^-$ and $[\text{MnO}_4]^-$ anions is relatively limited compared to $[\text{ReO}_4]^-$,^[141] the observed matere bonds in these systems are consistent with the general trend that heavier elements in a group (such as Re compared to Tc or Mn) are more prone to act as electrophilic

centers, forming stronger and more directional non-covalent interactions.

Beyond $[\text{TcO}_4]^-$ and $[\text{ReO}_4]^-$ anions acting as electron acceptors, neutral Tc derivatives have also been described as matere bond donors, significantly influencing the solid-state structure of these compounds.^[142,144] An illustrative example is shown in Figure 9b, featuring bis(μ 2-acetato)-tetrachlorido-di-technetium(III), refcode OSICUP.^[33–35] This structure consists of two bridging trans-acetate ligands and four terminal chlorido ligands. Notably, the compound propagates in the solid state through four symmetrically equivalent $\text{Tc}\cdots\text{Cl}$ MaBs, forming a supramolecular 1D assembly. The $\text{Tc}\cdots\text{Cl}$ distance is remarkably short, only 0.4 Å longer than the sum of the covalent radii, highlighting the strength of these interactions. This represents a unique example of a MaB involving Tc in a low oxidation state, where the σ -hole is located opposite the Tc–Tc bond (see Figure 11, right).

Finally, matere bonds have also been observed in metal-coordinated $[\text{TcO}_4]^-$ anions. One notable structure is illustrated in Figure 10. It corresponds to a hydrated magnesium pertechnetate with the formula $\text{Mg}(\text{H}_2\text{O})_4[\text{TcO}_4]_2$. In this structure, the Mg metal center is coordinated in an elongated octahedral geometry by four water molecules in the equatorial plane and two oxygen atoms from $[\text{TcO}_4]^-$ units that are trans to each other. In the extended structure, this compound forms two-

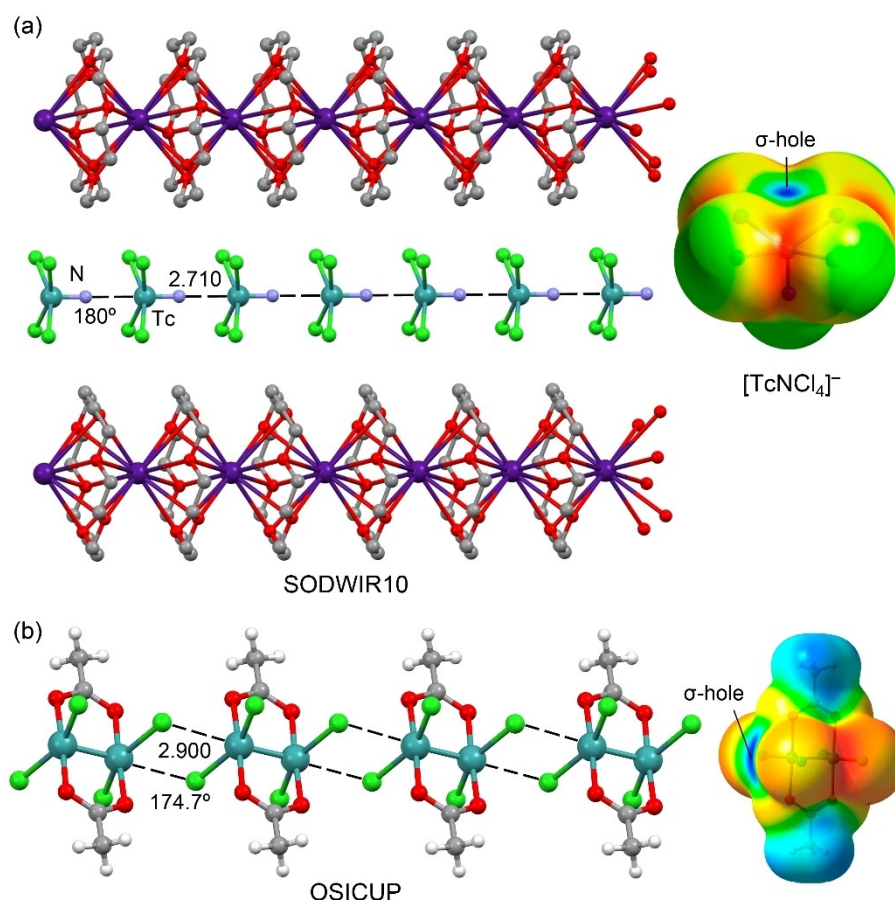


Figure 9. (a) Left: Ball and stick representation of the X-ray structure SODWIR10. Distance in Å. Right: MEP surface of $[\text{TcNCl}_4]^-$ anion. (b) Left: Ball and stick representation of the X-ray structure OSICUP. Distance in Å. Right: MEP surface of bis(μ 2-acetato)-tetrachlorido-di-technetium(III).

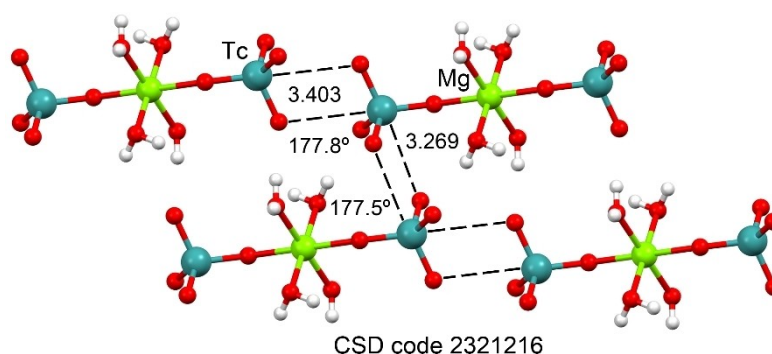


Figure 10. Partial view of the X-ray structure of $\text{Mg}(\text{H}_2\text{O})_4[\text{TcO}_4]_2$. Distances in Å.

dimensional assemblies characterized by two types of MaBs, as shown in Figure 11b and similar to those observed in HETRUT. One MaB is formed opposite to the Tc–O bond that coordinates to the Mg^{2+} ion (3.403 Å), with a nearly linear O–Tc...O angle (177.8°), which is typical of σ -hole interactions. The second MaB is formed opposite to a Tc=O bond, with a shorter distance (3.269 Å) and comparable linearity (177.5°).

Theoretical Insights into Matere Bond Formation

To gain a deeper understanding of the nature of matere bonds, several theoretical approaches have been employed, including molecular electrostatic potential (MEP) surface calculations, quantum theory of atoms-in-molecules (QTAIM), and non-covalent interaction (NCI) plot analyses. These methods offer detailed insights into the electronic environments that facilitate the formation of these interactions. For instance, MEP calculations, such as those depicted in Figures 8–10, reveal that the σ -holes on the metal centers of $[\text{TcO}_4]^-$, $[\text{ReO}_4]^-$ and $[\text{TcNCl}_4]^-$ are critical sites for electron donation from neighboring molecules or anions. This electron donation results in the formation of strong and directional matere bonds.

Other computational tools, such as QTAIM and NCIplot analyses, are equally valuable for confirming the existence and character of these bonds. QTAIM identifies bond critical points (BCPs) and bond paths that connect the interacting atoms, while NCIplot analysis uses reduced density gradient (RDG) isosurfaces to visualize noncovalent interactions in real space. These isosurfaces are color-coded to indicate the nature of the interactions: yellow and red represent weak and strong repulsive interactions, while green and blue denote weak and strong attractive interactions. Thus, these analyses not only allow for the visualization of matere bonds within crystal structures but also quantify the strength and directionality of these interactions, offering a deeper understanding of how these non-covalent forces contribute to the overall stability and organization of the crystal lattice.

Figure 11 provides such analyses for two of the examples discussed above: SODWIR10 and OSICUP.^[33–35] In the former, a tetrameric assembly is illustrated, where the combined QTAIM/NCIplot analysis reveals a BCP (red sphere) and bond path (orange line) connecting the Tc atom of one monomer to the N-atom of the adjacent monomer. This confirms the existence of the MaB and its role in directing the structure, as there are no additional BCPs or bond paths interconnecting the monomers. The MaB is further characterized by a dark blue RDG isosurface, coinciding with the location of the BCP, indicating a strong and attractive interaction as denoted by the blue color in the NCI plot analysis.

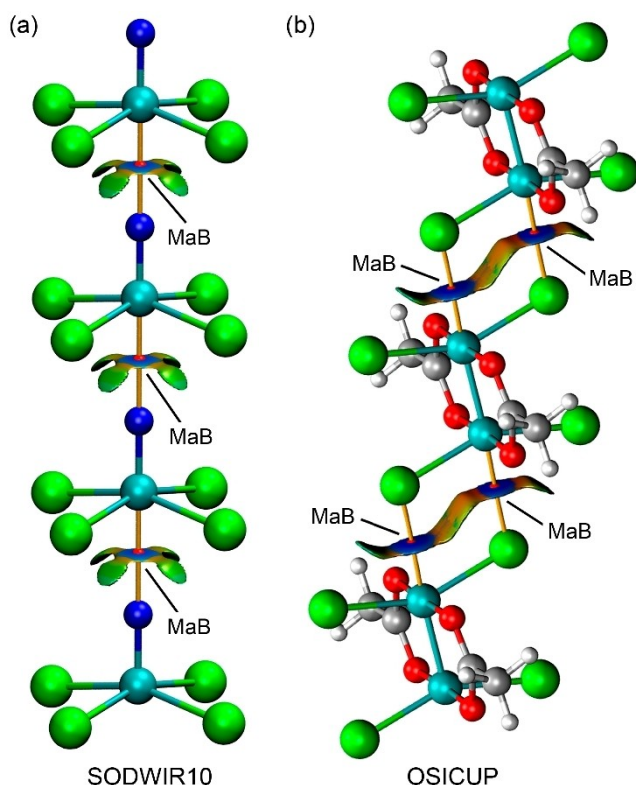


Figure 11. QTAIM/NCIplot analyses of the homotetramer of SODWIR10 (a) and the homotrimer of OSICUP (b). The NCIplot settings used are: RDG = 0.45, density cut-off 0.04 a.u., and color range ± 0.03 for $(\text{sign } \lambda_2) \rho$. Blue and green are used for attractive interactions and red and yellow for repulsive interactions.

For the OSICUP structure, a trimeric assembly is shown in Figure 11b, where the combined QTAIM/NCIplot analysis demonstrates that the central monomer is connected to the adjacent monomers by four BCPs and bond paths linking the Tc atoms to the Cl atoms. Each pair of MaBs that connects two monomers is characterized by two dark blue RDG isosurfaces, coinciding with the BCPs, which indicate the attractive nature of both symmetrically equivalent $\text{Tc}\cdots\text{Cl}$ contacts. The blue RDG isosurfaces are connected by an elongated yellow-reddish region, indicating the presence of $\text{Cl}\cdots\text{Cl}$ repulsion.

V Geochemistry

Research on Tc is relevant from the geo- and radiological point of view. In this case, the work so far available in the literature deals with the remediation technologies of Tc, with special focus on the long-term safety assessment of nuclear waste repositories and decontamination of Tc-polluted sites. Thus, multiple works report the scavenging of aqueous Tc by using naturally occurring minerals or materials to be present in the nuclear waste repository. Among them, clays and clay derivatives,^[148] cementitious matrices as ettringite^[149] and species that can be present in the repository, like microorganisms,^[150] or minerals such as pyrite,^[151] magnetite^[152] or chukanovite.^[153] In addition, in the last decade an increased interest has been oriented towards using other innovative materials, i.e., metal organic frameworks, as Tc scavengers, although the studies carried out so far only used rhenium as a Tc analogue.^[154–157]

Despite the large variety of oxidation states of Tc, it is considered that only Tc(VII) and Tc(IV) are environmentally relevant under oxidizing and reducing conditions, respectively. While Tc(VII) is inert against interaction with minerals and is, hence, very mobile in aqueous fluxes,^[158] Tc(IV) can be immobilized by different mechanisms. Tc(IV) retention mechanisms include the surface complexation on mineral (e.g., sorption on layered double hydroxides^[159,160] or on chukanovite^[153]), the incorporation into mineral structures (e.g., in magnetite and hematite^[161]), or the precipitation as poorly soluble solids such as TcO_2 ,^[162,163] or TcS_x .^[164]

Technetium Removal by Using Reducing Sorbents

Based on this, most of the reported studies deal with the Tc removal by using sorbents that can induce Tc(VII) reduction, such as Fe(II)-, Sn(II)-, S(–II)-containing materials,^[165] or microorganisms.^[166] These sorbents have been the most explored against Tc immobilization – being Fe(II)-minerals the main focus – since they will be relevant phases in the nuclear waste repository, and they are ubiquitous. Likewise these studies usually cover a range of pH from 4 to 9, and Eh from 400 to –400 mV, due to being very common environmental conditions.^[167] However, Tc immobilization is sometimes studied considering very limited parameter variability, which might not

convey a proper understanding of the actual Tc environmental chemistry.

Even though it is important, not all of the works have considered all the variables (time, pH, ionic strength and Tc concentration). Likewise, only a minority of the possible minerals have yet been explored, and only some of the molecular interactions of Tc with the minerals have been studied and reported. However, the knowledge generated over the last decades shows that redox-active sorbents induce the highest removal of Tc.

The majority of the available literature is based on Tc immobilization in binary systems, i.e., the interaction of Tc with a selected sorbent (mineral or microorganism) as a function of multiple parameters. However, this is an unrealistic scenario under environmental conditions. Hence, there is a need of studying the influence of the coexisting species in solution, as much as studying the sorbent materials to evaluate whether the presence of different species i) induces competition for Tc immobilization, ii) triggers the formation of soluble Tc species that do not interact with sorbents, iii) and/or affects Tc scavenging by their presence. Few studies report how the presence of other species can alter Tc immobilization. For example the competition for the immobilization by ettringite of technetium with other anions chromate and iodate,^[149] or the effect of organic ligands on the complexation of Tc in solution such as EDTA (Ethylenediaminetetraacetic acid),^[168] or on the solubility of TcO_2 .^[80]

Identification of the Immobilization Mechanism of Tc

Due to the few spectroscopic techniques by which Tc molecular environment can be identified, the immobilization mechanisms of Tc are primarily evaluated by XAS, which is a highly sophisticated method only available in synchrotron facilities. Therefore, user accessibility to this technique is limited and, in turn, a thorough mechanistic understanding of Tc immobilization by given sorbents is a time-demanding process. However, due to the high similitudes of the Fe(II)-, Fe(III)-, and Fe(II/III) mineral structures, it is tremendously tedious to unambiguously identify the exact interaction of Tc in the solid phase by XAS.^[159,169,170] In addition, usually, after the reduction of Tc(VII) by the selected Fe(II) mineral, Tc(IV) does not interact with the initial sorbent, but with its oxidation products. There are multiple examples in the literature, as an example, when Fe(II)-Al(III)-layered double hydroxide was used as sorbent, Tc(IV) formed surface complexes on hematite and incorporated into hematite structure.^[159]

Tc(VII) Reduction Mechanism and Lower-Valence Tc Species

It is remarkable that all the studies mentioned above have one thing in common: it has been historically assumed that the only relevant Tc species in the environment are inorganic Tc(VII) and Tc(IV) species. Nevertheless, this is not always the case. In 2004, it was found that in the Hanford nuclear waste site in the USA,

a Tc(I)-carbonyl species was stable in solution.^[74] In the same direction, other Tc species with oxidation states different than Tc(IV) or Tc(VII) are used for radiopharmaceutical purposes,^[171] and in fact, they are daily released via the patients' urine into the sewage systems and from there to the environment. Despite the environmental relevance of such Tc species, little is known to date about their interaction with sorbents such as minerals or microorganisms, although there are a few earlier publications dealing with microbial reduction of Tc.^[172–175]

Moreover, although the reduction of Tc(VII) to Tc(IV) is clearly the step limiting Tc migration in the environment, little is known about this reduction mechanism, and whether there are intermediary species. So far, electrochemical analyses have been done under extreme pH conditions.^[79] The only systematic work performed at different pH values shows that pH has a clear influence on Tc(VII) reduction,^[176] indicating that Tc(VII) reduction to Tc(IV) in NaClO₄ is a direct process from pH 4 to. In addition, the techniques available to explore *in situ* the molecular changes of Tc as a function of the redox potential are very limited. So far, the only method used for this purpose is the coupling of electrochemistry and UV-vis, which has often been used to evaluate the changes of absorption of aqueous Tc species.^[176–178] However, the characterization of Tc complexes takes part generally only *ex situ*, which can be hinder keeping a given redox potential.

In order to address this further, more thermodynamic data, in particular reduction potentials, are needed to understand the redox chemistry of Tc - not only for Tc(VII)–Tc(IV) redox pair. For example, the most critically evaluated thermodynamic database of Tc solely reports the reduction of [TcO₄][−] to TcO₂ and the reduction of [TcO₄][−] to [TcO₄]^{2−}.^[179]

Consequently, there are multiple knowledge gaps that need to be addressed in future studies from a chemical point of view (Figure 12).

Conclusions

Even though technetium is radiopharmaceutically important, radioecologically relevant, and from a health and safety point of

view relatively easy to handle, the numbers of papers on Tc chemistry has remained relatively constant over the last three decades. Compared to the general growing trends in scientific literature this shows that Tc chemistry is still under-researched, even though are significant knowledge gaps, in particular considering the differences in ^{99m}Tc chemistry and ⁹⁹Tc chemistry. This shows in many fields, such as spectroscopic data, particularly NMR and XAS. The lack of structural data is also underlined the relatively small number of inorganic and organic structures in the databases.

However, while physicochemical data, requiring often amounts >1 mg of material are somewhat stagnating, both inorganic chemistry and organometallic chemistry of Tc made significant progress in that time and some gaps in understanding fundamental bond interactions and geochemistry are slowly being filled.

Inorganic chemistry and organometallic chemistry both are strongly influenced by the redox behavior of Tc, which is often the key in understanding the fundamental differences between Tc and its homolog Re, just as much as the difference of ⁹⁹Tc and ^{99m}Tc is often affected by effects of low concentrations and temperature. Both these aspects are interconnected, and we believe that an expansion of Tc research both towards comparison with its neighbors as well as between its nuclear isomers will tell us a lot more about which drugs to synthesize, which form of waste disposal to choose or how to analyze our data.

A famous quote (probably misattributed to E. Rutherford) states that science is “either physics or stamp collecting”. While this is probably a sarcastic classification, we would emphasize that any conceptual interpretation must be preceded by some kind of data collection, at best in a systematic way. Looking at Tc chemistry, e.g., the knowledge on organometallic chemistry seems to consist of several islands developing around structures that are known from radiopharmaceutical applications. We are convinced that once these islands are connected, the resulting map of Tc organometallic chemistry will also contribute to deeper understanding and “physical” science.

In this respect, we may conclude with a few key points that may be of interest to the wider community, as they apply as

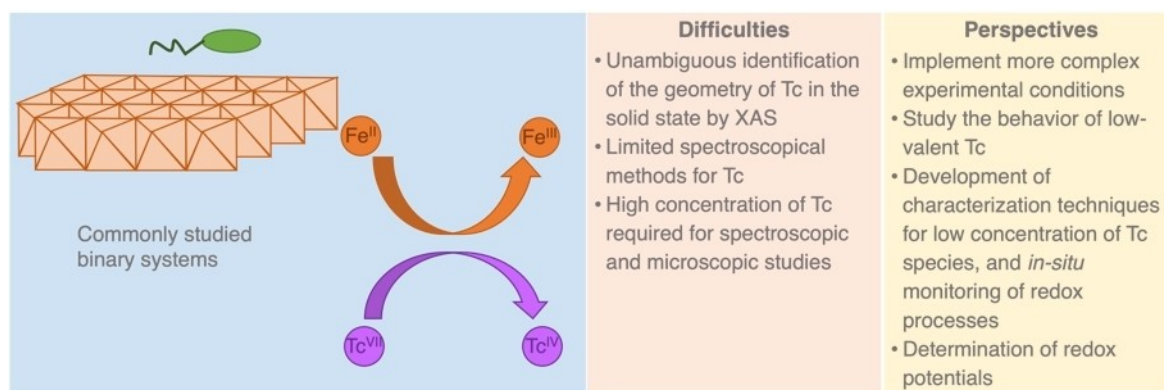


Figure 12. Usually studied Tc removal conditions in binary systems (blue box). Fe^{II} as an example of a reducing agent in solution or coming from microbial or mineral sources. Highlighted difficulties on Tc immobilization studies (orange box) and future perspectives (yellow box) of Tc geochemistry.

much to inorganic and geochemistry as to radiopharmacy and organic chemistry.

We do need to further our understanding of

- I) the chemistry of Tc at low concentrations in comparison with high concentrations
- II) Tc in the environment, and particularly focus on the difference between Tc and Re
- III) the oxidation states of Tc other than +4 and +7
- IV) spectroscopic data, and advance our usage of XAS as a versatile tool at hand to do this

Pertechnetate and related anions such as perrhenate can serve as versatile building blocks in crystal engineering due to their ability to form strong and directional mature bonds. These interactions not only stabilize the resulting crystal structures but also allow for the design of new materials with tailored properties. The examples from the CSD, combined with theoretical insights, underscore the significance of technetium and its congeners in advancing our understanding of non-covalent interactions in solid-state chemistry, paving the way for future innovations in the design of supramolecular materials, and understanding its interactions with other such oxoanions, both in the lab and in the environment.

Carbonyl complexes have been shown to be extremely relevant for radiopharmacy as well as for Tc speciation in environmental samples, and *vice versa*, radiopharmaceutical compounds have been proposed for the use in environmental remediation. The picture that Tc is mainly Tc(VII) or Tc(IV) under environmental conditions is probably oversimplified due to the fact that fundamental Tc chemistry is still under-researched. The inorganic chemistry of Tc is also highly relevant for medical applications – any metabolism resulting in pertechnetate anions will result in an uptake of $[TcO_4]^-$ into the thyroid where it is interchangeable with iodide.

Also, the future perspectives of Tc geochemistry are connected to the research results of redox and/or organo-metallic chemistry. In order to draw a realistic picture of the behavior of Tc in the environment, two fields of work have to be addressed. On the one hand, the Tc immobilization experiments need to be carried out under more realistic conditions. This implies the following points.

- I) Widening the experimental conditions in binary systems (time, pH, Tc concentration, salinity) and explore those that have not yet been deeply analyzed (temperature, imposed redox potentials). This will not only help to understand the basis of Tc removal under the most expected environmental conditions, but also it will help to assess the chemical behavior of Tc when the chemical surrounding induces speciation changes e.g., the mineral transformation.
- II) Expanding Tc immobilization studies to complex environments (ternary and quaternary systems) when multiple components coexist in suspension.
- III) Developing techniques that allow for identifying the Tc geometry under low Tc concentrations. They will offer a more realistic understanding of the actual behavior of Tc in the environment.

- IV) Always analyzing the changes in the mineralogy of the sorbent after Tc interaction with redox-active sorbents. This will help to overcome the difficulties on the identification of the Tc mechanistic scavenging process by XAS.
- V) Exploring the Tc scavenging behavior of new, synthetic, sorbents.
- VI) Limiting the use of Re as Tc analogue or carrying out more comparative studies between Re and Tc. In most of the cases, Re geochemistry is not analogue to Tc, and comparative works will help to assess their chemical differences.
- VII) The immobilization of other Tc species different than Tc(VII) and Tc(IV) needs to be analyzed. These includes Tc(II) species (identified in Hanford site) and other Tc complexes in low oxidation states that are used in radiodiagnostics. On the other hand, the redox chemistry of Tc requires a deep expansion. The following steps need to be fulfilled.
- VII) Studying Tc reduction potentials in presence of (in)organic ligands in a wide range of pH values. This will help to evaluate the effect of such ligands on the redox processes of Tc and to describe new thermodynamic parameters: Tc reduction potentials, and the complexation of aqueous Tc-ligand species that might be formed. Expanding the so far limited thermodynamic data of Tc will enormously benefit the use of modelling tools to predict the geochemical behavior of Tc, which in turn will support the long-term safety assessment of Tc in the nuclear waste repository.
- IX) Developing and optimizing the use of coupled electro-chemical and spectroscopic methods. They will allow for studying *in situ* the changes in Tc chemistry and Tc molecular environment in solution or at the solid-water interphase at given potentials. These methodologies will provide the most accurate picture of Tc geochemistry under any possible environmental conditions.

These are a few aspects that we think are potential valuable starting points for anyone interested in enhancing this field. It's a large field, but the goals are open. Tc is still an unknown, right at the center of the Periodic Table.

Author Contributions

E.S.: concept, writing, editing, graphics, D.B.: writing, J.B.: writing, A.F.: writing, graphics, N.M.H.: writing, graphics, A. S.: writing, M.R.J.: writing, graphics, M.W.: writing, C.Y.: writing, editing, graphics, M.Z.: writing, editing

Acknowledgements

Open Access funding enabled and organized by Projekt DEAL.

Conflict of Interests

The authors declare no conflict of interest.

Keywords: technetium · review · radiochemistry

- [1] D. Mendelejeff, *Z. Chem.* **1869**, 12, 405–406.
- [2] R. Zingales, *J. Chem. Edu.* **2005**, 82, 221.
- [3] C. Perrier, E. Segrè, *J. Chem. Phys.* **1937**, 5, 712–716.
- [4] C. Perrier, E. Segrè, *Nature* **1947**, 159, 24.
- [5] E. A. C. Crouch, *At. Data Nucl. Data* **1977**, 19, 417–532.
- [6] K. Schwochau, *Technetium: Chemistry and Radiopharmaceutical Applications*, Wiley-VCH, Weinheim, **2000**.
- [7] International Atomic Energy Agency, *Technetium-99 m Radiopharmaceuticals: Status and Trends*, International Atomic Energy Agency, Vienna, **2009**.
- [8] OECD/NEA, *The Supply of Medical Isotopes*, OECD Publishing, Paris, **2019**.
- [9] Google Scholar, **2024**.
- [10] R. Alberto, *Inorg. Chem.* **2023**, 62, 20539–20548.
- [11] FIZ Karlsruhe, **2024**.
- [12] E. V. Johnstone, N. Mayordomo, E. J. Mausolf, *EPJ Tech. Instrum.* **2023**, 10, 1.
- [13] E. J. Mausolf, E. V. Johnstone, N. Mayordomo, D. L. Williams, E. Y. Z. Guan, C. K. Gary, *Pharmaceuticals* **2021**, 14.
- [14] C. Busser, Ein Neuer Ansatz Für Die Beschleuniger-Massenspektrometrie von ⁹⁹Tc, Master's Thesis, Technische Universität München, **2018**.
- [15] B. E. Rogers, J. J. Parry, R. Andrews, P. Cordopatis, B. A. Nock, T. Maina, *J. Nucl. Med.* **2005**, 46, 1889.
- [16] B. T. Christian, R. J. Nickles, C. K. Stone, T. L. Mulnix, J. Clark, *Appl. Radiat. Isot.* **1995**, 46, 69–73.
- [17] A. Duatti, *Nucl. Med. Biol.* **2021**, 92, 202–216.
- [18] J. N. Zappey, E. E. Moore, O. Beneš, J.-C. Griveau, R. J. M. Konings, *J. Chem. Thermody.* **2024**, 189, 107200.
- [19] M. Chotkowski, A. Czerwiński, in *Electrochemistry of Technetium*, Springer International Publishing, Cham, **2021**.
- [20] S. Chatterjee, A. Andersen, Y. Du, M. H. Engelhard, G. B. Hall, T. G. Levitskaia, W. W. Lukens, V. Shutthanandan, E. D. Walter, N. M. Washton, *Characterization of Non-Pertechnetate Species Relevant to the Hanford Tank Waste*, United States, **2017**.
- [21] S. Chatterjee, V. E. Holfeltz, G. B. Hall, I. E. Johnson, E. D. Walter, S. Lee, B. Reinhart, W. W. Lukens, N. P. Machara, T. G. Levitskaia, *Anal. Chem.* **2020**, 92, 13961–13970.
- [22] M. Bühl, V. Golubnychiy, *Magn. Reson. Chem.* **2008**, 46, S36–S44.
- [23] G. B. Hall, A. Andersen, N. M. Washton, S. Chatterjee, T. G. Levitskaia, *Inorg. Chem.* **2016**, 55, 8341–8347.
- [24] T. F. C. B. de Andrade, H. F. Dos Santos, C. Fonseca Guerra, D. F. S. Paschoal, *J. Phys. Chem. A* **2022**, 126, 5434–5448.
- [25] V. V. Kuznetsov, F. Poineau, K. E. German, E. A. Filatova, *Comm. Chem.* **2024**, 7, 259.
- [26] S. Bauters, A. C. Scheinost, K. Schmeide, S. Weiss, K. Dardenne, J. Rothe, N. Mayordomo, R. Steudtner, T. Stumpf, U. Abram, S. M. Butorin, K. O. Kvashnina, *Chem. Commun.* **2020**, 56, 9608–9611.
- [27] K. Dardenne, S. Duckworth, X. Gaona, R. Polly, B. Schimmelpfennig, T. Pruessmann, J. Rothe, M. Altmaier, H. Geckeis, *Inorg. Chem.* **2021**, 60, 12285–12298.
- [28] M. Yamamoto, V.-K. Do, S. Taguchi, T. Kuno, Y. Takamura, *Spectrochim. Acta B* **2019**, 155, 134–140.
- [29] W. Trzebiatowski, J. Rudzinski, *J. Less-Common Met.* **1964**, 6, 244–245.
- [30] D. Zhou, D. V. Semenok, M. A. Volkov, I. A. Troyan, A. Yu. Seregin, I. V. Chepkasov, D. A. Sannikov, P. G. Lagoudakis, A. R. Oganov, K. E. German, *Phys. Rev. B* **2023**, 107, 64102.
- [31] M. R. Jungfer, L. Elsholz, U. Abram, *Organometallics* **2021**, 40, 3095–3112.
- [32] M. Elder, B. R. Penfold, *Inorg. Chem.* **1966**, 5, 1197–1200.
- [33] F. Poineau, E. V. Johnstone, P. F. Weck, P. M. Forster, E. Kim, K. R. Czerwinski, A. P. Sattelberger, *Inorg. Chem.* **2012**, 51, 4915–4917.
- [34] F. Poineau, E. V. Johnstone, P. F. Weck, E. Kim, P. M. Forster, B. L. Scott, A. P. Sattelberger, K. R. Czerwinski, *J. Am. Chem. Soc.* **2010**, 132, 15864–15865.
- [35] F. Poineau, E. E. Rodriguez, P. M. Forster, A. P. Sattelberger, A. K. Cheetham, K. R. Czerwinski, *J. Am. Chem. Soc.* **2009**, 131, 910–911.
- [36] F. Poineau, E. V. Johnstone, K. R. Czerwinski, A. P. Sattelberger, *Acc. Chem. Res.* **2014**, 47, 624–632.
- [37] E. V. Johnstone, F. Poineau, P. M. Forster, L. Ma, T. Hartmann, A. Cornelius, D. Antonio, A. P. Sattelberger, K. R. Czerwinski, *Inorg. Chem.* **2012**, 51, 8462–8467.
- [38] E. V. Johnstone, F. Poineau, J. Starkey, T. Hartmann, P. M. Forster, L. Ma, J. Hilgar, E. E. Rodriguez, R. Farmand, K. R. Czerwinski, A. P. Sattelberger, *Inorg. Chem.* **2013**, 52, 14309–14316.
- [39] J. Supel, U. Abram, A. Hagenbach, K. Seppelt, *Inorg. Chem.* **2007**, 46, 5591–5595.
- [40] H. P. A. Mercier, G. J. Schrobilgen, *Inorg. Chem.* **1993**, 32, 145–151.
- [41] A. J. Edwards, G. R. Jones, R. J. C. Sills, *J. Chem. Soc. A* **1970**, 2521–2523.
- [42] M. Schädel, D. Shaughnessy, in *The Chemistry of Superheavy Elements*, Springer Berlin Heidelberg, Berlin, Heidelberg, **2014**.
- [43] R. Eichler, W. Bröchle, R. Dressler, E. Düllmann, B. Eichler, H. W. Gäggeler, K. E. Gregorich, D. C. Hoffman, S. Hübener, D. T. Jost, U. W. Kirbach, C. A. Laue, V. M. Lavanchy, H. Nitsche, J. B. Patin, D. Piguet, M. Schädel, D. A. Shaughnessy, D. A. Strellis, S. Taut, L. Tobler, Y. S. Tsyganov, A. Türlér, A. Vahle, P. A. Wilk, A. B. Yakushev, *Nature* **2000**, 407, 63–65.
- [44] N. LeBlond, H. P. A. Mercier, D. A. Dixon, G. J. Schrobilgen, *Inorg. Chem.* **2000**, 39, 4494–4509.
- [45] S. M. Balasekaran, M. Molski, J. Spandl, A. Hagenbach, R. Alberto, U. Abram, *Inorg. Chem.* **2013**, 52, 7094–7099.
- [46] S. Mariappan Balasekaran, M. Molski, A. Hagenbach, U. Abram, *Z. anorg. allg. Chem.* **2013**, 639, 672–675.
- [47] S. M. Balasekaran, J. Spandl, A. Hagenbach, K. Köhler, M. Drees, U. Abram, *Inorg. Chem.* **2014**, 53, 5117–5128.
- [48] S. M. Balasekaran, A. Hagenbach, J. Spandl, U. Abram, *Z. anorg. allg. Chem.* **2017**, 643, 1146–1149.
- [49] S. M. Balasekaran, A. Hagenbach, M. Drees, U. Abram, *Dalton Trans.* **2017**, 46, 13544–13552.
- [50] S. M. Balasekaran, A. Hagenbach, U. Abram, *Z. anorg. allg. Chem.* **2018**, 644, 1158–1163.
- [51] I. V. Vinogradov, M. I. Konarev, L. L. Zajtseva, S. V. Shepel'kov, *Russ. J. Inorg. Chem.* **1978**, 23, 639–640.
- [52] L. H. Dietrich, W. Jeitschko, *J. Solid State Chem.* **1986**, 63, 377–385.
- [53] R. Rühl, W. Jeitschko, *Acta Crystallogr. B* **1982**, 38, 2784–2788.
- [54] R. Rühl, W. Jeitschko, K. Schwochau, *J. Solid State Chem.* **1982**, 44, 134–140.
- [55] B. Krebs, *Z. anorg. allg. Chem.* **1971**, 380, 146–159.
- [56] D. B. Rogers, R. D. Shannon, A. W. Sleight, J. L. Gillson, *Inorg. Chem.* **1969**, 8, 841–849.
- [57] E. Rodriguez, F. Poineau, A. Llobet, K. Czerwinski, R. Seshadri, A. K. Cheetham, *Inorg. Chem.* **2008**, 47, 6281–6288.
- [58] O. Muller, W. B. White, R. Roy, *J. Inorg. Nucl. Chem.* **1964**, 26, 2075–2086.
- [59] G. J. Thorogood, Z. Zhang, J. R. Hester, B. J. Kennedy, J. Ting, C. J. Glover, B. Johannessen, *Dalton Trans.* **2011**, 40, 10924–10926.
- [60] E. E. Rodriguez, F. Poineau, A. Llobet, J. D. Thompson, R. Seshadri, A. K. Cheetham, *J. Mater. Chem.* **2011**, 21, 1496–1502.
- [61] T. Hartmann, A. J. Alaniz, D. J. Antonio, *Procedia Chem.* **2012**, 7, 622–628.
- [62] G. J. Thorogood, M. Avdeev, M. L. Carter, B. J. Kennedy, J. Ting, K. S. Wallwork, *Dalton Trans.* **2011**, 40, 7228–7233.
- [63] M. Avdeev, G. J. Thorogood, M. L. Carter, B. J. Kennedy, J. Ting, D. J. Singh, K. S. Wallwork, *J. Am. Chem. Soc.* **2011**, 133, 1654–1657.
- [64] E. Strub, D. Grödler, D. Zaratti, C. Yong, L. Dünnebie, S. Bazhenova, M. Roca Jungfer, M. Breugst, M. Zegke, *Chem. Eur. J.* **2024**, 30, e202400131.
- [65] M. Shohel, J. Bustos, A. Roseborough, M. Nyman, *Chem. Eur. J.* **2024**, 30, e202303218.
- [66] M. Shohel, J. Bustos, G. D. Strosio, A. Sarkar, M. Nyman, *Inorg. Chem.* **2023**, 62, 10450–10460.
- [67] F. Poineau, P. F. Weck, K. German, A. Maruk, G. Kirakosyan, W. Lukens, D. B. Rego, A. P. Sattelberger, K. R. Czerwinski, *Dalton Trans.* **2010**, 39, 8616–8619.
- [68] I. Denden, R. Essehli, M. Fattahi, *J. Radioanal. Nucl. Chem.* **2013**, 296, 149–155.
- [69] I. Denden, J. Roques, F. Poineau, P. L. Solari, M. L. Schlegel, G. Blain, M. Fattahi, *Radiochim. Acta* **2017**, 105, 135–140.
- [70] M. Zegke, D. Grödler, M. Roca Jungfer, A. Haseloer, M. Kreuter, J. M. Neudörfl, T. Sittel, C. M. James, J. Rothe, M. Altmaier, A. Klein, M. Breugst, U. Abram, E. Strub, M. S. Wickleder, *Angew. Chem. Int. Ed.* **2022**, 61, e202113777.
- [71] M. Zegke, A. Raaf, J.-M. Neudörfl, E. Strub, *Z. Naturforsch. B* **2023**, 78, 339–342.
- [72] J. Supel, A. Hagenbach, U. Abram, K. Seppelt, *Z. anorg. allg. Chem.* **2008**, 634, 646–648.

- [73] K. E. German, A. M. Fedoseev, M. S. Grigoriev, G. A. Kirakosyan, T. Dumas, C. Den Auwer, P. Moisy, K. V. Lawler, P. M. Forster, F. Poineau, *Chem. Eur. J.* **2021**, *27*, 13624–13631.
- [74] W. W. Lukens, D. K. Shuh, N. C. Schroeder, K. R. Ashley, *Environ. Sci. Technol.* **2004**, *38*, 229–233.
- [75] D. Badea, S. Olthof, J. M. Neudörfl, R. Glaum, R. Pöttgen, M. K. Reimann, K. Meerholz, M. Reimer, C. Logemann, E. Strub, J. Bruns, *Eur. J. Inorg. Chem.* **2023**, *26*, e202300160.
- [76] D. Badea, K. Dardenne, R. Polly, J. Rothe, M. Hanrath, M. Reimer, K. Meerholz, J.-M. Neudörfl, E. Strub, J. Bruns, *Chem. Eur. J.* **2022**, *28*, e202201738.
- [77] W. Lukens Wayne, J. J. Bucher, N. M. Edelstein, D. K. Shuh, *J. Phys. Chem. A* **2001**, *105*, 9611–9615.
- [78] W. Lukens Wayne, J. J. Bucher, N. M. Edelstein, D. K. Shuh, *Environ. Sci. Technol.* **2002**, *36*, 1124–1129.
- [79] M. Chotkowski, M. Grdeń, B. Wrzosek, *J. Electroanal. Chem.* **2018**, *829*, 148–156.
- [80] N. A. DiBlasi, K. Dardenne, T. Prüssmann, S. Duckworth, M. Altmaier, X. Gaona, *Environ. Sci. Technol.* **2023**, *57*, 3661–3670.
- [81] J. C. Hileman, D. K. Huggins, H. D. Kaesz, *J. Am. Chem. Soc.* **1961**, *83*, 2953–2954.
- [82] G. D. Michels, H. J. Svec, *Inorg. Chem.* **1981**, *20*, 3445–3447.
- [83] J. C. Hileman, D. K. Huggins, H. D. Kaesz, *Inorg. Chem.* **1962**, *1*, 933–938.
- [84] G. V. Sidorenko, A. E. Miroslavov, M. Yu. Tyupina, *Coord. Chem. Rev.* **2023**, *476*, 214911.
- [85] R. Alberto, *ChemBioChem* **2020**, *21*, 2743–2749.
- [86] R. Alberto, R. Schibli, A. Egli, A. P. Schubiger, U. Abram, T. A. Kaden, *J. Am. Chem. Soc.* **1998**, *120*, 7987–7988.
- [87] J.-H. Kim, S.-J. Choi, Y.-D. Hong, *J. Radioanal. Nucl. Chem.* **2012**, *292*, 203–209.
- [88] H. Lambie, A. M. Cook, A. F. Scarsbrook, J. P. A. Lodge, P. J. Robinson, F. U. Chowdhury, *Clin. Radiol.* **2011**, *66*, 1094–1105.
- [89] C. Müller, P. A. Schubiger, R. Schibli, *Bioconjug. Chem.* **2006**, *17*, 797–806.
- [90] C. Müller, P. A. Schubiger, R. Schibli, *Nucl. Med. Biol.* **2007**, *34*, 595–601.
- [91] C. Müller, F. Forrer, R. Schibli, E. P. Krenning, M. de Jong, *J. Nucl. Med.* **2008**, *49*, 310.
- [92] M. H. Sanad, A. S. A. El-Bayoumy, A. A. Ibrahim, *J. Radioanal. Nucl. Chem.* **2017**, *311*, 1–14.
- [93] N. Yamamura, Y. Magata, Y. Arano, T. Kawaguchi, K. Ogawa, J. Konishi, H. Saji, *Bioconjug. Chem.* **1999**, *10*, 489–495.
- [94] Y. Liu, B. Spingler, P. Schmutz, R. Alberto, *J. Am. Chem. Soc.* **2008**, *130*, 1554–1555.
- [95] A. Mattern, S. Habermann, M. Zegke, M. S. Wickleder, R. Alberto, *Bioconjug. Chem.* **2022**, *33*, 1741–1749.
- [96] K. Kothari, S. Joshi, M. Venkatesh, N. Ramamoorthy, M. R. A. Pillai, *J. Label. Compd. Radiopharm.* **2003**, *46*, 633–644.
- [97] H. W. Peindy N'Dongo, P. D. Raposinho, C. Fernandes, I. Santos, D. Can, P. Schmutz, B. Spingler, R. Alberto, *Nucl. Med. Biol.* **2010**, *37*, 255–264.
- [98] B. L. Ellis, N. I. Gorshkov, A. A. Lumpov, A. E. Miroslavov, A. N. Yal'fimov, V. V. Gurzhiy, D. N. Suglobov, R. Braddock, J. C. Adams, A.-M. Smith, M. C. Prescott, H. L. Sharma, *J. Label. Compd. Radiopharm.* **2013**, *56*, 700–707.
- [99] G. V. Sidorenko, A. E. Miroslavov, M. Yu. Tyupina, V. V. Gurzhiy, A. P. Sakhonenkova, A. A. Lumpov, *Inorg. Chem.* **2023**, *62*, 15593–15604.
- [100] N. A. Lodhi, J. Y. Park, K. Kim, M. K. Hong, Y. J. Kim, Y.-S. Lee, G. J. Cheon, K. W. Kang, J. M. Jeong, *Inorganics (Basel)* **2020**, *8*, Doi: 10.3390/inorganics8010005.
- [101] L. Fuks, E. Gniazdowska, P. Kozminski, M. Lyczko, J. Mieczkowski, J. Narbutt, *Appl. Radiat. Isot.* **2010**, *68*, 90–95.
- [102] R. Waibel, R. Alberto, J. Willuda, R. Finnen, R. Schibli, A. Stichelberger, A. Egli, U. Abram, J.-P. Mach, A. Plückthun, P. A. Schubiger, *Nat. Biotechnol.* **1999**, *17*, 897–901.
- [103] S. Chatterjee, G. B. Hall, M. H. Engelhard, Y. Du, N. M. Washton, W. W. Lukens, S. Lee, C. I. Pearce, T. G. Levitskaia, *Inorg. Chem.* **2018**, *57*, 6903–6912.
- [104] T. G. Levitskaia, B. M. Rapko, A. Anderson, J. M. Peterson, S. Chatterjee, E. D. Walter, H. M. Cho, N. M. Washton, *Speciation and Oxidative Stability of Alkaline Soluble, Non-Perchnetate Technetium*, United States, **2014**.
- [105] A. E. Miroslavov, G. V. Sidorenko, A. A. Lumpov, V. A. Mikhalev, D. N. Suglobov, *Radiochem.* **2009**, *51*, 5–10.
- [106] A. E. Miroslavov, G. V. Sidorenko, A. A. Lumpov, V. A. Mikhalev, D. N. Suglobov, *Radiochem.* **2009**, *51*, 124–131.
- [107] A. E. Miroslavov, G. V. Sidorenko, A. A. Lumpov, D. N. Suglobov, O. V. Sizova, D. A. Maltsev, V. V. Gurzhiy, Yu. S. Polotskii, *J. Organomet. Chem.* **2012**, *720*, 1–6.
- [108] A. E. Miroslavov, V. V. Gurzhiy, M. Yu. Tyupina, A. A. Lumpov, G. V. Sidorenko, Y. S. Polotskii, D. N. Suglobov, *J. Organomet. Chem.* **2013**, *745–746*, 219–225.
- [109] E. S. Stepanova, V. V. Gurzhiy, M. Yu. Tyupina, A. E. Miroslavov, G. V. Sidorenko, A. A. Lumpov, *Dalton Trans.* **2016**, *45*, 8428–8432.
- [110] A. E. Miroslavov, A. P. Shishkina, G. V. Sidorenko, V. V. Gurzhiy, D. A. Maltsev, E. V. Kuryshva, *Inorg. Chem.* **2020**, *59*, 9239–9243.
- [111] G. V. Sidorenko, A. E. Miroslavov, M. S. Grigor'ev, V. V. Gurzhiy, A. A. Lumpov, V. A. Mikhalev, D. N. Suglobov, *Radiochem.* **2011**, *53*, 44–50.
- [112] A. P. Sakhonenkova, A. E. Miroslavov, G. V. Sidorenko, R. Alberto, M. L. Besmer, V. V. Gurzhiy, M. Yu. Tyupina, *Organometallics* **2024**, *43*, 1233–1245.
- [113] F. Salsi, M. Neville, M. Drance, A. Hagenbach, J. S. Figueroa, U. Abram, *Organometallics* **2021**, *40*, 1336–1343.
- [114] F. Salsi, S. Wang, C. Teutloff, M. Busse, M. L. Neville, A. Hagenbach, R. Bittl, J. S. Figueroa, U. Abram, *Angew. Chem. Int. Ed.* **2023**, *62*, e202300254.
- [115] F. Salsi, A. Hagenbach, J. S. Figueroa, U. Abram, *Chem. Commun.* **2023**, *59*, 4028–4031.
- [116] M. L. Besmer, H. Braband, S. Schneider, B. Spingler, R. Alberto, *Inorg. Chem.* **2021**, *60*, 6696–6701.
- [117] M. L. Besmer, H. Braband, T. Fox, B. Spingler, A. P. Sattelberger, R. Alberto, *Inorg. Chem.* **2023**, *62*, 10727–10735.
- [118] M. L. Besmer, F. Schwitter, F. Battistin, H. Braband, T. Fox, B. Spingler, R. Alberto, *Dalton Trans.* **2024**, *53*, 1434–1438.
- [119] M. Roca Jungfer, U. Abram, *Inorg. Chem.* **2021**, *60*, 16734–16753.
- [120] M. Roca Jungfer, L. Elsholz, U. Abram, *Inorg. Chem.* **2022**, *61*, 2980–2997.
- [121] M. Roca Jungfer, U. Abram, *Inorg. Chem.* **2022**, *61*, 7765–7779.
- [122] M. J. Ernst, M. Roca Jungfer, U. Abram, *Organometallics* **2022**, *41*, 2011–2021.
- [123] M. J. Ernst, M. Roca Jungfer, A. Hagenbach, U. Abram, *Organometallics* **2022**, *41*, 1216–1224.
- [124] B. Noschang Cabral, L. Kirsten, A. Hagenbach, P. C. Piquini, M. Patzschke, E. S. Lang, U. Abram, *Dalton Trans.* **2017**, *46*, 9280–9286.
- [125] M. A. Volkov, A. P. Novikov, M. S. Grigoriev, Y. M. Nevolin, K. E. German, *Inorg. Chem.* **2023**, *62*, 256–265.
- [126] M. A. Volkov, A. M. Fedoseev, E. G. Krivoborodov, I. Y. Toropygin, K. E. German, M. S. Grigoriev, V. V. Kuznetsov, N. A. Budantseva, A. P. Novikov, Y. O. Mezhev, *J. Organomet. Chem.* **2022**, *957*, 122146.
- [127] M. A. Volkov, E. V. Abkhalimov, A. P. Novikov, I. M. Nevolin, M. S. Grigoriev, *Inorg. Chem.* **2024**, *63*, 13613–13623.
- [128] E. Oehlke, S. Kong, P. Arciszewski, S. Wiebalck, U. Abram, *J. Am. Chem. Soc.* **2012**, *134*, 9118–9121.
- [129] M. Benz, B. Spingler, R. Alberto, H. Braband, *J. Am. Chem. Soc.* **2013**, *135*, 17566–17572.
- [130] Q. Nadeem, G. Meola, H. Braband, R. Bolliger, O. Blacque, D. Hernández-Valdés, R. Alberto, *Angew. Chem. Int. Ed.* **2020**, *59*, 1197–1200.
- [131] G. Claude, F. Salsi, A. Hagenbach, M. Gembicky, M. Neville, C. Chan, J. S. Figueroa, U. Abram, *Organometallics* **2020**, *39*, 2287–2294.
- [132] G. Claude, J. Genz, D. Weh, M. Roca Jungfer, A. Hagenbach, M. Gembicky, J. S. Figueroa, U. Abram, *Inorg. Chem.* **2022**, *61*, 16163–16176.
- [133] G. Claude, D. Puccio, M. Roca Jungfer, A. Hagenbach, S. Spreckelmeyer, U. Abram, *Inorg. Chem.* **2023**, *62*, 12445–12452.
- [134] A. C. Grunwald, C. Scholtysik, A. Hagenbach, U. Abram, *Inorg. Chem.* **2020**, *59*, 9396–9405.
- [135] M. Roca Jungfer, M. J. Ernst, A. Hagenbach, U. Abram, *Z. anorg. allg. Chem.* **2022**, *648*, e202100316.
- [136] J. Ackermann, A. Hagenbach, U. Abram, *Chem. Commun.* **2016**, *52*, 10285–10288.
- [137] M. J. Ernst, A. Abdulkader, A. Hagenbach, G. Claude, M. Roca Jungfer, U. Abram, *Molecules* **2024**, *29*, Doi: 10.3390/molecules29051114.
- [138] A. Abdulkader, A. Hagenbach, U. Abram, *Eur. J. Inorg. Chem.* **2021**, *2021*, 3812–3818.
- [139] C. Robinson, S. Shaw, K. Morris, T. Neill, C. Pearce, H. Williams, J. R. Lloyd, Brighton, UK, **2024**.
- [140] S. Burguera, R. M. Gomila, A. Bauzá, A. Frontera, *Crystals (Basel)* **2023**, *13*, Doi: 10.3390/cryst13020187.
- [141] A. Daolio, A. Pizzi, G. Terraneo, A. Frontera, G. Resnati, *ChemPhysChem* **2021**, *22*, 2281–2285.

- [142] D. Grödler, S. Burguera, A. Frontera, E. Strub, *Chem. Eur. J.* **2024**, *30*, e202400100.
- [143] Y. Xu, M. Calabrese, N. Demitri, A. Pizzi, T. Nag, I. Hung, Z. Gan, G. Resnati, D. L. Bryce, *Chem. Commun.* **2023**, *59*, 12609–12612.
- [144] R. M. Gomila, A. Frontera, *Molecules* **2022**, *27*, Doi: 10.3390/molecules27196597.
- [145] M. Karmakar, R. M. Gomila, A. Frontera, S. Chattopadhyay, *Cryst. Growth Des.* **2024**, *24*, 5990–6000.
- [146] P. Leibnitz, G. Reck, H.-J. Pietzsch, H. Spies, *Structure of Technetium and Rhenium Complexes*, Dresden, **2001**.
- [147] J. Baldas, J. F. Boas, S. F. Colmanet, D. A. Rae, G. A. Williams, *Proc. R. Soc. Lond. A* **1997**, *442*, 437–461.
- [148] A. V. Makarov, A. V. Safonov, Y. V. Konevnik, Yu. A. Teterin, K. I. Maslakov, A. Yu. Teterin, Y. Yu. Karaseva, K. E. German, E. V. Zakharova, *J. Hazard. Mater.* **2021**, *401*, 123436.
- [149] E. C. Gillispie, S. T. Mergelsberg, T. Varga, S. M. Webb, N. M. Avalos, M. M. V. Snyder, A. Bourchy, R. M. Asmussen, S. A. Saslow, *Environ. Sci. Technol.* **2021**, *55*, 1057–1066.
- [150] N. K. Masters-Waage, K. Morris, J. R. Lloyd, S. Shaw, J. F. W. Mosselmans, C. Boothman, P. Bots, A. Rizoulis, F. R. Livens, G. T. W. Law, *Environ. Sci. Technol.* **2017**, *51*, 14301–14310.
- [151] D. M. Rodríguez, N. Mayordomo, A. C. Scheinost, D. Schild, V. Brendler, K. Müller, T. Stumpf, *Environ. Sci. Technol.* **2020**, *54*, 2678–2687.
- [152] E. Yalçintaş, A. C. Scheinost, X. Gaona, M. Altmaier, *Dalton Trans.* **2016**, *45*, 17874–17885.
- [153] K. Schmeide, A. Rossberg, F. Bok, S. Shams Aldin Azzam, S. Weiss, A. C. Scheinost, *Sci. Total Environ.* **2021**, *770*, 145334.
- [154] D. Banerjee, W. Xu, Z. Nie, L. E. V. Johnson, C. Coghlan, M. L. Sushko, D. Kim, M. J. Schweiger, A. A. Kruger, C. J. Doonan, P. K. Thallapally, *Inorg. Chem.* **2016**, *55*, 8241–8243.
- [155] R. J. Drouot, K. Otake, A. J. Howarth, T. Islamoglu, L. Zhu, C. Xiao, S. Wang, O. K. Farha, *Chem. Mat.* **2018**, *30*, 1277–1284.
- [156] S. Rapti, S. A. Diamantis, A. Dafnomili, A. Pournara, E. Skliri, G. S. Armatas, A. C. Tsipis, I. Spanopoulos, C. D. Malliakas, M. G. Kanatzidis, J. C. Plakatouras, F. Noli, T. Lazarides, M. J. Manos, *J. Mater. Chem. A* **2018**, *6*, 20813–20821.
- [157] K. Lv, S. Fichter, M. Gu, J. März, M. Schmidt, *Coord. Chem. Rev.* **2021**, *446*, 214011.
- [158] K. H. Lieser, C. H. Bauscher, *Radiochim. Acta* **1988**, *44–45*, 125–128.
- [159] N. Mayordomo, D. M. Rodríguez, A. Rossberg, H. Foerstendorf, K. Heim, V. Brendler, K. Müller, *J. Chem. Eng.* **2021**, *408*, 127265.
- [160] N. Daniels, C. Franzen, G. L. Murphy, K. Kvashnina, V. Petrov, N. Torapava, A. Bukaemskiy, P. Kowalski, H. Si, Y. Ji, A. Hölzer, C. Walther, *Appl. Clay Sci.* **2019**, *176*, 1–10.
- [161] D. Boglailenko, T. G. Levitskaia, *Environ. Sci. Nano* **2019**, *6*, 3492–3500.
- [162] K. J. Cantrell, B. D. Williams, *J. Nucl. Mat. n.d.*, *437*, 424–431.
- [163] A. F. Oliveira, A. Kuc, T. Heine, U. Abram, A. C. Scheinost, *Chem. Eur. J.* **2022**, *28*, e202202235.
- [164] F. Poineau, B. P. Burton-Pye, A. P. Sattelberger, K. R. Czerwinski, K. E. German, M. Fattahi, *New J. Chem.* **2018**, *42*, 7522–7528.
- [165] T. Kobayashi, A. C. Scheinost, D. Fellhauer, X. Gaona, M. Altmaier, *Radiochim. Acta* **2013**, *101*, 323–332.
- [166] C. L. Thorpe, G. T. W. Law, J. R. Lloyd, H. A. Williams, N. Atherton, K. Morris, *Environ. Sci. Technol.* **2017**, *51*, 12104–12113.
- [167] D. Langmuir, *Aqueous Environmental Geochemistry*, Prentice-Hall, Inc, Upper Saddle River, **1997**.
- [168] M. T. Friend, C. E. Lledo, L. M. Lecrivain, D. E. Wall, N. A. Wall, *Radiochim. Acta* **2018**, *106*, 963–970.
- [169] D. Boglailenko, T. G. Levitskaia, *Environ. Sci.: Nano* **2019**, *6*, 3492–3500.
- [170] W. W. Lukens, S. A. Saslow, *Dalton Trans.* **2018**, *47*, 10229–10239.
- [171] D. Papagiannopoulou, *J. Label. Compd. Radiopharm.* **2017**, *60*, 502–520.
- [172] A. Geissler, G. T. W. Law, C. Boothman, K. Morris, I. T. Burke, F. R. Livens, J. R. Lloyd, *Geomicrobiol. J.* **2011**, *28*, 507–518.
- [173] C. L. Thorpe, G. T. W. Law, J. R. Lloyd, H. A. Williams, N. Atherton, K. Morris, *Environ. Sci. Technol.* **2017**, *51*, 12104–12113.
- [174] J. R. Lloyd, V. A. Sole, C. V. G. Van Praagh, D. R. Lovley, *Appl. Environ. Microbiol.* **2000**, *66*, 3743–3749.
- [175] J. D. C. Begg, I. T. Burke, K. Morris, *Sci. Total Environ.* **2007**, *373*, 297–304.
- [176] D. M. Rodríguez, N. Mayordomo, A. Parra-Puerto, D. Schild, V. Brendler, T. Stumpf, K. Müller, *Inorg. Chem.* **2022**, *61*, 10159–10166.
- [177] M. Chotkowski, A. Czerwinski, *J. Radioanal. Nucl. Chem.* **2014**, *300*, 229–234.
- [178] J. Paquette, W. E. Lawrence, *Can. J. Chem.* **1985**, *63*, 2369–2373.
- [179] NEA, *Second Update on the Chemical Thermodynamics of U, Np, Pu, Am and Tc*, OECD Publishing, Paris, **2020**.

Manuscript received: November 26, 2024
Revised manuscript received: February 10, 2025
Accepted manuscript online: February 10, 2025
Version of record online: February 28, 2025

4.2 Hydroflux Syntheses

The synthesis and characterization of new nitridotrioxometallates can help to understand the reaction to transition metal oxides and nitridooxides under hydroflux conditions and highly alkaline conditions. As the hydroflux technique also enables the growth of single crystals of metal hydroxides, which is uncommon in typical flux reactions that often result in oxides, hydroxymetallates were also synthesized and characterized within this work. This chapter focuses on using hydroflux and alkaline environments to obtain complex compounds including tetrahedral $[MO_3N]^{2-}$ anions with $M = \text{Tc, Re}$ starting from $\text{NH}_4[MO_4]$. Furthermore, hydroxoiridates containing the octahedral $[\text{Ir}(\text{OH})_6]^{2-}$ anion, which were obtained from hydroxide melts, are discussed. Figure 9 shows an overview over the compounds which were obtained using ultra alkaline conditions.

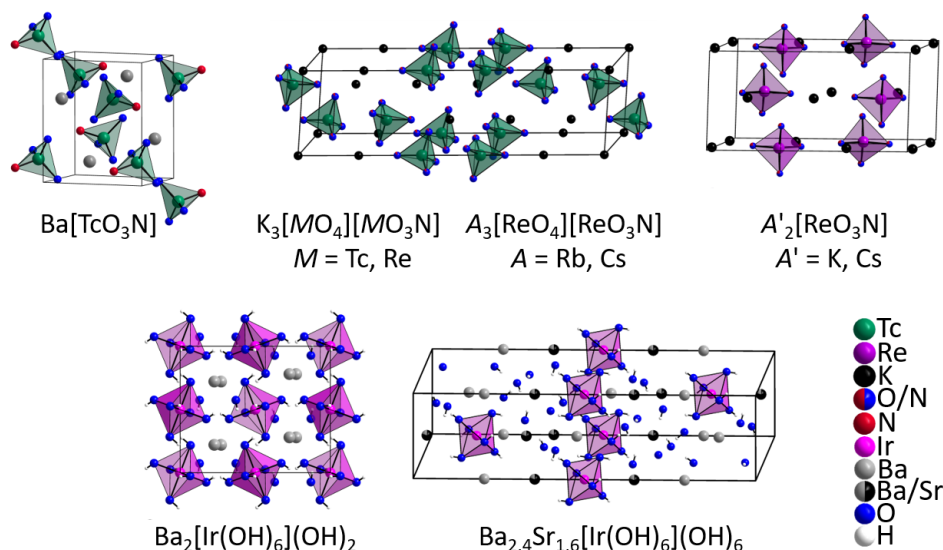


Figure 9. Overview over the compounds which were obtained using ultra alkaline conditions with exemplary crystal structures.^[77-80]

Through the introduction of several new compounds, this work enhances the understanding of the chemistry of nitridotrioxidometallates and transition metal hydroxides from highly alkaline conditions. It also demonstrates the controlled incorporation of varying amounts of nitrogen into oxoanions using NH_4^+ in hydroxide fluxes.

4.2.1 Ba[TcO₃N] from Highly Alkaline Ba(OH)₂ Medium (Publication 2)

Ba[TcO₃N] was synthesized by reacting ammonium pertechnetate in Ba(OH)₂ · 8 H₂O under highly alkaline conditions. The characterization of Ba[TcO₃N] showed isolated [TcO₃N]²⁻ tetrahedra and gave important information about how technetium behaves in alkaline environments, which is useful for nuclear waste management. *Raman* spectroscopy, XANES and DFT calculations were used to confirm the oxidation state of technetium +VII and to understand the bonding.

Publication 2

Reaction of Pertechnetate in Highly Alkaline Solution: Synthesis and Characterization of the Nitridotrioxotechnetate Ba[TcO₃N]

D. Badea, K. Dardenne, R. Polly, J. Rothe, M. Hanrath, M. Reimer, K. Meerholz,
J.-M. Neudörfl, E. Strub and J. Bruns*

Chem. Eur. J. **2022**, 28, e202201738.

doi.org/10.1002/chem.202201738

Explanation of the personal contribution to the previously mentioned publication:

All experiments were conducted by Désirée Badea, with the initial experiment originating from the master's thesis, while all the main experiments were carried out during the doctoral research. Désirée Badea synthesized all analyzed products, performed the characterization experiments, evaluated the collected data and prepared the corresponding plots for publication, unless otherwise noted below. SC-XRD, XANES, *Raman* and DFT data were obtained by co-authors. Désirée Badea prepared the draft of the manuscript. Supporting information is provided in the Appendix on page 105.

Reaction of Pertechnetate in Highly Alkaline Solution: Synthesis and Characterization of the Nitridotrioxotechnetate Ba[TcO₃N]

D. Badea,^[a] K. Dardenne,^[b] R. Polly,^[b] J. Rothe,^[b] M. Hanrath,^[a] M. Reimer,^[a] K. Meerholz,^[a] J.-M. Neudörfl,^[a] E. Strub,^[a] and J. Bruns^{*,[a]}

Abstract: The preparation of novel technetium oxides, their characterization and the general investigation of technetium chemistry are of significant importance, since fundamental research has so far mainly focused on the group homologues. Whereas the structure chemistry of technetium in strongly oxidizing media is dominated by the [TcO₄][−] anion, our recent investigation yielded the new [TcO₃N]^{2−} anion. Brown single crystals of Ba[TcO₃N] were obtained under hydrothermal conditions starting from Ba(OH)₂·8H₂O and NH₄[TcO₄] at

200 °C. Ba[TcO₃N] crystallizes in the monoclinic crystal system with the space group *P*2₁/*n* (*a* = 7.2159(4) Å, *b* = 7.8536(5) Å, *c* = 7.4931(4) Å and β = 104.279(2)°). The crystal structure of Ba[TcO₃N] consists of isolated [TcO₃N]^{2−} tetrahedra, which are surrounded by Ba²⁺ cations. XANES measurements complement the oxidation state +VII for technetium and Raman spectroscopic experiments on Ba[TcO₃N] single crystals exhibit characteristic Tc–O and Tc–N vibrational modes.

Introduction

⁹⁹Tc is a long-lived fission product of ²³⁵U accumulated in reprocessing residues upon the extraction of plutonium from irradiated uranium fuel rods. For each ton of spent nuclear fuel, technetium is formed in the order of kilograms.^[1] Therefore, it is essential to study the chemistry of technetium – especially with respect to its possible behavior in long-term storage facilities.

Due to the fact that working with technetium and its compounds requires a radionuclide laboratory, the majority of publications on fundamental technetium chemistry dates from the 1950s to the 1970s.^[2] Today's research is mainly concentrated on ^{99m}Tc, due to the medical importance of this isotope.^[3] About 40 million medical examinations are performed annually using ^{99m}Tc.^[4] In a radioactive waste repository, ⁹⁹Tc becomes

one of the most important radionuclides after plutonium on a timescale of about 50,000 years.^[5] In contrast to Pu, the chemistry of technetium is scarcely investigated.


Current studies on the long-lived isotope ⁹⁹Tc are mostly limited to the work of a few research groups, since working with the radioelement requires enhanced safety precautions.^[6] Considering the current fields of research, it is notable that the behavior of technetium during spent fuel reprocessing and in the environment has been investigated intensively by using acidic solutions.^[7] However, only a few publications with regard to technetium in alkaline media are known.^[8] For instance, the products from the radiolysis of the pertechnetate [TcO₄][−] in highly alkaline solutions were investigated.^[8c,9] As another example, the oxidation states of technetium in alkaline solutions were determined by electrochemical reduction reactions.^[10] Fundamental research has been resumed to reexamine the reaction of sulfide with pertechnetate in alkaline solutions.^[6b] However, the fundamental understanding of Tc redox chemistry in alkaline media is also important in the context of nuclear waste, since alkaline conditions prevail in some high level waste tanks.^[8a] Thus, the removal of [TcO₄][−] from highly alkaline legacy defense nuclear tank waste was studied.^[8b,d]

In this work, the reaction of ammonium pertechnetate in a highly alkaline Ba(OH)₂ medium was investigated. The obtained barium nitridotrioxotechnetate(VII) Ba[TcO₃N] was successfully synthesized and characterized. In addition to the crystal structure analysis, XAFS (XANES and EXAFS) and Raman experiments were performed. The experimental data has been complemented by computational studies.

[a] D. Badea, Dr. M. Hanrath, M. Reimer, Prof. Dr. K. Meerholz, Dr. J.-M. Neudörfl, Dr. E. Strub, Dr. J. Bruns
Department of Chemistry
University of Cologne
Greinstr. 4–6, 50939 Cologne (Germany)
E-mail: j.bruns@uni-koeln.de
Homepage: www.agbruns-iac.uni-koeln.de

[b] Dr. K. Dardenne, Dr. R. Polly, Dr. J. Rothe
Institute for Nuclear Waste Disposal
Karlsruhe Institute of Technology
Hermann-von-Helmholtz-Platz 1, 76344 Eggenstein-Leopoldshafen (Germany)

 Supporting information for this article is available on the WWW under <https://doi.org/10.1002/chem.202201738>

 © 2022 The Authors. Chemistry - A European Journal published by Wiley-VCH GmbH. This is an open access article under the terms of the Creative Commons Attribution Non-Commercial NoDerivs License, which permits use and distribution in any medium, provided the original work is properly cited, the use is non-commercial and no modifications or adaptations are made.

Results and Discussion

Single crystals of barium nitridotrioxotechnetate(VII) $\text{Ba}[\text{TcO}_3\text{N}]$ were obtained under highly alkaline conditions using $\text{NH}_4[\text{TcO}_4]$ and $\text{Ba}(\text{OH})_2 \cdot 8\text{H}_2\text{O}$ in water at 200°C . Figure 1 shows a picture of a $\text{Ba}[\text{TcO}_3\text{N}]$ single crystal positioned in a glass capillary.

The title compound crystallizes in the monoclinic crystal system with the space group $P2_1/n$. Crystallographic data for the refined structure is given in Table 1. The crystal structure consists of discrete $[\text{TcO}_3\text{N}]^{2-}$ tetrahedra, which are charge compensated by Ba^{2+} cations (Figure 2). The latter are surrounded by oxygen and nitrogen atoms in a distorted bicapped square antiprismatic fashion (Figure 3).

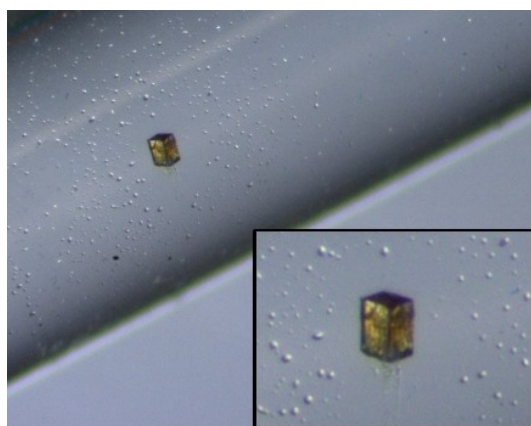


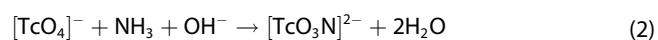
Figure 1. Microscopic picture of a single crystal of $\text{Ba}[\text{TcO}_3\text{N}]$ positioned in a glass capillary.

Table 1. Crystal and structure refinement data for $\text{Ba}[\text{TcO}_3\text{N}]$.

Empirical formula	$\text{Ba}[\text{TcO}_3\text{N}]$	
Formula weight	297.35	
Temperature	100(2) K	
Wavelength	1.54178 Å	
Crystal system	monoclinic	
Space group	$P2_1/n$	
Unit cell dimensions	$a = 7.2159(4)$ Å $b = 7.8536(5)$ Å $c = 7.4931(4)$ Å $\beta = 104.279(2)^\circ$	
Volume	411.52(4) Å ³	
Z	4	
Density (calculated)	4.799 g cm ⁻³	
F(000)	520	
Crystal size	0.02 × 0.02 × 0.01 mm ³	
2θ range for data collection	15.27° to 144.08°	
Index ranges	−8 ≤ h ≤ 8, −9 ≤ k ≤ 9, −9 ≤ l ≤ 9	
Reflections collected	6998	
Independent reflections	810 [$R_{\text{int}} = 0.0627$]	
Completeness to theta	99.7%	
Absorption correction	multi-scan	
Maximum/minimum transmission	0.0092/0.0853	
Data/restraints/parameters	810/0/56	
Goodness-of-fit on F^2	1.116	
Final R indices [$I > 2\sigma(I_o)$]	$R_1 = 0.0375$, $wR_2 = 0.0952$	
R indices (all data)	$R_1 = 0.0401$, $wR_2 = 0.0955$	
Largest diff. peak and hole	2.46/−1.13 e Å ⁻³	
CCDC number	2176571	

The structure contains one distinct technetium, nitrogen and barium atom, respectively. However, three crystallographically distinguishable oxygen atoms are found.

The technetium atom is coordinated by three oxygen atoms, exhibiting Tc–O bond lengths of 1.763(4) Å, 1.776(4) Å and 1.777(4) Å. The fourth technetium–ligand bond within the tetrahedron is significantly shorter, exhibiting a length of 1.692(5) Å and thus giving hint for a Tc–N bond. Accordingly, the formation of the nitridotrioxotechnetate anion can be assumed. Apart from the new $[\text{TcO}_3\text{N}]^{2-}$ anion, only a small number of other nitridotrioxometallates, such as $\text{K}_2[\text{ReO}_3\text{N}]$, $\text{M}[\text{OsO}_3\text{N}]$ ($\text{M} = \text{K}, \text{Rb}, \text{Ag}, \text{Cs}, \text{Ti}$), $\text{Ba}_2[\text{VO}_3\text{N}]$ and $\text{Ba}_3[\text{WO}_3\text{N}]_2$, are known.^[11] Even though some of the nitridotrioxometallates have already been synthesized, still not all of them have been structurally elucidated by single crystal X-ray diffraction.^[11] $\text{Ba}_3[\text{WO}_3\text{N}]_2$ was synthesized by heating $\text{Ba}_3\text{W}_2\text{O}_9$ at high temperatures in the range of 700°C in a stream of NH_3 gas.^[11e] $\text{K}[\text{OsO}_3\text{N}]$ can be obtained through milder reaction conditions starting from OsO_4 , KOH and NH_4OH , whereas the other nitridotrioxoosmates are synthesized by reacting the potassium salt with slightly soluble salts of the cations in aqueous solution.^[11c] By the use of liquid ammonia, $\text{K}_2[\text{ReO}_3\text{N}]$ has been prepared from the reaction of potassium amide with rhenium heptoxide.^[11b] In the case of $\text{Ba}[\text{TcO}_3\text{N}]$, an OH^- assisted ammonolysis to insert the nitrogen atom according to the following reaction equations can be assumed:



The reaction is quite similar to the synthesis of $\text{K}[\text{OsO}_3\text{N}]$, making OH^- assisted ammonolysis an efficient way for the insertion of nitrogen into oxometallates. In case of technetium's lighter and heavier homologues Mn and Re, the same reactions have not been successful. However, radiolytic effects can be excluded, since they have not been observed in any of our previous experimental studies with ^{99}Tc , even when dealing with macroscopic amounts of $\text{TcO}_2(\text{s})$ in solubility experiments.^[12]

In addition to the performed single crystal X-ray experiments, the structure of $\text{Ba}[\text{TcO}_3\text{N}]$ was optimized with DFT calculations. The calculated unit cell is shown in Figure 4. The optimized values comply excellently with the experimental data shown in Table S3 in the Supporting Information. The calculated values of the cell parameters $a = 7.32$ Å, $b = 8.00$ Å and $c = 7.62$ Å agree with the available structural data $a = 7.2159(4)$ Å, $b = 7.8536(5)$ Å and $c = 7.4931(4)$ Å. Furthermore, the lengths of 1.69 Å and 1.78 Å for the Tc–N and Tc–O bonds, which are in excellent agreement with the experimental results, were determined (see Table S3 for the other calculated distances as well). Figure 5 shows the DFT-optimized structures and schematic MO of tetrahedral pertechnetate $[\text{Tc}(\text{VII})\text{O}_4]^-$ and $[\text{Tc}(\text{VII})\text{O}_3\text{N}]^{2-}$ in the gas phase.

The optimization of the $[\text{Tc}(\text{VII})\text{O}_3\text{N}]^{2-}$ anion in the gas phase in C_{3v} symmetry yields similar results with 1.71 Å and 1.79 Å for the Tc–N and Tc–O distances, respectively. Hence,

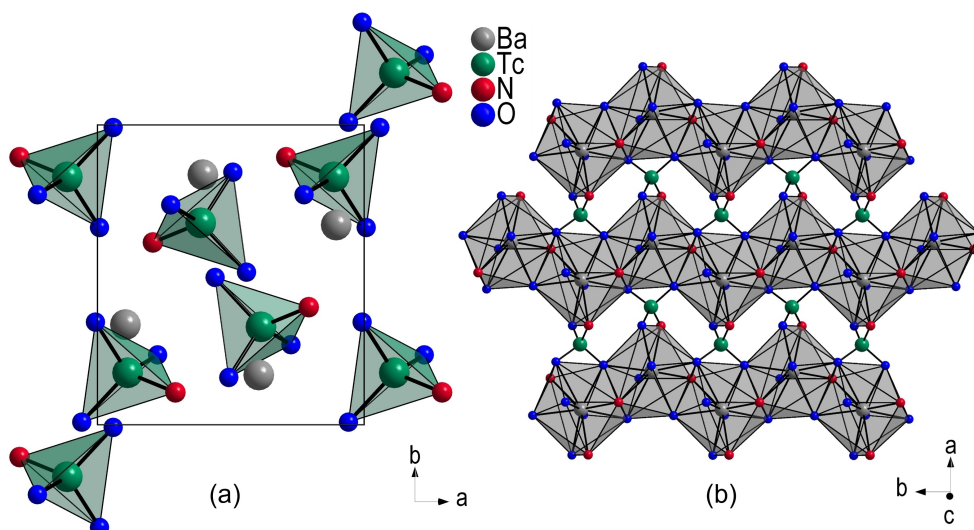


Figure 2. a) Crystal structure of Ba[TcO₃N] with the representation of the unit cell; b) coordination polyhedra of Ba²⁺ extending in the *a-b* plane.

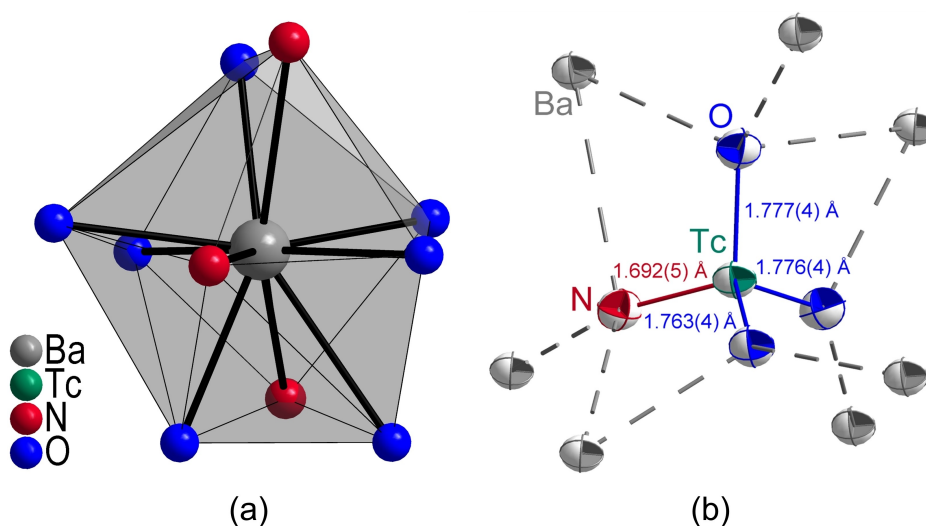


Figure 3. a) Coordination geometry around the barium cation and b) ellipsoid representation of the [TcO₃N]²⁻ anion with coordinating Ba²⁺ cations. The thermal ellipsoids are drawn with a probability of 70%.

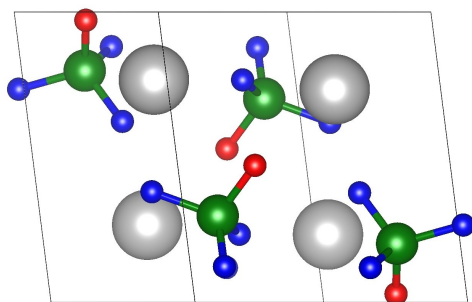


Figure 4. Unit cell of the optimized Ba[TcO₃N] structure; color code: grey-barium, blue-oxygen, red-nitrogen, green-technetium.

both approaches result in very similar structures of the [Tc(VII)O₃N]²⁻ species.

In addition to structural studies of Ba[TcO₃N], Raman spectroscopic experiments using a Renishaw inVia Raman microscope were performed on exactly the same single crystal which has been used for SCXRD. Figure 6 shows the Raman spectrum of Ba[TcO₃N]. The prominent bands are observed between 986 and 299 cm⁻¹.

In comparison with the spectra of [OsO₃N]⁻ and by the use of quantum chemical calculations, the bands of [TcO₃N]²⁻ have been assigned.^[11e,13] The calculated Raman and IR spectrum are given in the Supporting Information together with a detailed assignment of the respective vibrations (Figures S2, S3 and Table S7 in the Supporting Information). Accordingly, the strong absorption band at 986 cm⁻¹ belongs to the Tc–N stretching

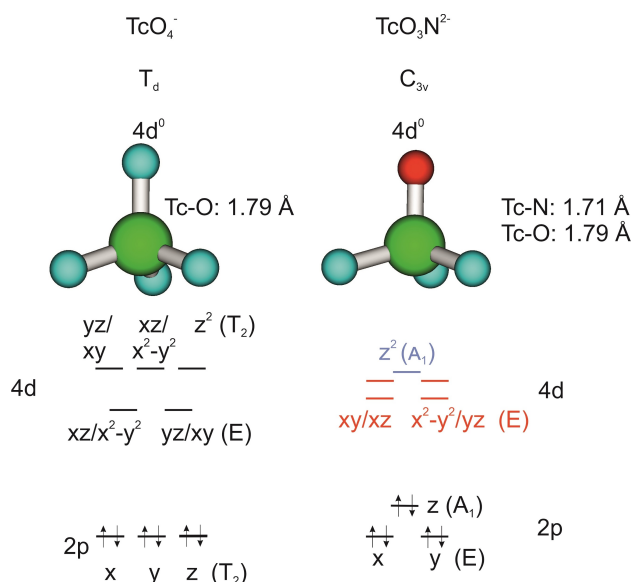


Figure 5. DFT-optimized structures (in the gas phase) and schematic MO of a) tetrahedral pertechnetate $[\text{Tc}(\text{VII})\text{O}_4]^-$, b) $[\text{Tc}(\text{VII})\text{O}_3\text{N}]^{2-}$ in C_{3v} symmetry.

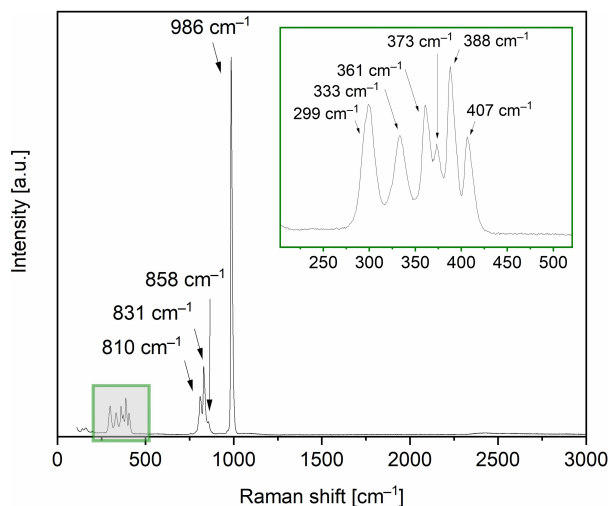


Figure 6. Raman spectrum of $\text{Ba}[\text{TcO}_3\text{N}]$ with a cutout for better clarity.

vibration. The less intense bands at 858, 831, 810 cm^{-1} can be attributed to Tc–O stretching modes. The bands between 407 and 361 cm^{-1} stem from O–Tc–N bending vibrations and those at 333 and 299 cm^{-1} from O–Tc–O bending vibrations.

To determine the valence state of technetium, X-ray absorption near edge structure (XANES) spectroscopy studies of the title compound were conducted at the Tc K- and L_3 -edges along with corresponding measurements of $[\text{Tc}(\text{VII})\text{O}_4]^-$ species in aqueous solution ($[\text{Tc}] = 20 \text{ mM}$ obtained by dissolution of $\text{Na}[\text{TcO}_4]$ in 0.1 M HCl) as a reference. In comparison to studies on the Tc K-edge, this is only the fifth known L_3 -edge XANES measurement performed with a technetium sample.^[14] Additionally, relativistic multi-reference ab initio calculations were applied to calculate the Tc L_3 -edge XANES spectra of both

compounds. The calculated spectra for both optimized gas phase structures, shown in Figure 7, are almost identical. This is also the case for the corresponding experimental Tc L_3 -XANES spectra of $[\text{Tc}(\text{VII})\text{O}_3\text{N}]^{2-}$ and $[\text{Tc}(\text{VII})\text{O}_4]^{2-}$ shown in Figure 7, right hand side. Note that the absolute energy positions between calculated and experimental spectra are off by more than 20 eV, indicating a systematic uncertainty in the determination of the Fermi level by the applied theory.

For the $[\text{Tc}(\text{VII})\text{O}_3\text{N}]^{2-}$ anion, the Tc–N bond is oriented along the z-axis. As the ground state has an empty 4d shell ($S = 0$), it is a single reference closed shell state. Since spin-orbit (SO) effects are important, all relevant excited singlet and triplet states, fifteen each, were determined in the calculations. From the MO diagram in Figure 5 it is evident that the energy of excited states with an electron occupying a mixed $4d_{\pm\pi}/4d_{\pm\delta}$ ($4d_{xz}/4d_{yz}/4d_{xy}/4d_{x^2-y^2}$) orbital (in the irreducible representation E) is lower compared to states with an $4d_z$ ($4d_{z^2}$) occupation (in the irreducible representation A_1), because $4d_z$ points directly towards the nitrogen atom with the Tc–N distance shorter compared to the Tc–O distances. Hence, there are more peaks to be expected compared to $[\text{Tc}(\text{VII})\text{O}_4]^-$.

Due to the ligand field splitting of the 4d orbitals in C_{3v} there are two lower lying states in the irreducible representation E of C_{3v} and one higher lying state in A_1 (see Figure 5). The two peaks visible in the spectrum (denoted as 1 and 2 in Figure 7) can be assigned to excitations from $2p_{3/2} \rightarrow 4d_{yz}/4d_{xz}$ ($4d_{xy}/4d_{x^2-y^2}$) (all 4d orbitals in E) and $2p_{3/2} \rightarrow 4d_{z^2}$ (4d orbitals in A_1), respectively. The excited states are predominantly singlet states ($S = 0$). The splitting between the two peaks is $\sim 2.3 \text{ eV}$ for the RASSCF calculations, being very close to the experimental value of 2.0 eV. Moreover, Figure 8 depicts the comparison of the Tc K-edge XANES spectra (corresponding to dipole-allowed $1s \rightarrow 5p$ excitations) obtained for both Tc compounds. Note that the distinct pre-edge peak above 21.050 eV generally indicates the presence of a tetrahedral pertechnetate ($\text{Tc}(\text{VII})\text{O}_4^-$)-like Tc bonding environment. The absence of an inversion center allows for the hybridization of the transition metal's 4d and 5p states, thus rendering the lowest lying unoccupied electronic states accessible for Tc 1s core electrons (cf.^[14a] and references therein). This coordination structure is as well reflected by Tc K EXAFS of the title compound compared to aqueous pertechnetate moieties (structural parameters and spectra obtained from EXAFS are shown in Table S5 and Figure S1 in the Supporting Information). Thus, the Tc oxidation state of +VII in $\text{Ba}[\text{TcO}_3\text{N}]$ has not only been proven indirectly by the detection of Tc–N bands in the Raman spectrum, but also directly by means of Tc K/ L_3 -edge XAFS spectroscopy and multireference ab initio calculations of Tc L_3 -edge XANES spectra.

Conclusion

Since technetium is formed in order of kilograms for each ton of spent nuclear fuel, technetium redox chemistry as well as its behaviour in long-term storage facilities needs to be investigated. Hitherto, there is a significant lack in knowledge about

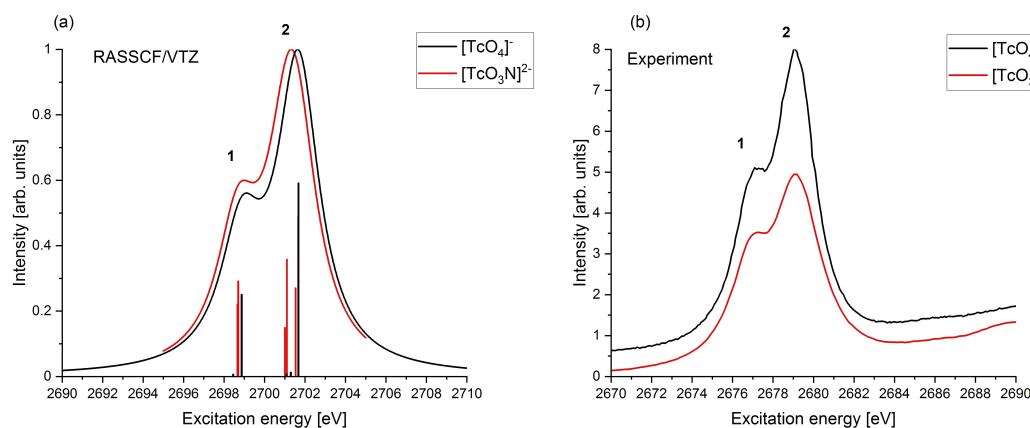


Figure 7. (a) ab initio Tc L₃-edge XANES spectra of [Tc(VII)O₃N]²⁻ ([Tc(VII)O₄]⁻ shown for comparison) obtained by RASSCF/ANO-VTZ calculations based on the DFT gas phase structure optimization (see Figure 5), vertical bars representing transition energies and oscillator strengths of relevant Tc 2p_{3/2}→4d_{5/2} excitations and spectral envelopes (solid lines) obtained by convoluting bars with Lorentzians. (b) Normalized Tc L₃-edge XANES spectra of [Tc(VII)O₃N]²⁻ and [Tc(VII)O₄]⁻ (the latter one vertically shifted for clarity).

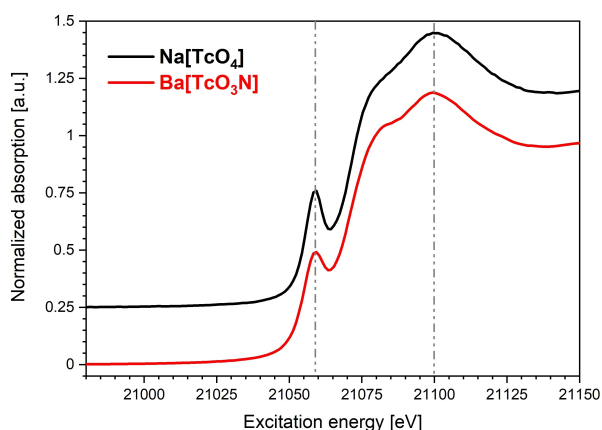


Figure 8. Normalized Tc K-edge XANES spectra of [Tc(VII)O₃N]²⁻ and [Tc(VII)O₄]⁻ (the latter one vertically shifted for clarity).

the behaviour of technetium species in alkaline media. With the synthesis of Ba[TcO₃N] from barium hydroxide, water and ammonium pertechnetate, the stability of the Tc oxidation state +VII even under as harsh conditions, as for example highly concentrated alkaline solution, can be underlined. It might occur in a final repository for nuclear waste in geological salt formations, for example, in case of the degradation of cementitious waste forms. The oxidation state has been proven by detailed XANES and EXAFS investigations, which have been corroborated by quantum chemical calculation.

From a preparative viewpoint, the introduced reaction of an OH⁻ assisted ammonolysis is an easy and energetically favourable way for the insertion of nitrogen into oxoanions for future reactions. Since so far only one nitrogen per technetium atom has been introduced, further experiments are planned to increase the nitrogen content per technetium atom by adding excess ammonium hydroxide in stoichiometric amounts.

Experimental Section

Caution! ⁹⁹Tc is a β⁻ emitter. All operations have to be done in a specially equipped radiochemical laboratory. Appropriate shielding has to be employed during all manipulations of ⁹⁹Tc containing samples.

Synthesis: Brown single crystals of Ba[TcO₃N] were obtained from a barium hydroxide octahydrate solution by applying hydrothermal conditions using a Teflon-lined stainless steel autoclave. A typical batch contained 5.4 mg NH₄[TcO₄] (*Oak Ridge National Laboratory*, purity not specified), 63.7 mg Ba(OH)₂·8H₂O (*Alfa Aesar*, 98 %) and 63.7 mL H₂O. The reagents were combined in a Teflon beaker and subsequently heated in a stainless steel autoclave at 200 °C for 10 h. After decreasing the temperature within 30 h to room temperature, the crystals of the title compound were obtained in a colorless matrix. The product formation is highly dependent on the used amount of water and Ba(OH)₂·8H₂O, so that even small changes prevent successful reaction. For the afore mentioned batch size at least 100 crystals were obtained. They were all of roughly uniform shape and color. The single crystals were removed from the flux mechanically. Removal of the flux to obtain a phase pure bulk material was neither successful by washing with water nor with methanol or other solvents. However, the crystal color and habitus remained unchanged after washing with water and methanol.

Single crystal X-ray diffraction: Single crystal XRD data were collected on a Bruker D8 Venture using Cu-K_α radiation (λ = 1.54178 Å), an X-ray optics mirror and a Photon III detector. The crystal was prepared under a polarization microscope and measured at reduced temperature. The lattice parameters, the refinement details, the atomic parameters and selected bond lengths are given in Tables S1–S4 in the Supporting Information. The structure solution and refinement was successful using ShelXL/ShelXT in Olex2.^[15] The pictures of the structure were developed with the Diamond program.^[16]

Deposition Number(s) 2176571 contain(s) the supplementary crystallographic data for this paper. These data are provided free of charge by the joint Cambridge Crystallographic Data Centre and Fachinformationszentrum Karlsruhe Access Structures service.

Raman spectroscopy: Single crystals of the title compound were selected in glass capillaries and placed under a Renishaw inVia

Raman microscope. The spectra were recorded with a 532 nm laser excitation at room temperature.

Tc K/L₃-edge XAFS spectroscopy: X-ray absorption fine structure (XAFS) measurements were performed at the Tc K-edge (E_{1s} (Tc^0) = 21.044 keV, Tc 1s→5p transitions, including extended X-ray absorption fine structure, EXAFS) and at the Tc L₃-edge ($E_{2p_{3/2}}$ (Tc^0) = 2.677 keV, Tc 2p_{3/2}→4d transitions, only covering the X-ray absorption near edge structure, XANES). The K- and L₃-edge spectra in the hard and 'tender' X-ray regime, respectively, were recorded at the INE-BEAMLINE^[17] of the KIT Light Source (KARA storage ring, KIT Campus North) in total fluorescence yield detection mode. Details of the data acquisition procedures have been recently reported elsewhere.^[14a] At the Tc K-edge, Ba[TcO₃N] crystals were accumulated in the tip of sealed polyethylene vials installed in an Ar-flushed flow-through sample holder. At the L₃-edge, the ground crystals were measured dispersed on adhesive KAPTON® (polyimide) film covered by a thin (13 μm) KAPTON foil. The resulting pouches were installed in the He-flushed low energy sample chamber described in Ref. [14a].

Quantum chemical calculations

Relativistic multireference ab initio study of Tc L₃-XANES spectra: Recently, relativistic multiconfiguration ab initio quantum chemistry methods have developed into a powerful tool supporting X-ray spectroscopy techniques.^[18] Because of the complexity of the detected signals, theoretical calculations are mandatory for the interpretation of the experimental data. For recent extensive reviews see, for example.^[19]

Structures of the [Tc(VII)O₃N]²⁻ species: The calculation of the XANES spectra of [Tc(VII)O₃N]²⁻ requires reliable structures. The structure of [Tc(VII)O₃N]²⁻ was optimized with Density Functional Theory (DFT).^[20] For the gas phase structure the RI-DFT method was used as available in TURBOMOLE (www.turbomole.com)^[21] employing the def2-TZVP^[22] basis set. Additionally, the crystal structure of the nitridotrioxotechnetate Ba[TcO₃N] was optimized with DFT based on periodic boundary conditions as implemented in the Vienna Ab Initio Simulation Package (VASP).^[23] The Kohn-Sham equations were solved using a plane-wave basis set. Electron exchange and correlation were described using the Perdew-Burke-Ernzerhof (PBE) version^[24] of the generalized gradient approximation (GGA). The core electrons were described by projector augmented wave (PAW) potentials^[25] as implemented by Kresse and Joubert.^[26] For the calculations an energy cutoff of E_{cut} = 500 eV was chosen. The resulting xyz coordinates are given in Table S6.

Tc L₃-XANES calculations: The calculation of the Tc L₃-XANES spectra (corresponding to 2p_{3/2}→4d_{3/2,5/2} excitations) of the [Tc(VII)O₃N]²⁻ were carried out as outlined in Ref. [27] using relativistic multireference ab initio methods available in MOLCAS8.4.^[28] The restricted active space (RASSCF) method^[29] was used for the calculation of Spin-orbit interactions (SO) in the restricted-active-space state-interaction (RASSI) scheme.^[30] For the RASSCF calculations the active space was subdivided. The RAS1 space contains the three 2p orbitals and the five 4d orbitals occupy the RAS3 space. In total six active electrons are distributed in the active space. Both scalar relativistic and spin-orbit coupling (SOC) were accounted for in our calculations. For the spin-orbit interaction calculations all relevant spin states were included in the calculations. The ANO-VTZ basis set available in MOLCAS was used.^[31] The calculations were performed using the full C_{3v} symmetry with the SUPERSYMMETRY option imposing higher supersymmetry by restricting rotations to irreducible representations in the RASSCF calculations. Experimental spectra were simulated by applying a Lorentzian profile at the calculated

transition energies with the intensities given by the oscillator strengths with a full width at half maximum of γ = 2.5 eV for the different species.

Vibrational spectroscopy calculation: Additionally, solid state calculations with the CRYSTAL program suite^[32] using pob-TZVP^[33] (Ba, O, N) and ERD_2017 (Tc) basis sets and PBESol^[34] and HSEsol^[35] density functional theory were carried out. All optimized geometries were confirmed by subsequent frequency calculations. Intensities were obtained for the PBESol functional using CRYSTAL's CPKS^[36] module. In order to achieve convergence all calculations were conducted in internal coordinates with the XXL integration grid.

IR and Raman frequencies were calculated using CRYSTAL^[37] within the harmonic approximation (Table S7). The simulated Raman and IR spectra were calculated using the PBESol functional only since CRYSTAL does not allow for the calculation of intensities for the HSEsol functional. However, we cross checked the locations of the transitions with the HSEsol functional and found no significant difference. Obtained normal modes were analyzed by visual inspection and classified as stretching, bending or skeletal modes. For visualization of the spectra, calculated Raman and IR intensities were fitted with Lorentzian functions (Figures S2 and S3).

Acknowledgements

We thank Dr. Markus Zegke for his constant support and help with the handling of Tc samples. Jörn Bruns thanks the Fonds der Chemischen Industrie (FCI) for financial support. Jörn Bruns and Désirée Badea thank Prof. Mathias Wickleder for the constant support. Open Access funding enabled and organized by Projekt DEAL.

Conflict of Interest

The authors declare no conflict of interest.

Data Availability Statement

The data that support the findings of this study are available in the supplementary material of this article.

Keywords: hydrothermal · oxoanions · technetium · X-ray · XANES

- [1] M. Y. Khalil, W. B. White, *J. Am. Ceram. Soc.* **1983**, *66*, 197–198.
- [2] a) J. W. Cobble, W. T. Smith, G. E. Boyd, *J. Am. Chem. Soc.* **1953**, *75*, 5777–5782; b) R. H. Colton, R. D. Peacock, *Q. Rev. Chem. Soc.* **1962**, *16*, 299–315; c) A. A. Pozdnyakov, *Russ. Chem. Rev.* **1965**, *34*, 129–141.
- [3] a) C. Gallini, F. Tutino, R. Martone, A. Ciacchio, E. N. Costanzo, G. Taborchi, S. Morini, S. Bartolini, S. Farsetti, C. Di Mario, F. Perfetto, F. Cappelli, *J. Nucl. Cardiol.* **2021**, *28*, 90–99; b) K. Koyanagawa, M. Naya, T. Aikawa, O. Manabe, M. Kuzume, H. Ohira, I. Tsujino, N. Tamaki, T. Anzai, *J. Nucl. Cardiol.* **2021**, *28*, 128–136; c) K. V. Zavadovsky, A. V. Mochula, A. A. Boshchenko, A. V. Vrublevsky, A. E. Baev, A. L. Krylov, M. O. Gulya, E. A. Nesterov, R. Liga, A. Gimelli, *J. Nucl. Cardiol.* **2021**, *28*, 249–259.
- [4] W. C. Eckelman, *J. Am. Coll. Cardiol.* **2009**, *2*, 364–368.
- [5] P. N. Swift, D. Sassani, *Impacts of Nuclear Fuel Cycle Choices on Permanent Disposal of High-Activity Radioactive Wastes*. **2019**, No.

- SAND2019-5941 C. Sandia National Lab.(SNL-NM), Albuquerque, NM (United States), 2019.
- [6] a) R. Alberto, *J. Organomet. Chem.* **2018**, *869*, 264–269; b) N. Edelstein, C. Burns, D. Shuh, W. Lukens, *Research Program to Investigate the Fundamental Chemistry of Technetium*, **2000**; c) F. Poineau, E. E. Rodriguez, P. F. Weck, A. P. Sattelberger, P. Forster, T. Hartmann, E. Mausolf, G. W. C. Silva, G. D. Jarvinen, A. K. Cheetham, K. R. Czerwinski, *J. Radioanal. Nucl. Chem.* **2009**, *282*, 605–609.
- [7] a) N. D. Goletskii, B. Y. Zilberman, Y. S. Fedorov, A. S. Kudinov, A. A. Timoshuk, L. V. Sytnik, E. A. Puzikov, S. A. Rodionov, A. P. Krinitsyn, V. I. Ryazantsev, D. V. Ryabkov, *Radiochemistry* **2014**, *56*, 501–514; b) M. Lin, I. Kajan, D. Schumann, A. Türlér, *J. Radioanal. Nucl. Chem.* **2019**, *322*, 1857–1862; c) M. Zegke, D. Grödlér, M. Roca Jungfer, A. Haseloer, M. Kreuter, J. M. Neudörfl, T. Sittel, C. M. James, J. Rothe, M. Altmaier, A. Klein, M. Breugst, U. Abram, E. Strub, M. S. Wickleder, *Angew. Chem. Int. Ed.* **2022**, *61*, e202113777.
- [8] a) W. W. Lukens, D. K. Shuh, N. C. Schroeder, K. R. Ashley, in *226 American Chemical Society Meeting*, United States, **2003**; b) J. Li, B. Li, N. Shen, L. Chen, Q. Guo, L. Chen, L. He, X. Dai, Z. Chai, S. Wang, *ACS Cent. Sci.* **2021**, *7*, 1441–1450; c) W. W. Lukens, J. J. Bucher, N. M. Edelstein, D. K. Shuh, *Environ. Sci. Technol.* **2002**, *36*, 1124–1129; d) N. Shen, Z. Yang, S. Liu, X. Dai, C. Xiao, K. Taylor-Pashow, D. Li, C. Yang, J. Li, Y. Zhang, M. Zhang, R. Zhou, Z. Chai, S. Wang, *Nat. Commun.* **2020**, *11*, 5571.
- [9] W. W. Lukens, J. J. Bucher, N. M. Edelstein, D. K. Shuh, *J. Phys. Chem. A* **2001**, *105*, 9611–9615.
- [10] M. Chotkowski, M. Grdeń, B. Wrzosek, *J. Electroanal. Chem.* **2018**, *829*, 148–156.
- [11] a) S. J. Clarke, P. R. Chalker, J. Holman, C. W. Michie, M. Puyet, M. J. Rosseinsky, *J. Am. Chem. Soc.* **2002**, *124*, 3337–3342; b) B. Krebs, A. Müller, *J. Inorg. Nucl. Chem.* **1968**, *30*, 463–466; c) A. Müller, F. Bollmann, *Z. Naturforsch. B* **1968**, *23*, 1539–1539; d) R. Pastuszak, P. L'Haron, R. Marchand, Y. Laurent, *Acta Crystallogr. Sect. B* **1982**, *38*, 1427–1430; e) P. Subramanya Herle, M. S. Hegde, G. N. Subbanna, *J. Mater. Chem.* **1997**, *7*, 2121–2125.
- [12] a) T. Kobayashi, A. C. Scheinost, D. Fellhauer, X. Gaona, M. Altmaier, *Radiochim. Acta* **2013**, *101*, 323–332; b) E. Yalcintas, X. Gaona, A. C. Scheinost, T. Kobayashi, M. Altmaier, H. Geckeis, *Radiochim. Acta* **2015**, *103*, 57–72; c) E. P. Yalcintas, X. Gaona, M. Altmaier, K. Dardenne, R. Polly, H. Geckeis, *Dalton Trans.* **2016**, *45*, 8916–8936; d) A. Baumann, E. Yalcintas, X. Gaona, R. Polly, K. Dardenne, T. Prüßmann, J. Rothe, M. Altmaier, H. Geckeis, *Dalton Trans.* **2018**, *47*, 4377–4392.
- [13] A. Müller, E. J. Baran, F. Bollmann, P. J. Aymonino, *Z. Naturforsch.* **1969**, *24*, 960–964.
- [14] a) K. Dardenne, S. Duckworth, X. Gaona, R. Polly, B. Schimmelpfennig, T. Pruessmann, J. Rothe, M. Altmaier, H. Geckeis, *Inorg. Chem.* **2021**, *60*, 12285–12298; b) P. E. R. Blanchard, E. Reynolds, B. J. Kennedy, C. D. Ling, Z. Zhang, G. Thorogood, B. C. C. Cowie, L. Thomsen, *J. Synchrotron Radiat.* **2014**, *21*, 1275–1281; c) S. Bauters, A. C. Scheinost, K. Schmeide, S. Weiss, K. Dardenne, J. Rothe, N. Mayordomo, R. Steudtner, T. Stumpf, U. Abram, S. M. Butorin, K. O. Kvashnina, *Chem. Commun.* **2020**, *56*, 9608–9611.
- [15] a) O. V. Dolomanov, L. J. Bourhis, R. J. Gildea, J. A. K. Howard, H. Puschmann, *J. Appl. Crystallogr.* **2009**, *42*, 339–341; b) G. Sheldrick, *Acta Crystallogr. Sect. C* **2015**, *71*, 3–8.
- [16] K. Brandenburg, *Diamond 4, Crystal and Molecular Structure Visualization*, Crystal Impact GbR, Bonn, Germany, **2019**.
- [17] J. Rothe, S. Butorin, K. Dardenne, M. A. Denecke, B. Kienzler, M. Löble, V. Metz, A. Seibert, M. Steppert, T. Vitova, C. Walther, H. Geckeis, *Rev. Sci. Instrum.* **2012**, *83*, 043105.
- [18] a) I. Josefsson, K. Kunnus, S. Schreck, A. Föhlisch, F. de Groot, P. Wernet, M. Odelius, *J. Phys. Chem. Lett.* **2012**, *3*, 3565–3570; b) R. V. Pinjari, M. G. Delcey, M. Guo, M. Odelius, M. Lundberg, *J. Phys. Chem. Lett.* **2015**, *142*, 069901; c) R. V. Pinjari, M. G. Delcey, M. Guo, M. Odelius, M. Lundberg, *J. Comput. Chem.* **2016**, *37*, 477–486.
- [19] a) P. Norman, A. Dreuw, *Chem. Rev.* **2018**, *118*, 7208–7248; b) S. I. Bokarev, O. Kühn, *Wiley Interdiscip. Rev.: Comput. Mol. Sci.* **2020**, *10*, e1433; c) M. Lundberg, M. G. Delcey, in *Transition Metals in Coordination Environments*, 1 ed., Springer International Publishing, Cham, Switzerland, **2019**, pp. 185–217.
- [20] a) P. Hohenberg, W. Kohn, *Phys. Rev.* **1964**, *136*, B864–B871; b) W. Kohn, L. J. Sham, *Phys. Rev.* **1965**, *140*, A1133–A1138.
- [21] a) A. Schäfer, H. Horn, R. Ahlrichs, *J. Chem. Phys.* **1992**, *97*, 2571–2577; b) K. Eichkorn, O. Treutler, H. Öhm, M. Häser, R. Ahlrichs, *Chem. Phys. Lett.* **1995**, *240*, 283–290; c) O. Treutler, R. Ahlrichs, *J. Chem. Phys.* **1995**, *102*, 346–354; d) K. Eichkorn, F. Weigend, O. Treutler, R. Ahlrichs, *Theor. Chem. Acc.* **1997**, *97*, 119–124; e) M. v. Arnim, R. Ahlrichs, *J. Chem. Phys.* **1999**, *111*, 9183–9190; f) P. Deglmann, K. May, F. Furche, R. Ahlrichs, *Chem. Phys. Lett.* **2004**, *384*, 103–107.
- [22] a) F. Weigend, M. Häser, H. Patzelt, R. Ahlrichs, *Chem. Phys. Lett.* **1998**, *294*, 143–152; b) F. Weigend, R. Ahlrichs, *Phys. Chem. Chem. Phys.* **2005**, *7*, 3297–3305; c) D. Andrae, U. Häußermann, M. Dolg, H. Stoll, H. Preuß, *Theor. Chim. Acta* **1990**, *77*, 123–141.
- [23] a) G. Kresse, J. Hafner, *Phys. Rev. B* **1993**, *48*, 13115–13118; b) G. Kresse, J. Furthmüller, *Phys. Rev. B* **1996**, *54*, 11169–11186; c) G. Kresse, J. Furthmüller, *Comput. Mater. Sci.* **1996**, *6*, 15–50.
- [24] J. P. Perdew, K. Burke, M. Ernzerhof, *Phys. Rev. Lett.* **1996**, *77*, 3865–3868.
- [25] P. E. Blöchl, *Phys. Rev. B* **1994**, *50*, 17953–17979.
- [26] G. Kresse, D. Joubert, *Phys. Rev. B* **1999**, *59*, 1758–1775.
- [27] a) K. Dardenne, S. Duckworth, X. Gaona, R. Polly, B. Schimmelpfennig, T. Pruessmann, J. Rothe, M. Altmaier, H. Geckeis, *Inorg. Chem.* **2021**, *60*, 12285–12298; b) R. Polly, B. Schacherl, J. Rothe, T. Vitova, *Inorg. Chem.* **2021**, *60*, 18764–18776.
- [28] F. Aquilante, J. Autschbach, R. K. Carlson, L. F. Chibotaru, M. G. Delcey, L. De Vico, I. Fdez. Galván, N. Ferré, L. M. Frutos, L. Gagliardi, M. Garavelli, A. Giussani, C. E. Hoyer, G. Li Manni, H. Lischka, D. Ma, P. Å. Malmqvist, T. Müller, A. Nenov, M. Olivucci, T. B. Pedersen, D. Peng, F. Plasser, B. Pritchard, M. Reiher, I. Rivalta, I. Schapiro, J. Segarra-Martí, M. Stenrup, D. G. Truhlar, L. Ungur, A. Valentini, S. Vancouillie, V. Veryazov, V. P. Vysotskiy, O. Weingart, F. Zapata, R. Lindh, *J. Comput. Chem.* **2016**, *37*, 506–541.
- [29] P. A. Malmqvist, A. Rendell, B. O. Roos, *J. Phys. Chem.* **1990**, *94*, 5477–5482.
- [30] P.-Å. Malmqvist, B. Roos, B. Schimmelpfennig, *Chem. Phys. Lett.* **2002**, *357*, 230–240.
- [31] a) B. O. Roos, R. Lindh, P.-Å. Malmqvist, V. Veryazov, P.-O. Widmark, *J. Phys. Chem. A* **2004**, *108*, 2851–2858; b) B. O. Roos, R. Lindh, P.-Å. Malmqvist, V. Veryazov, P.-O. Widmark, *J. Phys. Chem. A* **2005**, *109*, 6575–6579.
- [32] R. Dovesi, R. Orlando, A. Erba, C. Zicovich-Wilson, B. Civalieri, S. Casassa, L. Maschio, M. Ferrabone, M. De La Pierre, P. D'arco, M. Réat, B. Kirtman, *Int. J. Quantum Chem.* **2014**, *114*, 1287–1317.
- [33] a) M. F. Peintinger, D. V. Oliveira, T. Bredow, *J. Comput. Chem.* **2012**, *34*, 451–459; b) D. Vilela Oliveira, J. Laun, M. F. Peintinger, T. Bredow, *J. Comput. Chem.* **2019**, *40*, 2364–2376.
- [34] J. P. Perdew, A. Ruzsinszky, G. I. Csonka, O. A. Vydrov, G. E. Scuseria, L. A. Constantin, X. L. Zhou, K. Burke, *Phys. Rev. Lett.* **2008**, *100*, 136406–136406-4.
- [35] L. Schimka, J. Harl, G. Kresse, *J. Chem. Phys.* **2011**, *134*, 024116–1024116-11.
- [36] a) M. Ferrero, M. Réat, B. Kirtman, R. Dovesi, *J. Chem. Phys.* **2008**, *129*, 244110; b) M. Ferrero, M. Réat, R. Orlando, R. Dovesi, *J. Comput. Chem.* **2008**, *29*, 1450–1459; c) M. Ferrero, M. Réat, R. Orlando, R. Dovesi, *J. Chem. Phys.* **2008**, *128*, 014110.
- [37] a) F. Pascale, C. M. Zicovich-Wilson, F. López Gejo, B. Civalieri, R. Orlando, R. Dovesi, *J. Comput. Chem.* **2004**, *25*, 888–897; b) C. M. Zicovich-Wilson, F. Pascale, C. Roetti, V. R. Saunders, R. Orlando, R. Dovesi, *J. Comput. Chem.* **2004**, *25*, 1873–1881.

Manuscript received: June 6, 2022
Accepted manuscript online: August 11, 2022
Version of record online: September 12, 2022

4.2.2 $K_3[MO_4][MO_3N]$ with $M = \text{Tc, Re}$ from KOH Hydroflux (Publication 3)

For the synthesis of the mixed anionic nitridotrioxometallates $K_3[\text{ReO}_4][\text{ReO}_3\text{N}]$ and $K_3[\text{TcO}_4][\text{TcO}_3\text{N}]$, ammonium perrhenate and pertechnetate were used as starting materials and were reacted in KOH hydrofluxes. The structures of these compounds were analyzed using SC-XRD and supported by additional characterization techniques, such as XPS, *Raman* spectroscopy and quantum chemical calculations, which also confirmed the presence of Re-N and Tc-N bonds.

Publication 3

$K_3[MO_4][MO_3N]$ ($M = \text{Tc, Re}$) – Nitridotrioxidorhenate and -technetate from Highly Alkaline Media

D. Badea, S. Olthof, J. M. Neudörfl, R. Glaum, R. Pöttgen, M. K. Reimann, K. Meerholz, M. Reimer, C. Logemann, E. Strub and J. Bruns*

Eur. J. Inorg. Chem. **2023**, e202300160.

doi.org/10.1002/ejic.202300160

Explanation of the personal contribution to the previously mentioned publication:

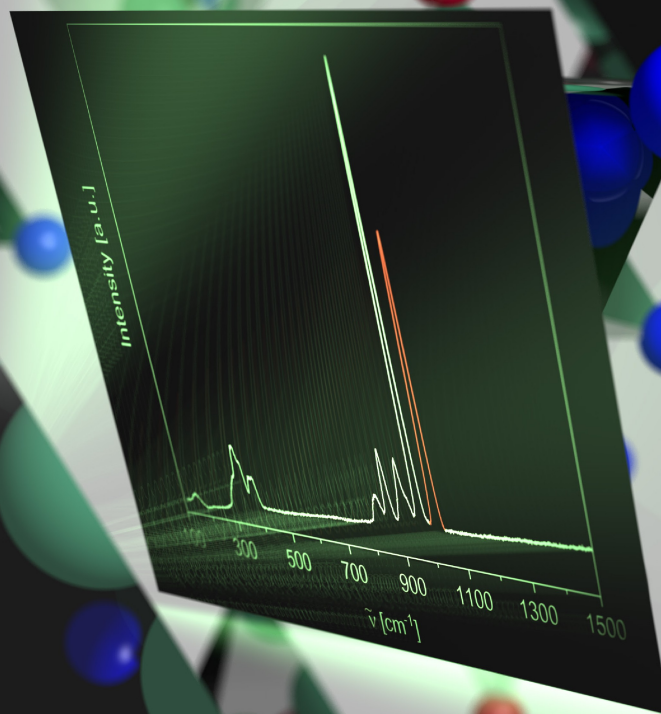
All experiments were conducted by Désirée Badea, with the initial experiment originating from the master's thesis, while all the main experiments were carried out during the doctoral research. Désirée Badea synthesized all analyzed products, performed the characterization experiments, evaluated the collected data and prepared the corresponding plots for publication, unless otherwise noted below. SC-XRD, XPS, *Raman*, UV-vis, magnetic susceptibility and elemental analysis data were obtained by co-authors. Désirée Badea prepared the draft of the manuscript. Supporting information is provided in the Appendix on page 112.

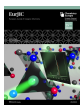


Cover Feature:

J. Bruns and co-workers

$K_3[MO_4][MO_3N]$ ($M=Tc, Re$) – Nitridotrioxidorhenate and -technetate from Highly Alkaline Media





$K_3[MO_4][MO_3N]$ ($M = \text{Tc, Re}$) – Nitridotrioxidorhenate and -technetate from Highly Alkaline Media

Désirée Badea,^[a] Selina Olthof,^[a] Jörg M. Neudörfl,^[a] Robert Glaum,^[b] Rainer Pöttgen,^[c] Maximilian Kai Reimann,^[c] Klaus Meerholz,^[a] Max Reimer,^[a] Christian Logemann,^[a] Erik Strub,^[a] and Jörn Bruns^{*[a]}

The reactions of ammonium perrhenate and pertechnetate in highly alkaline medium led to the isotopic mixed anionic nitridotrioxidorhenate and -technetate $K_3[MO_4][MO_3N]$ ($M = \text{Tc, Re}$). Both compounds occur as colorless crystals, which were investigated by single crystal X-ray diffraction. Furthermore,

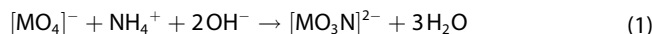
$K_3[ReO_4][ReO_3N]$ has been studied by means of X-ray photoelectron spectroscopy to determine the oxidation state of rhenium. The obtained results have been complemented by magnetic measurements. IR and Raman spectroscopy indicated the presence of Re–O as well as Re–N bonds.

Introduction

Exploratory crystal growth can be carried out by molten flux syntheses.^[1] This method includes an inorganic salt with a low melting temperature. In order to synthesize oxides or oxidic species, potassium or sodium hydroxide are frequently used as fluxes.^[2] By considering the water content, two different types of methods can be distinguished, namely the flux and the hydroflux technique. In the case of a flux reaction, the inorganic salt melt is free of water. A hydroflux occurs when a small but defined amount of water is added to the flux. The latter has to be clearly differentiated from a typical aqueous solution, which would be called hydrothermal reaction.^[1] Due to a variety of influences of the melt on the product, an ideal selection of a suitable flux has to be elucidated, since the redox potential of the melt influences the product with regard to the metal oxidation state.^[3] The redox equilibrium can be adjusted by controlling the atmosphere above the melt, e.g. by using an O_2 atmosphere.^[3] In the case of hydroxide melts, the acid-base chemistry of the melt is described by the Lux-Flood concept of oxoacidity.^[4] The latter allows for the prediction of the solubility of the starting materials.

Reactions in highly alkaline media have been well established for decades,^[2c,d,3,5] however reactions of technetium species in alkaline environment have not been studied extensively.^[6] Our recent investigations have shown that $Ba[Tc^{VII}O_3N]$ can be obtained from the reaction of ammonium pertechnetate in $Ba(OH)_2 \cdot 8H_2O$ and water.^[7] Frequently, technetium occurs in the oxidation states +4, +5 and +7, with the $[Tc^{VII}O_4]^-$ anion being the most prominent representative.^[8] However, $Ba[TcO_3N]$ is the first compound exhibiting the nitridotrioxidotechnetate anion $[TcO_3N]^{2-}$.^[7] So far only pertechnetate has been reacted with barium hydroxide, whereas identical approaches with rhenium and manganese did not lead to isostructural anions.^[7] Following the exploration of the redox chemistry of pertechnetate in an alkaline medium as barium hydroxide, the focus has now been directed to flux systems with monovalent cations, e.g. potassium hydroxide. Considering ternary potassium oxo-species of all group 7 elements, the number of crystallographically characterized manganates is comparably high.^[9] In contrast, so far the heavier homologues occur almost exclusively as metallates(VII).^[10]

During recent investigations on the reactions of perrhenates and -technetates in alkaline salt melts we now obtained the mixed anionic metallates(VII) $K_3[MO_4][MO_3N]$ ($M = \text{Tc, Re}$). Both compounds were obtained from a reaction of $NH_4[MO_4]$ ($M = \text{Tc, Re}$) in potassium hydroxide and defined amounts of water to achieve hydroflux conditions at elevated temperatures. With no additional nitrogen source present, the anions $[MO_3N]^{2-}$ ($M = \text{Tc, Re}$) presumably form according to following reaction:



Results and Discussion

The reaction conditions, specifically the amount of water, the maximum temperature and the cooling rate, play a crucial role for the phase pure synthesis of the material. In order to prepare a new technetate, the rhenium homologue as a non-radioactive reference was synthesized first and the reaction has been scaled down and adjusted for the synthesis of the technetium species.

[a] D. Badea, Dr. S. Olthof, Dr. J. M. Neudörfl, Prof. Dr. K. Meerholz, M. Reimer, Dr. C. Logemann, Dr. E. Strub, Dr. J. Bruns
Department of Chemistry
University of Cologne
Greinstrasse 4–6, 50939 Cologne (Germany)
E-mail: j.bruns@uni-koeln.de

[b] Prof. Dr. R. Glaum
Institute of Inorganic Chemistry
University of Bonn
Gerhard-Domagk-Strasse 1, 53121 Bonn (Germany)

[c] Prof. Dr. R. Pöttgen, Dr. M. K. Reimann
Institut für Anorganische und Analytische Chemie
Universität Münster
Corrensstrasse 30, 48149 Münster (Germany)

Supporting information for this article is available on the WWW under <https://doi.org/10.1002/ejic.202300160>

© 2023 The Authors. European Journal of Inorganic Chemistry published by Wiley-VCH GmbH. This is an open access article under the terms of the Creative Commons Attribution License, which permits use, distribution and reproduction in any medium, provided the original work is properly cited.

The properties of the rhenium species were investigated in detail, in order to gain as much information about the sample as possible. Since the technetate and the rhenate are isotopic and handling of technetium species requires significant safety precautions, the characterization of the technetate was not extended.

The crystal structure of $K_3[TcO_4][TcO_3N]$ is shown in Figure 1 and Figure 2 exemplary for both compounds. The phase pure synthesis of $K_3[ReO_4][ReO_3N]$ has been proven by powder X-ray diffraction (P-XRD) and X-ray photoelectron spectroscopy (XPS). The powder pattern can be found in Figure 3 and the XPS spectrum of a bulk sample in Figure S1. Both compounds crystallize in the trigonal space group $R\bar{3}m$ and contain three formula units per unit cell. Both exhibit two crystallographically distinguishable potassium cations and only one unique technetium or rhenium position, respectively. Tables S1–S10 in the Supporting Information list detailed crystallographic data of

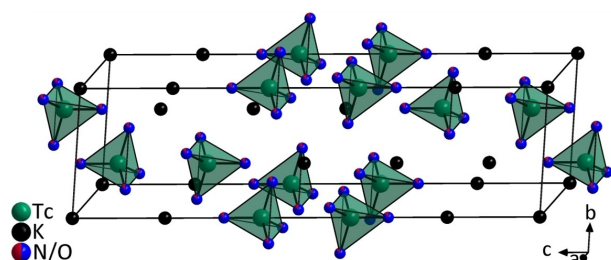


Figure 1. Crystal structure of $K_3[TcO_4][TcO_3N]$ with $[TcO_4]^-$ and $[TcO_3N]^{2-}$ polyhedra. The O/N ordering could not be resolved and the mixed colored atoms are occupied 12.5% by N (red) and 87.5% by O (blue).

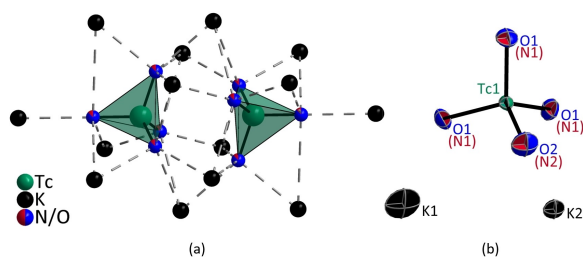


Figure 2. (a) Structure and environment of the $[TcO_4]^-$ and $[TcO_3N]^{2-}$ polyhedra in $K_3[TcO_4][TcO_3N]$ with mixed colored atoms, in each case proportionally occupied by 12.5% N (red) and by 87.5% O (blue). (b) The extended smallest asymmetric unit with ellipsoid representation with 70% probability.

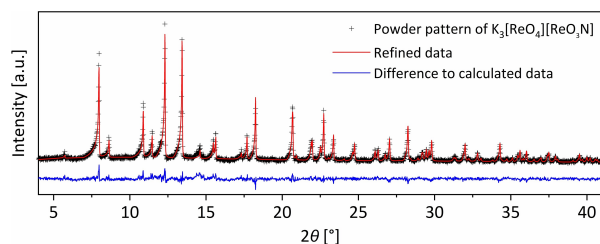


Figure 3. Rietveld refined XRD pattern of $K_3[ReO_4][ReO_3N]$ with the measured data (black), refined data (red) and difference to calculated values (blue).

$K_3[MO_4][MO_3N]$ ($M = Tc, Re$). Table 1 and 2 show selected crystallographic data and atomic distances of both compounds for comparison. The diffraction data give no hint for O/N ordering and the average structure is best described in the centrosymmetric subcell model. For $\{[ReN(PMe_2Ph)_3][ReO_3N]\}_2^{[11]}$ the authors found evidence for the $[ReO_3N]^{2-}$ anion based on bond lengths and angles. However, in this structure the (ReO_3N) -fragment is embedded in a molecular structure with $Re-O-Re$ and $Re-N-Re$ bonds, which makes the results hardly comparable to the free anion. Furthermore, different further solvates of $\{[ReN(PMe_2Ph)_3][ReO_3N]\}_2^{[11]}$, $K_2[ReO_3N]^{[12]}$ and $\{[ReN(OH_2)(L^{Et})_2]_2O\}[ReO_3N]^{[13]}$ (L^{Et} = 1,3-Diethyl-4,5-dimeth-

Table 1. Selected crystallographic data of $K_3[MO_4][MO_3N]$ ($M = Tc, Re$).

Empirical formula	$K_3[ReO_4][ReO_3N]$	$K_3[TcO_4][TcO_3N]$
Formula weight	615.71 g/mol	439.31 g/mol
Temperature	100(2) K	100(2) K
Wavelength	0.71073 Å	0.71073 Å
Crystal system	trigonal	trigonal
Space group	$R\bar{3}m$ (no. 166)	$R\bar{3}m$ (no. 166)
Unit cell dimensions	$a = 6.0184(6)$ Å $c = 21.216(3)$ Å	$a = 5.9696(2)$ Å $c = 21.298(1)$ Å
Volume	$665.5(2)$ Å ³	$657.28(6)$ Å ³
Z	3	3
Density (calculated)	4.61 g cm ⁻³	3.33 g cm ⁻³
F(000)	810	618
Crystal size	$0.10 \times 0.05 \times 0.03$ mm ³	$0.10 \times 0.05 \times 0.03$ mm ³
2θ range for data collection	5.76° to 75.67°	5.74° to 74.77°
Index ranges	$-10 \leq h \leq 10$, $-10 \leq k \leq 10$, $-36 \leq l \leq 36$	$-10 \leq h \leq 10$, $-10 \leq k \leq 10$, $-36 \leq l \leq 36$
Reflections collected	37262	12044
Independent reflections	491 [$R_{int} = 0.0561$, $R_{sigma} = 0.0182$]	468 [$R_{int} = 0.0532$, $R_{sigma} = 0.0187$]
Completeness to θ	100%	97.2%
Absorption correction	multi-scan	multi-scan
Absorption coefficient	28.67 mm ⁻¹	4.58 mm ⁻¹
Data / parameters	491/19	468/18
Extinction coefficient	$0.0049(3)$	—
Goodness-of-fit on F^2	1.243	1.161
Final R indices	$R_1 = 0.0152$, $wR_2 = 0.0359$	$R_1 = 0.0164$, $wR_2 = 0.0386$
R indices (all data)	$R_1 = 0.0152$, $wR_2 = 0.0359$	$R_1 = 0.0176$, $wR_2 = 0.0390$
Largest diff. peak and hole	$1.84/-1.33$ e Å ⁻³	$1.24/-1.24$ e Å ⁻³
CCDC number	2224694	2224695

Table 2. Overview of M-O/N bond lengths in $K_3[MO_4][MO_3N]$ ($M = Tc, Re$) and literature known compounds with $[ReO_4]^-$, $[ReN_4]^{5-}$ and $[TcO_3N]^{2-}$ anions.

Compound	Atom	Atom	Length/Å
$K_3[ReO_4][ReO_3N]$	Re1	O1/N1	1.742(2)
	Re1	O2/N2	1.729(4)
$K_3[TcO_4][TcO_3N]$	Tc1	O1/N1	1.737(1)
	Tc1	O2/N2	1.718(3)
$Ba[TcO_3N]^{[7]}$	Tc1	O1	1.776(4)
	Tc1	O2	1.777(4)
	Tc1	O3	1.763(4)
	Tc1	N1	1.692(5)
$K[ReO_4]^{[14]}$	Re1	O1	1.7238(2)
$LiSr_2[ReN_4]^{[15]}$	Re1	N1	1.845(8)
	Re1	N2	1.830(7)
	Re1	N3	1.810(4)

ylimidazol-2-ylidene) have been reported. However, $K_2[ReO_3N]^{[12]}$ has so far not been characterized via single crystal or powder X-ray diffraction and the results of single crystal X-ray measurements on $[(ReN(OH_2)(L^E)_2)_2O][ReO_3N]^{[13]}$ were not discussed in detail since the crystals decomposed during the measurement.

The Pearson data base^[16] reveals a manifold of oxides, besides fluorides and oxide nitrides for the crystallographic fingerprint of space group 166, Pearson code $hR39$ and Wyckoff sequence hc^3a . The coloring variants of the different Wyckoff sites for various examples are summarized in Table S11. It is remarkable, that mixed occupancies were observed for all Wyckoff positions, requested for an electron precise description of the given phases. The largest crystal chemical similarity to $K_3[ReO_4][ReO_3N]$ was observed for the barium compounds $Ba_3[MoO_3N]_2$ and $Ba_3[WO_3N]_2$.^[17] The crucial question for these three compounds concerns the O/N ordering within the tetrahedral entities. Neutron diffraction studies on the barium compounds revealed refined composition of $Ba_3Mo_2O_{6.04}N_{1.96}$ and $Ba_3W_2O_{2.67}N_{1.73}$ ^[17b] which are close to the ideal one, keeping the standard deviations of the occupancy parameters in mind. Nevertheless, the O/N mixing for both compounds concerns the $18h$ and $6c$ positions as well. The subgroup table in the International Tables A1^[18] shows that splitting of the $18h$ and $6c$ sites in different ratios is possible in subgroups $R3m$, $C2/m$ and $P3m1$. However, since both sites show O/N mixing already in the subcell refinement, these three subgroups do not allow for complete O/N ordering.

The possibility for O/N ordering for $K_3[ReO_4][ReO_3N]$ studied herein was tested. In contrast to $Ba[TcO_3N]$, the potassium compound has an oxygen-to-nitrogen ratio of 7:1. If one assumes that only the $6c$ subcell position shows O/N mixing, a simple 1:1 ordering is possible in the subgroup $R3m$ as presented in the group-subgroup scheme in Figure 4. A literature known example is the structure of $K_3[CrO_4][MnO_4]^{[19]}$ with chromium manganese ordering; however, given the almost similar scattering factors of chromium and manganese, the reliability of such a refinement is probably limited.

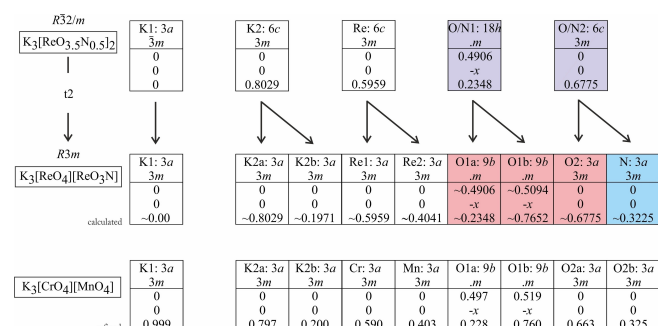


Figure 4. Group-subgroup scheme in the Bärnighausen formalism^[21] for the structures of $K_3[ReO_{3.5}N_{0.5}]_2$ and $K_3[ReO_4][ReO_3N]$. The index for the *translationalengleiche* (t) symmetry reduction and the evolution of the atomic parameters are given. The violet shading highlights the O/N disorder (12.5% N on the O sites) in the centrosymmetric model. The refined coordinates for $K_3[CrO_4][MnO_4]^{[19]}$ are listed for comparison.

Refinements of the occupancy parameters of $K_3[ReO_4][ReO_3N]$ in the $R\bar{3}m$ model gave no hint for a site preference of nitrogen on one of the two Wyckoff positions (this is similar to the findings for the barium compounds discussed above). Therefore, the $K_3[MO_4][MO_3N]$ ($M = Tc, Re$) structures were refined with a 7:1 O/N ratio on both Wyckoff positions. A refinement in the non-centrosymmetric superstructure model (space group $R3m$) converged; however, with large correlations. A clear discrimination of oxygen and nitrogen was impossible. The same holds true for the monoclinic and trigonal subgroups. Only well resolved neutron diffraction data might resolve this problem.

Obviously, it is hard to distinguish between O and N only by judging on the basis of single crystal X-ray diffraction. However, vibrational spectroscopy underlines the assumption of Re–O and Re–N bonds. The Raman spectrum of $K_3[ReO_4][ReO_3N]$ is shown in Figure 5 and the IR spectrum in Figure S3. In addition, the CHNS analysis also confirms the presence of nitrogen with an amount of 2.2(3)%, which is consistent with the calculated value of 2.27% per formula unit.

The Raman bands at 970 cm^{-1} and 919 cm^{-1} can be assigned to symmetric and antisymmetric stretching vibrations since they resemble closely the findings for $K[ReO_4]^{[20]}$. When comparing to the bands occurring in the Raman spectrum of $Ba[TcO_3N]$, the most prominent Re–N vibration occurs at highest wavenumbers, which is 1023 cm^{-1} in case of $K_3[ReO_4][ReO_3N]$.^[7] The vibrations at lower wavenumbers between 383 cm^{-1} and 314 cm^{-1} are attributed to symmetric and antisymmetric bending modes of $K_3[ReO_4][ReO_3N]$.^[20]

The magnetic properties of a $K_3[ReO_4][ReO_3N]$ sample, pure on the level of X-ray powder diffraction, was investigated by magnetic susceptibility and magnetization experiments (see Experimental Section).

The temperature dependence of the magnetic susceptibility (10 kOe data) is presented in Figure 6. The susceptibilities are negative within the complete temperature range investigated, classifying $K_3[ReO_4][ReO_3N]$ as diamagnetic, in agreement with the electron-precise description. The tiny anomalies observed in the low-temperature regime can be attributed to traces of impurities. The room temperature magnetic susceptibility amounts to $-4.1(1) \times 10^{-4}\text{ emu mol}^{-1}$ and is within the same

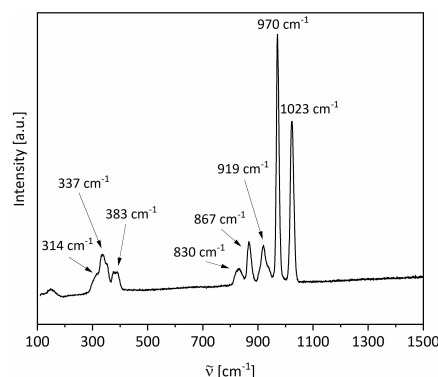


Figure 5. Raman spectrum of $K_3[ReO_4][ReO_3N]$ powder.

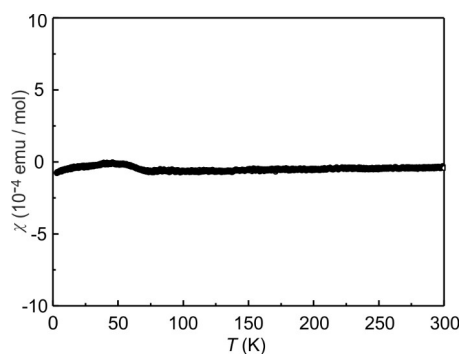


Figure 6. Temperature dependence of the magnetic susceptibility of $K_3[ReO_4][ReO_3N]$ measured with an applied field of 10 kOe.

order of magnitude as the estimated value of $-1.65 \times 10^{-4} \text{ emu mol}^{-1}$ obtained from the diamagnetic increments^[22] (in units of $10^{-6} \text{ emu mol}^{-1}$) of K^+ (−14.9), Re^{7+} (−12), O^{2-} (−12) and N^{3-} (−13). Similar magnetic behavior was observed for two different $K_3[ReO_4][ReO_3N]$ samples.

For the pure powder (checked by powder X-ray diffraction) of $K_3[ReO_4][ReO_3N]$, XPS measurements were carried out. A wide range survey spectrum is shown in Figure S1 in the Supporting Information, in which no traces of impurity elements can be detected. Figure 7 depicts the close-ups of signals related to Re 4f and Re $4d_{5/2}$ core levels.

Notably, two contributions with similar intensities have to be fitted in either spectrum to explain the measured data, suggesting the presence of two oxidation states (e.g. +VI and +VII) of rhenium. This comes as a surprise, since the formal oxidation state is expected to be exclusively +VII. Either the material contains unintended Re species, or differences in binding environment of the Re atoms within the structure lead to the observed effects.

To clarify the underlying reason, two additional Re +VII compounds were investigated. Since the Raman spectrum clearly gives hint to the presence of Re–N bonds, $K_2[ReO_3N]$ was synthesized according to a published procedure.^[12] It has to be noted, that this sample has only been identified by comparing the IR spectrum profile since no further characterization has been published so far.^[12] Nevertheless, in addition to the IR spectrum of $K_2[ReO_3N]$, powder XRD and Raman data is addi-

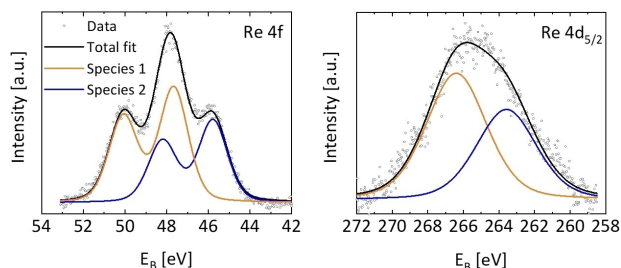


Figure 7. XPS core level spectra of the Re 4f doublet (left) and Re $4d_{5/2}$ (right) region of $K_3[ReO_4][ReO_3N]$. The data is fitted by two dissimilar Re^{VII} species represented in orange $[ReO_4]^-$ and blue $[ReO_3N]^{2-}$.

tionally listed in the Supporting Information for completeness, see Figures S2, S4 and S5. The IR spectrum of the herein investigated sample $K_2[ReO_3N]$ exhibits similar values found for the literature known sample.^[12] XPS measurements of this compound, as well as $K[ReO_4]$ are presented in Figure 8, together with the previously shown $K_3[ReO_4][ReO_3N]$. A clear difference of $\Delta E_b = 2.3 \text{ eV}$ in core level binding energy is observed in the fits of the two lower panels in Figure 8. Assuming that both compounds are Re^{+VII} species, the difference is most likely related to the electron-donating properties of the nitrogen ligand in case of the $[ReO_3N]^{2-}$ anion. The binding energies found here correlate well to the ones observed in $K_3[ReO_4][ReO_3N]$ and thereby confirm the predicted crystal structure.

In contrast to mixed-valent (oxo)-compounds like Pb_3O_4 ^[23] and Prussian blue,^[24] which impress by intensive coloration of the crystals, both title compounds are colorless. The UV/vis spectrum obtained from investigations on single crystals of $K_3[ReO_4][ReO_3N]$ is depicted in Figure 9. The literature known bands of perrhenate(VII) anions from UV/vis spectroscopic measurements occur at 47620 cm^{-1} and 29410 cm^{-1} .^[25] The larger bump observed around 21000 cm^{-1} might result from a

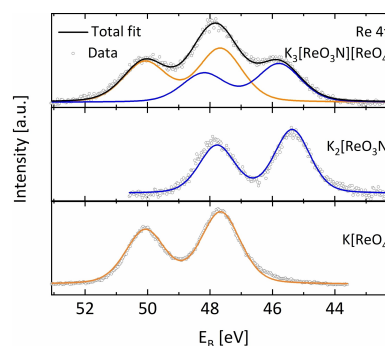


Figure 8. Comparison of the Re 4f XPS core level spectra of $K_3[ReO_4][ReO_3N]$, $K_2[ReO_3N]$ and $K[ReO_4]$.

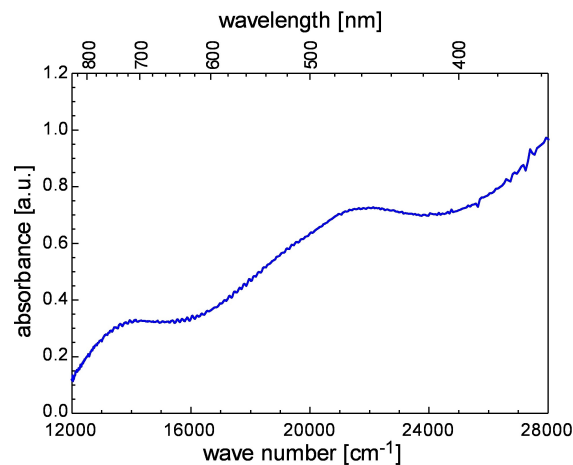


Figure 9. UV/vis spectrum of a $K_3[ReO_4][ReO_3N]$ single crystal measured with a strongly modified Cary 17 spectrometer.

$\text{N}^{3-} \rightarrow \text{Re}^{7+}$ ligand-to-metal-charge-transfer and underpins the XPS data.

Conclusions

In summary, the synthesis of the nitridotrioxidometallates $\text{K}_3[\text{ReO}_4][\text{ReO}_3\text{N}]$ and $\text{K}_3[\text{TcO}_4][\text{TcO}_3\text{N}]$ requires hydroflux conditions. Both compounds are isotypic and $\text{K}_3[\text{ReO}_4][\text{ReO}_3\text{N}]$ has been investigated intensively to determine the oxidation states of the metal, the magnetic behavior and the formation of Re-N besides Re-O bonds. When comparing the reactions of ammonium permethylates of group 7 elements in barium hydroxide with those in potassium hydroxide, significant differences have been observed. With barium hydroxide only the pertechnetate reacted according to our experimental procedure to give the $[\text{TcO}_3\text{N}]^{2-}$ anion. In the case of reactions with potassium hydroxide, pertechnetates and perrhenates reacted successfully forming finally the anions $[\text{TcO}_3\text{N}]^{2-}$ and $[\text{ReO}_3\text{N}]^{2-}$. Thus, in combination with the monovalent cation K^+ we observe identical reactions for the rhenium and technetium species, whereas the permanganate does not react in a potassium hydroxide hydroflux to form $\text{K}_3[\text{MnO}_4][\text{MnO}_3\text{N}]$ under the given conditions. Furthermore, an influence caused by the β^- decay can be excluded for the reaction with $\text{NH}_4[\text{TcO}_4]$, since the non-radioactive product $\text{K}_3[\text{ReO}_4][\text{ReO}_3\text{N}]$ has also formed. It is furthermore an important XPS finding that changes in the ligands significantly affect the binding energy of the metal without changing the actual oxidation state.

Experimental Section

Caution!

^{99}Tc is a β^- emitter. All reactions have to be conducted under special safety precautions in a designated radiochemical laboratory. While handling ^{99}Tc appropriate shielding must be guaranteed.

Synthesis

Colorless single crystals of $\text{K}_3[\text{MO}_4][\text{MO}_3\text{N}]$ ($M = \text{Tc}, \text{Re}$) were obtained from a potassium hydroxide hydroflux by using a Teflon-lined stainless steel autoclave. A typical batch contained 1 equivalent $\text{NH}_4[\text{MO}_4]$, 110 equivalents KOH (*Thermo Scientific*, ~85%) and additional 69 equivalents H_2O . Due to the radioactivity of technetium, a smaller approach was performed for $\text{NH}_4[\text{TcO}_4]$ (2.00 mg, 0.01 mmol, *Oak Ridge National Laboratory*, purity not specified) as opposed to $\text{NH}_4[\text{ReO}_4]$ (26.82 mg, 0.10 mmol, *Sigma-Aldrich*, $\geq 99\%$). The reagents were heated in closed autoclaves at 200°C for 10 h and cooled to room temperature with a cooling rate of 0.5 K/min. Single crystals of $\text{K}_3[\text{TcO}_4][\text{TcO}_3\text{N}]$ were mechanically removed from the matrix of KOH/ H_2O and transferred to perfluorinated oil. Here, the remaining parts of adhesive flux were washed away and a suitable crystal for X-ray diffraction has been isolated. Crystals of $\text{K}_3[\text{ReO}_4][\text{ReO}_3\text{N}]$ were isolated after washing the reaction product with methanol. In order to obtain a phase-pure powder of $\text{K}_3[\text{ReO}_4][\text{ReO}_3\text{N}]$ (22.15 mg, 0.036 mmol 72% yield) for further characterization, a slow cooling rate of 0.03 K/min needs to be applied.

Single crystal X-ray diffraction (SC-XRD)

Single crystal XRD data was collected on a Bruker D8 Venture using Mo-K_α radiation ($\lambda = 0.71073 \text{ \AA}$). The crystals were prepared under a polarization microscope and measured at reduced temperature. The lattice parameters, the refinement details, the atomic parameters and selected bond lengths are given in Table 1 and Tables S1–S10 in the Supporting Information. The structure solution and refinement was successful using ShelXT/ShelXL in Olex2.^[26] The pictures of the structure were developed with the Diamond program.^[27]

Deposition Numbers 2224694 (for $\text{K}_3[\text{ReO}_4][\text{ReO}_3\text{N}]$) and 2224695 (for $\text{K}_3[\text{TcO}_4][\text{TcO}_3\text{N}]$) contain the supplementary crystallographic data for this paper. These data are provided free of charge by the joint Cambridge Crystallographic Data Centre and Fachinformationszentrum Karlsruhe Access Structures service.

Powder X-ray diffraction and Rietveld refinement (P-XRD)

Powder XRD data was collected on a Stoe Stadi-P powder diffractometer (Mythen detector, Debye-Scherrer geometry) using Mo-K_α radiation ($\lambda = 0.70930 \text{ \AA}$). The samples were ground and sealed in glass capillaries with $\phi = 0.30 \text{ mm}$. The data was recorded within 30 min in a range of $2\theta = 0\text{--}60^\circ$. The Rietveld refinement was carried out using Topas, with the lattice parameters freely refined and applying the Thompson-Cox-Hastings profile function.^[28] The background was described using six Chebyshev polynomials. The diffractogram was plotted with the Origin Software.^[29] Refinement details are given in Table S12.

Raman spectroscopy

Single crystals of $\text{K}_3[\text{ReO}_4][\text{ReO}_3\text{N}]$ were transferred into a glass capillary (wall thickness 0.01 mm, outside $\phi = 0.5 \text{ mm}$), whereas powder of $\text{K}_2[\text{ReO}_3\text{N}]$ was prepared in a glass ampoule. The data was measured with a Renishaw inVia Raman microscope and the spectra were recorded with a 532 nm laser excitation at room temperature. The data was plotted with the Origin Software.^[29]

Elemental analysis

The elemental analyses was performed with a CHNS Euro EA 3000 analyzer of HEKAtech GmbH. $\text{K}_3[\text{ReO}_4][\text{ReO}_3\text{N}]$ (615.71 g/mol): experimental N 2.2(3), C 0.1(3), H 0.0(3), S 0.0(3), calculated N 2.27, C 0.00, H 0.00, S 0.00%. We attribute the finding of C and H to remaining amounts of adhesive solvent since the crystals were washed with methanol.

Susceptibility and magnetization

The sample was ground to a fine powder, filled into a polypropylene capsule and then attached to the brass sample holder rod of a vibrating sample magnetometer (VSM) of a Quantum Design Physical Property Measurement System (PPMS). The experiment was conducted in the temperature range of 2.5 to 300 K with applied external magnetic fields of up to 80 kOe. Fitting and plotting of the data was done with OriginPro 2016G^[30] and the graphical editing with the program CorelDRAW2017.^[31]

Optical spectrum (UV/vis spectroscopy)

A single-crystal electronic absorption spectrum of an arbitrary face of a $\text{K}_3[\text{ReO}_4][\text{ReO}_3\text{N}]$ crystal was measured at ambient temperature

using a strongly modified CARY 17 microcrystal spectrophotometer (Spectra Services, ANU Canberra, Australia). The spectrometer allows the measurement of very small single-crystals with diameters down to 0.1 mm. Details on the spectrometer have already been published.^[32] The crystal was contained in a borosilicate capillary for protection. The baseline was measured with the empty capillary.

X-ray photoelectron spectroscopy (XPS)

The finely grounded powders were applied inside a glovebox onto a conductive tape and loaded into the vacuum chamber without exposing them to air. XPS measurements were performed using a non-monochromatic Mg_{Kα} excitation at 1253.6 eV. Slight charging of the powders occurred during the measurement which were corrected by setting the binding energy of adventitious carbon to 284.7 eV. The photoelectrons were detected using a hemispherical analyzer (Specs Phoibos 100) at a pass energy of 10 eV, except for the survey scan where 90 eV pass energy was used. The core levels were fitted by Voigt profiles after a Shirley background was subtracted. The data was plotted with the Origin Software.^[29]

Supporting Information

Additional references cited within the Supporting Information.^[12,17,33]

Acknowledgements

We thank Aimée Cammiade and Lisa Körtgen for their support. Furthermore, we thank Dr. Markus Zegke for the assistance via conducting experiments with technetium, Dirk Pullem for the elemental analysis and J.-Prof. Dr. Bertold Rasche for the support with the Rietveld refinement. Additionally, we would like to thank Dr. David van Gerven for his support in creating the cover. Jörn Bruns thanks the Fonds der Chemischen Industrie (FCI) for financial support. Open Access funding enabled and organized by Projekt DEAL.

Conflict of Interests

There are no conflicts to declare.

Data Availability Statement

The data that support the findings of this study are available in the supplementary material of this article.

Keywords: rhenium • technetium • hydroflux • XPS • oxoanions

- [1] D. Elwell, H. J. Scheel, *Crystal growth from high-temperature solutions*, Academic Press, New York, 1975.
- [2] a) D. E. Bugaris, M. D. Smith, H.-C. zur Loye, *Inorg. Chem.* **2013**, *52*, 3836–3844; b) W. M. Chance, D. E. Bugaris, A. S. Sefat, H.-C. zur Loye, *Inorg. Chem.* **2013**, *52*, 11723–11733; c) D. S. Cook, G. J. Clarkson, D. M. Dawson, S. E. Ashbrook, J. M. Fisher, D. Thompsett, D. M. Pickup, A. V.

- Chadwick, R. I. Walton, *Inorg. Chem.* **2018**, *57*, 11217–11224; d) R. Albrecht, T. Doert, M. Ruck, *Z. Anorg. Allg. Chem.* **2020**, *646*, 1517–1524.
- [3] D. E. Bugaris, H.-C. zur Loye, *Angew. Chem. Int. Ed.* **2012**, *51*, 3780–3811.
- [4] H. Flood, T. Förland, *Acta Chem. Scand.* **1947**, *1*, 592–604.
- [5] a) R. Scholder, H. Kyri, *Z. Anorg. Allg. Chem.* **1952**, *270*, 56–68; b) K. D. zur Loye, W. M. Chance, J. Yeon, H.-C. zur Loye, *Solid State Sci.* **2014**, *37*, 86–90; c) A. M. Latshaw, M. D. Smith, W. M. Chance, H.-C. zur Loye, *Solid State Sci.* **2015**, *42*, 14–19; d) R. Albrecht, M. Ruck, *Angew. Chem. Int. Ed.* **2021**, *60*, 22570–22577.
- [6] a) N. Shen, Z. Yang, S. Liu, X. Dai, C. Xiao, K. Taylor-Pashow, D. Li, C. Yang, J. Li, Y. Zhang, M. Zhang, R. Zhou, Z. Chai, S. Wang, *Nat. Commun.* **2020**, *11*, 5571; b) J. Li, B. Li, N. Shen, L. Chen, Q. Guo, L. Chen, L. He, X. Dai, Z. Chai, S. Wang, *ACS Cent. Sci.* **2021**, *7*, 1441–1450.
- [7] D. Badea, K. Dardenne, R. Polly, J. Rothe, K. Meerholz, M. Hanrath, M. Reimer, J. Neudörfl, E. Strub, J. Bruns, *Chem. Eur. J.* **2022**, *28*, e202201738.
- [8] S. Bauters, A. C. Scheinost, K. Schmeide, S. Weiss, K. Dardenne, J. Rothe, N. Mayordomo, R. Steudtner, T. Stumpf, U. Abram, S. M. Butorin, K. O. Kvashnina, *Chem. Commun.* **2020**, *56*, 9608–9611.
- [9] a) R. D. Cannon, U. A. Jayasooriya, C. Tilford, C. E. Anson, F. E. Sowrey, D. R. Rosseinsky, J. A. Stride, F. Tasset, E. Ressouche, R. P. White, R. Ballou, *Inorg. Chem.* **2004**, *43*, 7061–7067; b) G. J. Palenik, *Inorg. Chem.* **1967**, *6*, 507–511; c) R. C. L. Mooney, *Phys. Rev.* **1931**, *37*, 1306–1310; d) G. Brachtel, R. Hoppe, *Z. Anorg. Allg. Chem.* **1978**, *446*, 64–76; e) M. Jansen, F. M. Chang, R. Hoppe, *Z. Anorg. Allg. Chem.* **1982**, *490*, 101–110; f) J. Nuss, P. L. V. K. Dasari, M. Jansen, *Z. Anorg. Allg. Chem.* **2015**, *641*, 316–321; g) J. Nuss, R. K. Kremer, M. Jansen, *Z. Anorg. Allg. Chem.* **2018**, *644*, 1715–1720; h) R. Olazcuaga, J.-M. Reau, G. LeFlem, P. Hagenmüller, *Z. Anorg. Allg. Chem.* **1975**, *412*, 271–280; i) E. Seipp, R. Hoppe, *Z. Anorg. Allg. Chem.* **1985**, *530*, 117–126.
- [10] a) B. Krebs, K.-D. Hasse, *Acta Crystallogr. Sect. B* **1976**, *32*, 1334–1337; b) J. Morrow, *Acta Crystallogr.* **1960**, *13*, 443–445.
- [11] H. Braband, E. Yegen, E. Oehlke, U. Abram, *Z. Anorg. Allg. Chem.* **2005**, *631*, 2408–2410.
- [12] a) A. F. Clifford, R. R. Olsen, *Inorg. Synth.* **1960**, *6*, 167; b) B. Krebs, A. Müller, *J. Inorg. Nucl. Chem.* **1968**, *30*, 463–466.
- [13] a) H. Braband, *Dissertation*, Freie Universität Berlin, **2006**; b) H. Braband, E. Oehlke, U. Abram, *Z. Anorg. Allg. Chem.* **2006**, *632*, 1051–1056.
- [14] C. Chay, M. Avdeev, H. E. A. Brand, S. Injac, T. A. Whittle, B. J. Kennedy, *Dalton Trans.* **2019**, *48*, 17524–17532.
- [15] O. Hochrein, H. Borrmann, R. Kniep, *Z. Anorg. Allg. Chem.* **2001**, *627*, 37–42.
- [16] P. Villars, K. Cenzual, *Pearson's Crystal Data: Crystal Structure Database for Inorganic Compounds* (release 2022/23), ASM International®, Materials Park, Ohio (USA) 2022.
- [17] a) W. Li, D. Li, X. Gao, A. Gurlo, S. Zander, P. Jones, A. Navrotsky, Z. Shen, R. Riedel, E. Ionescu, *Dalton Trans.* **2015**, *44*, 8238–8246; b) M. T. Weller, S. J. Skinner, *Int. J. Inorg. Mater.* **2000**, *2*, 463–467.
- [18] *International Tables for Crystallography, Vol. A1, Symmetry relations between space groups*, 2 ed. (Eds. H. Wondratschek, U. Müller), John Wiley & sons, Ltd, Chichester, **2010**.
- [19] E. Stanley, *Z. Kristallogr.* **1968**, *127*, 450–455.
- [20] P. L. Gassman, J. S. McCloy, C. Z. Soderquist, M. J. Schweiger, *J. Raman Spectrosc.* **2014**, *45*, 139–147.
- [21] a) H. Bärnighausen, *Commun. Math. Chem.* **1980**, *9*, 139–175; b) U. Müller, *Z. Anorg. Allg. Chem.* **2004**, *630*, 1519–1537; c) *International Tables for Crystallography, Vol. A1, Symmetry relations between space groups*, 2nd ed. (Eds.: H. Wondratschek, U. Müller), Wiley, Chichester, **2010**, pp. 44–56; d) U. Müller, *Symmetriebeziehungen zwischen verwandten Kristallstrukturen*, Vieweg+Teubner Verlag, Wiesbaden, **2012**.
- [22] a) G. A. Bain, J. F. Berry, *J. Chem. Educ.* **2008**, *85*, 532–536; b) S. Leoni, R. Niewa, L. Akse, Y. Prots, W. Schelle, T. Göksu, M. Cetinkol, M. Somer, R. Kniep, *Z. Anorg. Allg. Chem.* **2005**, *631*, 1818–1824.
- [23] S. T. Gross, *J. Am. Chem. Soc.* **1943**, *65*, 1107–1110.
- [24] J. F. Keggin, F. D. Miles, *Nature* **1936**, *137*, 577–578.
- [25] N. Gorshkov, Y. Pokhvoshchev, A. Murko, O. Nazarova, Y. Zolotova, V. D. Krasikov, E. F. Panarin, *Dokl. Chem.* **2015**, *462*, 137–140.
- [26] a) O. V. Dolomanov, L. J. Bourhis, R. J. Gildea, J. A. K. Howard, H. Puschmann, *J. Appl. Crystallogr.* **2009**, *42*, 339–341; b) G. Sheldrick, *Acta Crystallogr. Sect. C* **2015**, *71*, 3–8.
- [27] K. Brandenburg, *Diamond 4, Crystal and Molecular Structure Visualization*, Crystal Impact GbR, Bonn, Germany, **2019**.
- [28] a) A. A. Coelho, *J. Appl. Crystallogr.* **2018**, *51*, 210–218; b) Topas-Academic (version V6), Brisbane, Australia, **2016**.

- [29] OriginPro 2019b (version 9.6.5.169), OriginLab Corporation, Northampton, MA, USA, **2019**.
- [30] OriginPro 2016G (version 9.3.2.303), OriginLab Corporation, Northampton, MA, USA, **2016**.
- [31] CorelDRAW Graphics Suite 2017 (version 19.0.0.328), Corel Corporation, Ontario Canada, **2017**.
- [32] a) E. Krausz, *AOS News* **1998**, 12, 21; b) E. Krausz, *Aust. J. Chem.* **1993**, 46, 1041–1054.
- [33] a) W. H. Zachariasen, *Acta Crystallogr.* **1948**, 1, 263–265; b) I. Mayer, E. Fischbein, S. Cohen, *J. Solid State Chem.* **1975**, 14, 307–312; c) Y. L. Fur, P. S. Aleonard, *Bull. Soc. Fr. Mineral. Cristallogr.* **1970**, 93, 260–262; d) B. Mossner, S. Kemmler-Sack, *J. Less-Common Met.* **1985**, 114, 333–341; e) H. Schwarz, *Z. Anorg. Allg. Chem.* **1966**, 344, 41–55; f) H. Schwarz, *Z. Anorg. Allg. Chem.* **1966**, 344, 214–224; g) D. Blaize, F. Pertillon, J. E. Guerchais, *C. R. Seances Acad. Sci. Ser. C* **1970**, 270, 52–55; h) C. K. Moller, *Acta Chem. Scand.* **1954**, 8, 81–87; i) R. Scholder, W. Klemm, *Angew. Chem.* **1954**, 66, 461–474; j) H. G. Bachmann, *Neues Jahrb. Mineral. Monatsh.* **1953**, 209–223; k) A. S. Trunin, G. E. Shter, V. M. Serezhkin, *Zh. Neorg. Khim.* **1975**, 20, 2209–2213; l) H. Schwarz, *Z. Anorg. Allg. Chem.* **1966**, 345, 230–245; m) G. Le Flem, R. Olazcuaga, *Bull. Soc. Chim. Fr.* **1968**, 2769–2780.
-
- Manuscript received: March 23, 2023
Revised manuscript received: June 15, 2023
Accepted manuscript online: June 21, 2023

4.2.3 $A_3[\text{ReO}_4][\text{ReO}_3\text{N}]$ and $A'_2[\text{ReO}_3\text{N}]$ with $A = \text{Rb}, \text{Cs}$ and $A' = \text{K}, \text{Cs}$ from Alkali Metal Hydroxide (Publication 4)

Crystallographically phase pure samples of $A_3[\text{ReO}_4][\text{ReO}_3\text{N}]$ ($A = \text{Rb}, \text{Cs}$) were synthesized by reacting ammonium perrhenate in an alkali metal hydroxide hydroflux. Both compounds are structurally isotypic to $\text{K}_3[\text{ReO}_4][\text{ReO}_3\text{N}]$ and crystallize in the space group $R\bar{3}m$. Additionally, $A'_2[\text{ReO}_3\text{N}]$ ($A' = \text{K}, \text{Cs}$) were obtained through a similar hydroflux, using ammonium chloride to increase the nitrogen content. $\text{K}_2[\text{ReO}_3\text{N}]$ crystallizes in the space group $C2/m$, while $\text{Cs}_2[\text{ReO}_3\text{N}]$ shows the space group $Pnma$. All four novel compounds were further analyzed using *Raman* spectroscopy and quantum chemical calculations were performed to support the experimental results.

Publication 4

Synthesis and Characterization of $A_3[\text{ReO}_4][\text{ReO}_3\text{N}]$ and $A'_2[\text{ReO}_3\text{N}]$ ($A = \text{Rb}, \text{Cs}$; $A' = \text{K}, \text{Cs}$)

D. Badea, C. Lenting, M. Hanrath and J. Bruns*

Eur. J. Inorg. Chem. **2025**, 28, e202500036.

Explanation of the personal contribution to the previously mentioned publication:

The experiments were carried out by Désirée Badea. The first author synthesized all analyzed products, performed the characterization experiments, evaluated the collected data and prepared the corresponding plots for publication, unless otherwise noted below. *Raman* experiments and DFT calculations were carried out by Dr. Christoph Lenting and Prof. Dr. Michael Hanrath. Désirée Badea prepared the draft of the manuscript. Supporting information is provided in the Appendix on page 121.

Front Cover:

J. Bruns and co-workers

Synthesis and Characterization of $A_3[ReO_4][ReO_3N]$ and $A'_2[ReO_3N]$ ($A = Rb, Cs$; $A' = K, Cs$)



Synthesis and Characterization of $A_3[ReO_4][ReO_3N]$ and $A'_2[ReO_3N]$ ($A = Rb, Cs$; $A' = K, Cs$)

Désirée Badea, Christoph Lenting, Michael Hanrath, and Jörn Bruns*

Crystallographically phase-pure samples of $A_3[ReO_4][ReO_3N]$ with $A = Rb, Cs$ are obtained from the reaction of $NH_4[ReO_4]$ in an alkali metal hydroxide flux. Both compounds are isotypic to the known compound $K_3[ReO_4][ReO_3N]$ and crystallize in the space group $R\bar{3}m$.^[1] $A'_2[ReO_3N]$ with $A' = K, Cs$ are also synthesized from the respective alkali metal hydroxides, but with an increased amount

of the nitrogen source via adding ammonium chloride to the starting mixture. $K_2[ReO_3N]$ crystallizes in the space group $C2/m$, whereas $Cs_2[ReO_3N]$ crystallizes in the space group $Pnma$. Along with the characterization of the four novel crystal structures, the experimental results are further supported by Raman spectroscopy and quantum chemical calculations.

1. Introduction

Oxometallates and nitrido-oxometallates represent two interesting classes of inorganic compounds that have garnered significant attention over decades.^[2–8] Considering the nitridotrioxometallates of transition metals, it is noticeable that only a few publications on technetium and rhenium in form of the nitridotrioxodotchnetate(VII) and nitridotrioxidorhenate(VII) salts $[MO_3N]^{2-}$ ($M = Tc, Re$) are reported. Some of them have been published only recently.^[1,3,9,10] The nitridotrioxometallates of other transition metals, such as $K[OsO_3N]$, $Ba_3[WO_3N]_2$, and $Ba_2[VO_3N]$ have been studied in more detail.^[2,11,12] In the literature, the reactions are performed either by using gaseous/liquid NH_3 or by salt metathesis of an already existing nitridotrioxometallate.^[3,4,9,11] Pure nitrides, usually synthesized by high-temperature reactions involving nitrogen or ammonia as the nitrogen source,^[13,14] are already known for their challenging synthesis. Similarly, the preparation of nitridotrioxometallates can also be demanding. However, recently we were able to show that nitrogen from ammonium permethylates can be converted to a nitridotrioxometallate in metal hydroxide hydrofluxes even at moderate temperatures.^[1,10]

The recent work focuses on nitridotrioxidorhenates. $K_2[ReO_3N]$, the first compound featuring the respective $[ReO_3N]^{2-}$ anion

has been published in 1960.^[9] The latter has been obtained from the reaction of Re_2O_7 with KNH_2 in liquid NH_3 . However, the obtained sample was not characterized via single crystal X-ray diffraction but by means of vibrational spectroscopy.^[3,15] One crystallographic hint for the existence of the free anion $[ReO_3N]^{2-}$ was achieved via the characterization of a compound with the sum formula $K_3[ReO_4][ReO_3N]$, which has been synthesized via a hydroflux approach from ammonium perrhenate in a mixture of potassium hydroxide and water.^[1,10] Similarly, $Ba[TcO_3N]$ has been obtained from ammonium pertechnetate in a mixture of barium hydroxide and water.^[10] Similar to the two previously described syntheses, the title compounds $A_3[ReO_4][ReO_3N]$ ($A = Rb, Cs$) can be synthesized from $NH_4[ReO_4]$ in a flux of the respective alkali metal hydroxides, making these reactions less complex than working with liquid or gaseous ammonia. Furthermore, the amount of nitrogen in the synthesized compounds can be increased by adding more of a suitable ammonium compound as nitrogen source. Accordingly, it is possible to synthesize the nitridotrioxidorhenates $A'_2[ReO_3N]$ ($A' = K, Cs$).

2. Results and Discussion

Crystallographically phase-pure $A_3[ReO_4][ReO_3N]$ ($A = Rb, Cs$) could be obtained from $NH_4[ReO_4]$ in an alkaline flux of $RbOH$ or $CsOH$, respectively. Both compounds were characterized by means of single-crystal structure analysis and via powder X-ray diffraction. The crystal structure of $Rb_3[ReO_4][ReO_3N]$ is shown in **Figure 1** and will be depicted in the following as an example for the two isotypic species $A_3[ReO_4][ReO_3N]$ ($A = Rb, Cs$). Both crystallize in the trigonal space group $R\bar{3}m$ and are isotypic to $K_3[ReO_4][ReO_3N]$, see **Table 1**.^[1] The structures contain two crystallographically distinguishable alkali metal cations, whereas only one unique rhenium atom is present. Since the bond lengths give no hint for a predominant location of nitrogen all three distinguishable oxygen positions are refined as partially occupied by nitrogen with a fixed N:O ratio of 1:7, resulting in the total

D. Badea, M. Hanrath, J. Bruns
Department of Chemistry and Biochemistry
University of Cologne
Greinstrasse 4-6, 50939 Cologne, Germany
E-mail: j.bruns@uni-koeln.de

C. Lenting
Institute of Geology and Mineralogy
University of Cologne
Zùlpicher Strasse 49b, 50674 Cologne, Germany

Supporting information for this article is available on the WWW under <https://doi.org/10.1002/ejic.202500036>

© 2025 The Author(s). European Journal of Inorganic Chemistry published by Wiley-VCH GmbH. This is an open access article under the terms of the Creative Commons Attribution License, which permits use, distribution and reproduction in any medium, provided the original work is properly cited.

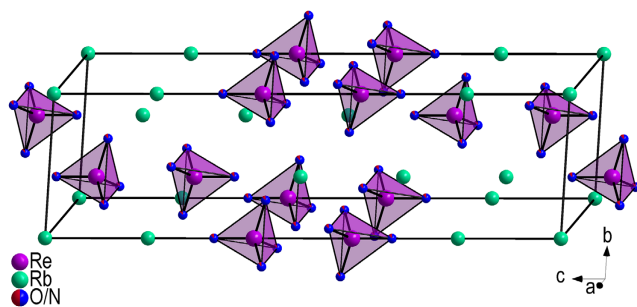


Figure 1. Crystal structure of $\text{Rb}_3[\text{ReO}_4][\text{ReO}_3\text{N}]$ with $[\text{ReO}_4]^-$ and $[\text{ReO}_3\text{N}]^{2-}$ polyhedra, whereas the mixed colored atoms are occupied with a ratio of 12.5% by N (red) and 87.5% by O (blue).

Empirical formula	$\text{Rb}_3[\text{ReO}_4][\text{ReO}_3\text{N}]$	$\text{Cs}_3[\text{ReO}_4][\text{ReO}_3\text{N}]$
Formula weight	754.82 g mol ⁻¹	897.14 g mol ⁻¹
Temperature	100(2) K	100(2) K
Wavelength	0.71073 Å	0.71073 Å
Crystal system	Trigonal	Trigonal
Space group	$R\bar{3}m$ (no. 166)	$R\bar{3}m$ (no. 166)
Unit cell dimensions	$a = 6.1747(3)$ Å $c = 22.062(1)$ Å	$a = 6.3947(2)$ Å $c = 23.160(1)$ Å
Volume	728.46(8) Å ³	820.18(6) Å ³
Z	3	3
Density (calculated)	5.16 g cm ⁻³	5.45 g cm ⁻³
F(000)	972	1134
Crystal size	$0.10 \times 0.06 \times 0.01$ mm ³	$0.10 \times 0.05 \times 0.07$ mm ³
2 θ range for data collection	5.54° to 59.91°	5.28° to 57.95°
Index ranges	$-8 \leq h \leq 8$, $-8 \leq k \leq 8$, $-30 \leq l \leq 30$	$-8 \leq h \leq 8$, $-8 \leq k \leq 8$, $-31 \leq l \leq 31$
Reflections collected	6254	18322
Independent reflections	306 [$R_{\text{int}} = 0.0371$, $R_{\text{sigma}} = 0.0122$]	308 [$R_{\text{int}} = 0.0436$, $R_{\text{sigma}} = 0.0090$]
Completeness to θ	100%	100%
Absorption correction	Multi-scan	Multi-scan
Data/parameters	306/18	308/19
Goodness-of-fit on F^2	1.265	1.159
Final R indices [$I \geq 2\sigma(I_o)$]	$R_1 = 0.0197$, $wR_2 = 0.0474$	$R_1 = 0.0125$, $wR_2 = 0.0327$
R indices (all data)	$R_1 = 0.0207$, $wR_2 = 0.0477$	$R_1 = 0.0125$, $wR_2 = 0.0327$
Largest diff. peak and hole	1.69/−1.64 e Å ⁻³	1.91/−1.34 e Å ⁻³
CCDC number	2414620	2414618

composition $\text{A}_3[\text{ReO}_{3.5}\text{N}_{0.5}]_2$ ($\text{A} = \text{Rb}, \text{Cs}$), in the following written as $\text{A}_3[\text{ReO}_4][\text{ReO}_3\text{N}]$.

The same holds true for the previously published structure of $\text{K}_3[\text{ReO}_4][\text{ReO}_3\text{N}]$.^[1] A detailed crystallographic analysis is provided in the literature from 2023, where the possibility of an O/N

ordering has already been studied.^[1] A comparison of the bond lengths within the $[\text{ReO}_3\text{N}]^{2-}$ tetrahedra across the three known mixed anionic species reveals consistent values. The Re–O/N bond lengths fall in the narrow range of 1.710(8)–1.747(4) Å.^[1] **Figure 2** shows the coordination polyhedra of both crystallographically distinguishable rubidium cations.

Rb1 is coordinated by 12 O/N atoms with distances of 2.912(4) Å up to 3.5673(4) Å, building an icosahedron as confirmed by the program Polynator.^[16] By using CHARDI2015, the coordinating ligands were verified.^[17,18] In contrast, Rb2 is coordinated by 10 O/N atoms and forms the rather unusual polyhedron “mono-capped trigonal cupola” as determined by Polynator.^[16,18] The bond lengths for Rb2 range from 2.825(8) Å to 3.185(1) Å. Similar metal-oxygen polyhedra are found for the potassium and cesium salts, with the respective distances depending on the central cation.^[1]

Figure 3 shows the powder X-ray data and Rietveld refinement patterns, whereas Raman spectroscopy data can be found in **Figure 4**. The spectra were recorded for single crystals of the respective compounds. All spectra show the characteristic Re–N vibration in the range of 1010–1023 cm⁻¹ and Re–O vibrations in the range of 966–971 cm⁻¹. The vibrations at lower wavenumbers are assigned to the symmetric and antisymmetric bending modes of the compounds and agree with the literature.^[1] The bands shift to lower wavenumbers with increasing size of the alkali metal cations.

In addition to $\text{A}_3[\text{ReO}_4][\text{ReO}_3\text{N}]$ ($\text{A} = \text{Rb}, \text{Cs}$), single crystals of $\text{K}_2[\text{ReO}_3\text{N}]$ and $\text{Cs}_2[\text{ReO}_3\text{N}]$ could be obtained from a CsOH flux and a KOH hydroflux, respectively. Therefore, ammonium chloride as an additional nitrogen source was added. However, so far it was not possible to crystallize $\text{Rb}_2[\text{ReO}_3\text{N}]$. Furthermore, it was not possible to increase the amount of nitrogen in the oxo-anions even further.

$\text{K}_2[\text{ReO}_3\text{N}]$ crystallizes in the monoclinic space group $\text{C2}/m$ with four formula units per unit cell. The latter is not isotopic to $\text{Cs}_2[\text{ReO}_3\text{N}]$, which crystallizes in the orthorhombic space group Pnma with four formula units per unit cell, see **Figure 5** and **6**, and **Table 2**.

As described for the mixed anionic compounds before, the nitrogen atoms are refined with a fixed N:O ratio of 1:3 as distributed over all four ligand positions in the tetrahedra of $\text{A}'_2[\text{ReO}_3\text{N}]$ with $\text{A}' = \text{K}, \text{Cs}$. Even though, freely refined oxygen atoms give

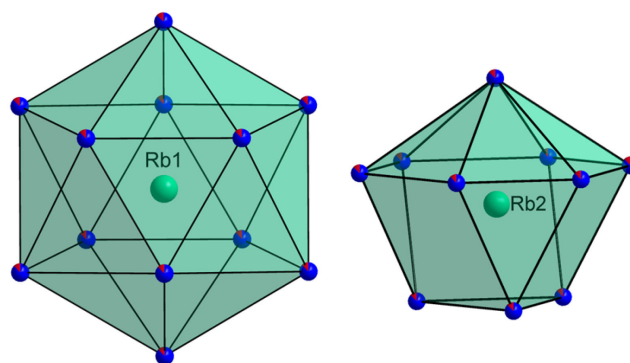


Figure 2. Rb–O/N polyhedra of $\text{Rb}_3[\text{ReO}_4][\text{ReO}_3\text{N}]$.

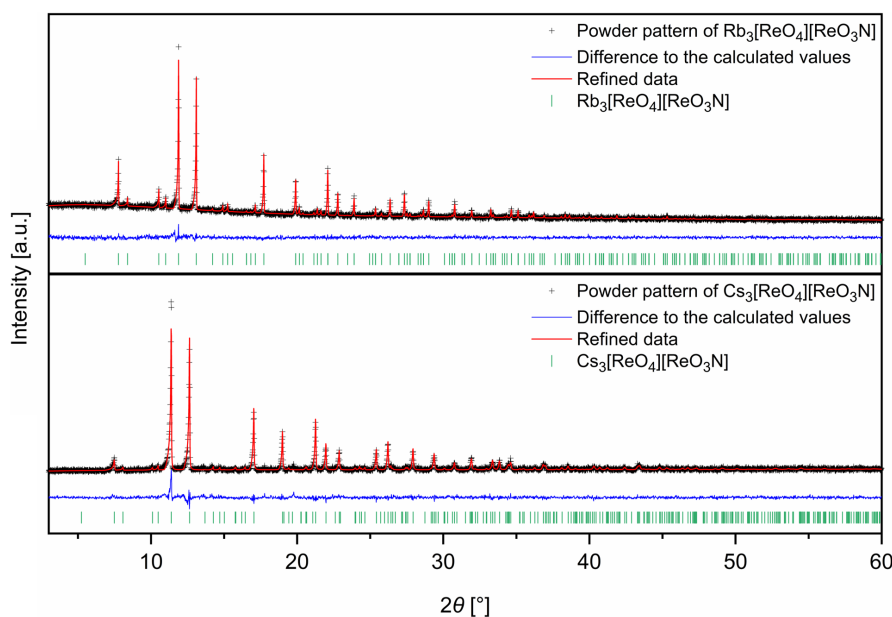


Figure 3. Powder X-ray data and Rietveld refinement patterns of $\text{Rb}_3[\text{ReO}_4][\text{ReO}_3\text{N}]$ and $\text{Cs}_3[\text{ReO}_4][\text{ReO}_3\text{N}]$.

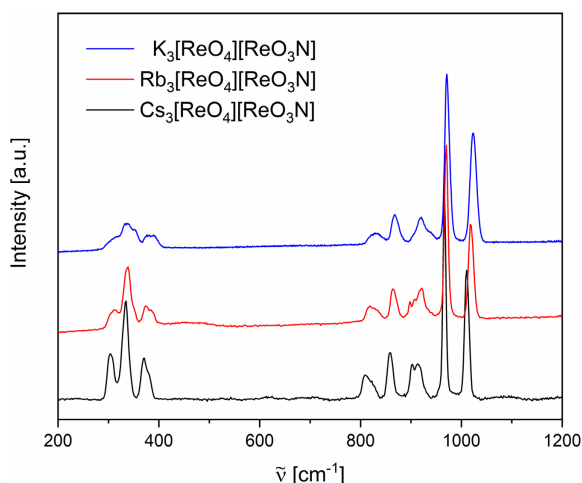


Figure 4. Raman spectra of $\text{A}_3[\text{ReO}_4][\text{ReO}_3\text{N}]$ ($\text{A} = \text{K}, \text{Rb}, \text{Cs}$).^[1]

hint for a preferred occupancy of the O3 position in $\text{K}_2[\text{ReO}_3\text{N}]$ and the O2 and O3 position in $\text{Cs}_2[\text{ReO}_3\text{N}]$ with nitrogen, a localization of the nitrogen atom is not doubtless since the metal–ligand bond lengths do not differ significantly. Furthermore, a stable refinement failed due to strong correlation effects. Both, $\text{K}_2[\text{ReO}_3\text{N}]$ and $\text{Cs}_2[\text{ReO}_3\text{N}]$ contain one distinguishable rhenium atom which is coordinated by four O/N ligands and exhibit three crystallographically distinguishable O/N atoms. **Table 3** shows the bond lengths of the $[\text{ReO}_3\text{N}]^{2-}$ tetrahedra. It is noticeable that no significant differences in the bond lengths of both compounds can be observed. $\text{K}_2[\text{ReO}_3\text{N}]$ exhibits Re–ligand bond lengths of 1.764(3) Å, 1.779(4) Å and 1.756(3) Å, whereas $\text{Cs}_2[\text{ReO}_3\text{N}]$ has Re–ligand bond lengths of 1.770(2) Å, 1.737(4) Å and 1.762(3) Å. Compared to the mixed anionic species $\text{A}_3[\text{ReO}_4][\text{ReO}_3\text{N}]$ ($\text{A} = \text{K}, \text{Rb}, \text{Cs}$), the homoleptic compounds reveal slightly longer Re–O/N bonds.^[1]

Examining the coordination polyhedra of the potassium and cesium cations, only irregular polyhedra can be determined

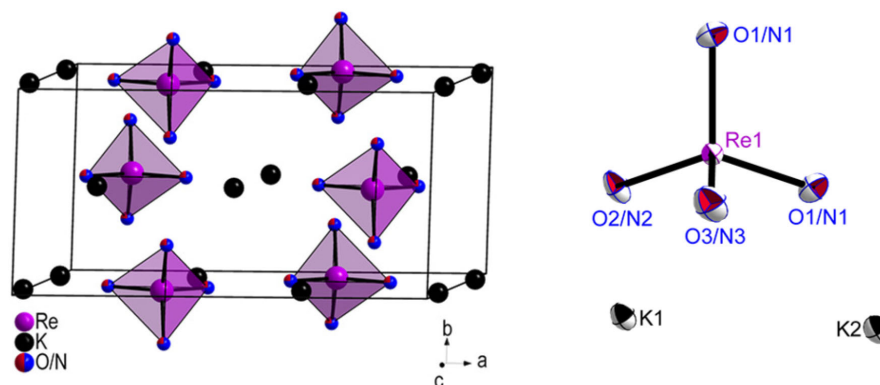


Figure 5. Crystal structure of $\text{K}_2[\text{ReO}_3\text{N}]$ (left) and the extended asymmetric unit with ellipsoid representation (70% probability, right). The mixed colored atoms are occupied with a ratio of 25% by N (red) and 75% by O (blue).

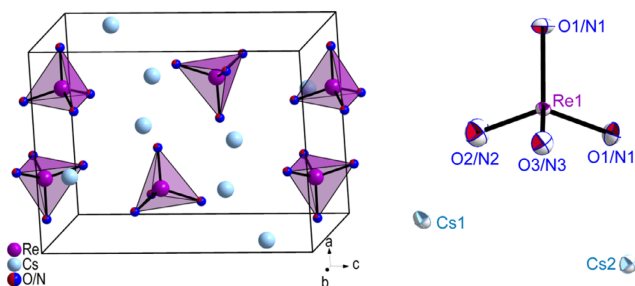


Figure 6. Extended unit cell of the crystal structure of $\text{Cs}_2[\text{ReO}_3\text{N}]$ (left) and the extended asymmetric unit with ellipsoid representation (70% probability, right). The mixed colored atoms are occupied 25% by N (red) and 75% by O (blue).

Table 2. Selected crystallographic data of $A'_2[\text{ReO}_3\text{N}]$ with $A' = \text{K}, \text{Cs}$.		
Empirical formula	$\text{K}_2[\text{ReO}_3\text{N}]$	$\text{Cs}_2[\text{ReO}_3\text{N}]$
Formula weight	326.41 g mol ⁻¹	514.03 g mol ⁻¹
Temperature	100(2) K	100(2) K
Wavelength	0.71073 Å	0.71073 Å
Crystal system	Monoclinic	Orthorhombic
Space group	$C2/m$ (no. 12)	$Pnma$ (no. 62)
Unit cell dimensions	$a = 12.3380(8)$ Å $b = 6.0361(4)$ Å $c = 7.4694(5)$ Å $\beta = 114.687(3)^\circ$	$a = 8.5375(2)$ Å $b = 6.4813(2)$ Å $c = 11.5049(3)$ Å
Volume	505.43(6) Å ³	636.61(3) Å ³
Z	4	4
Density (calculated)	4.29 g cm ⁻³	5.36 g cm ⁻³
$F(000)$	576	864
Crystal size	$0.04 \times 0.03 \times 0.03$ mm ³	$0.40 \times 0.30 \times 0.10$ mm ³
2θ range for data collection	6.00° to 51.98°	5.94° to 61.19°
Index ranges	$-15 \leq h \leq 15$, $-7 \leq k \leq 7$, $-9 \leq l \leq 9$	$-12 \leq h \leq 12$, $-9 \leq k \leq 9$, $-16 \leq l \leq 16$
Reflections collected	5525	29483
Independent reflections	551 [$R_{\text{int}} = 0.0432$, $R_{\text{sigma}} = 0.0205$]	1062 [$R_{\text{int}} = 0.0814$, $R_{\text{sigma}} = 0.0202$]
Completeness to θ	99.8%	100%
Absorption correction	Multi-scan	Multi-scan
Data/parameters	551/40	1062/41
Goodness-of-fit on F^2	1.119	1.157
Final R indices [$I \geq 2\sigma(I_o)$]	$R_1 = 0.0113$, $wR_2 = 0.0258$	$R_1 = 0.0149$, $wR_2 = 0.0339$
R indices (all data)	$R_1 = 0.0116$, $wR_2 = 0.0259$	$R_1 = 0.0162$, $wR_2 = 0.0343$
Largest diff. peak and hole	$0.59/-0.58$ e Å ⁻³	$2.41/-1.28$ e Å ⁻³
CCDC number	2414619	2414617

with Polynator.^[16] The coordinating ligands were verified with CHARDI2015.^[17,18] **Figure 7** and **8** show the irregular polyhedra of the counter cations in $\text{K}_2[\text{ReO}_3\text{N}]$ and $\text{Cs}_2[\text{ReO}_3\text{N}]$, respectively.

Table 3. Selected bond lengths of $A'_2[\text{ReO}_3\text{N}]$ with $A' = \text{K}, \text{Cs}$.			
$\text{K}_2[\text{ReO}_3\text{N}]$		$\text{Cs}_2[\text{ReO}_3\text{N}]$	
Atoms	Bond length [Å]	Atoms	Bond length [Å]
Re-O1/N1	1.764(3)	Re-O1/N1	1.770(2)
Re-O2/N2	1.779(4)	Re-O2/N2	1.737(4)
Re-O3/N3	1.756(3)	Re-O3/N3	1.762(3)

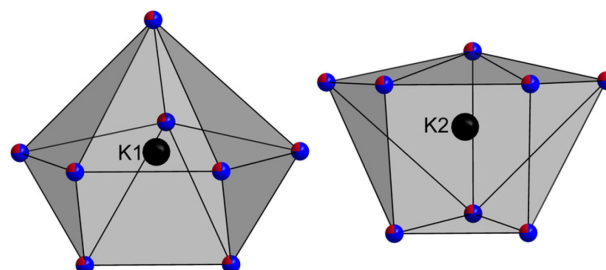


Figure 7. K-O/N polyhedra of $\text{K}_2[\text{ReO}_3\text{N}]$.

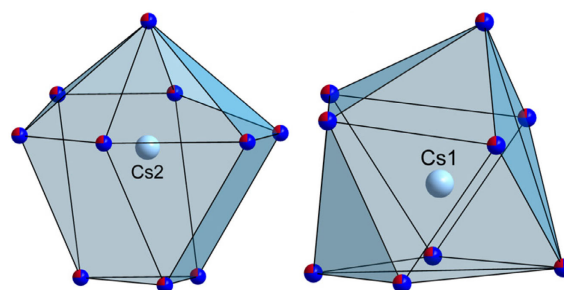


Figure 8. Cs-O/N polyhedra of $\text{Cs}_2[\text{ReO}_3\text{N}]$.

Raman spectra measured on single crystals of $\text{K}_2[\text{ReO}_3\text{N}]$ and $\text{Cs}_2[\text{ReO}_3\text{N}]$ are shown in Figure 6. A suitable reference compound is $\text{Ba}[\text{TcO}_3\text{N}]$.^[10] Similar to the technetium salt, $A'_2[\text{ReO}_3\text{N}]$ ($A' = \text{K}, \text{Cs}$) exhibit bands in the range between 306 and 381 cm⁻¹, which can be identified as the Re–O/N bending vibrations. In the range of 814–869 cm⁻¹ the stretching modes can be assigned.

The bands at wavenumbers >1000 cm⁻¹ can be attributed to the Re–N stretching vibrations. Compared to $\text{Ba}[\text{TcO}_3\text{N}]$,^[10] where only one band for the Re–N vibrations has been found at large wavenumbers, $\text{K}_2[\text{ReO}_3\text{N}]$ and $\text{Cs}_2[\text{ReO}_3\text{N}]$ clearly reveal two bands above 1000 cm⁻¹. Since the spectra were recorded on single crystals, no impurities are assumed to be present. Moreover, the additional band observed for $\text{K}_2[\text{ReO}_3\text{N}]$ and $\text{Cs}_2[\text{ReO}_3\text{N}]$ appears at wavenumbers comparable to those associated with the Re–N stretching vibration. This distinction can likely be attributed to differences in their crystal structures compared to $\text{Ba}[\text{TcO}_3\text{N}]$ ^[10] and should be investigated by means of quantum chemical calculations (**Figure 9**).

As a representative compound, quantum chemical calculations on the solid-state structure of $\text{K}_2[\text{ReO}_3\text{N}]$ were performed using the CRYSTAL program suite, see Section 3 for detail on utilized basis sets and functionals. Calculated Raman spectra were obtained

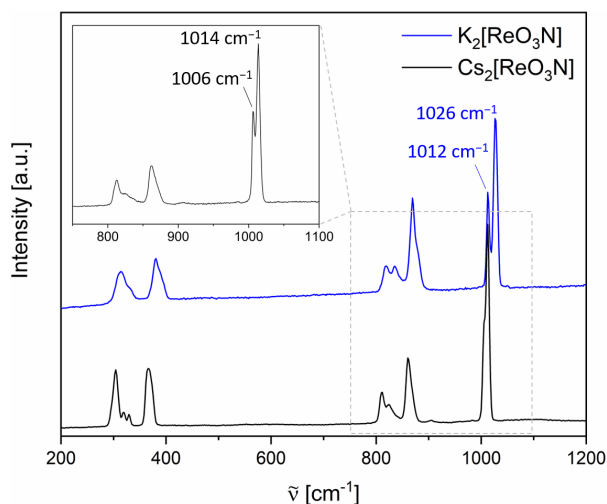


Figure 9. Raman spectra of $A'_2[\text{ReO}_3\text{N}]$ ($A' = \text{K}, \text{Cs}$). The top-left cutout of the $\text{Cs}_2[\text{ReO}_3\text{N}]$ spectrum was measured using the same single crystal but at a higher resolution compared to the overall measurement range of 200–1200 cm^{-1} .

for geometry optimized structures with either nitrogen on the O2 or O3 site, naming according to **Figure 10** and Figure S4, Supporting Information. These *in silico* obtained Raman spectra agree very well with experimental result, besides the fact that all bands are slightly shifted to higher wavenumbers which has been observed frequently in quantum chemical calculations.^[19,20] The obtained bands at wavenumbers above 1000 cm^{-1} are almost identical for both nitrogen positions and reveal values of 1025 and 1019 cm^{-1} , see **Table 4**. Since the structure in $C2/m$ shows two crystallographically identical ligand sites (O1), calculations with nitrogen on these different positions are impossible. Thus, the symmetry was reduced to space group $C2$ and the calculations were repeated with nitrogen on the two new different sites O1 and O1², respectively. See Figure S4, Supporting Information for the different positions in both symmetries. With reduced symmetry the maxima for nitrogen on both sites (O1 and O1²) differ a little more, revealing values of 1039 and 1042 cm^{-1} , but are still consistent with the experimental data, see Table 4. All calculated spectra can be found in the Supporting Information.

Accordingly, the different crystallographic positions of the oxygen and nitrogen atoms seem to have a significant influence

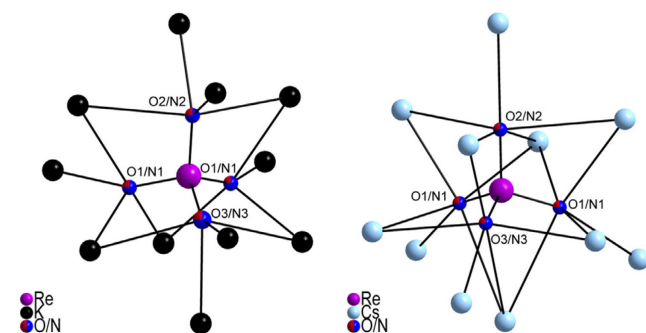


Figure 10. Structure of the coordination of O/N atoms by K/Cs in $\text{K}_2[\text{ReO}_3\text{N}]$ (left) and $\text{Cs}_2[\text{ReO}_3\text{N}]$ (right).

Table 4. Calculated Raman shifts when using the four different N positions in the $[\text{ReO}_3\text{N}]^{2-}$ tetrahedra, see also Figure S4, Supporting Information.

$\text{K}_2[\text{ReO}_3\text{N}]$ in $C2/m$		$\text{K}_2[\text{ReO}_3\text{N}]$ in $C2$	
N position	Raman shift [cm^{-1}]	N position	Raman shift [cm^{-1}]
2	1025.38	1	1039.11
3	1019.42	1 ²	1041.86

on the vibrational modes. Figure 10 shows the different coordination spheres of $\text{K}_2[\text{ReO}_3\text{N}]$ ($C2/m$) and $\text{Cs}_2[\text{ReO}_3\text{N}]$ ($Pnma$). Overall, the finding of more than one band at highest wavenumbers is in good agreement with results of the similar $[\text{VO}_3\text{N}]^{4-}$ anion in $\text{Ba}_2\text{VO}_3\text{N}$ exhibiting nonzero occupancies for nitrogen and oxygen as well as C_s symmetry.^[2] In contrast, one band has been observed for an anion in C_{3v} symmetry like for $[\text{ReO}_3\text{N}]^{2-}$ in the herein presented mixed-anionic species and $[\text{OsO}_3\text{N}]^-$ in the respective sodium salt.^[21]

Since it was now possible for the first time to determine the crystal structure of $\text{K}_2[\text{ReO}_3\text{N}]$, the results can be compared to known data of a bulk sample.^[3,9] However, the latter has so far only been characterized by means of IR spectroscopy. The powder pattern of $\text{K}_2[\text{ReO}_3\text{N}]$ simulated from single crystal X-ray data from this publication does not agree with the pattern obtained for the species synthesized via the already published synthesis route with liquid ammonia, see Figure S1, Supporting Information.^[3,9] However, the Raman spectra of the compounds from the two different routes agree very well, except a less pronounced splitting of the band at highest wavenumbers for the compound obtained from liquid ammonia, see Figure S2, Supporting Information.^[9]

In summary, the syntheses of the nitridotrioxidometallates were obtained from flux reactions with water being present in small to moderate amounts. $\text{Rb}_3[\text{ReO}_4][\text{ReO}_3\text{N}]$ and $\text{Cs}_3[\text{ReO}_4][\text{ReO}_3\text{N}]$ are isotopic to $\text{K}_3[\text{ReO}_4][\text{ReO}_3\text{N}]$ and crystallize in the space group $R\bar{3}am$.^[1] Both compounds have been investigated by powder X-ray diffraction, Rietveld refinement, and Raman spectroscopy. By increasing the nitrogen content in the starting mixture by simply adding ammonium chloride it was also possible to obtain $A'_2[\text{ReO}_3\text{N}]$ ($A' = \text{K}, \text{Cs}$). While the mixed anionic compounds crystallize in the same space group, $A'_2[\text{ReO}_3\text{N}]$ ($A' = \text{K}, \text{Cs}$) are not isotopic. $\text{K}_2[\text{ReO}_3\text{N}]$ crystallizes in the space group $C2/m$, whereas $\text{Cs}_2[\text{ReO}_3\text{N}]$ crystallizes in the orthorhombic space group $Pnma$. Raman spectroscopic measurements support the crystallographic results and prove the presence of Re-N bands. Quantum chemical calculations support the experimentally obtained Raman spectra.

3. Experimental Section

Syntheses

Colorless crystals of $A_3[\text{ReO}_4][\text{ReO}_3\text{N}]$ ($A = \text{Rb}, \text{Cs}$) were obtained from a flux reaction with alkali metal hydroxides by using a Teflon-lined stainless-steel autoclave. A batch contained 1 equivalent $\text{NH}_4[\text{ReO}_4]$ and 10–20 equivalents alkali metal hydroxide. The detailed batch information can be found in **Table 5**. The closed

Table 5. Detailed batch information for the syntheses of $A_3[ReO_4][ReO_3N]$ ($A = Rb, Cs$).

Reagent	<i>n</i> [mmol]	<i>m</i> [mg]	Equation	Product
$NH_4[ReO_4]$ (<i>Sigma-Aldrich</i> , $\geq 99\%$)	0.1	26.8	1	$Rb_3[ReO_4][ReO_3N]$
$RbOH \cdot xH_2O$ (<i>Thermo Scientific</i> , 99%)	2.0 ^{a)}	205.0	20 ^{a)}	
$NH_4[ReO_4]$ (<i>Sigma-Aldrich</i> , $\geq 99\%$)	0.3	80.5	1	$Cs_3[ReO_4][ReO_3N]$
$CsOH \cdot H_2O$ (<i>Acros Organics</i> , 99.95%)	3.0	503.8	10	

^{a)}RbOH was purchased as a x-hydrate. The molar mass and equivalents were calculated based on RbOH anhydrate ($102.48 \text{ g mol}^{-1}$).

autoclaves were heated at 200 °C for 10 h and cooled to room temperature with a cooling rate of 0.1 K min^{-1} . Single crystals of $A_3[ReO_4][ReO_3N]$ ($A = Rb, Cs$) were isolated after washing the reaction mixture with methanol. For the synthesis of phase-pure bulk samples, longer cooling times are required, specifically 0.02 K min^{-1} for $Rb_3[ReO_4][ReO_3N]$ and 0.03 K min^{-1} for $Cs_3[ReO_4][ReO_3N]$.

Colorless single crystals of $A'_2[ReO_3N]$ ($A' = K, Cs$) were obtained from an alkali metal hydroxide flux by using a Teflon-lined stainless-steel autoclave. A batch contained 1 equivalent $NH_4[ReO_4]$ and 49–110 equivalents alkali metal hydroxide. Additionally, ammonium chloride as a nitrogen source was added. For $K_2[ReO_3N]$, 50 equivalents H_2O were added, so this reaction might be called hydroflux reaction. The detailed batch information can be found in Table 6. The closed autoclaves were heated at 200 °C for 10 h and cooled to room temperature with a cooling rate of 0.1 K min^{-1} . Single crystals of $A'_2[ReO_3N]$ ($A' = K, Cs$) were mechanically removed from the flux. Phase-pure syntheses of bulk material were not successful.

Powder X-Ray Diffraction (P-XRD) and Rietveld Refinement

P-XRD data were collected on a Stoe Stadi-P powder diffractometer with a Mythen detector and a Debye–Scherrer geometry by using Mo– $K\alpha_1$ radiation of $\lambda = 0.70930 \text{ \AA}$. The samples were ground and sealed in glass capillaries with 0.3 mm diameter. The data was recorded in a range of $2\theta = 0^\circ\text{--}60^\circ$ within 30 min. The Rietveld refinement was performed with Topas, refining the lattice parameters freely using the Thompson–Cox–Hastings profile function, see Table S1

Table 6. Detailed batch information for the syntheses of $A'_2[ReO_3N]$ ($A' = K, Cs$).

Reagent	<i>n</i> [mmol]	<i>m</i> [mg]	Equation	Product
$NH_4[ReO_4]$ (<i>Sigma-Aldrich</i> , $\geq 99\%$)	0.2	53.7	1	$K_2[ReO_3N]$
NH_4Cl (stock, not specified)	0.6	32.1	3	
KOH (<i>Thermo Scientific</i> , $\approx 85\%$)	22.0	1234.3	110	
H_2O	10.0	180.2	50	
$NH_4[ReO_4]$ (<i>Sigma-Aldrich</i> , $\geq 99\%$)	0.1	26.8	1	$Cs_2[ReO_3N]$
NH_4Cl (stock, not specified)	0.3	16.1	3	
$CsOH \cdot H_2O$ (<i>Acros Organics</i> , 99.95%)	4.9	824.6	49	

and S2, Supporting Information.^[22,23] For $Rb_3[ReO_4][ReO_3N]$ the atomic displacement parameters were also refined freely. The background was described with six Chebychev polynomials. The diffractogram was plotted using Origin software.^[24]

Single-Crystal X-Ray Diffraction (SC-XRD)

The single-crystal XRD data were collected with a Bruker D8 Venture by using Mo– $K\alpha$ radiation of $\lambda = 0.71073 \text{ \AA}$. The crystals were prepared under a polarization microscope and measured at a temperature of 100(2) K. The lattice parameters, the refinement details, the atomic parameters and selected bond lengths are given in Table 1 and 3. Further data can be found in Table S3–S22, Supporting Information. The solution and refinement of the structures were carried out using ShelXL/ShelXT in Olex2.^[25,26] The pictures of the structures were generated using the Diamond software.^[27]

Deposition Numbers 2414620 (for $Rb_3[ReO_4][ReO_3N]$), 2414618 (for $Cs_3[ReO_4][ReO_3N]$), 2414619 (for $K_2[ReO_4]$) and 2414617 (for $Cs_2[ReO_4]$) contain the supplementary crystallographic data for this paper. These data are provided free of charge by the joint Cambridge Crystallographic Data Centre and Fachinformationszentrum Karlsruhe Access Structures service.

Raman Spectroscopy

Raman spectra of single crystals were obtained with a Renishaw InVia Qontor spectrometer by a frequency-doubled Ne:YAG laser with 532 nm wavelength and 100 mW output energy in 180 °C backscatter geometry, a slit opening of $65 \mu\text{m}$, a Rayleigh edge filter with a cut-off below approx. 50 cm^{-1} and a back-illuminated CCD Centrus detector. The estimated spectral resolutions are about 0.7 cm^{-1} ($1800 \text{ lines mm}^{-1}$ grating) and 0.4 cm^{-1} ($3000 \text{ lines mm}^{-1}$ grating), respectively. The spectrometer was calibrated to a Si single crystal before measurements. Spectra were recorded at room temperature with a transmission filter of 5% over 20–60 times for 5 s using a 50x LWD objective. The data was plotted using the Origin Software.^[24]

Quantum Chemical Calculations

DFT calculations were carried out with the Crystal 17 program suite^[28–32] using the PBEsol^[33] functional at pob-TZVP^[34,35] basis set quality with an 8,8 k space grid. Raman spectra were calculated using geometry optimizations with subsequent frequency calculations ensuring optimized structures to be a minimum. See Figure S3 and Table 23–26, Supporting Information.

Acknowledgements

The authors thank Dr. Tobias Rennebaum and Katrin Eppers for the measurement of Raman data and S. Kremer for the single-crystal X-ray measurements. Furthermore, they thank Prof. Mathias Wickleder for the constant support and helpful discussions.

Open Access funding enabled and organized by Projekt DEAL.

Conflict of Interest

The authors declare no conflict of interest.

Data Availability Statement

The data that support the findings of this study are available from the corresponding author upon reasonable request.

Keywords: flux · oxoanion · Raman spectroscopy quantum chemistry · rhenium

- [1] D. Badea, S. Olthof, J. Neudörfl, R. Glaum, R. Pöttgen, M. Reimann, K. Meerholz, M. Reimer, C. Logemann, E. Strub, J. Bruns, *Eur. J. Inorg. Chem.* **2023**, 26, e202300160.
- [2] S. J. Clarke, P. R. Chalker, J. Holman, C. W. Michie, M. Puyet, M. J. Rosseinsky, *J. Am. Chem. Soc.* **2002**, 124, 3337.
- [3] B. Krebs, A. Müller, *J. Inorg. Nucl. Chem.* **1968**, 30, 463.
- [4] A. Müller, F. Bollmann, *Z. Naturforsch.* **1968**, 23b, 1539.
- [5] H. Müller-Buschbaum, *J. Alloys Compd.* **2003**, 349, 49.
- [6] R. Pastuszak, P. L'Haridon, R. Marchand, Y. Laurent, *Acta Crystallogr., Sect. B: Struct. Sci.* **1982**, 38, 1427.
- [7] M. T. Pope, A. Müller, *Angew. Chem. Int. Ed.* **1991**, 30, 34.
- [8] P. Subramanya Herle, M. S. Hegde, G. N. Subbanna, *J. Mater. Chem.* **1997**, 7, 2121.
- [9] A. F. Clifford, R. R. Olsen, *Inorg. Synth.* **1960**, 6, 167.
- [10] D. Badea, K. Dardenne, R. Polly, J. Rothe, K. Meerholz, M. Hanrath, M. Reimer, J. Neudörfl, E. Strub, J. Bruns, *Chem. Eur. J.* **2022**, 28, e202201738.
- [11] A. Müller, E. J. Baran, F. Bollmann, P. J. Aymonino, *Z. Naturforsch.* **1969**, 24, 960.
- [12] M. T. Weller, S. J. Skinner, *Int. J. Inorg. Mater.* **2000**, 2, 463.
- [13] R. Niewa, H. Jacobs, *Chem. Rev.* **1996**, 96, 2053.
- [14] R. Niewa, F. J. DiSalvo, *Chem. Mater.* **1998**, 10, 2733.
- [15] A. Müller, E. Baran, F. Bollmann, P. Aymonino, *Z. Naturforsch., B: J. Chem. Sci.* **1969**, 24, 960.
- [16] L. Link, R. Niewa, *J. Appl. Crystallogr.* **2023**, 56, 1855.
- [17] M. Nespolo, *Acta Crystallogr., Sect. A: Found. Adv.* **2016**, 72, 51.
- [18] M. Nespolo, B. Guillot, *J. Appl. Crystallogr.* **2016**, 49, 317.
- [19] A. P. Scott, L. Radom, *J. Chem. Phys.* **1996**, 100, 16502.
- [20] K. K. Irikura, R. D. Johnson, R. N. Kacker, *J. Phys. Chem. A* **2005**, 109, 8430.
- [21] L. A. Woodward, J. A. Creighton, K. A. Taylor, *Trans. Faraday Soc.* **1960**, 56, 1267.
- [22] A. A. Coelho, *J. Appl. Crystallogr.* **2018**, 51, 210.
- [23] A. A. Coelho *Topas-Academic Version V6*, Brisbane **2016**.
- [24] *OriginPro 2019b, Version 9.6.5.169*, OriginLab Corporation, Northampton **2019**.
- [25] O. V. Dolomanov, L. J. Bourhis, R. J. Gildea, J. A. K. Howard, H. Puschmann, *J. Appl. Crystallogr.* **2009**, 42, 339.
- [26] G. Sheldrick, *Acta Crystallogr., Sect. A: Found. Adv.* **2015**, C71, 3.
- [27] K. Brandenburg, Diamond 4, Crystal and Molecular Structure Visualization, Crystal Impact GbR, Bonn **2019**.
- [28] L. Maschio, B. Kirtman, M. Rérat, R. Orlando, R. Dovesi, *J. Chem. Phys.* **2013**, 139, 167101.
- [29] M. Ferrero, M. Rérat, B. Kirtman, R. Dovesi, *J. Chem. Phys.* **2008**, 129, 244110.
- [30] M. Ferrero, M. Rérat, R. Orlando, R. Dovesi, *J. Chem. Phys.* **2008**, 128, 014110.
- [31] M. Ferrero, M. Rérat, R. Orlando, R. Dovesi, *J. Comput. Chem.* **2008**, 29, 1450.
- [32] R. Dovesi, R. Orlando, A. Erba, C. Zicovich-Wilson, B. Civalleri, S. Casassa, L. Maschio, M. Ferrabone, M. De La Pierre, P. D'arco, M. Rérat, B. Kirtman, *Int. J. Quantum Chem* **2014**, 114, 1287.
- [33] J. P. Perdew, A. Ruzsinszky, G. I. Csonka, O. A. Vydrov, G. E. Scuseria, L. A. Constantin, X. L. Zhou, K. Burke, *Phys. Rev. Lett.* **2008**, 100, 136406.
- [34] D. Vilela Oliveira, J. Laun, M. F. Peintinger, T. Bredow, *J. Comput. Chem.* **2019**, 40, 2364.
- [35] M. F. Peintinger, D. V. Oliveira, T. Bredow, *J. Comput. Chem.* **2012**, 34, 451.

Manuscript received: January 22, 2025

Revised manuscript received: April 8, 2025

Version of record online: May 20, 2025

4.2.4 Ba₂[Ir(OH)₆](OH)₂ from Alkaline Earth Metal Hydroxide (Publication 5)

In 2013, *zur Loye* and coworkers synthesized platinum group metal hydroxides, e.g. Ba₂Pt(OH)₈, using alkali metal hydroxide hydrofluxes, showing also their utility as precursors for metal oxides.^[13] As the crystal structure of the respective iridium hydroxide from a hydroxide hydroflux is not known, attempts were conducted using (NH₄)₂[IrCl₆] and a Ba(OH)₂ · 8 H₂O hydroflux. The novel compound Ba₂[Ir(OH)₆](OH)₂ crystallizes in the orthorhombic space group *Pbca* with Ir⁴⁺ coordinated by six OH⁻ anions, forming a slightly distorted octahedron better described as a rectangular bipyramid. Since the publication contains mainly a simple structure description of Ba₂[Ir(OH)₆](OH)₂ and one single picture, further figures are depicted in the Appendix, see Figure 29, Figure 30 and Figure 31.

Publication 5

The crystal structure of barium hexahydroxidoiridate(IV) dihydroxide,

Ba₂[Ir(OH)₆](OH)₂

D. Badea and J. Bruns*

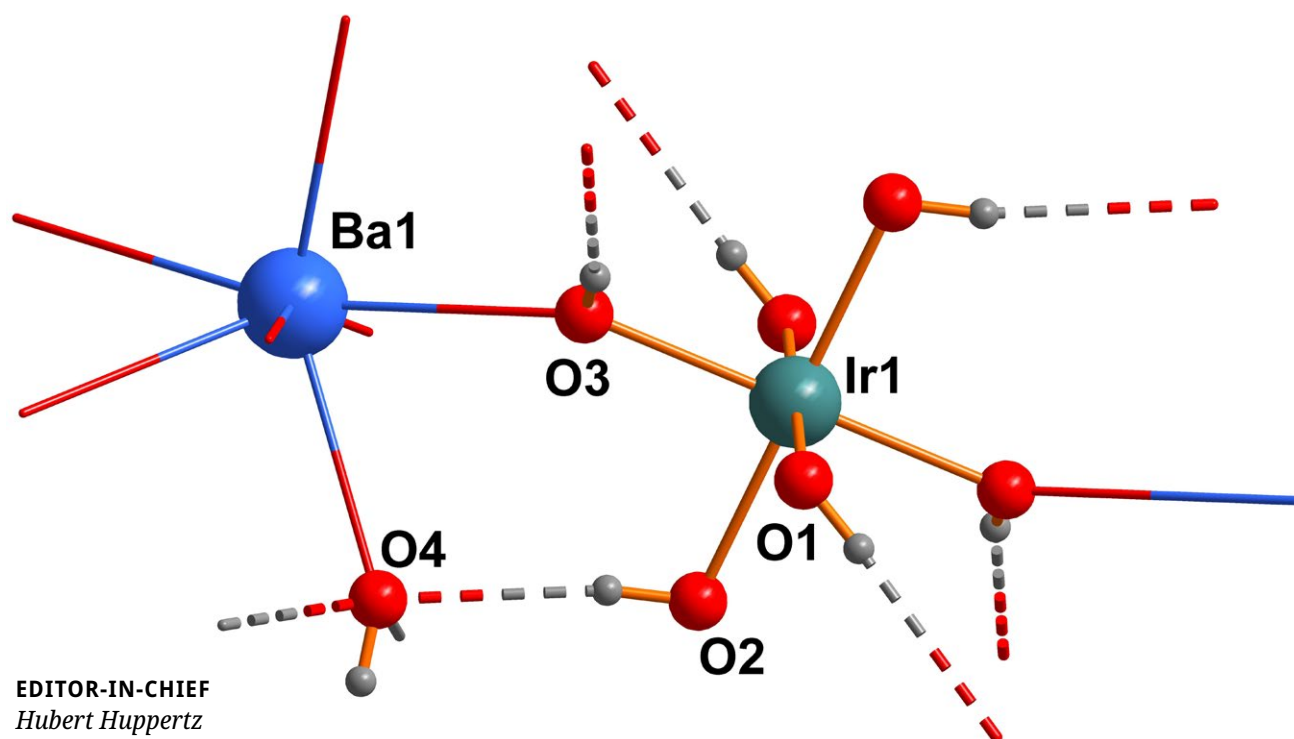
Z. Kristallogr. N. Cryst. Struct. **2025**, 240, 255-256.

doi.org/10.1515/ncrs-2024-0455

Explanation of the personal contribution to the previously mentioned publication:

The experiments were carried out by Désirée Badea. The first author synthesized the analyzed product, performed the characterization experiments, evaluated the collected data and prepared the corresponding plots for publication. Désirée Badea prepared the draft of the manuscript.

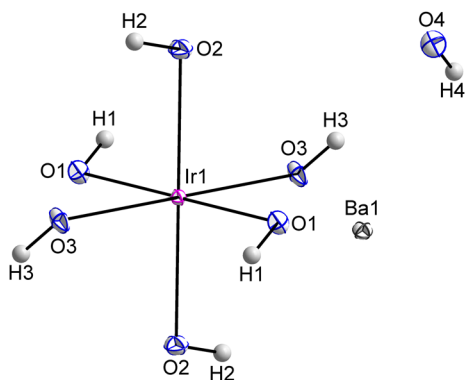
ZEITSCHRIFT FÜR KRISTALLOGRAPHIE NEW CRYSTAL STRUCTURES

**EDITOR-IN-CHIEF***Hubert Huppertz***EDITORIAL BOARD***Marek Daszkiewicz**Christian Hübschle**Oliver Janka**Andreas Lemmerer**Guido J. Reiss**Marko Rodić**Svitlana V. Shishkina**Edward R. T. Tiekink*

A section of the crystal structure of
 $\text{Ba}_2[\text{Ir}(\text{OH})_6](\text{OH})_2$

Jörn Bruns* and Désirée Badea

The crystal structure of barium hexahydroxidoiridate(IV) dihydroxide, $\text{Ba}_2[\text{Ir}(\text{OH})_6](\text{OH})_2$

**Table 1:** Data collection and handling.

Crystal:	Brown plate
Size:	0.10 × 0.10 × 0.05 mm
Wavelength:	Mo K α radiation (0.71073 Å)
μ :	27.3 mm ⁻¹
Diffractometer, scan mode:	BRUKER D8 Venture, φ and ω
θ_{max} , completeness:	35.0°, 98 %
$N(hkl)_{\text{measured}}$, $N(hkl)_{\text{unique}}$, R_{int} :	21435, 1677, 0.041
Criterion for I_{obs} , $N(hkl)_{\text{gt}}$:	$I_{\text{obs}} > 2\sigma(I_{\text{obs}})$, 1,592
$N(\text{param})_{\text{refined}}$:	69
Programs:	SHELX ^{1,2} , Diamond ³ , Olex2 ⁴ , Bruker ⁵

<https://doi.org/10.1515/ncrs-2024-0455>

Received November 29, 2024; accepted January 21, 2025;

published online February 7, 2025

Abstract

$\text{Ba}_2[\text{Ir}(\text{OH})_6](\text{OH})_2$, orthorhombic, *Pbca* (no. 61), $a = 8.5717(4)$ Å, $b = 8.6814(4)$ Å, $c = 10.3683(5)$ Å, $V = 771.55(6)$ Å³, $Z = 4$, $R_{\text{gt}}(F) = 0.0154$, $wR_{\text{ref}}(F^2) = 0.0304$, $T = 100(2)$ K.

CCDC no.: 2418530

A part of the molecular structure is shown in the figure. Table 1 contains crystallographic data and Table 2 contains the list of the atoms including atomic coordinates and displacement parameters.

1 Source of materials

The synthesis of $\text{Ba}_2[\text{Ir}(\text{OH})_6](\text{OH})_2$ was carried out in an autoclave with PTFE inlay. The starting mixture contained of 22.05 mg $(\text{NH}_4)_2[\text{IrCl}_6]$ (0.05 mmol, 1 eq), 867.57 mg $\text{Ba}(\text{OH})_2 \cdot 8\text{H}_2\text{O}$ (2.75 mmol, 55 eq) and 49.54 mg H_2O (2.75 mmol,

55 eq). $(\text{NH}_4)_2[\text{IrCl}_6]$ was first loaded into the PTFE inlay. After adding $\text{Ba}(\text{OH})_2 \cdot 8\text{H}_2\text{O}$ and H_2O , the closed autoclave was heated to 200 °C with a heating rate of 2 °C/min. After holding the temperature for 10 h, the temperature of the autoclave was reduced to room temperature with a rate of 0.05 °C/min. The title compound was obtained as brown crystals in a colorless matrix.

2 Experimental details

Structural solutions, refinements and visualization were carried out with the ShelX software packages by using Olex2 and Diamond 4.^{1–5} Anisotropic refinement was applied to the Ba, Ir and O atoms. The hydrogen atoms were refined without any constraints or restraints.

3 Comment

With the help of alkali metal hydroxide hydrofluxes, zur Løye and co-workers were able to obtain several platinum group metal hydroxides in 2013.⁶ They stated, that one benefit of synthesizing metal hydroxides lies in their role as precursors for oxides. By gently heating metal hydroxides to dehydration, the synthesis of metal oxides can be performed at lower temperatures than those typically required for traditional solid-state reactions. Dehydrating metal hydroxides could also be an effective method for obtaining other industrially important metal oxides, e.g. for the production of catalysts. Zur Løye published the structure of $\text{Sr}_2\text{Pt}(\text{OH})_8$, which crystallizes in the space group $P2_1/c$.⁶ The

*Corresponding author: Jörn Bruns, Department für Chemie und Biochemie, Institut für Anorganische und Materialchemie, Universität zu Köln, Greinstrasse 6, D-50939 Köln, Germany, E-mail: j.bruns@uni-koeln.de. <https://orcid.org/0000-0002-8589-6154>

Désirée Badea, Department für Chemie und Biochemie, Institut für Anorganische und Materialchemie, Universität zu Köln, Greinstrasse 6, D-50939 Köln, Germany, E-mail: dbadea@smail.uni-koeln.de. <https://orcid.org/0000-0002-8837-9988>

Table 2: Fractional atomic coordinates and isotropic or equivalent isotropic displacement parameters (Å²).

Atom	x	y	z	$U_{\text{iso}}^*/U_{\text{eq}}$
Ir1	0.500000	0.500000	0.500000	0.00296 (3)
Ba1	0.78456 (2)	0.77957 (2)	0.77279 (2)	0.00418 (4)
O1	0.2829 (2)	0.5258 (2)	0.5663 (2)	0.0059 (3)
O2	0.5014 (2)	0.7164 (2)	0.4309 (2)	0.0066 (3)
O3	0.5748 (2)	0.5752 (2)	0.6735 (2)	0.0061 (3)
O4	0.5668 (3)	0.9261 (2)	0.6297 (2)	0.0072 (3)
H3	0.519 (5)	0.532 (5)	0.724 (5)	0.01 (1)*
H2	0.528 (6)	0.769 (6)	0.490 (4)	0.02 (1)*
H1	0.231 (9)	0.537 (8)	0.508 (6)	0.04 (2)*
H4	0.527 (7)	0.995 (7)	0.608 (7)	0.04 (2)*

structure consists of a three-dimensional framework of Sr(OH)₈ dodecahedra and Pt(OH)₆ octahedra filling the cavities. Each Sr(OH)₈ dodecahedron shares corners and edges with both Pt(OH)₆ octahedra and other Sr(OH)₈ units. In contrast, Ba₂Pt(OH)₈, which was also published by zur Loye, crystallizes in the orthorhombic space group *Pbca*, with Ba(OH)₉ polyhedra forming sheets which are separated by Pt(OH)₆ octahedra.⁶ The Pt⁴⁺ cations are in regular octahedral coordination and the Ba²⁺ cations exhibit irregular coordination to nine OH[−] ions.⁶ Therefore, the compound could also be written as Ba₂[Pt(OH)₆](OH)₂.

The title compound Ba₂[Ir(OH)₆](OH)₂ crystallizes in the orthorhombic space group *Pbca* and is isotypic to Ba₂[Pt(OH)₆](OH)₂.⁶ The asymmetric unit consists of one crystallographically distinct Ir atom coordinated by six OH[−] anions forming a slightly distorted octahedron (see Figure). More precisely, the polyhedron can be described as a rectangular bipyramid with a Polynator delta-value of 1.147.^{7,8} The structure contains one distinct barium cation which is coordinated by nine OH[−] anions. Each Ba(OH)₉ polyhedron is corner-linked to one Ir(OH)₆ polyhedron and edge-linked to three Ir(OH)₆ polyhedra. All Ir–O bond lengths, which amount to 1.996(2) Å, 2.011(2) Å and 2.018(2) Å, are consistent with the literature known values, i.e. 2.0124(9) Å in Na₂[Ir(OH)₆].⁹ Ba₂[Ir(OH)₆](OH)₂ exhibits four crystallographically distinguishable oxygen and hydrogen atoms, respectively. All of them are part of OH[−] anions and were freely refined. Since the

compound could not be obtained phase-pure, further attempts to conclusively verify the +IV oxidation state of iridium were not possible. However, confidence in the structural determination is justified, as all atoms were freely refined. Any additional protonation, and consequently a reduction in the oxidation state of iridium, would result in elongated O–H bonds. Furthermore, Ba₂[Ir(OH)₆](OH)₂ is isotypic to Ba₂[Pt(OH)₆](OH)₂, which once more supports the structural integrity of the compound.⁶

Acknowledgments: We thank Dr. David van Gerven for the helpful discussion.

Author contribution: All the authors have accepted responsibility for the entire content of this submitted manuscript and approved submission.

Conflict of interest: The authors declare no conflicts of interest regarding this article.

References

- Sheldrick, G. M. Crystal Structure Refinement with SHELXL. *Acta Crystallogr.* **2015**, C71, 3–8.
- Sheldrick, G. M. SHELXTL – Integrated Space-Group and Crystal-Structure Determination. *Acta Crystallogr.* **2015**, A71, 3–8.
- Brandenburg, K. *Diamond 4, Crystal and Molecular Structure Visualization*; Crystal Impact GbR: Bonn, Germany, 2019.
- Dolomanov, O. V.; Bourhis, L. J.; Gildea, R. J.; Howard, J. A. K.; Puschmann, H. OLEX2: A Complete Structure Solution, Refinement and Analysis Program. *J. Appl. Crystallogr.* **2009**, 42, 339–341.
- SAINT 8.40B. *Area Detector Control and Integration Software*; Bruker AXS Inc.: Madison, Wisconsin, USA, 2021.
- Bugaris, D. E.; Smith, M. D.; zur Loye, H.-C. Hydroflux Crystal Growth of Platinum Group Metal Hydroxides: Sr₆NaPd₂(OH)₁₇, Li₂Pt(OH)₆, Na₂Pt(OH)₆, Sr₂Pt(OH)₈, and Ba₂Pt(OH)₈. *Inorg. Chem.* **2013**, 52, 3836–3844.
- Link, L.; Niewa, R. Polynator: A Tool to Identify and Quantitatively Evaluate Polyhedra and Other Shapes in Crystal Structures. *J. Appl. Crystallogr.* **2023**, 56, 1855–1864.
- Nespolo, M.; Guillot, B. CHARDI2015: Charge Distribution Analysis of Non-Molecular Structures. *J. Appl. Crystallogr.* **2016**, 49, 317–321.
- Albrecht, R.; Poddig, H.; Hunger, J.; Ruck, M.; Benrath, P.; Möller, A.; Doert, T. Hydrothermal Synthesis, Crystal Structure, and Magnetism of Na₂[Ir(OH)₆] and its Dehydration to Na₂IrO₃. *Z. Anorg. Allg. Chem.* **2021**, 647, 667–672.

4.2.5 $\text{Ba}_{2.4}\text{Sr}_{1.6}[\text{Ir}(\text{OH})_6](\text{OH})_6$ from Alkaline Earth Metal Hydroxides

Similar to $\text{Ba}_2[\text{Ir}(\text{OH})_6](\text{OH})_2$, further attempts were conducted reacting $(\text{NH}_4)_2[\text{IrCl}_6]$ in a $\text{Ba}(\text{OH})_2 \cdot 8 \text{H}_2\text{O}/\text{Sr}(\text{OH})_2 \cdot 8 \text{H}_2\text{O}$ mixture.^[78] Figure 10 shows a microscopic picture of yellow single crystals of $\text{Ba}_{2.4}\text{Sr}_{1.6}[\text{Ir}(\text{OH})_6](\text{OH})_6$ which were measured by SC-XRD. Table 2 and Table 13 in the Appendix contain the crystallographic data of the compound.

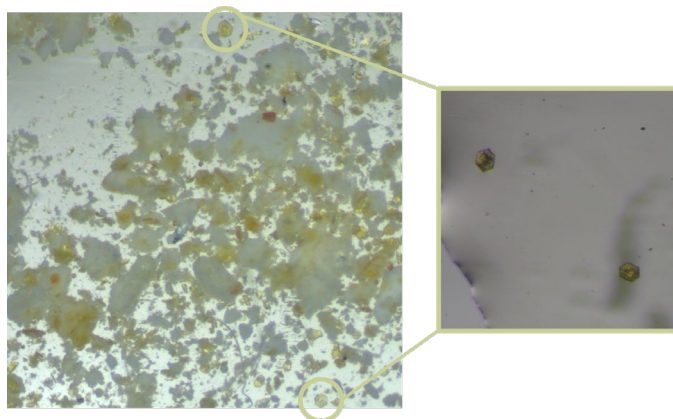


Figure 10. Microscopic image of yellow single crystals of $\text{Ba}_{2.4}\text{Sr}_{1.6}[\text{Ir}(\text{OH})_6](\text{OH})_6$ in a $\text{Ba}(\text{OH})_2/\text{Sr}(\text{OH})_2$ hydroflux (left) and selected single crystals (right).

$\text{Ba}_{2.4}\text{Sr}_{1.6}[\text{Ir}(\text{OH})_6](\text{OH})_6$ crystallizes in the trigonal space group $R\bar{3}$. The formal oxidation state of iridium is +IV. The asymmetric unit consists of one crystallographically distinct Ir and two unique O atoms. The central Ir atom is coordinated by six OH^- anions associated with O1, forming a perfect trigonal antiprism with a *Polynator* δ -value of 0.000, see Figure 11 and Figure 12.^[81]

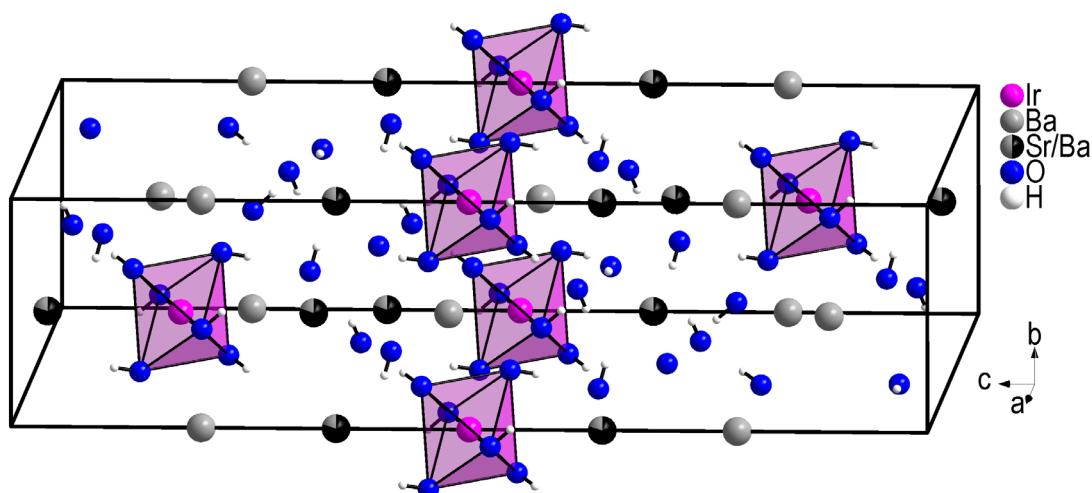


Figure 11. Unit cell of the crystal structure of $\text{Ba}_{2.4}\text{Sr}_{1.6}[\text{Ir}(\text{OH})_6](\text{OH})_6$ with pink $\text{Ir}(\text{OH})_6$ octahedra.

The structure contains two distinct alkaline earth metal sites, each coordinated by nine OH^- anions. All cations occupy special positions, specifically 3b for Ir and 6c for Ba/Sr. One 6c position is exclusively occupied by Ba, while the second exhibits partial occupancy by

Sr (80%) and Ba (20%), yielding the composition $\text{Ba}_{2.4}\text{Sr}_{1.6}[\text{Ir}(\text{OH})_6](\text{OH})_6$. This cation distribution was determined using SHELX^[82-83], ensuring the best fit to observed diffraction data. The refinement was performed in OLEX, employing EADP and EXYZ constraints.^[84]

Both alkaline earth metal polyhedra can be described as strongly distorted tricapped trigonal prisms determined with *Polynator* with δ -values of 10.080 and 13.722.^[81] The mixed Ba/Sr-O polyhedra are connected in the *a-b*-plane to form layers with the $\text{Ir}(\text{OH})_6$ polyhedra in between, see Figure 13 (below). Furthermore, the Ba-O polyhedra are also forming layers, see Figure 13 (above). Within the layer, one $\text{Ba}(\text{OH})_9$ polyhedron is face-sharing with three additional $\text{Ba}(\text{OH})_9$ polyhedra via four oxygen atoms and corner-sharing with six further $\text{Ba}(\text{OH})_9$ polyhedra. The same applies to the polyhedron containing the mixed cationic site.

Table 2. Selected crystallographic data of $\text{Ba}_{2.4}\text{Sr}_{1.6}[\text{Ir}(\text{OH})_6](\text{OH})_6$.

Crystal system	trigonal	Space group	$R\bar{3}$
Lattice parameters	$a = 6.3403(2) \text{ \AA}$	$R_1 (I_o \geq 2\sigma(I_o))$	0.0158
	$c = 26.430(1) \text{ \AA}$	$wR_2 (I_o \geq 2\sigma(I_o))$	0.0334
	$V = 920.12(7) \text{ \AA}^3$	<i>goof</i>	1.279
Formula units	3		

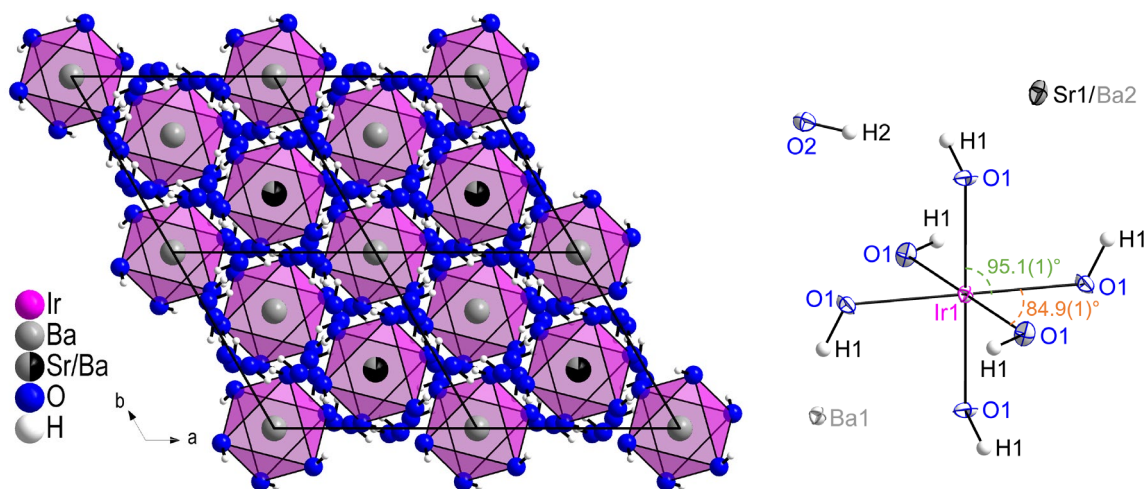


Figure 12. Arrangement of the pink $\text{Ir}(\text{OH})_6$ polyhedra with view along the *c*-axis (left) and extended asymmetric unit of $\text{Ba}_{2.4}\text{Sr}_{1.6}[\text{Ir}(\text{OH})_6](\text{OH})_6$ with thermal ellipsoids with a probability of 70% (right).

The Ir-O bond, which amounts to $2.014(2) \text{ \AA}$, is nearly identical with the literature known bond length, i.e. $2.0124(9) \text{ \AA}$ in $\text{Na}_2[\text{Ir}(\text{OH})_6]$.^[66] All hydrogen atoms are associated with OH^- anions and were refined without constraints. Due to the fact that it was not possible to isolate the compound in a phase-pure form, further synthesis attempts need to be done to definitively confirm the +IV oxidation state of iridium. With the use of a phase-pure bulk sample of $\text{Ba}_{2.4}\text{Sr}_{1.6}[\text{Ir}(\text{OH})_6](\text{OH})_6$, XAFS or XPS data can be obtained.

Nevertheless, the structural determination is considered reliable, as all atomic positions were refined freely. Any additional protonation, and thereby a reduction in the iridium oxidation state, would lead to notably change of bond lengths.

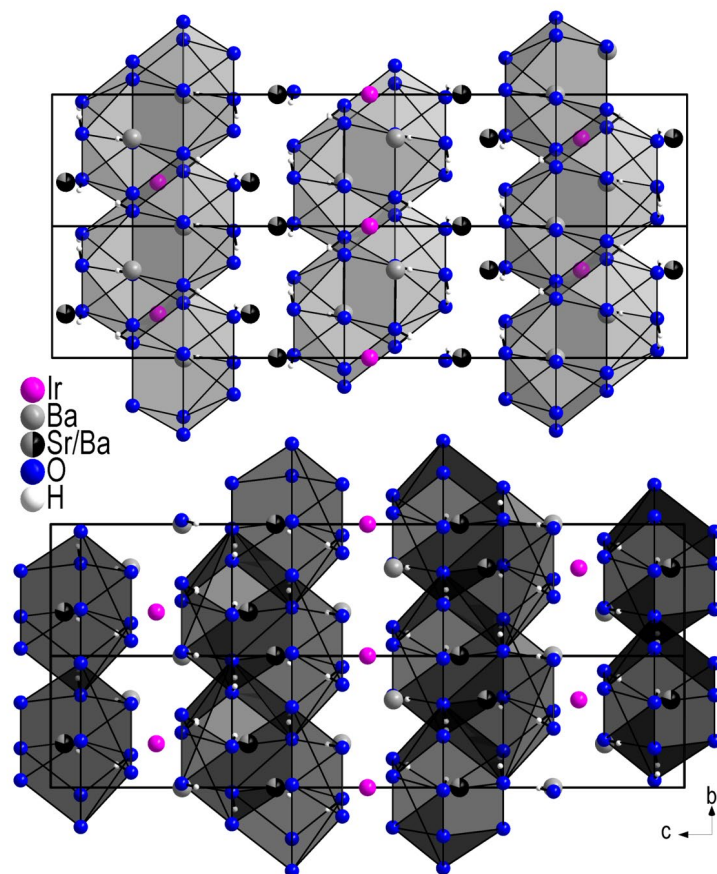


Figure 13. Arrangement of the grey Ba-O polyhedra (above) and of the black Sr/Ba-O polyhedra with view along the *a*-axis (below).

4.3 Syntheses in the Multi Anvil Press

The multi anvil press is a crucial technique for studying compounds under extreme conditions. It enables the use of high pressure and high temperature environments, replicating conditions found deep within the earth's interior or in industrial processes.^[6, 85] This allows investigation of phase transitions, synthesis of novel compounds and characterization of the behavior of elements and compounds under extreme conditions. Multi anvil experiments can improve state of knowledge in geochemistry, solid state chemistry and materials science, providing useful information for basic research and practical applications.

This chapter describes the synthesis and characterization of the new ternary lead compound Ag_2PbO_3 from the *Walker*-type multi anvil press.^[28] Additionally, it presents further experiments aimed at obtaining ternary and quaternary oxygen-containing compounds using this high pressure technique.

4.3.1 Ag_2PbO_3 from High Pressure and High Temperature Experiments

A new ternary silver lead oxide, i.e. Ag_2PbO_3 , could be obtained from the reaction of Ag_2PbO_2 in the *Walker*-type multi anvil press.^[28] The synthesis of the starting material Ag_2PbO_2 can be carried out by evaporating an aqueous solution containing $\text{Na}_2\text{Pb}(\text{OH})_4$ and $\text{Ag}[\text{NH}_3]_2\text{NO}_3$ at room temperature.^[86-88] This method produces pale yellow to brown crystals of Ag_2PbO_2 . The starting material crystallizes in the space group *I2/c* with $a = 6.0775(9) \text{ \AA}$, $b = 8.704(1) \text{ \AA}$, $c = 6.553(1) \text{ \AA}$, $\beta = 93.545(8)^\circ$ and $V = 345.98(8) \text{ \AA}^3$.^[86] Therein Ag atoms are arranged in linear coordination by two O atoms, forming continuous chains. In contrast, the Pb atoms are coordinated in a distorted square pyramid by four O atoms, resembling the coordination in orthorhombic PbO. The PbO_4 polyhedra are edge-connected to form chains, with silver atoms forming a substructure characterized by Ag-Ag distances ranging from 3.04 Å to 3.27 Å.^[86] Ag_2PbO_2 exhibits distinct anisotropic properties, especially in terms of electrical conductivity and UV-vis spectroscopy, which result from its layered silver interactions.^[86]

For the synthesis of the title compound Ag_2PbO_3 , freshly crystallized Ag_2PbO_2 is reacted at high temperatures and high pressures by applying about 8 GPa (300 bar oil pressure) and 900 W, see Figure 14. Black metallic crystals were obtained and characterized with SC-XRD.

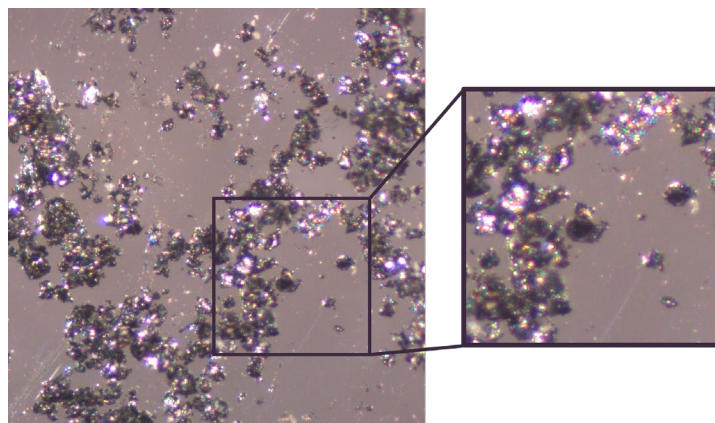


Figure 14. Microscopic image of black metallic single crystals of Ag₂PbO₃ (left) and enlarged section (right).

Ag₂PbO₃ crystallizes in the space group *Fddd* with 16 formula units per cell. Table 3 and Table 20 in the Appendix contain the crystallographic data of Ag₂PbO₃. The cell parameter amount to $a = 7.0352(5) \text{ \AA}$, $b = 9.4729(6) \text{ \AA}$, $c = 20.1261(1) \text{ \AA}$ and $V = 1341.28(2) \text{ \AA}^3$.

Table 3. Selected crystallographic data of Ag₂PbO₃.

Crystal system	orthorhombic	Space group	<i>Fddd</i>
Lattice parameters	$a = 7.0352(5) \text{ \AA}$	Formula units	16
	$b = 9.4729(6) \text{ \AA}$	$R_1 (I_o \geq 2\sigma(I_o))$	0.0268
	$c = 20.126(1) \text{ \AA}$	$wR_2 (I_o \geq 2\sigma(I_o))$	0.0675
	$V = 1341.3(2) \text{ \AA}^3$	<i>goof</i>	1.117

The compound exhibits one crystallographically distinct Pb atom, whereas two Ag and two O atoms are present. Ag₂PbO₃ consists of octahedrally coordinated Ag, Pb and O atoms each, see Figure 15. Two consecutive edge-linked AgO₆ octahedra are followed by two PbO₆ octahedra, following this order. The Ag-O bond lengths range from 2.398(1) Å to 2.658(7) Å, with Pb-O exhibiting lengths of 2.198(7) Å and 2.212(6) Å. All observed bond lengths are consistent with those reported for analogous compounds in the literature. For instance, Ag(I)-O bond lengths range from 2.26(2) Å to 2.75(2) Å in Ag₂WO₄, while Pb(IV)-O bond lengths vary between 2.145(7) Å and 2.206(7) Å in Pb₃O₄.^[89-90]

As all atoms are octahedrally coordinated, it may be understood as a rock-salt structure type. When considering Ag/Pb as Na of the NaCl structure and the O atoms as Cl, Ag₂PbO₃ can be seen as a strongly distorted NaCl structure, see Figure 16. This distortion may be attributed to the differing ionic radii of Ag and Pb. Furthermore, the Ag:Pb ratio of 2:1 serves as an additional factor contributing to the structural distortion. A structural analogue, where these factor result in the same space group may be found in Na₂PtO₃.^[91] Table 4 shows the *Polynator* δ -values for the polyhedra associated with the respective central atom.^[81] For comparison, the δ -values for an octahedron as well as the smallest δ -values

observed for the most suitable polyhedron types are also provided. Both AgO_6 polyhedra show the most significant deviation from an ideal octahedron. This may be attributed to the larger ionic radius of Ag^+ compared to Pb^{4+} , which is also reflected in the corresponding bond lengths of Ag-O and Pb-O.

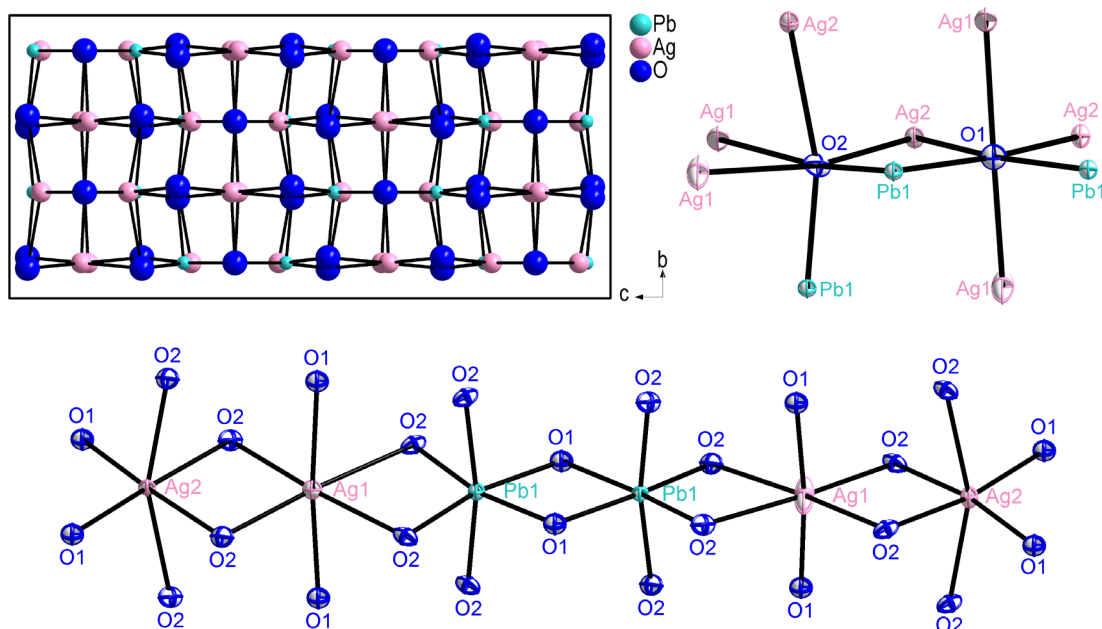


Figure 15. Unit cell of the crystal structure of Ag_2PbO_3 viewed along the a -axis (above left), arrangement of the OM_6 octahedra (above right) and arrangement of the distorted MO_6 octahedra along the a -axis (below) with $M = \text{Ag, Pb}$. The thermal ellipsoids are depicted with a probability of 70%.

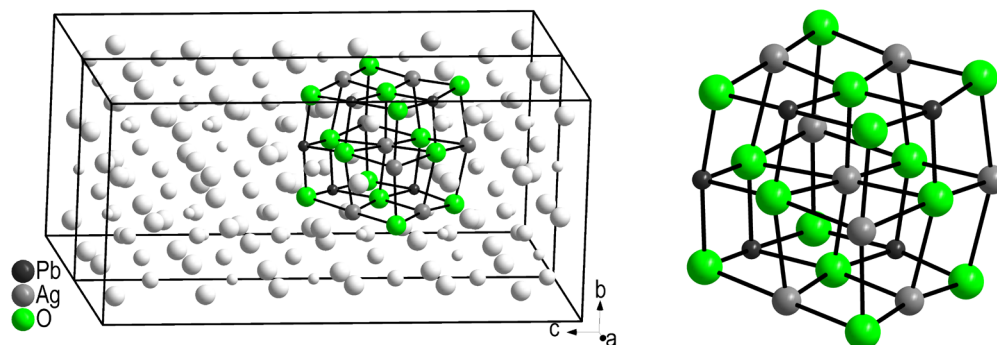


Figure 16. Visualization of the distorted rock-salt structure type in Ag_2PbO_3 , considering Ag/Pb (grey/black) as Na and the O (green) atoms as Cl of the NaCl structure.

Table 4. *Polynator* δ -values for the polyhedra associated with the respective atoms in Ag_2PbO_3 with δ -values for an octahedron as well as the smallest δ -values observed for each atom and polyhedron type.^[81]

Central atom	δ -value for octahedron	Smallest δ -value, polyhedron
Ag1	11.582	5.424, twisted trigonal prism
Ag2	13.527	9.765, rectangular bipyramid
Pb1	10.612	3.572, twisted trigonal prism
O1	8.509	7.273, twisted trigonal prism
O2	6.785	5.677, didigonal scalenohedron

Since the reaction leads to by-products as elemental Ag which was confirmed by P-XRD, a synthesis was carried out starting from a stoichiometric mixture of freshly precipitated Ag_2O and PbO_2 , see experimental chapter 6.2.2 and equation 3. With the help of the new synthesis route, an X-ray crystallographically phase pure sample could be obtained. Further characterization, including *Rietveld* refinement and XPS, was performed.

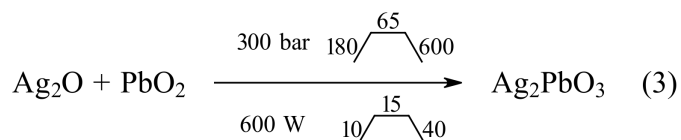


Figure 17 shows the P-XRD data and *Rietveld* refinement pattern of Ag_2PbO_3 which confirms the X-ray crystallographically phase purity. For the refinement, the cell parameters and the equivalent isotropic displacement parameters were refined freely. The lattice parameters and refinement factors are shown in Table 25 in the Appendix.

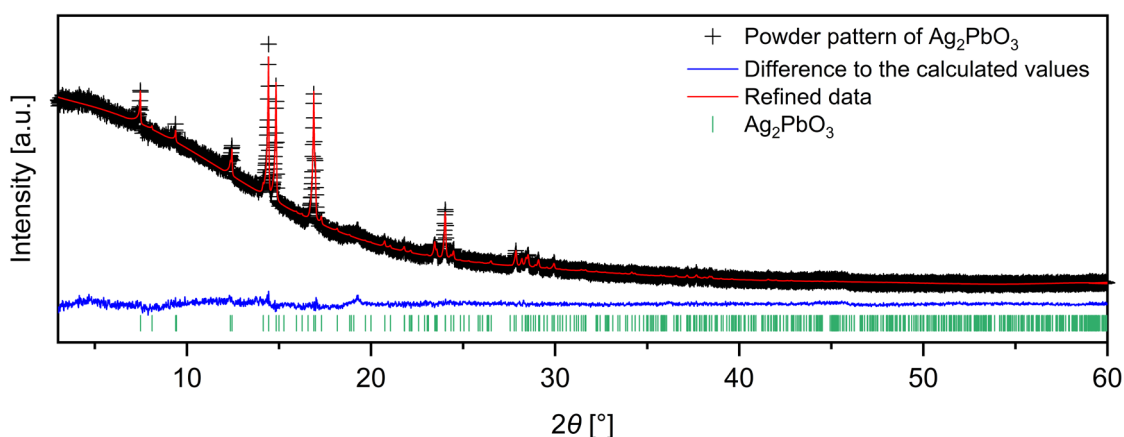
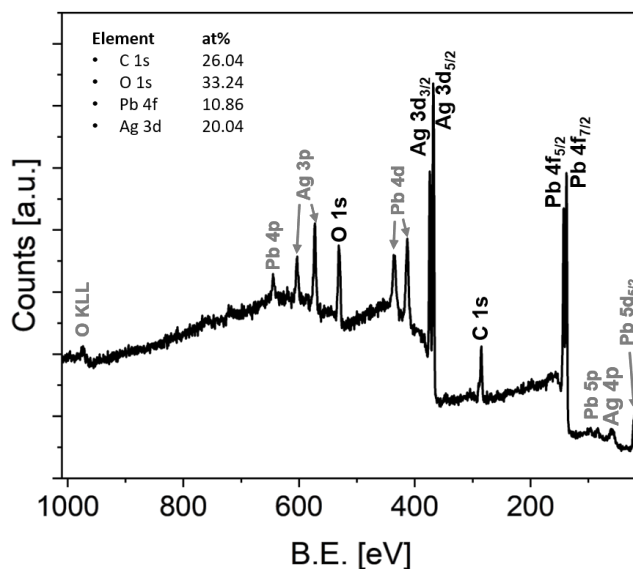
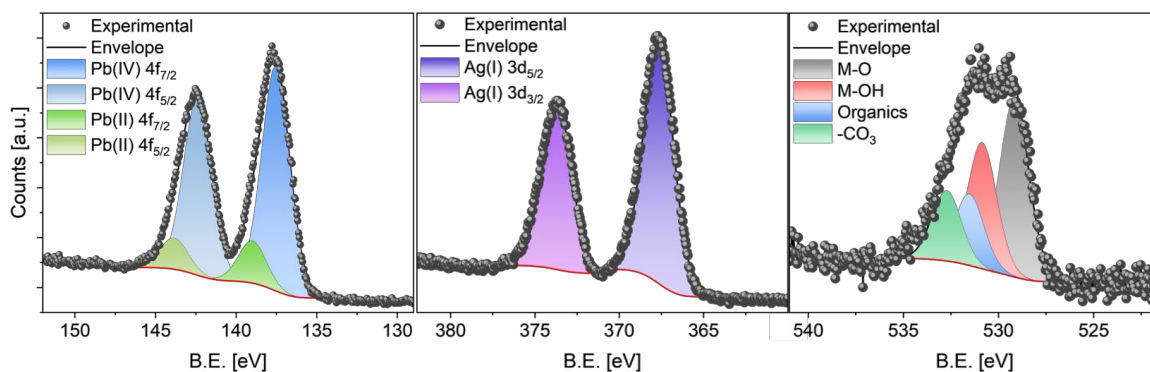


Figure 17. Powder X-ray data measured with Mo- $\text{K}\alpha_1$ radiation and *Rietveld* refinement patterns of Ag_2PbO_3 .

With the help of this sample XPS data could be obtained. Figure 18 and Figure 19 depict the XPS survey spectrum and the Pb 4f, Ag 3d and O 1s XPS core level spectra of Ag_2PbO_3 . The survey spectrum of Ag_2PbO_3 shows that no traces of impurity elements can be detected and exhibits the expected signals of silver, lead and oxygen. The elemental composition of Ag_2PbO_3 can be confirmed by the core level spectra, see Figure 19. The element ratio from overall atomic distribution is 2:0.9:2.9 for Ag:Pb:O. The deviation from the ideal 2:1:3 stoichiometry may be attributed to the partial reduction of lead(IV) oxide, resulting in the formation of a carbonate species. The observed carbon can be attributed to adventitious carbon originating from environmental substances absorbed on the surface of the sample. Additionally, carbonate contamination is commonly known to occur due to the reduction of certain metal oxides upon exposure to CO_2 in the atmosphere.^[92-93]

Figure 18. XPS survey spectrum of Ag_2PbO_3 .Figure 19. Pb 4f, Ag 3d and O 1s XPS core level spectra of Ag_2PbO_3 .

The Pb 4f spectrum shows the typical doublet split between Pb 4f_{7/2} and Pb 4f_{5/2} at 4.86 eV and confirms small amounts of reduced lead(II) (< 2%), due to the reduction to metal carbonate. The minor phase of lead shows the expected oxidation state +IV. The Ag 3d spectrum shows silver in the oxidation state +I. As expected, four different types of oxygen are visible in the O 1s spectrum, i.e. lattice-bound oxygen (M-O), hydroxide groups on the surface (M-OH), C-OR groups and carbonate (CO_3).^[92-93] For a further characterization, magnetization measurements could be considered which would verify diamagnetism.

4.3.2 Further Synthesis Attempts in the Multi Anvil Press

Building on the successful synthesis of Ag_2PbO_3 from the multi anvil press, further experiments were conducted to synthesize new ternary and quaternary oxygen-containing compounds using this high pressure technique.

Since the previous research from other extreme conditions led to the synthesis of a few new rhenium compounds, a significant part of the experiments conducted in the multi anvil press focused on the synthesis of novel rhenium compounds. Attempts were made to obtain ternary and quaternary silver/rhenium compounds, such as “ Ag_2ReO_4 ”, “ $\text{Ag}_2\text{ReO}_4\text{Cl}$ ” and similar compounds. Table 5 shows selected experiments which were conducted in the multi anvil press. It seems reasonable to first conduct experiments starting only with $\text{Ag}[\text{ReO}_4]$, as perrhenate can also have a high pressure modification. For this, $\text{Ag}[\text{ReO}_4]$ was heated with an oil pressure of 400 bar by applying 300 W, but no reaction occurred, see P-XRD pattern in Figure 32 in the Appendix.

Since $\text{Ag}_2[\text{MnO}_4]$ has already been characterized using SC-XRD, the synthesis of “ $\text{Ag}_2[\text{ReO}_4]$ ” using the multi anvil press can also be explored.^[94] For this purpose, ReO_3 and Ag_2O were weighed stoichiometrically, finely ground and subsequently pressed with an oil pressure of 500 bar with a power of 400 W. However, the expected reaction did not occur. Instead, a mixture of $\text{Ag}[\text{ReO}_4]$, ReO_2 and Ag was formed. The corresponding P-XRD pattern is shown in Figure 20.

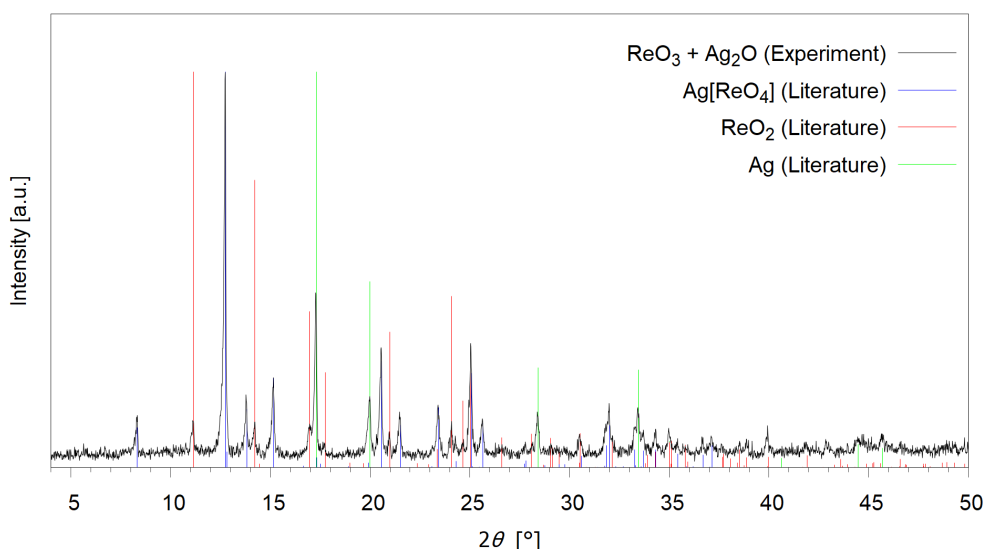


Figure 20. Powder X-ray data of the experiment of heating ReO_3 and Ag_2O in the multi anvil press measured with $\text{Mo-K}\alpha_1$ radiation and literature data.^[95-97]

When Ag_2O and $\text{Ag}[\text{ReO}_4]$ are reacted in the press, $\text{Ag}[\text{ReO}_4]$ does not undergo any reaction, whereas Ag_2O decomposes to form Ag , see P-XRD pattern in Figure 33 in the Appendix. It cannot be excluded that an unstable intermediate product forms initially and then decomposes. However, previous observations suggest that $\text{Ag}[\text{ReO}_4]$ is thermodynamically stable and often remains unreactive.

Table 5. Conducted multi anvil press experiments.

Starting materials	Power [W]	Oil pressure [bar]	Pressure program [min]		
			\nearrow	\rightarrow	\searrow
Ag[ReO ₄]	300	400	300	65	600
ReO ₃ + Ag ₂ O	400	500	300	65	600
Ag[ReO ₄] + Ag ₂ O	250	400	300	65	600
Re ₂ O ₇ + Ag ₂ O + 2 AgCl	250	400	300	65	600
H ₃ BO ₃ + 2 K ₂ S ₂ O ₇	400	600	180	65	540
Ag ₂ O + SnO ₂	300	900	180	65	600
Cu ₂ O + PbO ₂	300	300	180	65	600

Since no single crystal structures of silver oxychlorides containing 7d elements are known, an attempt was also made to react Re₂O₇, Ag₂O and AgCl. Although Re₂O₇ underwent a reaction, no new quaternary compound was formed. Instead, a reduction to ReO₂, as well as a reaction to form Ag[ReO₄], was observed. This once again highlights the high stability of Ag[ReO₄], see Figure 21 for the corresponding P-XRD pattern. It has not yet been determined how the reduction occurred, as none of the starting materials were oxidized. However, it is known that the parts used for the octahedron can participate in the reaction, which could provide an explanation for the reduction.

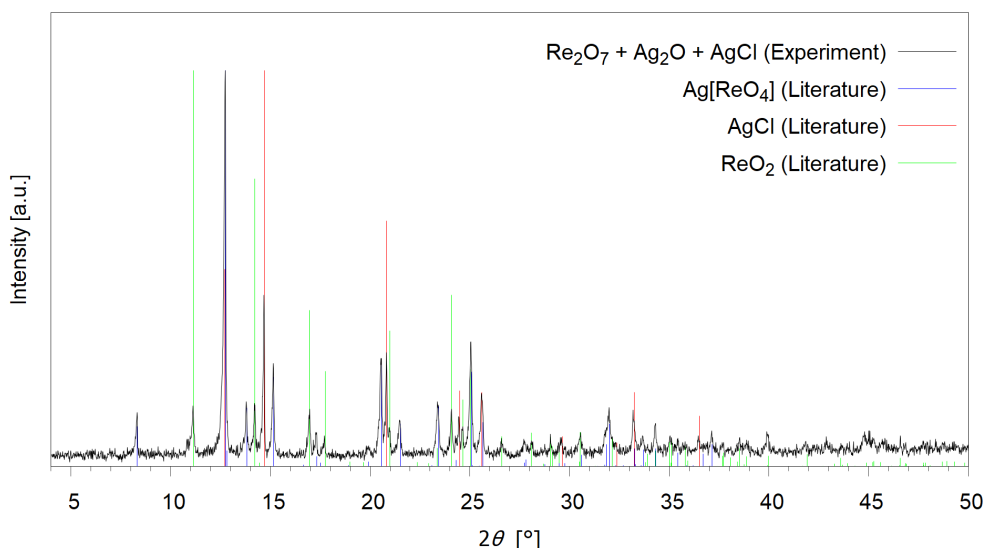


Figure 21. Powder X-ray data of the experiment of heating Re₂O₇, Ag₂O and AgCl in the multi anvil press measured with Mo-K α_1 radiation and literature data.^[96-98]

Huppertz et al. have described that the synthesis of new borates, such as Tb₃B₁₀O₁₇(OH)₅ and Sc₃B₅O₁₂, is possible under high pressure conditions using the multi anvil press.^[69-70] Since the synthesis of new borosulfates under extreme SO₃ conditions has been established within the Wickleder group, the question arises whether borosulfates, similar to borates, can also be synthesized using the multi anvil press.^[99-100]

To investigate this, experiments were conducted by reacting boric acid with various sulfur sources in the press. A mixture of H_3BO_3 and $\text{K}_2\text{S}_2\text{O}_8$ in the press did not yield a borosulfate. Nevertheless, the literature describes that $\text{K}[\text{B}(\text{SO}_4)_2]$ can be obtained by reacting $\text{K}[\text{B}(\text{S}_2\text{O}_7)_2]$ in oleum.^[101] Therefore, another similar synthesis using the multi anvil press was carried out using H_3BO_3 and two equivalents $\text{K}_2\text{S}_2\text{O}_7$, resulting in the formation of $\text{K}[\text{B}(\text{SO}_4)_2]$, $\text{K}_3\text{H}(\text{SO}_4)_2$ and KHSO_4 . The corresponding P-XRD pattern and the *Rietveld* refinement is presented in Figure 22. The refinement factors are shown in Table 26 in the Appendix. The *Rietveld* refinement is of limited quality due to a high background in the P-XRD pattern. However, it still provides first insight into the composition of the product mixture.

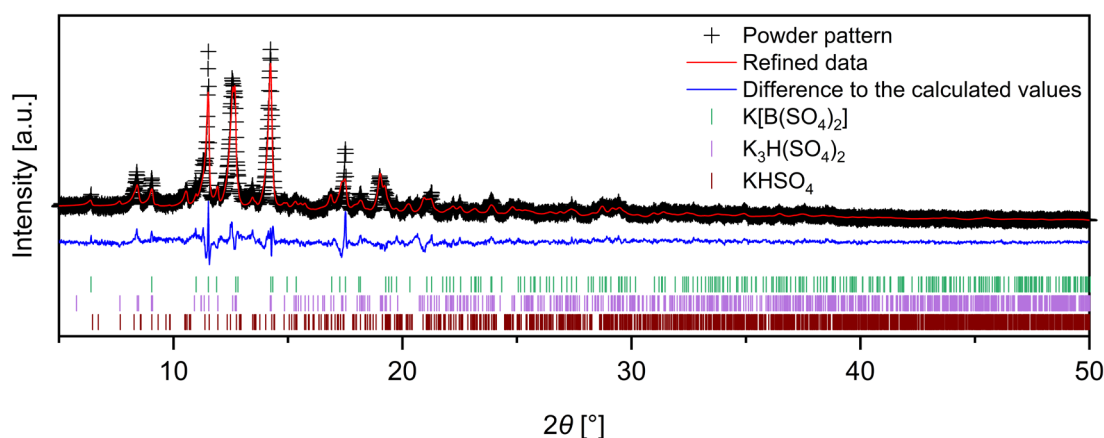


Figure 22. Powder X-ray data measured with Mo- $\text{K}\alpha_1$ radiation and *Rietveld* refinement pattern of the product mixture from the multi anvil experiment with H_3BO_3 and $\text{K}_2\text{S}_2\text{O}_7$.

These findings suggest that by varying the starting materials and optimizing the reaction parameters, it will be possible to synthesize new borosulfates using the multi anvil press.

In addition to experiments aimed at synthesizing novel rhenium-containing oxides or new borosulfates, further experiments were conducted building on the successful synthesis of Ag_2PbO_3 , see chapter 4.3.1. Instead of Ag_2O and PbO_2 , Cu_2O and PbO_2 were used in an attempt to synthesize the analogous product “ Cu_2PbO_3 ”. However, the outcoming product could not be analyzed via P-XRD, as the diffraction pattern showed that the product is amorphous. Increasing the heating power could potentially resolve this problem, as experience has shown that products synthesized at higher temperatures often exhibit higher crystallinity. Additionally, Ag_2O and SnO_2 were reacted, but this resulted in the formation of Ag with SnO_2 remaining unreacted, see Figure 34 for the P-XRD pattern in the Appendix. Further experiments using the multi anvil press could result in the formation of homologues of Ag_2PbO_3 . The method is promising and continues to demonstrate significant potential for the discovery of novel high pressure compounds.

4.4 Intermediates During Ethylene Oxide Catalysis

Ethylene oxide is a key industrial chemical made through the gas phase oxidation of ethylene using oxygen and a silver-based catalyst on an Al_2O_3 support, see chapter 2.4. In 2021, the EO market reached a volume of 30.7 million tons.^[102] Commercial EO catalysts also include alkali and transition metal promoters, such as Li, Cs and Re, to enhance selectivity, activity and lifetime.^[60-61] The production of EO catalysts typically involves vacuum impregnation of a silver complex solution on the Al_2O_3 support, followed by thermal treatment.^[58] Silver solutions with ethylenediamine and oxalic acid have been used for decades, though excessive solubility can lead to unwanted crystal formation, reducing production efficiency.^[65]

Karpov, Jansen et al. investigated the nature of crystals precipitating from aqueous silver ethylenediamine oxalate solutions, which are used for producing supported EO catalysts.^[65] They identified a crystalline compound, i.e. $[\text{Ag}(\mu\text{-en})]_2(\text{C}_2\text{O}_4) \cdot 2 \text{H}_2\text{O}$, where silver atoms are bridged by ethylenediamine ligands, forming one-dimensional chains.^[65] The oxalate groups act as counterions without directly coordinating to the silver atoms, while weak interactions with lattice water molecules slightly distort the silver-nitrogen bonds. Thermal analysis shows that the compound decomposes endothermically between 130-160°C, resulting in metallic silver.^[65] The characteristics of the compound make it ideal as a starting material for catalyst production and offer useful insights for the industrial use.

This chapter discusses the crystal formation in ethylenediamine solutions which are used for the catalyst preparation similar to *Karpov* and *Jansen*.^[65] Besides the discussion of two novel compounds which can occur during the preparation of the EO catalyst, the work focuses on the key characteristics of the EO catalyst currently employed by BASF. Furthermore, it explores various attempts to synthesize novel oxidic compounds that could serve as alternative candidates for catalyst preparation or potentially form during the catalyst production. In this context, solid state reactions from high pressure O_2 syntheses are discussed.

4.4.1 Characterization of Laboratory Model EO Catalytic Samples and Intermediates

The first step for obtaining more information about the EO catalyst is to characterize fresh and spent catalyst samples. For this purpose, P-XRD measurements of laboratory model samples provided by BASF, available according to Patent EP3749450B1^[58], were carried out. The diffractograms and *Rietveld* refinements of fresh and spent catalyst samples were analyzed. In addition to the P-XRD data, EDX data and magnetization data were measured for both samples. Since these results are subject to a confidentiality agreement, the corresponding figures and analyses have not been included here.

Given the possibility that various ternary and quaternary oxide compounds may form during the production of the EO catalyst, solid state reactions appeared to be a reasonable approach for further investigation of the EO catalyst. Pure O₂ is introduced in the industrial production of EO leading to a significant increase in selectivity. Nevertheless, potential side reactions of the EO catalyst with O₂ cannot be excluded and need to be investigated. Therefore, solid state syntheses under O₂ high pressures were carried out to obtain possible intermediates or to identify side phases, see also experimental chapter 6.2.4. Table 6 lists selected experiments which were conducted in high pressure O₂ autoclaves. A selection of rhenium and silver compounds were reacted with each other, as both Ag and Re have a significant influence on catalytic activity.

Table 6. Selected O₂ high pressure experiments with information about starting materials, O₂ volume, temperatures and products.

No.	Starting materials		O ₂ [ml]*	T [°C]	Products	
	A	B			A	B
1	1 eq Re	3 eq Ag ₂ O	11.2	300	Ag[ReO ₄]	Ag ₂ O
2	1 eq ReO ₃	4 eq Ag ₂ O	11.2	300	Ag[ReO ₄]	Ag ₂ O
3	1 eq ReO ₃	4 eq Ag ₂ O	8.0	600	Ag[ReO ₄]	Ag ₂ O
4	1 eq ReO ₃	2 eq AgCl	5.0	400	Ag[ReO ₄]	AgCl
5	1 eq Ag[ReO ₄]	1 eq Ag	8.0	550	Ag[ReO ₄]	unknown phase
6	1 eq Ag[ReO ₄]	5 eq Ag ₂ O	8.0	500	Ag[ReO ₄]	Ag ₂ O

*11.2 ml O₂ at 300°C corresponds to about 2400 bar, 8.0 ml O₂ at 600°C corresponds to about 1800 bar and 5.0 ml O₂ at 400°C corresponds to about 620 bar pressure.

Compared to manganese chemistry, fewer ternary or quaternary rhenium compounds are known. Since both can exhibit similar chemistry, previously known manganese compounds can serve as references for synthesis attempts with rhenium.

Several ternary silver-manganese compounds have already been characterized with SC-XRD.^[94, 103-104] One example is Ag_2MnO_4 , which was obtained from an aqueous solution.^[94] Another compound, e.g. $\text{Ag}_4\text{Mn}_3\text{O}_8$, was successfully synthesized using an O_2 high pressure autoclave by *Jansen et al.*^[103] Additionally, a modification of $\text{AgMn}_7\text{O}_{12}$ was obtained under high pressure and high temperature conditions.^[104] Therefore, it seems reasonable to conduct similar experiments with rhenium compounds.

If the individual experiments are now considered, the reaction of elemental rhenium with 3 eq of Ag_2O at 300°C under an O_2 pressure of approximately 3800 bar can be examined first, as represented by experiment No. 1 in Table 6. The associated P-XRD pattern is shown in Figure 35 in the Appendix. $\text{Ag}[\text{ReO}_4]$ and Ag_2O can be identified in the product mixture, while an additional minor phase is also present that cannot be assigned based on literature data. The addition of two drops of H_2O or a KOH solution as mineralizers, a common O_2 high pressure approach in crystallization, does not lead to the formation of a new phase as single crystals.

It is conceivable to obtain a product with the composition “ $\text{Ag}_2[\text{ReO}_4]$ ”, as reactions conducted under high O_2 pressures do not necessarily lead to the oxidation of the transition metal.^[103] To achieve this, ReO_3 was reacted with Ag_2O in an O_2 high pressure atmosphere. In Table 6, the reaction of ReO_3 with 4 eq Ag_2O is presented, corresponding to experiment No. 2. Additional experiments were conducted using 1.5 eq and 3 eq of Ag_2O . All reactions yielded the same product mixture, consisting of $\text{Ag}[\text{ReO}_4]$ and Ag_2O , as shown in the P-XRD pattern in Figure 23. Furthermore, a minor additional phase is observed again, which cannot be assigned based on literature data. Similar to the reaction of elemental Re with Ag_2O , no single crystals suitable for SC-XRD analysis could be obtained. Using higher temperatures, i.e. 600°C in experiment No. 3, also yielded the same product mixture, see Figure 36 in the Appendix.

A literature search revealed that no single crystal structures of quaternary silver oxychlorides containing 7d elements are known and it is conceivable that silver rhenium oxychlorides may also play a role as intermediates or side products in the synthesis of the EO catalyst. Therefore, it appears reasonable to investigate the reaction of 1 eq ReO_3 with 2 eq AgCl under high pressure O_2 conditions. However, this experiment once again resulted in the formation of $\text{Ag}[\text{ReO}_4]$ along with unreacted AgCl , as shown in Figure 37 in the Appendix.

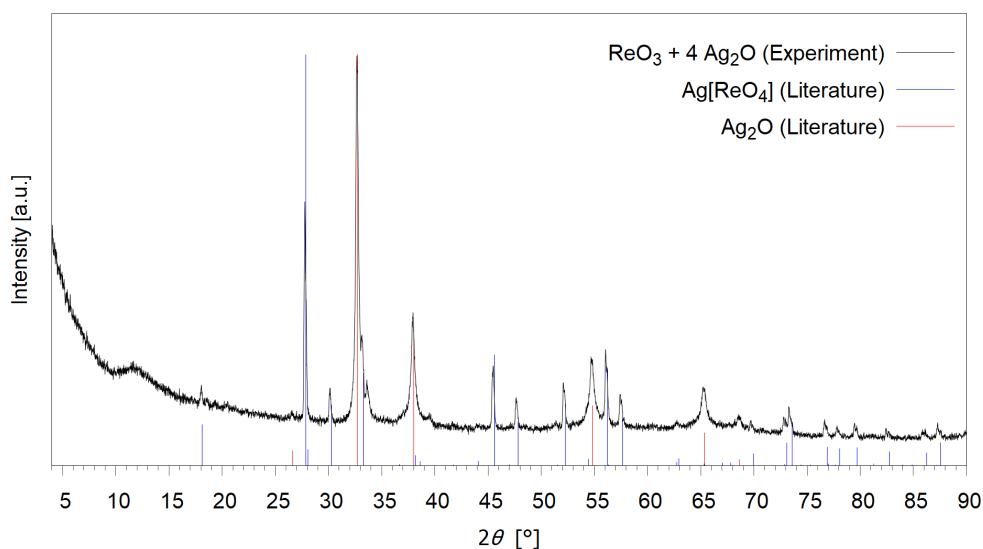


Figure 23. Powder X-ray data of the O₂ high pressure experiment No. 2 of combining 1 eq ReO₃ with 4 eq Ag₂O at 300°C measured with Mo-K α_1 radiation and literature data.^[96, 105]

Starting from Ag[ReO₄], reactions were conducted with elemental Ag (experiment No. 5) and, in a separate experiment, with Ag₂O (experiment No. 6). In both cases, the P-XRD patterns reveal the presence of Ag[ReO₄], as shown in Figure 38 and Figure 39 in the Appendix. However, when using elemental Ag, an additional different unidentified phase is observed. Unfortunately, no single crystals could be obtained and therefore, further investigation of this reaction would be of great interest, potentially leading to the isolation of single crystals for SC-XRD analysis.

All in all, Ag[ReO₄]₄ is consistently formed as a reaction product. Regardless of whether the starting material is elemental rhenium, ReO₃ or Ag[ReO₄], silver perrhenate is obtained with rhenium in the +VII oxidation state. In comparison, Ag₄Mn₃O₈, for example could be synthesized from Ag₂O and MnO₂ in an O₂ autoclave without any oxidation of the transition metals occurring.^[103] However, manganese stabilizes lower oxidation states due to ligand-field effects, while rhenium is more readily oxidized to Re +VII due to its higher oxidation potential.

In addition to synthesizing novel oxides that may form during EO production from solid state reactions using O₂ high pressures, as well as analyzing both fresh and spent catalyst samples, systematic studies were conducted on various combinations of promoter solutions involved in the catalyst production process. These combinations were analyzed and reacted under varying conditions of pH, temperature and concentration. The focus therefore relied on the use of Ag, Re and Cs containing compounds.

Karpov, Jansen et al. already investigated a crystalline compound, i.e. $[\text{Ag}(\mu\text{-en})]_2(\text{C}_2\text{O}_4) \cdot 2 \text{H}_2\text{O}$, where silver atoms are bridged by ethylenediamine ligands, forming one-dimensional chains.^[65] This compound may occur during the production of the EO catalyst and gives insights into the production process. $[\text{Ag}(\mu\text{-en})]_2(\text{C}_2\text{O}_4) \cdot 2 \text{H}_2\text{O}$ is obtained from a solution of Ag_2O , *en* and $\text{C}_2\text{H}_2\text{O}_4 \cdot 2 \text{H}_2\text{O}$.

Since Cs plays an important role in EO catalysis and is added in the form of CsOH during catalyst production^[58], it seems reasonable to perform an analogous approach with CsOH, *en* and $\text{C}_2\text{H}_2\text{O}_4 \cdot 2 \text{H}_2\text{O}$ to obtain the analogous product “ $[\text{Cs}(\mu\text{-en})]_2(\text{C}_2\text{O}_4) \cdot 2 \text{H}_2\text{O}$ ”. Unfortunately, no crystallization occurred and the further analysis was not possible yet. Nevertheless, the solution could also further be used for a combination with $\text{NH}_4[\text{ReO}_4]$ and $\text{Cs}[\text{ReO}_4]$ respectively. Solutions of $\text{NH}_4[\text{ReO}_4]$ are commonly used as promoters in the EO production process. Both mixtures led to a precipitation of a colorless compound which could be identified as $\text{Cs}[\text{ReO}_4]$ as shown in the P-XRD pattern in Figure 40 and Figure 41 in the Appendix.

Although no novel oxides were obtained, the findings nevertheless indicate that perrhenates, particularly $\text{Ag}[\text{ReO}_4]$ and $\text{Cs}[\text{ReO}_4]$, exhibit high stability, as confirmed by experiments conducted in high pressure O_2 autoclaves and approaches involving the combination of promoter solutions.

In addition to the previously mentioned attempts at synthesizing new intermediates, two further approaches using promoter solutions were conducted. These are presented separately in the following two chapters 4.4.2 and 4.4.3, as they resulted novel single crystal structures and were partially published.

4.4.2 $[\text{Ag}(\mu\text{-en})][\text{ReO}_4]$ Intermediate During Catalysis (Publication 6)

The preparation of a catalyst for EO production involves impregnating a porous Al_2O_3 support with a silver ethylenediamine oxalate solution, including $\text{NH}_4[\text{ReO}_4]$. From this mixture, the title compound $[\text{Ag}(\mu\text{-en})][\text{ReO}_4]$ precipitates. Structural analysis showed that the $[\text{Ag}(\mu\text{-en})]^+$ unit is similar to that in $[\text{Ag}(\mu\text{-en})]_2(\text{C}_2\text{O}_4) \cdot 2 \text{H}_2\text{O}$ ^[65], with Ag coordinating to N atoms of the *en* ligands. The $[\text{ReO}_4]^-$ anions form hydrogen bonds with *en* rather than silver. The thermal decompositions of both compounds begin at similar temperatures.^[65] $[\text{Ag}(\mu\text{-en})][\text{ReO}_4]$ decomposes to elemental Ag, in analogy with industrial processes for Re-promoted catalysts.

Publication 6

$[\text{Ag}(\mu\text{-en})][\text{ReO}_4]$: An Intermediate during Preparation of the Ethylene Epoxidation Catalyst

D. Badea, A. Karpov, M. Jansen and J. Bruns*

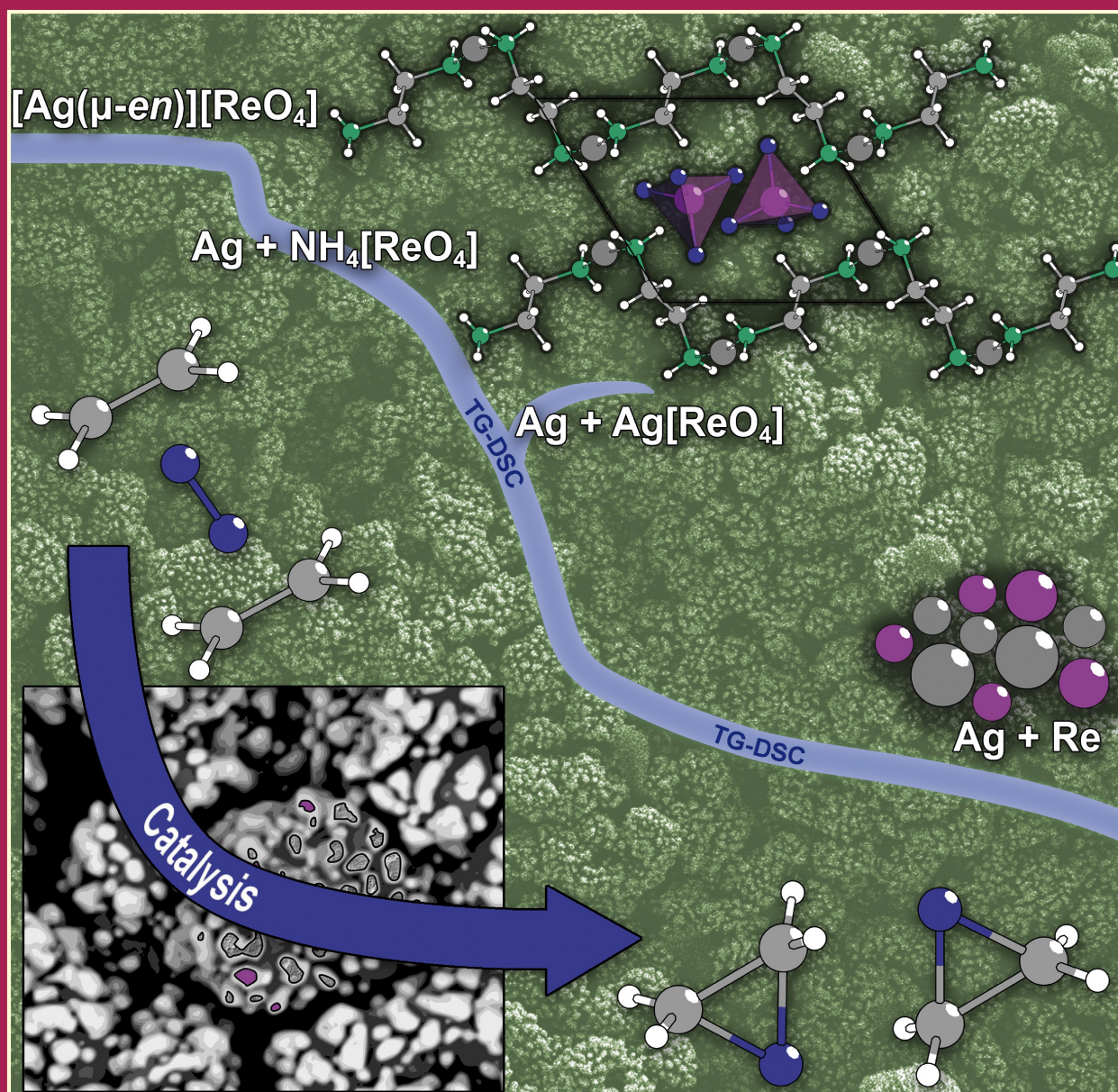
Z. Anorg. Allg. Chem. **2022**, e202200267.

doi.org/10.1002/zaac.202200267

Explanation of the personal contribution to the previously mentioned publication:

The experiments were carried out by Désirée Badea. The first author synthesized the analyzed product, performed the characterization experiments, evaluated the collected data and prepared the corresponding plots for publication, unless otherwise noted below. Thermal analysis was conducted by Dr. Christian Tobeck. Désirée Badea prepared the draft of the manuscript with support of the co-authors. Supporting information is provided in the Appendix on page 155.

2022
648/23



Cover Feature: $[\text{Ag}(\mu\text{-en})][\text{ReO}_4]$: An Intermediate during Preparation of the Ethylene Epoxidation Catalyst

Désirée Badea, Andrey Karpov, Martin Jansen and Jörn Bruns

DOI: 10.1002/zaac.202200267

[Ag(μ -en)][ReO₄]: An Intermediate during Preparation of the Ethylene Epoxidation Catalyst

Désirée Badea,^[a] Andrey Karpov,^{*,[b]} Martin Jansen,^{*,[a, c]} and Jörn Bruns^{*,[a]}

Dedicated to Professor Thomas Schleid on the Occasion of his 65th Birthday

Preparation of a catalyst for the ethylene oxide production requires impregnation of a porous corundum support with an aqueous silver ethylene diamine oxalate complex solution, to which among others NH₄[ReO₄] is added. Here we report on [Ag(μ -en)][ReO₄] that precipitates from such a mixture. Single crystal structure analysis has revealed a striking similarity of the [Ag(μ -en)]⁺ entity with the same complex cation encountered in

[Ag(μ -en)]₂(C₂O₄) \times 2H₂O. Silver is coordinated end-on to the nitrogen atoms of the *en* ligands. The [ReO₄][−] anions are not bonded to the silver cations, but instead involved in N–H \cdots O

hydrogen bonds to the ethylene diamine molecules. The first step of thermal degradation occurs at approximately the same temperature for both, the main component precipitate [Ag(μ -en)]₂(C₂O₄) \times 2H₂O and [Ag(μ -en)][ReO₄], warranting proximity of the rhenium promoter and the elemental silver deposit. At 300 °C, the temperature at which the catalyst for EO synthesis is commonly calcined, the decomposition product of plain [Ag(μ -en)][ReO₄] under synthetic air is Ag[ReO₄], in full analogy to industrial manufacturing process for selected Re-promoted EO catalyst formulations.

Introduction

Optimizing heterogeneous catalysts is of key relevance for improving the economic performance and environmental footprint of many large-scale industrial production processes. This task, however, is posing quite demanding challenges since various stages need to be considered, from preparing and conditioning the catalyst to finally controlling and understanding it “in operando”. A particular intricacy results from the commonly multi-component nature of such catalyst systems, which leads to a combinatorial explosion of the parameter space to be examined in research and development. Prototypi-

cally, this holds true for the catalyst used for producing ethylene oxide (EO), a major intermediate in fine-chemical production lines, by gas phase oxidation of ethylene with oxygen. Here, a silver catalyst deposited on a porous α -Al₂O₃ support (EO catalyst) is employed.^[1] In addition to submicron sized silver plaquettes as the main catalytically active ingredient, combinations of alkali and transition metal compounds containing e.g. Li, Cs, Re, W, Mo, or Mn in concentration ranges of 100–1000 ppmw are incorporated as promoters, boosting product yields and catalyst selectivity.^[2]

The basic process of manufacturing an EO catalyst consists of vacuum impregnation of the α -Al₂O₃ support with an Ag complex solution (Ag-CS), followed by drying and thermal decomposition of the organic components.^[2] An aqueous complex solution of silver with ethylenediamine (*en*) and oxalic acid is the most widely applied silver precursor, to date.^[2c] The promoter additives are dissolved in the pristine Ag-CS. Since even small pieces of firm knowledge of the complex catalyst system may help to reduce the degrees of freedom to be addressed in its optimization, we aim at identifying configuration and thermal decomposition behavior of the solid phases that populate the α -Al₂O₃ support after removing the solvent, i.e. before starting pyrolysis. As a first result, it was established that from plain Ag-CS crystalline [Ag(μ -en)]₂(C₂O₄) \times 2H₂O precipitates, which decomposes to elemental silver already at about 150 °C.^[3]

Here, we report the results of a single-crystal structure analysis of crystals precipitated from Ag *en* oxalate complex solution after adding NH₄[ReO₄] in the same way as applied in preparing the Ag-CS for impregnation of the α -Al₂O₃ support. The crystal structure analysis has revealed the composition as [Ag(μ -en)][ReO₄]. DSC/TG analyses show that the first step of

[a] D. Badea, Prof. Dr. M. Jansen, Dr. J. Bruns
University of Cologne
Institute of Inorganic Chemistry
Greinstr. 6, 50939 Cologne, Germany
E-mail: j.bruns@uni-koeln.de
m.jansen@fkf.mpg.de

[b] Dr. A. Karpov
BASF SE, Catalysis Research
Carl-Bosch-Street 38, 67059
Ludwigshafen, Germany
E-mail: andrey.karpov@basf.com

[c] Prof. Dr. M. Jansen
Max Planck Institute for Solid State Research
Heisenbergstr. 1, 70569
Stuttgart, Germany

Supporting information for this article is available on the WWW under <https://doi.org/10.1002/zaac.202200267>

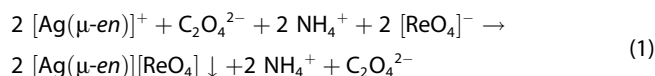
© 2022 The Authors. Zeitschrift für anorganische und allgemeine Chemie published by Wiley-VCH GmbH. This is an open access article under the terms of the Creative Commons Attribution License, which permits use, distribution and reproduction in any medium, provided the original work is properly cited.

thermal decomposition occurs at approximately the same temperature for the perrhenate and the respective oxalate.

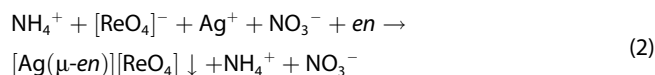
Results and Discussion

Synthesis

Synthesis and crystal growth of $[\text{Ag}(\mu\text{-en})][\text{ReO}_4]$ was achieved by precipitation from combined aqueous solutions of Ag-CS and $\text{NH}_4[\text{ReO}_4]$ (see equation (1)). This procedure corresponds to the preparation of an aqueous complex solution for impregnation of an $\alpha\text{-Al}_2\text{O}_3$ support for EO catalysis.^[3]



Alternatively, the title compound can be prepared from $\text{NH}_4[\text{ReO}_4]$, AgNO_3 and *en* according to equation (2).



Crystal Structure Analysis

Single crystals of the title compound were grown from an aqueous solution as described by reaction (1). $[\text{Ag}(\mu\text{-en})][\text{ReO}_4]$ appears as block shaped crystals, see Figure S1 in the Supporting Information. The investigated crystal had a size of about $0.03 \times 0.02 \times 0.01 \text{ mm}^3$. The sample is stable in contact with air, but decomposes when exposed to light. Therefore, storage in the dark is required.

$[\text{Ag}(\mu\text{-en})][\text{ReO}_4]$ crystallizes in space group $P\bar{1}$ with cell parameters of $a=7.4566(7) \text{ \AA}$, $b=8.1260(6) \text{ \AA}$, $c=8.1597(7) \text{ \AA}$, $\alpha=117.306(3)^\circ$, $\beta=115.322(3)^\circ$, $\gamma=93.114(3)^\circ$, $V=377.30(6) \text{ \AA}^3$ and $Z=2$, see Figures 1 and 2 for presentations of the crystal structure, crystallographic and structural details are given in Table 1 and Tables S1–S4. The asymmetric unit includes one Ag atom, which is coordinated end-on by two *en* molecules. Each of the two ligands is bridging to adjacent silver atoms, which results in a zig-zag type one dimensional $\text{Ag}(\mu\text{-en})$ arrangement extending along $[110]$, see Figure 2. Noteworthy, the N–Ag–N angle deviates significantly from linearity amounting to $168.8(1)^\circ$ which is probably caused by the contact with perrhenate anions, see Table S4. A similar zig-zag like arrangement has been observed for the oxalate species $[\text{Ag}(\mu\text{-en})]_2(\text{C}_2\text{O}_4) \times 2\text{H}_2\text{O}$.^[3]

The Re–O distances fall into the narrow range of $1.723(3)$ to $1.735(3) \text{ \AA}$ and correspond to $1.720(5)$ and $1.723(4) \text{ \AA}$ as reported for $\text{NH}_4[\text{ReO}_4]$ and $\text{K}[\text{ReO}_4]$, respectively.^[4] The shortest Ag–Ag distance of $3.2484(6) \text{ \AA}$ is close to the sum of the van der Waals radii of the element.^[5] The Ag–N distances amount to $2.134(3)$ and $2.141(3) \text{ \AA}$, whereas the shortest Ag–O distance is as wide as 2.8 \AA .

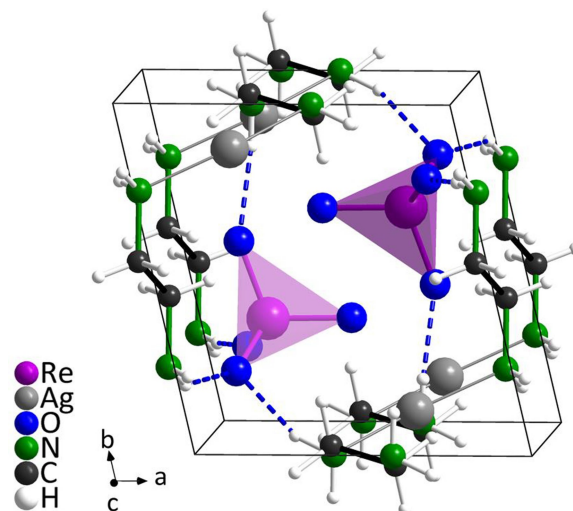


Figure 1. Crystal structure of $[\text{Ag}(\mu\text{-en})][\text{ReO}_4]$, N–H...O hydrogen bonding is indicated by dashed lines.

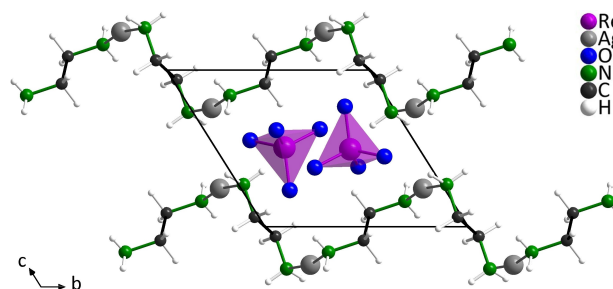


Figure 2. Crystal structure of $[\text{Ag}(\mu\text{-en})][\text{ReO}_4]$ in projection onto the *bc*-plane.

All hydrogen atoms were freely refined, resulting in O–H bond lengths of 0.9 \AA on average. The (N)–H atoms participate in hydrogen bonding and coordinate to oxygen atoms of the complex $[\text{ReO}_4]^-$ anions. The donor-acceptor distances N(H)–O range from $2.911(5)$ to $3.041(4) \text{ \AA}$. According to Steiner, such hydrogen bonds can be classified as of moderate strength.^[6]

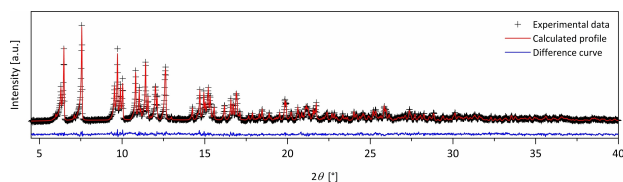
A phase pure bulk sample of $[\text{Ag}(\mu\text{-en})][\text{ReO}_4]$ has been obtained according to the reaction described by equation (2). Phase purity was confirmed by a Rietveld profile refinement of a powder X-ray diffractogram using the data as obtained from the single crystal structure determination as starting parameters, see Figure 3, Table S5 and Table S6.

Thermal analysis (TGA/DSC)

The mass loss during thermal decomposition of the title compound was monitored simultaneously with the heat flow associated (TGA/DSC). The measurements were conducted on a phase pure bulk sample either in a flow of argon or synthetic air. When using argon gas, $[\text{Ag}(\mu\text{-en})][\text{ReO}_4]$ undergoes a multi-step decomposition process which was monitored up to 995°C .

Table 1. Crystal data and structure refinement details for $[\text{Ag}(\mu\text{-en})][\text{ReO}_4]$. The lattice parameters at ambient temperature from a Rietveld profile refinement are given in brackets.

Empirical formula	$\text{C}_2\text{H}_8\text{AgN}_2\text{O}_4\text{Re}$
Formula weight	418.17 g/mol
Temperature	100(2) K
Crystal system	triclinic
Space group	$P\bar{1}$
<i>a</i>	7.4566(7) Å (7.5396(2) Å)
<i>b</i>	8.1260(6) Å (8.2046(2) Å)
<i>c</i>	8.1597(7) Å (8.2128(2) Å)
α	117.306(3)° (116.902(2)°)
β	115.322(3)° (115.557(2)°)
γ	93.114(3)° (93.529(2)°)
<i>V</i>	377.30(6) Å ³ (387.36(3) Å ³)
<i>Z</i>	2
ρ_{calc}	36.81 g/cm ³
μ	18.58 mm ⁻¹
<i>F</i> (000)	376
Crystal size	0.03 × 0.02 × 0.01 mm ³
Radiation	Mo-K α (λ = 0.71073)
2 θ range for data collection	5.94° to 52.14°
Index ranges	−9 ≤ <i>h</i> ≤ 9, −10 ≤ <i>k</i> ≤ 10, −10 ≤ <i>l</i> ≤ 10
Reflections collected	8593
Independent reflections	1472 [<i>R</i> _{int} = 0.0369, <i>R</i> _o = 0.0244]
Data/restraints/parameters	1472/0/124
Goodness-of-fit on <i>F</i> ²	1.069
Final <i>R</i> indexes (<i>I</i> _o ≥ 2 σ (<i>I</i> _o))	<i>R</i> ₁ = 0.0151, <i>wR</i> ₂ = 0.0348
Final <i>R</i> indexes (all data)	<i>R</i> ₁ = 0.0155, <i>wR</i> ₂ = 0.0350
Largest diff. peak/hole	0.57/−0.84 e Å ⁻³
CCDC number	1947598

**Figure 3.** Rietveld fit of the ambient temperature powder diffraction pattern of $[\text{Ag}(\mu\text{-en})][\text{ReO}_4]$.

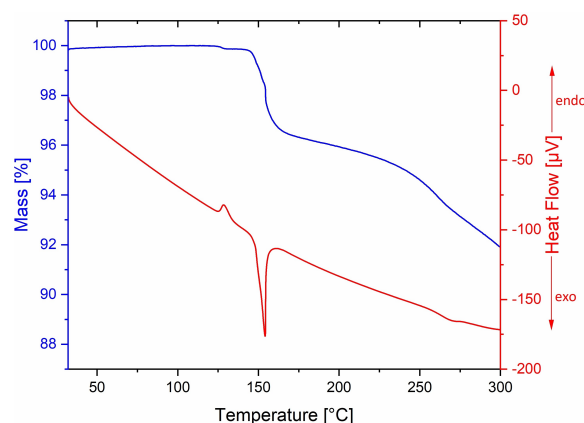
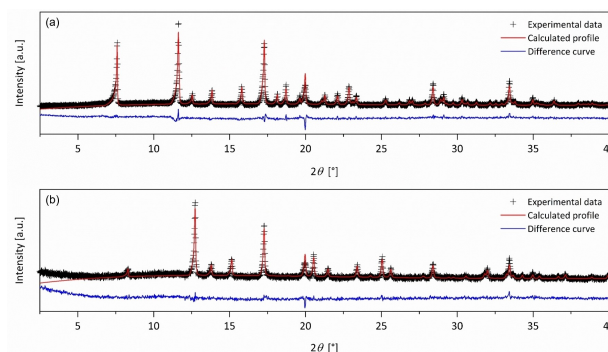
(Figure S2). After a first tiny endothermic signal in the DSC trace, which is most likely due to release of small amounts of adherent water or *en* inclusions, the first decomposition step at 170 °C is accompanied by a strong exothermic heat tone. The powder diffractogram of the residue formed after heating to 170 °C exhibits $\text{NH}_4[\text{ReO}_4]$ and elemental silver as intermediate products of decomposition (Figure S3). After heating to 1000 °C, elemental silver and rhenium are the final residual products, which was confirmed by powder X-ray diffraction (Figure S4). The total mass loss of 31 % complies well with 29.9 %, the value calculated for the degradation reaction assumed. The melting point of elemental silver can clearly be seen from the DSC curve at about 960 °C, which may serve as an internal reference.^[7]

The technical process of conditioning the EO catalyst includes treatment of the impregnated support in air.^[2] There-

fore, studying the decomposition of $[\text{Ag}(\mu\text{-en})][\text{ReO}_4]$ under such a condition is of key relevance. Comparing the decomposition in a flow of argon gas to the decomposition under a stream of synthetic air (20 % O_2 , 80 % N_2), reveals differences in the decomposition process only above ~265 °C (Figure S2 and S5). Even under synthetic air the first decomposition step of $[\text{Ag}(\mu\text{-en})][\text{ReO}_4]$ corresponds to the formation of $\text{NH}_4[\text{ReO}_4]$ and elemental silver (Figure 4), which has been corroborated by PXRD (Figure 5a).

Further, the IR spectrum of the intermediate product exhibits a characteristic N–H absorption band around 3195 cm⁻¹ and the strong $[\text{ReO}_4]^-$ asymmetric stretching band at 889 cm⁻¹ (Figure S6).^[8] The first decomposition step is accompanied by an exothermic heat tone as previously seen for the decomposition under argon. The PXRD of the intermediate of the thermal decomposition until 300 °C (Figure 4) confirms presence of $\text{Ag}[\text{ReO}_4]$ ^[4c] and elemental silver (Figure 5b). The IR spectrum of this intermediate product exhibits no N–H bands, but still the strong characteristic Re–O band at 870 cm⁻¹ (Figure S7).^[8]

After multiple further steps, that cannot be unambiguously resolved, elemental silver was identified via PXRD as final

**Figure 4.** TG-DSC trace for $[\text{Ag}(\mu\text{-en})][\text{ReO}_4]$ in synthetic air stream up to 300 °C.**Figure 5.** Rietveld fit of the ambient temperature powder diffraction pattern of the decomposition products of $[\text{Ag}(\mu\text{-en})][\text{ReO}_4]$, (a) at 170 °C ($\text{Ag} + \text{NH}_4[\text{ReO}_4]$ ^[9]), and (b) at 300 °C ($\text{Ag} + \text{Ag}[\text{ReO}_4]$ ^[9b,10]).

residual product for the overall decomposition reaction (Figure S8). Thus, the multi-step decomposition under synthetic air corresponds to a total experimental mass loss of 80.0% after heating to 995 °C, which fits fairly well the calculated mass of 74.2%.

Infrared Spectroscopy

The IR spectrum and the assignment of the vibrational bands of $[\text{Ag}(\mu\text{-en})][\text{ReO}_4]$ are depicted in Figure 6 and Table S6, respectively. The characteristic strong and weak asymmetric stretching vibrations of $[\text{ReO}_4]^-$ have been assigned according to literature data of $\text{Ag}[\text{ReO}_4]$ and occur at 870 cm^{-1} and 890 cm^{-1} .^[8] Comparison with IR spectroscopic data of *en* confirms that all other absorption bands between 3500 and 650 cm^{-1} arise from the organic substructure.^[11]

Conclusions

Ag-CS is the key precursor complex solution for producing ethylene oxide catalysts, to which among others $\text{NH}_4[\text{ReO}_4]$ is added for introducing $[\text{ReO}_4]^-$ as one of the promoting agents. The reaction of Ag-CS with $\text{NH}_4[\text{ReO}_4]$ results in crystallization of $[\text{Ag}(\mu\text{-en})][\text{ReO}_4]$. This silver *en* perrhenate complex and its decomposition behavior provides valuable insights into the pathways and intermediates involved in loading and conditioning of the EO catalyst. The crystal structure of $[\text{Ag}(\mu\text{-en})][\text{ReO}_4]$ was determined using SC-XRD at 100(2) K and shows similarities with $[\text{Ag}(\mu\text{-en})]_2(\text{C}_2\text{O}_4) \times 2\text{H}_2\text{O}$. The two compounds display similar 1D complex cations $[\text{Ag}(\mu\text{-en})]^+$ as zig-zag chains of alternating Ag^+ and *en* ligands. The complex $[\text{ReO}_4]^-$ anions are acceptors within N–H...O hydrogen bonds, however, do not coordinate the silver cations.

$[\text{Ag}(\mu\text{-en})][\text{ReO}_4]$ shows almost the same onset temperature for the thermal decomposition as $[\text{Ag}(\mu\text{-en})]_2(\text{C}_2\text{O}_4) \times 2\text{H}_2\text{O}$. Thus,

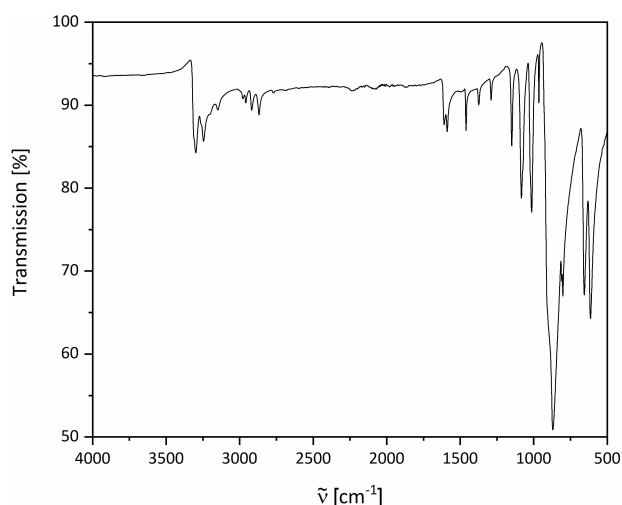


Figure 6. Infrared spectrum of $[\text{Ag}(\mu\text{-en})][\text{ReO}_4]$.

the deposition of silver platelets from the latter accompanied by the degradation of $[\text{Ag}(\mu\text{-en})][\text{ReO}_4]$ is suited to generate an active surface silver-rhenium species which is a crucial ingredient of the catalyst for EO production.

Experimental Section

Sample preparation and crystal growth. For phase-pure synthesis of $[\text{Ag}(\mu\text{-en})][\text{ReO}_4]$ 0.035 ml of ethane-1,2-diamine (0.5 mmol, 1 eq, Alfa Aesar 99%) were added under stirring to 1 ml of distilled H_2O at room temperature. After adding 90 mg AgNO_3 (0.5 mmol, 1 eq, BASF), the mixture was stirred at room temperature for 1 h. Subsequently, an aqueous solution of 138 mg $\text{NH}_4[\text{ReO}_4]$ (0.5 mmol, 1 eq, BASF) in 2 ml of distilled H_2O was added slowly and the reaction mixture stirred for another 30 minutes. The colorless precipitate formed was separated by centrifugation and washed with H_2O (2x) and ethanol (1x) while avoiding exposure of the product to light.

Thermal analysis. The thermal decomposition of the title compound in argon atmosphere was studied using a STARe System of the company METTLER TOLEDO. 11.6 mg of $[\text{Ag}(\mu\text{-en})][\text{ReO}_4]$ powder were placed in an Al_2O_3 sample pan and heated over a temperature range of 30–1000 °C with a heating rate of 10 °C/min under a constant gas flow with a rate of 20 ml/min. The thermal decomposition in synthetic air atmosphere was studied using a calorimeter of the company Perkin Elmer. 10.8 mg of $[\text{Ag}(\mu\text{-en})][\text{ReO}_4]$ were placed in an Al_2O_3 sample pan and heated over a temperature range of 30–995 °C with a heating rate of 5 °C/min under a constant gas flow with a rate of 20 ml/min.

X-Ray diffraction and structure analysis. Single crystal XRD data were collected on a Bruker D8 Venture diffractometer using $\text{Mo-K}\alpha$ radiation ($\lambda = 0.71073\text{ \AA}$) with a graphite monochromator and an image plate detector. A suitable single crystal was prepared using a polarization microscope, intensity data were measured at 100(2) K. The lattice parameters, the refinement details, the atomic parameters and selected bond lengths are given in Tables 1 and S1–S4. The structure solution and refinement was carried out using ShelXT/ShelXL in Olex2.^[12] The graphical presentations of the structure were created with the Diamond program.^[13]

Deposition Number 1947598 contains the supplementary crystallographic data for this paper. These data are provided on request free of charge by the joint Cambridge Crystallographic Data Centre and Fachinformationszentrum Karlsruhe Access Structures service.

The powder XRD data was collected at room temperature on a Stoe Stadi-P powder diffractometer ($\text{Mo-K}\alpha$ radiation) and on a Rigaku MiniFlex diffractometer ($\text{Cu-K}\alpha$ radiation). For the measurements on the Stoe Stadi-P powder diffractometer, the samples were ground in an agate mortar and sealed in glass capillaries ($\varnothing = 0.3\text{ mm}$). The samples which were measured on the Rigaku MiniFlex diffractometer were placed on a flat-plate. All samples were measured with typical recording times of 30 min with ranges of $2\theta = 3\text{--}60^\circ$ or $2\theta = 3\text{--}90^\circ$, respectively. The WinXPow and GnuPlot software were used for data handling and visualization of the patterns.^[14] The Rietveld refinement was performed with the Topas software^[15] applying the Thompson-Cox-Hastings profile function. The background was described by 6 Chebyshev polynomials and the graphical presentations of the final fits were created with the Origin software.^[16]

IR spectroscopy. The IR spectrum was recorded with the Spectrum Two FT IR Spectrometer by Perkin Elmer at room temperature with a maximal resolution of 1 cm^{-1} . The samples were ground in an

agate mortar and directly placed on the spectrometer in air. The visualization of the spectra was done with the Origin software.^[16]

Acknowledgements

We thank Christian Tobeck for carrying out the TG-DSC measurements and Prof. Mathias Wickleder for constant support. Jörn Bruns gratefully acknowledges financial support by the Fonds der Chemischen Industrie. Open Access funding enabled and organized by Projekt DEAL.

Conflict of Interest

The authors declare no conflict of interest.

Data Availability Statement

The data that support the findings of this study are available from the corresponding author upon reasonable request.

Keywords: crystal structure · EO catalysis · rhenium · silver · thermal decomposition

- [1] S. Rebsdat, D. Mayer, in *Ullmann's Encyclopedia of Industrial Chemistry*, 7 ed., Wiley-VCH, **2011**, p. 547.
- [2] a) A. M. Lauritzen, Patent US4766105, **1986**; b) E. M., Thorsteinson, M. M. Bhasin, S. R. Seyedmonir, Patent US5187140, **1990**; c) A. Karpov, C. Walsdorff, M. Kraemer, A. L. d. Oliveira, G. Krennrich, C. Bartosch, J. Zuehlke, Patent WO2019/154832, **2019**.
- [3] C. Kunz, C. Walsdorff, M. Viertelhaus, C. Adam, A. Karpov, J. Nuss, M. Jansen, *Z. Anorg. Allg. Chem.* **2021**, 647, 1348–1353.
- [4] a) C. J. L. Lock, G. Turner, *Acta Crystallogr. Sect. B* **1975**, 31, 1764–1765; b) G. J. Kruger, E. C. Reynhardt, *Acta Crystallogr. Sect. B* **1978**, 34, 259–261; c) C. Chay, M. Avdeev, H. E. A. Brand, S. Injac, T. A. Whittle, B. J. Kennedy, *Dalton Trans.* **2019**, 48, 17524–17532.
- [5] N. Wiberg, in *Lehrbuch der anorganischen Chemie*, 102 ed., Walter de Gruyter GmbH & Co KG, Berlin, Germany, **2008**, p. 99.
- [6] T. Steiner, *Angew. Chem.* **2002**, 114, 50–80; *Angew. Chem. Int. Ed.* **2002**, 41, 48–76.
- [7] G. Brauer, in *Handbuch der präparativen anorganischen Chemie*, Vol. 3, Enke, Stuttgart, Germany, **1975**, p. 993.
- [8] K. Ulbricht, H. Kriegsmann, *Z. Anorg. Allg. Chem.* **1968**, 358, 193–209.
- [9] a) E. M. Reynolds, M. Yu, G. J. Thorogood, H. E. A. Brand, F. Poineau, B. J. Kennedy, *J. Solid State Chem.* **2019**, 274, 64–68; b) H. E. Swanson, E. Tatge, *Natl. Bur. Stand. Circ.* **1953**, 359, 1–95.
- [10] C. Chay, M. Avdeev, H. E. A. Brand, S. Injac, T. A. Whittle, B. J. Kennedy, *Dalton Trans.* **2019**, 48, 17524–17532.
- [11] Y.-I. Lam, H. H. Huang, *J. Mol. Struct.* **1997**, 412, 141–152.
- [12] a) O. V. Dolomanov, L. J. Bourhis, R. J. Gildea, J. A. K. Howard, H. Puschmann, *J. Appl. Crystallogr.* **2009**, 42, 339–341; b) G. Sheldrick, *Acta Crystallogr. Sect. C* **2015**, 71, 3–8.
- [13] K. Brandenburg, *Diamond 4, Crystal and Molecular Structure Visualization*, Crystal Impact GbR, Bonn, Germany, **2019**.
- [14] a) WinXPow, version 3.6.0.1, Stoe & Cie GmbH, Darmstadt, Germany, **2018**; b) T. Williams, C. Kelley, R. Lang, *Gnuplot*, version 5.2, **2019**.
- [15] a) Topas-Academic, Bruker, Billerica, MA, USA, **2016**; b) A. Coelho, *J. Appl. Crystallogr.* **2018**, 51, 210–218.
- [16] Origin, version 2019, OriginLab Corporation, Northampton, MA, USA, **2019**.

Manuscript received: August 4, 2022
 Revised manuscript received: August 24, 2022
 Accepted manuscript online: August 28, 2022

4.4.3 $[\text{Ag}_2(\text{DHPP})](\text{C}_2\text{O}_4)$ Possible Side Phase During Catalysis

Since promoters containing cesium and chloride are also used in EO catalysis along with rhenium to improve selectivity, further experiments were conducted with modified experimental conditions. In analogy to $[\text{Ag}(\mu\text{-en})][\text{ReO}_4]$ which can be synthesized by combining an Ag complex solution with $\text{NH}_4[\text{ReO}_4]$, experiments with $\text{Cs}[\text{ReO}_4]$ instead of $\text{NH}_4[\text{ReO}_4]$ were carried out.^[106] A combination of the Ag complex solution with $\text{Cs}[\text{ReO}_4]$ appeared to be a promising experiment, as cesium promoters are also used in the production of the EO catalysts. The Ag complex solution typically contains *en*, Ag_2O and $\text{C}_2\text{H}_2\text{O}_4 \cdot 2 \text{H}_2\text{O}$.^[58]

Although the experiment aimed to obtain an *en* product with Cs as a cation, namely “ $[\text{Cs}(\mu\text{-en})][\text{ReO}_4]$ ”, the by-product decahydropyrazino[2,3-*b*]pyrazine (DHPP) silver(I) oxalate $[\text{Ag}_2(\text{DHPP})](\text{C}_2\text{O}_4)$ was formed instead. Colorless needles of $[\text{Ag}_2(\text{DHPP})](\text{C}_2\text{O}_4)$ were measured by SC-XRD. The compound crystallizes in the space group $C2/m$, see Table 7 and Table 27 in the Appendix. Figure 24 and Figure 25 show the extended asymmetric unit of $[\text{Ag}_2(\text{DHPP})](\text{C}_2\text{O}_4)$ and the cell along the *c*-axis and along the *b*-axis.

Table 7. Selected crystallographic data of $[\text{Ag}_2(\text{DHPP})](\text{C}_2\text{O}_4)$.

Crystal system	monoclinic	Space group	$C2/m$
Lattice parameters	$a = 10.485(2) \text{ \AA}$	Formula units	2
	$b = 9.339(2) \text{ \AA}$	$R_1 (I_o \geq 2\sigma(I_o))$	0.0429
	$c = 6.162(1) \text{ \AA}$	$wR_2 (I_o \geq 2\sigma(I_o))$	0.0941
	$\beta = 103.495(7)^\circ$	<i>goof</i>	1.049
	$V = 586.8(2) \text{ \AA}^3$		

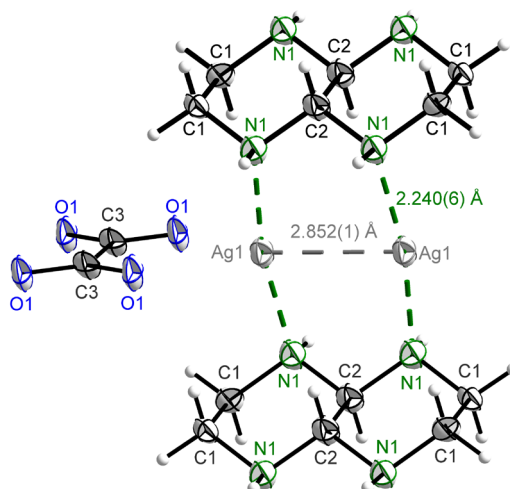


Figure 24. Extended asymmetric unit of $[\text{Ag}_2(\text{DHPP})](\text{C}_2\text{O}_4)$ with thermal ellipsoids with a probability of 70%.

[Ag₂(DHPP)](C₂O₄) contains one crystallographically distinguishable silver atom Ag1. The DHPP molecule exhibits two distinguishable carbon atoms C1/C2 and one nitrogen atom N1, whereas the oxalate anion contains one carbon atom C3 and one oxygen atom O1, see Figure 24. Ag1 is coordinated by two DHPP ligands via one N1 atom each along the *c*-axis without forming any layers or chains. The Ag-N distance amounts to 2.240(6) Å and the Ag-Ag distance to 2.852(1) Å which is much shorter than the sum of the van der Waals radii for silver (3.44 Å). Therefore, Ag(I) d¹⁰-d¹⁰ interactions can be assumed, which have been well documented, allowing for a comparison with the existing literature.^[107] Ag-Ag contacts often exhibit bond lengths comparable to the interatomic distances observed in elemental Ag (2.88 Å), reaching up to 3.30 Å.^[107-108] Ag[SC(NH₂)₂]₃ClO₄, AgSC(CH₃)(C₂H₅)₂ and [Bis(diphenylphosphino)methane]bromosilver(I) are notable examples in which the Ag-Ag distances are 2.845(1) Å, 2.886(4) Å and 2.964(8) Å respectively.^[109-111] Consequently, the Ag-Ag distance of 2.852(1) Å in [Ag₂(DHPP)](C₂O₄) falls within the range of the literature reported values.

When considering the bond lengths of DHPP and C₂O₄²⁻ in [Ag₂(DHPP)](C₂O₄), literature single crystal data of DHPP and Ag₂C₂O₄ serve as valuable data of comparison.^[112-113] Table 8 shows selected bond lengths of [Ag₂(DHPP)](C₂O₄) and literature data of DHPP and Ag₂C₂O₄.^[112-113] Both the bond lengths in DHPP and those in the oxalate anion of [Ag₂(DHPP)](C₂O₄) are in complete agreement with the literature, taking the respective uncertainties into account.^[112-113] Along the *b*-axis of the title compound it is noticeable that the DHPP ligands are separated by unconnected layers of silver and oxalate fragments, see Figure 25. Both the Ag(I) d¹⁰-d¹⁰ interactions and the coordination of Ag1 to N1 of the DHPP ligand appear to have no significant influence on the bond lengths in DHPP and C₂O₄²⁻.

Table 8. Selected bond lengths of [Ag₂(DHPP)](C₂O₄) and literature data of DHPP and Ag₂C₂O₄.^[112-113]

Fragment	Atoms	Bond length [Å]	
		[Ag ₂ (DHPP)](C ₂ O ₄)	Reference data
DHPP	C1-C1	1.51(1)	1.508(5)
	C2-C2	1.53(2)	1.520(5)
	C1-N1	1.479(8)	1.463(5)
	C2-N1	1.471(7)	1.452(4)
C ₂ O ₄ ²⁻	C3-C3	1.58(1)	1.595(9)
	C3-O1	1.247(5)	1.230(9)-1.241(9)

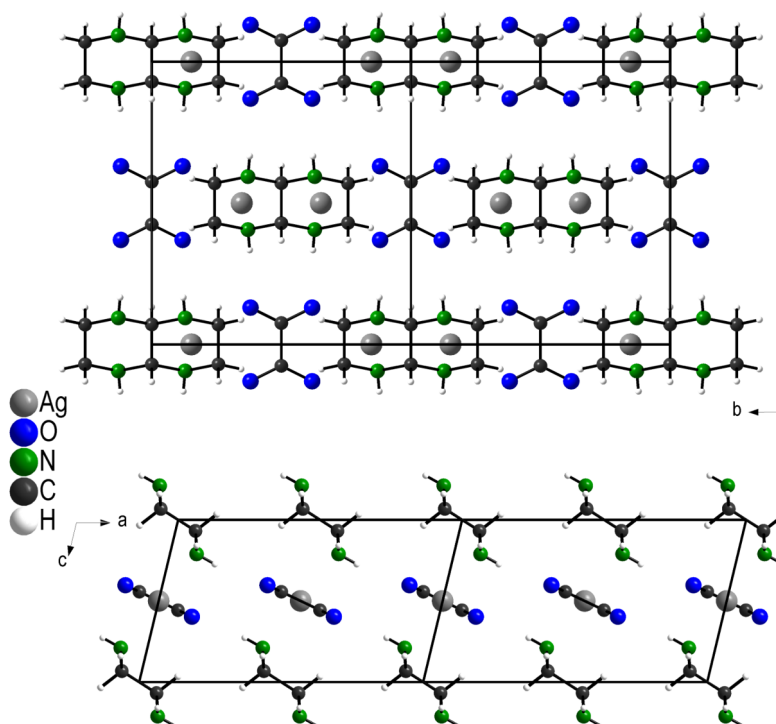


Figure 25. Crystal structure of $[\text{Ag}_2(\text{DHPP})](\text{C}_2\text{O}_4)$ along the c -axis (above) and along the b -axis (below).

Notably, $[\text{Ag}_2(\text{DHPP})](\text{C}_2\text{O}_4)$ exhibits similarities to the previously reported intermediate $[\text{Ag}(\mu\text{-en})]_2(\text{C}_2\text{O}_4) \cdot 2 \text{H}_2\text{O}$.^[65] As stated before, $[\text{Ag}(\mu\text{-en})]_2(\text{C}_2\text{O}_4) \cdot 2 \text{H}_2\text{O}$ was investigated as an intermediate during the production of the EO catalyst.^[65] This suggests that the novel DHPP containing product may also function as an intermediate in the production of the EO catalyst. However, the analysis of the processes and mechanisms involved in such a complex synthesis remains to be analyzed.

Without the use of DHPP during the reaction to $[\text{Ag}_2(\text{DHPP})](\text{C}_2\text{O}_4)$, the question arises as to how the product was formed. The synthesis of $[\text{Ag}_2(\text{DHPP})](\text{C}_2\text{O}_4)$ was carried out using $\text{C}_2\text{H}_2\text{O}_4 \cdot 2 \text{H}_2\text{O}$, *en* and Ag_2O . According to the literature, DHPP is typically synthesized by heating 40% aqueous glyoxal with *en* at 78°C for 5 hours.^[114] Given that $\text{C}_2\text{H}_2\text{O}_4 \cdot 2 \text{H}_2\text{O}$ was used instead of glyoxal, the reduction of oxalic acid to glyoxal must have occurred. As the reaction to $[\text{Ag}_2(\text{DHPP})](\text{C}_2\text{O}_4)$ seems to be a complex process, the exact mechanism for this reaction needs further investigation.

5 Conclusion and Outlook

The work successfully yielded various novel oxygen-containing compounds from ultra alkaline conditions and through the use of the hydroflux method. A unique aspect of this work was the use of starting materials containing technetium. By employing an appropriate nitrogen source, specifically NH_4^+ , it was possible to precisely incorporate varying amounts of nitrogen into oxoanions, demonstrating the control and specificity in the synthesis. As this work covers approaches with radioactive technetium, the safe working with this element was described and a review (**Publication 1**) summarizing the current chemistry of technetium was collaborated on.^[115]

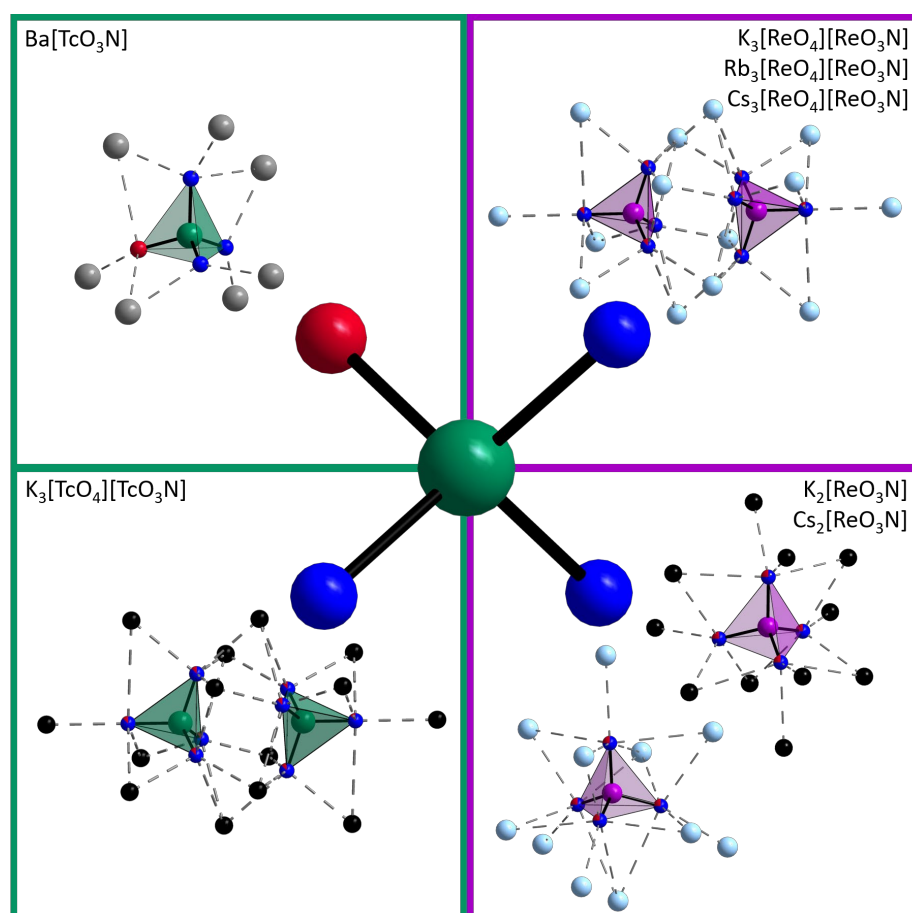


Figure 26. Summary of the compounds containing the $[\text{MO}_3\text{N}]^{2-}$ anion ($M = \text{Tc}, \text{Re}$) obtained in this work.

Green: Tc, purple: Re, blue: O, red: N, gray: Ba, black: K, light blue: Cs.^[77-80]

The second outcome of this work (**Publication 2**) was the synthesis of $\text{Ba}[\text{TcO}_3\text{N}]$, a compound featuring the nitridotrioxidotechnetate anion $[\text{TcO}_3\text{N}]^{2-}$, prepared under ultra alkaline conditions using $\text{NH}_4[\text{TcO}_4]$ and $\text{Ba}(\text{OH})_2 \cdot 8 \text{H}_2\text{O}$ at 200°C .^[80] The compound crystallizes in the monoclinic space group $P2_1/n$ isotypic to the monazite structure and contains isolated $[\text{TcO}_3\text{N}]^{2-}$ tetrahedra surrounded by Ba^{2+} cations.^[116] Raman and XANES spectroscopy with the help of quantum chemical calculations confirmed the oxidation state

+VII for technetium and the Tc-O and Tc-N bonding.^[80] This work highlights the potential of OH⁻ assisted ammonolysis as an efficient method for nitrogen incorporation into oxometallates.

The third publication expands on this chemistry by exploring the synthesis of isotopic compounds K₃[TcO₄][TcO₃N] and K₃[ReO₄][ReO₃N] through the reactions of NH₄[MO₄] (*M* = Tc, Re) in KOH hydroflux (**Publication 3**).^[79] Both compounds crystallize in the trigonal space group $R\bar{3}m$ and contain the anionic species [MO₄]⁻ and [MO₃N]²⁻. *Raman* and UV/vis spectroscopy confirmed the presence of *M*-O and *M*-N bonds, showing the successful nitrogen incorporation from NH₄⁺ without additional nitrogen sources.^[79] In contrast to Ba[TcO₃N], a specific O/N ordering could not be observed as the nitrogen atoms are distributed over all O positions.^[79-80]

Besides of K₃[TcO₄][TcO₃N] and K₃[ReO₄][ReO₃N], the corresponding Rb and Cs salt of the rhenium compound could be obtained from the respective alkali metal hydroxide and were investigated by SC-XRD (**Publication 4**).^[77] These compounds were further characterized by *Rietveld* refinement and *Raman* spectroscopy to confirm the presence of Re-O and Re-N bonds. The same publication reports the synthesis of the homoleptic nitridotrioxidometallates K₂[ReO₃N] and Cs₂[ReO₃N] from hydroflux reactions with KOH and CsOH, using ammonium chloride as an additional nitrogen source.^[77] K₂[ReO₃N] crystallizes in the monoclinic space group *C2/m*, while Cs₂[ReO₃N] shows an orthorhombic structure in *Pnma*. Both compounds feature tetrahedral [ReO₃N]²⁻ anions with Re-N and Re-O bonds, as confirmed by *Raman* spectroscopy.^[77] As with the previous mixed anionic compound, the N positions could not be assigned, as they are distributed over all O positions.

In addition to the previously mentioned nitrogen containing compounds, two other new structures were obtained. Two hydroxide compounds which contain [Ir(OH)₆]²⁻ anions were characterized, i.e. Ba₂[Ir(OH)₆](OH)₂ (**Publication 5**) and Ba_{2.4}Sr_{1.6}[Ir(OH)₆](OH)₆.^[78] The compounds were obtained from a Ba(OH)₂ or Ba(OH)₂/Sr(OH)₂ hydroflux, respectively. Ba₂[Ir(OH)₆](OH)₂ crystallizes in the orthorhombic space group *Pbca* and is isotopic with the literature known compound Ba₂[Pt(OH)₆](OH)₂.^[13] The Ir-O bond lengths align with literature values of Na₂[Ir(OH)₆].^[66] In contrast, Ba_{2.4}Sr_{1.6}[Ir(OH)₆](OH)₆ crystallizes in a rhombohedral crystal structure with the space group $R\bar{3}$. The asymmetric unit contains one crystallographically distinguishable Ir atom, which is surrounded by six OH⁻ anions, forming a slightly distorted octahedron. Both compounds exhibit iridium with the formal

oxidation state of +IV. Since both compounds could not be obtained phase pure, further attempts need to be carried out in order to verify the proposed oxidation state. IR spectroscopy is useful for verifying OH vibrations, while XPS or XANES can provide insights into the oxidation states. Furthermore, the distribution of Ba/Sr in $\text{Ba}_{2.4}\text{Sr}_{1.6}[\text{Ir}(\text{OH})_6](\text{OH})_6$ needs to be confirmed by XPS.

In addition to hydroflux syntheses, attempts towards novel oxides from high pressure and high temperature experiments in a *Walker*-type multi anvil press were presented.^[28] Black metallic crystals of Ag_2PbO_3 could be grown at high pressures by starting from Ag_2PbO_2 . Ag_2PbO_3 crystallizes in the space group $Fddd$ with one crystallographically distinguishable Pb and two distinguishable Ag and O atoms each. Compared to NaCl, Ag_2PbO_3 shows a symmetry reduction from $Fm\bar{3}m$ to $Fddd$, resulting in a distorted rock-salt structure where all atoms adopt an irregular octahedral coordination. Starting from a stoichiometric mixture of Ag_2O and PbO_2 , phase pure samples could be obtained. Figure 27 shows the extended asymmetric unit of Ag_2PbO_3 and the WC cubes with an octahedron which are used in the multi anvil press.

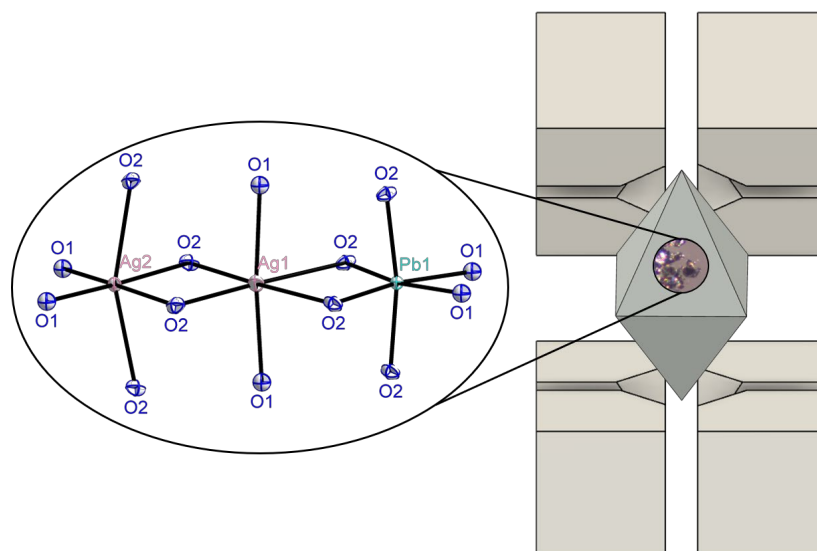


Figure 27. Extended asymmetric unit of Ag_2PbO_3 (left) and WC cubes with octahedron (right), which are used in the multi anvil press. The octahedron contains a small picture of a microscopic picture of Ag_2PbO_3 .

Using the phase pure sample, XPS data could be obtained and the oxidation states of Ag^+ and Pb^{4+} could be verified. In addition to the Ag_2PbO_3 , further attempts could be made to exchange both Pb^{4+} and Ag^+ . It is quite conceivable that the corresponding products could exist with Sn^{4+} or Cu^+ , for example.

In the last part of this work, a significant advancement in the understanding of ethylene oxide catalyst preparation was made. In the first step, the ethylene oxide catalyst was

thoroughly examined to better understand its production process. P-XRD and EDX spectroscopy measurements were performed on the fresh as well as on the spent catalyst supplied in collaboration with BASF.

Furthermore, promoter solutions typically used for catalyst preparation were combined, resulting in two novel structures. The new compound $[\text{Ag}(\mu\text{-en})][\text{ReO}_4]$ crystallizes in the space group $P\bar{1}$ (**Publication 6**).^[106] It shows a zig-zag arrangement of alternating Ag ions and ethylenediamine (*en*) ligands, forming one-dimensional chains. The silver ions are coordinated end-on by the nitrogen atoms of the *en* ligands, while the $[\text{ReO}_4]^-$ anions are not directly bonded to the Ag but instead participate in moderate hydrogen bonds. The analysis of the crystal structure by SC-XRD, with thermal and spectroscopic data shows that the compound can have a relevance in optimizing the EO catalyst.^[106]

In another experiment, colorless needles of $[\text{Ag}_2(\text{DHPP})](\text{C}_2\text{O}_4)$ were measured by SC-XRD. The compound crystallizes in the space group $C2/m$ with isolated DHPP (decahydropyrazino[2,3-*b*]pyrazine) molecules. The Ag-Ag distance of 2.852(1) Å is significantly shorter than the sum of the van der Waals radii for silver (3.44 Å), suggesting the presence of $d^{10}\text{-}d^{10}$ interactions. However, the formation mechanism of DHPP during the synthesis remains unclear. Consequently, further investigations are required to elucidate this process.

All in all, by identifying and characterizing the possible intermediate compounds $[\text{Ag}(\mu\text{-en})][\text{ReO}_4]$ and $[\text{Ag}_2(\text{DHPP})](\text{C}_2\text{O}_4)$, insights into the thermal decomposition pathways and the structural role of silver and rhenium components in EO catalyst production could be given.

6 Experimental

6.1 General Procedures and Analytic Methods

6.1.1 Hydroflux Technique

The syntheses were carried out using 23 ml high temperature stainless steel autoclaves from Parr Instrument Company, utilizing alkali metal or alkaline earth metal hydroxides as melts. A setup of the autoclave is presented in Figure 28. These general-purpose vessels featured a spring-loaded closure within a stainless-steel casing, sealed by tightening the cap with a spanner wrench. The PTFE inlays had a capacity of 23 ml, whereas for small-scale syntheses, additional 1 ml or 5 ml PTFE beakers were placed inside the inlays.

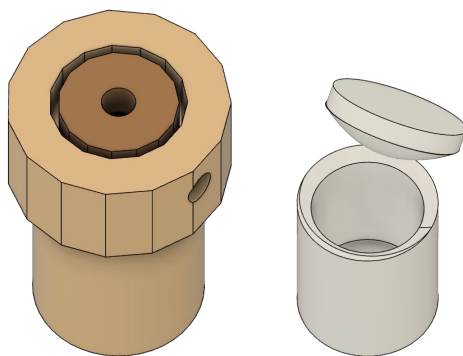


Figure 28. Schematic of an autoclave (left) and a PTFE inlay (right).

6.1.2 Multi Anvil Press

High pressure experiments were performed using a *Voggenreiter* multi anvil press with a standard *Walker*-type module.^[28] The powder samples were loaded in gold crucibles, which were then positioned within a standard 14/8 assembly. A comprehensive description of the *Walker*-type setup can be found in the work by *Huppertz*.^[27]

6.1.3 High Pressure O₂ Autoclave

The sample was placed in a corundum crucible and O₂ was introduced by first condensing a precisely defined volume into a glass finger using liquid nitrogen and then transferring it to the autoclave. For details on the construction of the autoclaves and the filling system, see chapter 2.3. The amount of O₂ was carefully controlled to achieve the required pressure. Once the autoclave was sealed, it was heated in an oven to the target temperature according to a defined heating and cooling program. After the reaction, the O₂ was gradually released and the final product was removed from the crucible.

6.1.4 Chemicals

Table 9. List of used chemicals with information about supply source, form and purity.

Sum formula	Supply source	Form	Purity [%]
AgCl	<i>abcr</i>	crystals	99
AgNO ₃	<i>BASF</i>	crystals	not specified
Ba(OH) ₂ · 8 H ₂ O	<i>Alfa Aesar</i>	powder	98
C ₂ H ₂ O ₄ · 2 H ₂ O	<i>Sigma Aldrich</i>	crystals	>99.5
Cu ₂ O	<i>Alfa Aesar</i>	powder	97
Cs ₂ CO ₃	<i>Alfa Aesar</i>	powder	99.95
ethane-1,2-diamine	<i>Alfa Aesar</i>	liquid	99
H ₃ BO ₃	stock	powder	not specified
H ₂ WO ₄	<i>BASF</i>	powder	not specified
KOH	<i>Thermo Scientific</i>	pellets	~85
K ₂ S ₂ O ₇	<i>Sigma Aldrich</i>	powder	99
(NH ₄) ₁₀ (H ₂ W ₁₂ O ₄₂) · 4 H ₂ O	<i>BASF</i>	powder	not specified
(NH ₄) ₂ [IrCl ₆]	not specified	crystals	not specified
PbO ₂	<i>Riedel-de Haën</i>	powder	not specified
ReO ₃	<i>Sigma Aldrich</i>	powder	99.9
Re ₂ O ₇	<i>abcr</i>	crystals	99.99
SnO ₂	<i>Alfa Aesar</i>	powder	99.9
Sr(OH) ₂ · 8 H ₂ O	<i>Riedel-de Haën</i>	powder	98

6.1.5 X-ray Single Crystal Diffraction

The data were collected using *Bruker D8 Venture Dual Beam* (Mo-K α radiation, multilayer mirror, Photon III detector). The samples were prepared under a polarization microscope and measured at 100(2) K. Structural solutions and refinements were carried out with the *ShelX* software package^[82] in *Olex 2.0*^[84], while *Diamond*^[117] was used for the visualization.

6.1.6 X-ray Powder Diffraction and *Rietveld* Refinement

The data were collected at room temperature using a *Stoe Stadi-P* powder diffractometer (Mo-K α_1 radiation, Ge(111) monochromator, Mythen detector) or a *RIGAKU MiniFlex* powder diffractometer (Cu-K α_1 and Cu-K α_2 radiation, Bragg-Brentano geometry, HyPix-400 MF 2D hybrid detector). The samples were ground in an agate mortar, sealed in 0.3 mm glass capillaries and measured over a 2θ range of 3-60° using the *Stoe Stadi-P* powder diffractometer. For sensitive samples, the preparation took place in an inert gas

atmosphere using a glove box. Samples which were measured on the *RIGAKU MiniFlex* were ground in an agate mortar, prepared on flat low background glass or monocrystalline silicon holders and measured over a 2θ range of 3-90°. Data processing and pattern visualization were carried out using the *WinXPow*^[118] and *Gnuplot*^[119] software.

The *Rietveld* refinements were performed using *Topas*^[120-121], applying the Thompson-Cox-Hastings profile function with the background modeled by six or ten Chebychev polynomials. The data were plotted using the *Origin*^[122] software.

6.1.7 IR Spectroscopy

The characterization was performed using a *Bruker Optics Alpha* IR spectrometer. The measurements were obtained at room temperature with a diamond ATR module, achieving a maximum resolution of 1 cm⁻¹. Data visualization was carried out using *Origin*^[122] software.

6.1.8 Raman Spectroscopy

The *Raman* measurements were conducted using a *Renishaw inVia Raman* microscope, with spectra collected from the single crystal using a 532 nm laser excitation at room temperature. The data were analyzed and visualized with the *Origin*^[122] software.

6.1.9 X-ray Photoelectron Spectroscopy

XPS data were measured on an *ESCA M-Probe* from *Surface Science Instruments* with an Al-K α source. The data were analyzed with *CasaXPS* software (*Casa Software Ltd.*)^[123] after calibration to the adventitious carbon signal at 284.8 eV.

6.1.10 Energy-dispersive X-ray Spectroscopy

Analyses utilizing EDX spectroscopy were carried out on a *JEOL JEM-2200FS* transmission electron microscope, operated with an acceleration voltage of 200.0 kV.

6.1.11 Polynator

The program *Polynator*^[81] was used to analyze the coordination polyhedra, identifying their geometry and calculating distortion parameters (δ). Unlike the rigid models of *SHAPE*^[124-125], *Polynator*^[81] allows dynamic fitting with adjustable parameters. A perfect fit yields $\delta = 0$, while values above $\delta = 30$ are unreliable. The cif files served as an input for the polyhedral analysis.

6.1.12 CHARDI

Charge distribution analysis was conducted using *CHARDI2015*^[126-127], applying a Madelung-type approach. The oxidation states of cations and anions were used to calculate charge distribution and the effective coordination number, which considers both bond number and strength. The cif files with the oxidation states were used as input.

6.2 Experimental Procedures

6.2.1 $\text{Ba}_{2.4}\text{Sr}_{1.6}[\text{Ir}(\text{OH})_6](\text{OH})_6$

The synthesis of $\text{Ba}_{2.4}\text{Sr}_{1.6}[\text{Ir}(\text{OH})_6](\text{OH})_6$ was carried out in a PTFE inlay with a capacity of 23 ml. The sample contained of 22.05 mg $(\text{NH}_4)_2[\text{IrCl}_6]$ (0.05 mmol, 1 eq), 433.79 mg $\text{Ba}(\text{OH})_2 \cdot 8 \text{H}_2\text{O}$ (1.38 mmol, 28 eq), 365.42 mg $\text{Sr}(\text{OH})_2 \cdot 8 \text{H}_2\text{O}$ (1.38 mmol, 28 eq) and 49.54 mg H_2O (2.75 mmol 55 eq). $(\text{NH}_4)_2[\text{IrCl}_6]$ was first loaded into the PTFE inlay. After adding the hydroxides and H_2O , the closed autoclave was heated at 200°C for 10 h with a heating rate of 2 °C/min and a cooling rate of 0.055 °C/min.

6.2.2 Ag_2PbO_3



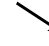
The synthesis of Ag_2PbO_3 is carried out using freshly precipitated Ag_2O . Therefore, Ag_2O was obtained according to the literature with aqueous solutions of AgNO_3 and KOH .^[128] 466.95mg of Ag_2O (2.01 mmol, 1 eq) and 481.27 mg PbO_2 (2.01 mmol, 1 eq) were milled with a *Retsch 400 MM* mill using a steel ball and a 5 ml container, i.e. 20 min with 10 Hz and additionally 45 min with 20 Hz. The mixture was filled in a gold foil and the octahedron prepared as described in chapter 2.2. The experiment was conducted in a *Voggenreiter* multi anvil press using a *Walker*-type module with a standard 14/8-assembly.^[27] The crucible was compressed with an oil pressure of 300 bar and heated for 65 minutes with a heating power of 600 W. See equation 3 in chapter 4.3.1 for a detailed pressure/heating program which is given in minutes. Black metallic crystals of Ag_2PbO_3 were isolated from the gold foil mechanically.

6.2.3 Further Synthesis Attempts in the Multi Anvil Press

The experiments were conducted in a *Voggenreiter* multi anvil press using a *Walker*-type module with a standard 14/8-assembly.^[27] All mixtures were ground and filled in a gold foil. The octahedra were prepared as described in chapter 2.2. The crucibles were compressed with the targeted oil pressure and heated for 65 minutes with the targeted heating power. The samples were subjected to a thermal program consisting of a 10 minute heating phase, a 15 minute holding period and a 40 minute cooling phase. See Table 10 for the detailed information about the starting materials and the used programs. Ag_2O and $\text{Ag}[\text{ReO}_4]$ were synthesized according to the literature.^[128-129]

Experimental

Table 10. Details about starting materials and conditions of selected experiments in the multi anvil press.

Starting materials			Power [W]	Oil pressure [bar]	Pressure program [min]		
A	B	C					
1 eq Ag[ReO ₄]			300	400	300	65	600
1 eq ReO ₃	1 eq Ag ₂ O		400	500	300	65	600
1 eq Ag[ReO ₄]	1 eq Ag ₂ O		250	400	300	65	600
1 eq Re ₂ O ₇	1 eq Ag ₂ O	2 eq AgCl	250	400	300	65	600
1 eq H ₃ BO ₃	2 eq K ₂ S ₂ O ₇		400	600	180	65	540
1 eq Ag ₂ O	1 eq SnO ₂		300	900	180	65	600
1 eq Cu ₂ O	1 eq PbO ₂		300	300	180	65	600

6.2.4 Characterization of the EO Catalyst

Several solid state reaction experiments in O₂ high pressure autoclaves were conducted, see Table 11 and Table 12 for information about starting materials, the heating programs and products. The starting materials were ground in an agate mortar, filled into Al₂O₃ crucibles which are placed into the O₂ autoclave according to the literature.^[37] For experiment No. 5 a pellet was pressed of the mixed starting materials. The autoclaves were filled with a specific volume of liquid O₂ according to the method described in chapter 2.3 and heated in furnaces.

Table 11. Information about starting materials and temperature program of selected experiments in O₂ autoclaves.



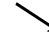
No.	Starting materials		O ₂ [ml]	T [°C]	Program in day/s		
	A	B					
1	1 eq Re	3 eq Ag ₂ O	11.2	300	1	4	1
2	1 eq ReO ₃	4 eq Ag ₂ O	11.2	300	1	4	1
3	1 eq ReO ₃	4 eq Ag ₂ O	8.0	600	1.25	6	11
4	1 eq ReO ₃	2 eq AgCl	5.0	400	1	3	1.7
5	1 eq Ag[ReO ₄]	1 eq Ag (pellet)	8.0	550	1	3	1.7
6	1 eq Ag[ReO ₄]	5 eq Ag ₂ O	8.0	500	1.7	1	2

Table 12. Information about starting materials and products of selected experiments in O₂ autoclaves.

No.	Starting materials		Products	
	A	B	A	B
1	1 eq Re	3 eq Ag ₂ O	Ag[ReO ₄]	Ag ₂ O
2	1 eq ReO ₃	4 eq Ag ₂ O	Ag[ReO ₄]	Ag ₂ O
3	1 eq ReO ₃	4 eq Ag ₂ O	Ag[ReO ₄]	Ag ₂ O
4	1 eq ReO ₃	2 eq AgCl	Ag[ReO ₄]	AgCl
5	1 eq Ag[ReO ₄]	1 eq Ag (pellet)	Ag[ReO ₄]	unknown phase
6	1 eq Ag[ReO ₄]	5 eq Ag ₂ O	Ag[ReO ₄]	Ag ₂ O

6.2.5 [Ag₂(DHPP)](C₂O₄)

Similar as known for [Ag(μ -*en*)] [ReO₄], 0.070 ml of ethane-1,2-diamine (1.0 mmol, 2 eq) were added to 1 ml of distilled H₂O under stirring at room temperature.^[106] After adding 63.0 mg C₂H₂O₄ · 2 H₂O (0.5 mmol, 1 eq) and 115.9 mg freshly precipitated Ag₂O (0.5 mmol, 1 eq), the mixture was stirred at room temperature overnight. Ag₂O was freshly precipitated from AgNO₃ and KOH in H₂O.^[128] Subsequently, an aqueous solution of 127.7 mg freshly crystallized Cs[ReO₄] (0.3 mmol, 1.5 eq) in 1 ml of distilled H₂O was added slowly to 0.66 ml of the *en* mixture. Cs[ReO₄] was freshly precipitated from Cs₂CO₃ and NH₄[ReO₄] in H₂O in analogy to literature.^[129] The reaction mixture was stirred for another 30 minutes and stored at 8°C for crystallization. Colorless needles were obtained.

7 Appendix

7.1 Ba[TcO₃N]

Supporting Information

of

Publication 2

Reaction of Pertechnetate in Highly Alkaline Solution: Synthesis and Characterization of the Nitridotrioxotechnetate Ba[TcO₃N]

D. Badea, K. Dardenne, R. Polly, J. Rothe, M. Hanrath, M. Reimer, K. Meerholz,
J.-M. Neudorfl, E. Strub and J. Bruns*

Chem. Eur. J. **2022**, 28, e202201738.

doi.org/10.1002/chem.202201738

Table of Contents

- A. Structure determination and crystallographic details
- B. Experimental and calculated EXAFS data
- C. Calculated IR and Raman data

A. Structure determination and crystallographic details

Table S1. Atomic coordinates ($\times 10^4$) and equivalent isotropic displacement parameters ($\text{\AA}^2 \times 10^3$) for Ba[TcO₃N]. $U(eq)$ is defined as one third of the trace of the orthogonalized U_{ij} tensor.

Atom	x	y	z	$U(eq)$
Ba1	3952.2(5)	8339.3(4)	2372.5(6)	19.8(3)
N1	7923(7)	3921(6)	4732(7)	22.3(9)
O1	4410(7)	4912(5)	2294(7)	24.1(9)
O2	4925(6)	1578(5)	3775(7)	23.2(1)
O3	7254(5)	2670(5)	1209(6)	22.6(8)
Tc1	6130.7(6)	3266.3(5)	2953.5(9)	19.4(3)

Table S2. Anisotropic displacement parameters ($\text{\AA}^2 \times 10^3$) for Ba[TcO₃N]. The anisotropic displacement factor exponent takes the form: $-2\pi^2 [h^2 a^{*2} U_{11} + 2 h k a^* b^* U_{12} + \dots]$.

Atom	U_{11}	U_{22}	U_{33}	U_{23}	U_{13}	U_{12}
Ba1	19.2(4)	21.6(3)	20.5(3)	-0.11(1)	8.6(2)	0.41(9)
N1	25(2)	23(2)	20(3)	-2.1(2)	7.8(2)	-1.7(2)
O1	23.1(2)	23.3(2)	28(2)	4.1(2)	10.6(2)	4.4(2)
O2	23(2)	28(2)	21(3)	1.6(1)	8.8(2)	0.8(1)
O3	21.8(2)	26.3(2)	22(2)	-0.4(2)	8.9(2)	0.1(2)
Tc1	18.7(4)	21.5(4)	20.3(4)	0.29(1)	9.1(2)	-0.09(1)

Table S3. Experimental and calculated bond lengths for Ba[TcO₃N].

Atom	Atom	Length [\AA]		Atom	Atom	Length [\AA]	
		experimental	calculated			experimental	calculated
Ba1	N1 ¹	3.088(5)	2.92	Ba1	O3 ¹	2.732(4)	2.76
Ba1	N1 ³	3.337(5)	3.46	Ba1	O3 ⁵	2.727(4)	2.78
Ba1	N1 ⁴	2.893(5)	2.92	Ba1	Tc1 ¹	3.6166(5)	3.64
Ba1	O1	2.714(4)	2.80	Ba1	Tc1 ²	3.6157(5)	3.64
Ba1	O1 ²	2.788(5)	2.85	Tc1	N1	1.692(5)	1.69
Ba1	O2 ²	3.049(4)	3.17	Tc1	O1	1.776(4)	1.78
Ba1	O2 ³	2.800(5)	2.85	Tc1	O2	1.777(4)	1.78
Ba1	O2 ⁶	2.775(4)	2.83	Tc1	O3	1.763(4)	1.79

¹3/2-x,1/2+y,1/2-z, ²1/2-x,1/2+y,1/2-z, ³1-x,1-y,1-z, ⁴-1/2+x,3/2-y,-1/2+z, ⁵1-x,1-y,-z, ⁶+x,1+y,+z

Table S4. Bond angles for Ba[TcO₃N].

Atom	Atom	Atom	Angle [°]	Atom	Atom	Atom	Angle [°]
Ba1	O1	Ba1 ⁸	108.91(2)	O2 ⁶	Ba1	N1 ³	64.89(1)
Ba1 ¹⁰	O2	Ba1 ⁴	113.18(2)	O2 ¹	Ba1	N1 ⁴	56.69(1)
Ba1 ¹⁰	O2	Ba1 ⁸	100.38(2)	O2 ⁴	Ba1	N1 ⁴	53.33(1)
Ba1 ⁴	O2	Ba1 ⁸	106.99(2)	O2 ⁶	Ba1	N1 ⁴	110.28(1)
Ba1 ⁵	O3	Ba1 ⁷	118.99(2)	O2 ⁶	Ba1	O1 ¹	72.81(1)
Ba1 ⁷	N1	Ba1 ⁴	135.85(2)	O2 ⁴	Ba1	O2 ¹	108.26(1)
Ba1 ⁷	Tc1	Ba1 ⁴	108.146(2)	O2 ⁶	Ba1	O2 ¹	130.66(9)
Ba1 ⁸	Tc1	Ba1 ⁴	79.526(1)	O2 ⁶	Ba1	O2 ⁴	66.82(2)
Ba1 ⁸	Tc1	Ba1 ⁷	172.27(3)	O2 ¹	Ba1	Tc1 ¹	29.39(8)
Ba1 ⁹	N1	Ba1 ⁴	91.61(1)	O2 ⁴	Ba1	Tc1 ¹	95.78(9)
Ba1 ⁹	N1	Ba1 ⁷	111.26(2)	O2 ⁶	Ba1	Tc1 ¹	101.41(9)
N1	Tc1	Ba1 ⁴	63.25(2)	O2 ¹	Ba1	Tc1 ²	145.20(8)
N1	Tc1	Ba1 ⁷	58.44(2)	O2 ⁴	Ba1	Tc1 ²	91.77(9)
N1	Tc1	Ba1 ⁸	127.86(2)	O2 ⁶	Ba1	Tc1 ²	83.07(9)
N1	Tc1	O1	110.1(2)	O2	Tc1	Ba1 ⁴	45.67(2)
N1	Tc1	O2	107.3(2)	O2	Tc1	Ba1 ⁷	127.40(1)
N1	Tc1	O3	105.3(2)	O2	Tc1	Ba1 ⁸	57.33(1)
N1 ²	Ba1	N1 ⁴	151.04(1)	O3 ²	Ba1	N1 ²	55.90(1)
N1 ²	Ba1	Tc1 ¹	145.51(1)	O3 ⁵	Ba1	N1 ²	68.68(1)
N1 ²	Ba1	Tc1 ²	27.83(9)	O3 ²	Ba1	N1 ³	118.21(1)
N1 ³	Ba1	N12	68.74(2)	O3 ⁵	Ba1	N1 ³	65.01(1)
N1 ³	Ba1	N1 ⁴	139.75(7)	O3 ²	Ba1	N1 ⁴	99.95(1)
N1 ³	Ba1	O2 ¹	94.69(1)	O3 ⁵	Ba1	N1 ⁴	113.76(1)
N1 ³	Ba1	Tc1 ¹	83.14(9)	O3 ²	Ba1	O1 ¹	149.42(1)
N1 ³	Ba1	Tc1 ²	93.23(9)	O3 ⁵	Ba1	O1 ¹	98.25(1)
N1 ⁴	Ba1	Tc1 ¹	57.88(9)	O3 ²	Ba1	O2 ¹	141.65(1)
N1 ⁴	Ba1	Tc1 ²	126.68(9)	O3 ⁵	Ba1	O2 ¹	62.78(1)
O1	Ba1	N1 ²	91.57(1)	O3 ²	Ba1	O2 ⁴	66.18(1)
O1	Ba1	N1 ³	137.29(2)	O3 ⁵	Ba1	O2 ⁴	164.23(1)
O1	Ba1	N1 ⁴	63.75(1)	O3 ²	Ba1	O2 ⁶	83.87(1)
O1	Ba1	O1 ¹	123.69(1)	O3 ⁵	Ba1	O2 ⁶	128.95(1)
O1	Ba1	O2 ¹	69.64(1)	O3 ⁵	Ba1	O3 ²	111.89(1)
O1	Ba1	O2 ⁴	92.27(1)	O3 ²	Ba1	Tc1 ¹	157.76(9)
O1	Ba1	O2 ⁶	153.66(1)	O3 ⁵	Ba1	Tc1 ¹	81.76(8)
O1	Ba1	O3 ²	72.66(1)	O3 ²	Ba1	Tc1 ²	28.07(9)
O1	Ba1	O3 ⁵	72.62(1)	O3 ⁵	Ba1	Tc1 ²	90.53(8)
O1	Ba1	Tc1 ¹	96.30(1)	O3	Tc1	Ba1 ⁴	136.22(1)
O1	Ba1	Tc1 ²	81.72(1)	O3	Tc1	Ba1 ⁷	46.84(1)
O1 ¹	Ba1	N1 ²	137.85(1)	O3	Tc1	Ba1 ⁸	126.75(1)
O1 ¹	Ba1	N1 ³	69.48(1)	O3	Tc1	O1	113.9(2)
O1 ¹	Ba1	N1 ⁴	71.10(1)	O3	Tc1	O2	114.4(2)
O1 ¹	Ba1	O2 ¹	57.86(1)	Tc1 ¹	Ba1	Tc1 ²	172.27(3)
O1 ¹	Ba1	O2 ⁴	86.22(1)	Tc1	N1	Ba1 ⁴	89.82(2)
O1 ¹	Ba1	Tc1 ¹	28.65(9)	Tc1	N1	Ba1 ⁷	93.73(2)
O1 ¹	Ba1	Tc1 ²	154.55(9)	Tc1	N1	Ba1 ⁹	141.5(2)
O1	Tc1	Ba1 ⁴	109.56(2)	Tc1	O1	Ba1	142.8(2)
O1	Tc1	Ba1 ⁷	126.85(2)	Tc1	O2	Ba1 ¹⁰	130.7(2)
O1	Tc1	Ba1 ⁸	48.84(2)	Tc1	O2	Ba1 ⁴	107.3(2)
O1	Tc1	O2	105.7(2)	Tc1	O3	Ba1 ⁵	135.52(2)
O2 ¹	Ba1	N1 ²	131.15(1)	Tc1	O3	Ba1 ⁷	105.08(2)
O2 ⁴	Ba1	N1 ²	117.46(1)	Tc1	O1	Ba1 ⁸	102.51(2)
O2 ⁶	Ba1	N1 ²	84.80(1)	Tc1	O2	Ba1 ⁸	93.28(2)
O2 ⁴	Ba1	N1 ³	130.38(1)				

¹1/2-x, 1/2+y, 1/2-z, ²3/2-x, 1/2+y, 1/2-z, ³1-x, 1-y, 1-z, ⁴-1/2+x, 3/2-y, -1/2+z, ⁵1-x, 1-y, -z, ⁶+x, 1+y, +z, ⁷1/2-x, -1/2+y, 1/2-z,

⁸3/2-x, -1/2+y, 1/2-z, ⁹1/2+x, 3/2-y, 1/2+z, ¹⁰+x, -1+y, +z

B. Experimental and calculated EXAFS data

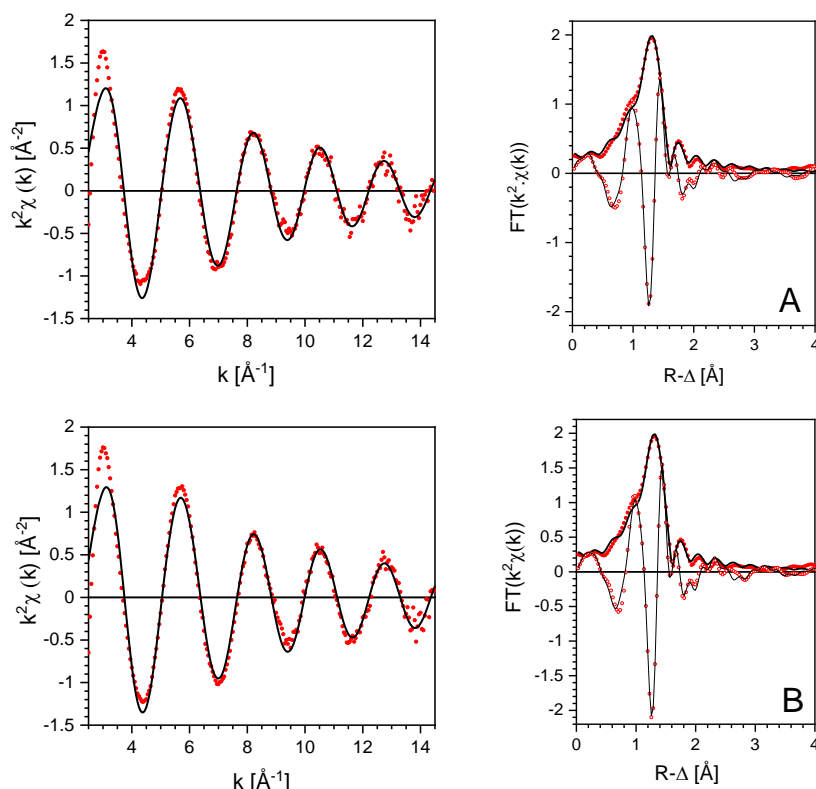


Figure S1. Tc K-edge EXAFS obtained for (A – top row) the title compound and (B – bottom row) an aqueous solution of Na[TcO₄]. Left hand side panels: k^2 -weighted $\chi(k)$ EXAFS signal (red symbols) and best fit (solid line), right hand side panels: R-space fit results comprising Fourier transform (FT) magnitude of k^2 -weighed $\chi(k)$ (red symbols), best fit FT magnitude (thick solid line), FT imaginary part of EXAFS signal (open red symbols) and FT imaginary part of best fit (thin solid line).

Table S5. Structural parameters obtained from EXAFS evaluation of the title compound (A) and an aqueous pertechnetate reference sample (B).

Sample description	Path	CN	R (Å)	k^2 (Å ²)	ΔE_0 (eV)	R-factor
Sample A / Ba[TcO ₃ N] cryst. solid	Tc-O(N)	3.9(2)	1.733(5)	0.0014(5)	-1.8	0.0024
Sample B / Na[TcO ₄] aq. solution	Tc-O	4*	1.732(5)	0.0012(6)	-1.4	0.0012

*value fixed in fit, resulting in $S_0^2=0.89$ applied for sample A

Figure S1 depicts the Tc K-edge EXAFS fit results obtained for the title compound (top row) and an aqueous pertechnetate reference solution (bottom row). The best fit results obtained by least-squares fitting of the EXAFS $\chi(k)$ signals using standard procedures as implemented in the Demeter program package (<https://bruceravel.github.io/demeter/>) are summarized in Table S5. As in case of the pertechnetate [Tc(VII)O₄][−] reference, the fit of the tetrahedral first shell coordination environment of Tc in the TcO₃N[−] entity requires only a single Tc-O(N) scattering path. Note that backscattering signals from the Z-1 neighbor atoms oxygen and nitrogen cannot be differentiated. The EXAFS signatures of both Tc(VII) compounds - both in electron momentum (k -) and neighbor distance R -space (FT) - are almost indiscernible. Hence, within the indicated EXAFS error margins, both fits point to the same coordination environment for both samples.

Table S6. xyz coordinates from the geometry optimization of the solid state structure of Ba[TcO₃N] with VASP.

Atom	x	y	z
Ba	2.496201	6.691327	1.723694
Ba	2.957705	1.311558	5.665872
Ba	0.231638	2.689490	1.971010
Ba	5.222268	5.313394	5.418555
Tc	3.928080	2.624798	2.203276
Tc	1.525827	5.378087	5.186290
Tc	6.123627	6.626729	1.491388
Tc	-0.669720	1.376156	5.898177
N	4.901930	3.156330	3.483446
N	0.551977	4.846556	3.906120
N	5.148702	7.156743	0.211368
N	0.305204	0.846142	7.178198
O	5.056780	2.171529	0.909827
O	0.397126	5.831357	6.479739
O	4.995308	6.173386	2.785025
O	0.458599	1.829499	4.604540
O	2.935057	1.267396	2.812761
O	2.518849	6.735488	4.576805
O	-0.207611	5.269254	0.882170
O	5.661517	2.733631	6.507395
O	2.797045	3.912300	1.729274
O	2.656861	4.090585	5.660292
O	-0.069080	7.914057	1.965308
O	5.522987	0.088828	5.424258
O	7.116532	5.269254	0.882170
O	7.255062	7.914057	1.965308
O	-1.801156	0.088828	5.424258
O	-1.662626	2.733631	6.507395

C. Calculated IR and Raman data

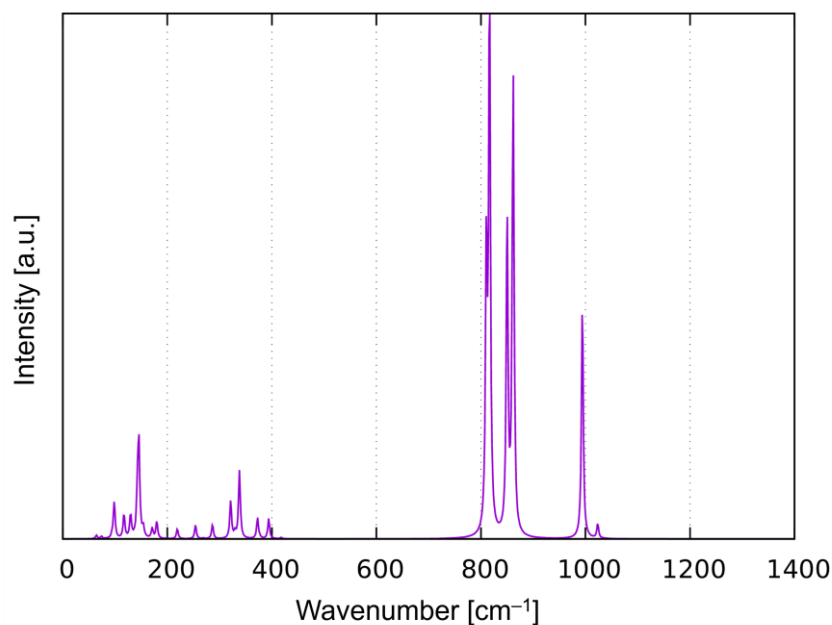


Figure S2. IR spectrum of Ba[TcO₃N] which was calculated by using the PBEsol density functional. Lorentzian line broadening was applied and the highest intensity was arbitrarily set to 100%.

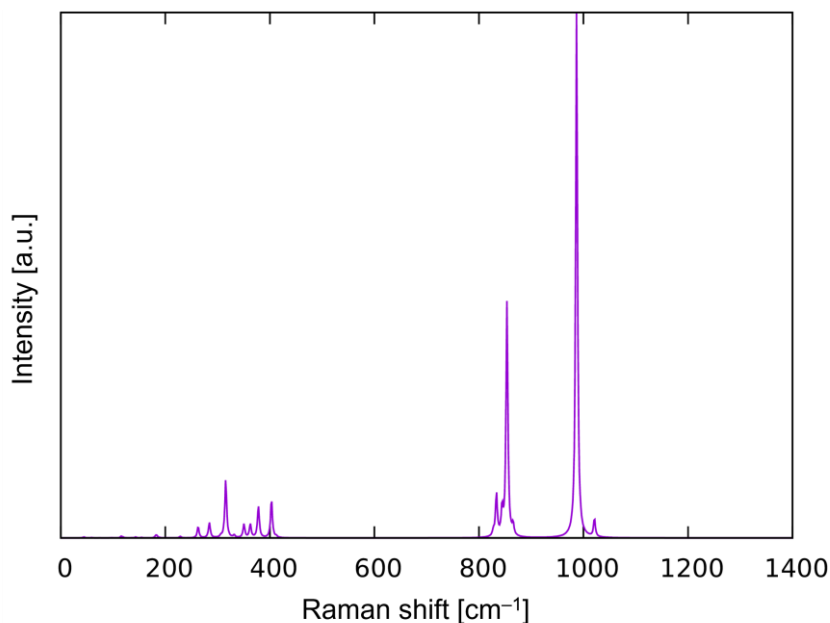


Figure S3. Raman spectrum of Ba[TcO₃N] which was calculated by using the PBEsol density functional. Lorentzian line broadening was applied and the highest intensity was arbitrarily set to 100%.

Table S7. Calculated IR and Raman frequencies, irreducible representation of the vibration and mode classification for Ba[TcO₃N]. The results were obtained with the PBEsol density functional. Abbreviations: ν , stretching; δ , bending; s, symmetric; as, anti-symmetric; A, active; I, inactive.

Frequency [cm ⁻¹]	Irreducible representation	IR	Raman	Mode
40.83	A _g	I	A	δ_{lattice}
42.27	B _g	I	A	δ_{lattice}
44.28	A _g	I	A	δ_{lattice}
54.22	B _g	I	A	δ_{lattice}
57.42	A _u	A	I	δ_{lattice}
58.91	A _g	I	A	δ_{lattice}
64.19	B _u	A	I	$\delta(\text{O-Tc-N})$
69.29	A _u	A	I	δ_{lattice}
73.87	B _u	A	I	δ_{lattice}
74.63	B _g	I	A	δ_{lattice}
94.54	A _u	A	I	δ_{lattice}
94.94	B _g	I	A	δ_{lattice}
97.12	A _g	I	A	$\delta(\text{O-Tc-O})$
98.33	B _u	A	I	δ_{lattice}
115.54	A _g	I	A	δ_{lattice}
116.97	A _u	A	I	δ_{lattice}
118.89	B _g	I	A	δ_{lattice}
124.03	A _g	I	A	δ_{lattice}
129.64	A _u	A	I	δ_{lattice}
135.43	B _g	I	A	δ_{lattice}
142.68	B _u	A	I	δ_{lattice}
143.19	A _g	I	A	δ_{lattice}
145.47	B _u	A	I	δ_{lattice}
153.96	A _u	A	I	δ_{lattice}
154.59	B _g	I	A	δ_{lattice}
170.96	A _u	A	I	$\delta(\text{O-Tc-O})$
179.79	B _u	A	I	$\delta(\text{O-Tc-N})$
181.41	B _g	I	A	$\delta(\text{O-Tc-O})$
183.65	A _g	I	A	$\delta(\text{O-Tc-O})$
189.37	B _g	I	A	$\delta(\text{O-Tc-O})$
199.41	A _u	A	I	$\delta(\text{O-Tc-N})$

219.09	B _u	A	I	$\delta(\text{O-Tc-N})$
228.63	A _g	I	A	$\delta(\text{O-Tc-N})$
253.85	A _u	A	I	$\delta(\text{O-Tc-N})$
262.70	A _g	I	A	$\delta(\text{O-Tc-N})$
268.86	B _u	A	I	$\delta(\text{O-Tc-N})$
284.18	B _g	I	A	$\delta(\text{O-Tc-O})$
286.32	A _u	A	I	$\delta(\text{O-Tc-O})$
306.13	B _g	I	A	$\delta(\text{O-Tc-N})$
315.52	A _g	I	A	$\delta(\text{O-Tc-O})$
321.10	B _u	A	I	$\delta(\text{O-Tc-O})$
329.34	A _u	A	I	$\delta(\text{O-Tc-O})$
331.66	B _g	I	A	$\delta(\text{O-Tc-O})$
337.89	B _u	A	I	$\delta(\text{O-Tc-N})$
350.38	A _g	I	A	$\delta(\text{O-Tc-N})$
362.53	A _g	I	A	$\delta(\text{O-Tc-N})$
372.56	B _u	A	I	$\delta(\text{O-Tc-N})$
376.69	A _u	A	I	$\delta(\text{O-Tc-N})$
377.96	B _g	I	A	$\delta(\text{O-Tc-N})$
393.90	B _u	A	I	$\delta(\text{O-Tc-N})$
403.04	B _g	I	A	$\delta(\text{O-Tc-N})$
412.35	B _g	I	A	$\delta(\text{O-Tc-N})$
417.70	A _u	A	I	$\delta(\text{O-Tc-N})$
810.37	B _u	A	I	$\nu_{\text{as}}(\text{O-Tc-O})$
816.43	A _u	A	I	$\nu_{\text{as}}(\text{O-Tc-O})$
827.55	A _g	I	A	$\nu_{\text{as}}(\text{O-Tc-O})$
833.49	A _g	I	A	$\nu_{\text{s}}(\text{O-Tc-O})$
844.27	B _g	I	A	$\nu_{\text{s}}(\text{O-Tc-O})$
850.12	B _u	A	I	$\nu_{\text{s}}(\text{O-Tc-O})$
853.29	B _g	I	A	$\nu_{\text{s}}(\text{O-Tc-O})$
853.39	A _u	A	I	$\nu_{\text{s}}(\text{O-Tc-O})$
853.66	A _g	I	A	$\nu_{\text{s}}(\text{O-Tc-O})$
860.13	A _u	A	I	$\nu_{\text{s}}(\text{O-Tc-O})$
861.84	B _u	A	I	$\nu_{\text{s}}(\text{O-Tc-O})$
865.33	B _g	I	A	$\nu(\text{Tc-O})$
986.86	A _g	I	A	$\nu(\text{Tc-N})$
994.06	B _u	A	I	$\nu(\text{Tc-N})$
1021.00	B _g	I	A	$\nu(\text{Tc-N})$
1023.46	A _u	A	I	$\nu(\text{Tc-N})$

7.2 $\text{K}_3[\text{MO}_4][\text{MO}_3\text{N}]$ ($M = \text{Tc}, \text{Re}$)

Supporting Information

of

Publication 3

$\text{K}_3[\text{MO}_4][\text{MO}_3\text{N}]$ ($M = \text{Tc}, \text{Re}$) – Nitridotrioxidorhenate and -technetate from Highly Alkaline Media

D. Badea, S. Olthof, J. M. Neudörfl, R. Glaum, R. Pöttgen, M. K. Reimann, K. Meerholz,
M. Reimer, C. Logemann, E. Strub and J. Bruns*

Eur. J. Inorg. Chem. **2023**, e202300160.

doi.org/10.1002/ejic.202300160

Table of Contents

- A. Structure determination and crystallographic details
- B. Spectroscopic methods
- C. Powder X-ray diffraction and Rietveld refinement details

A. Structure determination and crystallographic details

Table S1 Atomic coordinates ($\times 10^4$) and equivalent isotropic displacement parameters ($\text{\AA}^2 \times 10^3$) for $\text{K}_3[\text{TcO}_4][\text{TcO}_3\text{N}]$. $U(eq)$ is defined as one third of the trace of the orthogonalized U_{ij} tensor.

Atom	x	y	z	$U(eq)$
K1	0	0	0	41.0(4)
K2	0	0	8018.7(3)	16.5(1)
N1	4916(1)	-x	2343.7(6)	18.3(2)
N2	0	0	6757(1)	26.8(6)
O1	4916(1)	-x	2343.7(6)	18.3(2)
O2	0	0	6757(1)	26.8(6)
Tc1	0	0	5949.8(2)	9.96(7)

Table S2 Anisotropic displacement parameters ($\text{\AA}^2 \times 10^3$) for $\text{K}_3[\text{TcO}_4][\text{TcO}_3\text{N}]$. The anisotropic displacement factor exponent takes the form: $-2\pi^2 [h^2 a^{*2} U_{11} + 2 h k a^* b^* U_{12} + \dots]$.

Atom	U_{11}	U_{22}	U_{33}	U_{23}	U_{13}	U_{12}
K1	56.0(6)	U_{11}	11.1(4)	0	0	28.0(3)
K2	19.5(2)	U_{11}	10.7(2)	0	0	9.73(9)
N1	18.1(4)	U_{11}	23.6(5)	0.2(2)	$-U_{23}$	12.7(5)
N2	32.0(9)	U_{11}	16(1)	0	0	16.0(4)
O1	18.1(4)	U_{11}	23.6(5)	0.2(2)	$-U_{23}$	12.7(5)
O2	32.0(9)	U_{11}	16(1)	0	0	16.0(4)
Tc1	8.39(7)	U_{11}	13.1(1)	0	0	4.20(4)

Table S3 Bond lengths for $\text{K}_3[\text{TcO}_4][\text{TcO}_3\text{N}]$.

Atom	Atom	Length [\AA]	Atom	Atom	Length [\AA]
K1	O1 ¹⁹	2.778(1)	K2	O1 ¹⁶	3.0842(4)
K1	O1 ²⁰	2.778(1)	K2	O1 ¹⁷	3.0842(4)
K1	O1 ²¹	2.778(1)	K2	O1 ¹⁸	3.0842(4)
K1	O1 ²²	2.778(1)	K2	O2	2.688(3)
K1	O1 ²³	2.778(1)	Tc1	K1 ⁵	3.7696(1)
K1	O1 ²⁴	2.778(1)	Tc1	K1 ⁶	3.7696(2)
K1	O2 ²⁵	3.4519(2)	Tc1	K1 ⁷	3.7696(1)
K1	O2 ²⁶	3.4519(2)	Tc1	K2 ¹	3.7025(3)
K1	O2 ²⁷	3.4519(2)	Tc1	K2 ²	3.7025(3)
K1	O2 ²⁸	3.4519(2)	Tc1	K2 ³	4.3738(4)
K2	N2	2.688(3)	Tc1	K2 ⁴	3.7025(3)
K2	O1 ¹¹	2.781(2)	Tc1	N2	1.718(3)
K2	O1 ¹²	3.0842(4)	Tc1	O1 ⁸	1.737(1)
K2	O1 ¹³	2.781(2)	Tc1	O1 ⁹	1.737(1)
K2	O1 ¹⁴	3.0842(4)	Tc1	O1 ¹⁰	1.737(1)
K2	O1 ¹⁵	2.781(1)	Tc1	O2	1.718(3)

¹-1/3-x,-2/3-y,4/3-z; ²-1/3-x,1/3-y,4/3-z; ³-2/3+x,-1/3+y,-1/3+z; ⁴2/3-x,1/3-y,4/3-z; ⁵1/3+x,2/3+y,2/3+z; ⁶-2/3+x,-1/3+y,2/3+z; ⁷1/3+x,-1/3+y,2/3+z; ⁸-1/3+x,1/3+y,1/3+z; ⁹-1/3-y,-2/3+x-y,1/3+z; ¹⁰2/3+y-x,1/3-x,1/3+z; ¹¹4/3+y-x,2/3-x,2/3+z; ¹²-x,-1-y,1-z; ¹³-2/3-y,-4/3+x-y,2/3+z; ¹⁴1-x,-y,1-z; ¹⁵-2/3+x,2/3+y,2/3+z; ¹⁶1+y,1-x+y,1-z; ¹⁷y,1-x+y,1-z; ¹⁸-1-y+x,-1+x,1-z; ¹⁹-4/3-y+x,-2/3+x,1/3-z; ²⁰-2/3-y,-4/3+x-y,-1/3+z; ²¹2/3+y,4/3-x+y,1/3-z; ²²4/3+y-x,2/3-x,-1/3+z; ²³2/3-x,-2/3-y,1/3-z; ²⁴-2/3+x,2/3+y,-1/3+z; ²⁵-2/3-x,-1/3-y,2/3-z; ²⁶-1/3+x,-2/3+y,-2/3+z; ²⁷2/3+x,1/3+y,-2/3+z; ²⁸1/3-x,2/3-y,2/3-z

Table S4 Bond angles for K₃[TcO₄][TcO₃N].

Atom	Atom	Atom	Angle [°]	Atom	Atom	Atom	Angle [°]
K1 ²⁷	N1	K2 ¹⁴	99.88(3)	N2	K2	O1 ¹¹	139.41(3)
K1 ²⁷	N1	K2 ¹⁵	99.88(3)	N2	K2	O1 ¹²	75.51(3)
K1 ²⁷	N1	K2 ²⁶	98.75(4)	N2	Tc1	O1 ⁹	109.54(5)
K1 ⁵	N2	K1 ⁶	119.696(9)	O1 ¹⁶	K1	O1 ¹⁷	180.00(6)
K1 ⁵	N2	K1 ⁷	119.694(9)	O1 ¹⁸	K1	O1 ¹⁷	68.69(4)
K1 ⁶	N2	K1 ⁷	119.694(9)	O1 ¹⁹	K1	O1 ¹⁷	111.31(4)
K1 ²⁷	O1	K2 ¹⁴	99.88(3)	O1 ²⁰	K1	O1 ¹⁷	111.31(4)
K1 ²⁷	O1	K2 ¹⁵	99.88(3)	O1 ²¹	K1	O1 ¹⁷	68.69(4)
K1 ²⁷	O1	K2 ²⁶	98.75(4)	O1 ¹⁸	K1	O1 ¹⁹	111.31(4)
K1 ⁵	O2	K1 ⁶	119.696(9)	O1 ²⁰	K1	O1 ¹⁹	68.69(4)
K1 ⁵	O2	K1 ⁷	119.694(9)	O1 ¹⁶	K1	O2 ²²	111.55(4)
K1 ⁶	O2	K1 ⁷	119.694(9)	O1 ¹⁷	K1	O2 ²²	68.45(4)
K1 ⁶	Tc1	K1 ⁵	104.711(4)	O1 ¹⁸	K1	O2 ²²	68.45(4)
K1 ⁵	Tc1	K1 ⁷	104.710(4)	O1 ¹⁹	K1	O2 ²²	52.53(5)
K1 ⁶	Tc1	K1 ⁷	104.710(4)	O1 ²⁰	K1	O2 ²²	111.55(4)
K1 ⁵	Tc1	K2 ⁴	61.895(7)	O1 ²¹	K1	O2 ²²	127.47(5)
K1 ⁶	Tc1	K2 ⁴	127.561(2)	O1 ¹⁰	K2	O1 ¹¹	68.60(5)
K1 ⁷	Tc1	K2 ⁴	127.560(2)	O1 ¹⁰	K2	O1 ¹²	136.57(2)
K2 ¹⁵	N1	K2 ¹⁴	150.83(5)	O1 ¹¹	K2	O1 ¹²	102.02(3)
K2 ²⁶	N1	K2 ¹⁵	77.98(3)	O1 ¹³	K2	O1 ¹²	68.62(5)
K2 ²⁶	N1	K2 ¹⁴	77.98(3)	O1 ¹⁴	K2	O1 ¹²	113.96(2)
K2	N2	K1 ⁵	93.18(4)	O1 ¹⁵	K2	O1 ¹²	54.72(5)
K2	N2	K1 ⁶	93.18(4)	O1 ⁸	Tc1	O1 ⁹	109.40(5)
K2	N2	K1 ⁷	93.18(4)	O2 ²³	K1	O2 ²²	119.696(9)
K2 ¹⁵	O1	K2 ¹⁴	150.83(5)	O2 ²⁴	K1	O2 ²²	60.304(9)
K2 ²⁶	O1	K2 ¹⁵	77.98(3)	O2	K2	O1 ¹¹	139.41(3)
K2 ²⁶	O1	K2 ¹⁴	77.98(3)	O2	K2	O1 ¹²	75.51(3)
K2	O2	K1 ⁶	93.18(4)	O2	Tc1	O1 ⁹	109.54(5)
K2	O2	K1 ⁵	93.18(4)	Tc1 ²⁵	N1	K1 ²⁷	111.12(6)
K2	O2	K1 ⁷	93.18(4)	Tc1 ²⁵	N1	K2 ¹⁴	96.32(3)
K2 ¹	Tc1	K1 ⁵	73.883(5)	Tc1 ²⁵	N1	K2 ¹⁵	96.32(3)
K2 ²	Tc1	K1 ⁵	177.54(1)	Tc1 ²⁵	N1	K2 ²⁶	150.13(7)
K2 ³	Tc1	K1 ⁵	73.884(5)	Tc1	N2	K1 ⁵	86.82(4)
K2 ¹	Tc1	K1 ⁶	177.54(1)	Tc1	N2	K1 ⁶	86.82(4)
K2 ²	Tc1	K1 ⁶	73.883(5)	Tc1	N2	K1 ⁷	86.82(4)
K2 ³	Tc1	K1 ⁶	73.884(5)	Tc1	N2	K2	180
K2 ¹	Tc1	K1 ⁷	73.884(5)	Tc1 ²⁵	O1	K1 ²⁷	111.12(6)
K2 ²	Tc1	K1 ⁷	73.884(5)	Tc1 ²⁵	O1	K2 ¹⁴	96.32(3)
K2 ³	Tc1	K1 ⁷	177.54(1)	Tc1 ²⁵	O1	K2 ¹⁵	96.32(3)
K2 ¹	Tc1	K2 ²	107.45(1)	Tc1 ²⁵	O1	K2 ²⁶	150.13(7)
K2 ¹	Tc1	K2 ³	107.45(1)	Tc1	O2	K1 ⁵	86.82(4)
K2 ²	Tc1	K2 ³	107.45(1)	Tc1	O2	K1 ⁶	86.82(4)
K2 ¹	Tc1	K2 ⁴	53.722(5)	Tc1	O2	K1 ⁷	86.82(4)
K2 ²	Tc1	K2 ⁴	120.570(7)	Tc1	O2	K2	180
K2 ³	Tc1	K2 ⁴	53.723(5)				

¹1/3-x,-2/3-y,4/3-z; ²2/3-x,1/3-y,4/3-z; ³1/3-x,1/3-y,4/3-z; ⁴-2/3+x,-1/3+y,-1/3+z; ⁵-2/3+x,-1/3+y,2/3+z; ⁶1/3+x,2/3+y,2/3+z; ⁷1/3+x,-1/3+y,2/3+z; ⁸-1/3+x,1/3+y,1/3+z; ⁹2/3+y-x,1/3-x,1/3+z; ¹⁰-2/3+x,2/3+y,2/3+z; ¹¹4/3+y-x,2/3-x,2/3+z; ¹²-1-y+x,-1+x,1-z; ¹³-2/3-y,-4/3+x-y,2/3+z; ¹⁴-1-x,-y,1-z; ¹⁵-x,-1-y,1-z; ¹⁶-4/3-y+x,-2/3+x,1/3-z; ¹⁷4/3+y-x,2/3-x,-1/3+z; ¹⁸-2/3+x,2/3+y,-1/3+z; ¹⁹2/3+y,4/3-x+y,1/3-z; ²⁰2/3-x,-2/3-y,1/3-z; ²¹-2/3-y,-4/3+x-y,-1/3+z; ²²1/3-x,2/3-y,2/3-z; ²³-2/3-x,-1/3-y,2/3-z; ²⁴2/3+x,1/3+y,-2/3+z; ²⁵1/3+x,-1/3+y,-1/3+z; ²⁶2/3+x,-2/3+y,-2/3+z; ²⁷2/3+x,-2/3+y,1/3+z

Table S5 Atomic occupancy for K₃[TcO₄][TcO₃N].

Atom	Occupancy	Atom	Occupancy
O1	0.875	N1	0.125
O2	0.875	N2	0.125

Table S6 Atomic coordinates (×10⁴) and equivalent isotropic displacement parameters (Å²×10³) for K₃[ReO₄][ReO₃N]. *U*(eq) is defined as one third of the trace of the orthogonalized *U*_{ij} tensor.

Atom	<i>x</i>	<i>y</i>	<i>z</i>	<i>U</i> (eq)
K1	0	0	0	34.1(5)
K2	0	0	8028.9(5)	18.0(2)
N1	4906(2)	- <i>x</i>	2348(1)	18.2(4)
N2	0	0	6774(2)	30(1)
O1	4906(2)	- <i>x</i>	2348(1)	18.2(4)
O2	0	0	6774(2)	30(1)
Re1	0	0	5959.4(2)	8.55(7)

Table S7 Anisotropic displacement parameters (Å²×10³) for K₃[ReO₄][ReO₃N]. The anisotropic displacement factor exponent takes the form: -2π² [*h*² *a*² *U*₁₁ + 2 *h k a*^{*} *b*^{*} *U*₁₂ +...].

Atom	<i>U</i> ₁₁	<i>U</i> ₂₂	<i>U</i> ₃₃	<i>U</i> ₂₃	<i>U</i> ₁₃	<i>U</i> ₁₂
K1	45.0(8)	<i>U</i> ₁₁	12.3(6)	0	0	22.5(4)
K2	20.7(3)	<i>U</i> ₁₁	12.6(3)	0	0	10.3(2)
N1	17.3(7)	<i>U</i> ₁₁	25.2(9)	-0.5(3)	- <i>U</i> ₂₃	12.7(8)
N2	39(2)	<i>U</i> ₁₁	12(2)	0	0	19.6(9)
O1	17.3(7)	<i>U</i> ₁₁	25.2(9)	-0.5(3)	- <i>U</i> ₂₃	12.7(8)
O2	39(2)	<i>U</i> ₁₁	12(2)	0	0	19.6(9)
Re1	7.07(8)	<i>U</i> ₁₁	11.52(9)	0	0	3.53(4)

Table S8 Bond lengths for K₃[ReO₄][ReO₃N].

Atom	Atom	Length [Å]	Atom	Atom	Length [Å]
K1	O1 ¹⁹	2.782(2)	K2	O1 ¹⁶	3.1152(8)
K1	O1 ²⁰	2.782(2)	K2	O1 ¹⁷	3.1152(8)
K1	O1 ²¹	2.782(2)	K2	O1 ¹⁸	3.1152(8)
K1	O1 ²²	2.782(2)	K2	O2	2.661(5)
K1	O1 ²³	2.781(2)	Re1	K1 ⁵	3.7848(3)
K1	O1 ²⁴	2.781(2)	Re1	K1 ⁶	3.7848(3)
K1	O2 ²⁵	3.4822(5)	Re1	K1 ⁷	3.7849(3)
K1	O2 ²⁶	3.4822(5)	Re1	K2 ¹	3.7422(5)
K1	O2 ²⁷	3.4822(5)	Re1	K2 ²	3.7422(5)
K1	O2 ²⁸	3.4822(5)	Re1	K2 ³	4.3891(8)
K2	N2	2.661(5)	Re1	K2 ⁴	3.7422(5)
K2	O1 ¹¹	2.783(3)	Re1	N2	1.729(4)
K2	O1 ¹²	3.1152(8)	Re1	O1 ⁸	1.742(2)
K2	O1 ¹³	2.783(3)	Re1	O1 ⁹	1.742(2)
K2	O1 ¹⁴	3.1152(8)	Re1	O1 ¹⁰	1.742(2)
K2	O1 ¹⁵	2.783(3)	Re1	O2	1.729(4)

¹-1/3-*x*, -2/3-*y*, 4/3-*z*; ²-1/3-*x*, 1/3-*y*, 4/3-*z*; ³-2/3+*x*, -1/3+*y*, -1/3+*z*; ⁴2/3-*x*, 1/3-*y*, 4/3-*z*; ⁵1/3+*x*, 2/3+*y*, 2/3+*z*; ⁶-2/3+*x*, -1/3+*y*, 2/3+*z*; ⁷1/3+*x*, -1/3+*y*, 2/3+*z*; ⁸2/3+*y*, -1/3-*x*, 1/3+*z*; ⁹-1/3+*x*, 1/3+*y*, 1/3+*z*; ¹⁰-1/3-*y*, -2/3+*x*, -1/3+*z*; ¹¹4/3+*y*, -2/3-*x*, 2/3+*z*; ¹²-1-*y*+*x*, -1+*x*, 1-*z*; ¹³-2/3-*y*, -4/3+*x*, -2/3+*z*; ¹⁴1+*y*, 1-*x*+*y*, 1-*z*; ¹⁵-2/3+*x*, 2/3+*y*, 2/3+*z*; ¹⁶+*y*, 1-*x*+*y*, 1-*z*; ¹⁷1-*x*, -*y*, 1-*z*; ¹⁸-*x*, -1-*y*, 1-*z*; ¹⁹-4/3-*y*+*x*, -2/3+*x*, 1/3-*z*; ²⁰-2/3-*y*, -4/3+*x*, -1/3+*z*; ²¹2/3+*y*, 4/3-*x*+*y*, 1/3-*z*; ²²4/3+*y*, -2/3-*x*, -1/3+*z*; ²³2/3-*x*, -2/3-*y*, 1/3-*z*; ²⁴-2/3+*x*, 2/3+*y*, -1/3+*z*; ²⁵-2/3-*x*, -1/3-*y*, 2/3-*z*; ²⁶-1/3+*x*, -2/3+*y*, -2/3+*z*; ²⁷2/3+*x*, 1/3+*y*, -2/3+*z*; ²⁸1/3-*x*, 2/3-*y*, 2/3-*z*

Table S9 Bond angles for K₃[ReO₄][ReO₃N].

Atom	Atom	Atom	Angle [°]	Atom	Atom	Atom	Angle [°]
K1 ²⁶	N1	K2 ²³	97.46(7)	K2 ²	Re1	K2 ⁴	120.54(1)
K1 ²⁶	N1	K2 ²⁴	99.92(5)	K2 ³	Re1	K2 ⁴	53.532(8)
K1 ²⁶	N1	K2 ²⁵	99.92(5)	N2	K2	O1 ¹⁰	138.74(5)
K1 ⁵	N2	K1 ⁶	119.57(2)	N2	K2	O1 ¹²	75.12(5)
K1 ⁵	N2	K1 ⁷	119.57(2)	N2	Re1	O1 ⁸	109.78(8)
K1 ⁶	N2	K1 ⁷	119.57(2)	O1 ¹³	K1	O1 ¹⁴	69.69(8)
K1 ²⁶	O1	K2 ²⁴	99.92(5)	O1 ¹⁵	K1	O1 ¹⁴	69.69(8)
K1 ²⁶	O1	K2 ²⁵	99.92(5)	O1 ¹⁶	K1	O1 ¹⁴	110.31(8)
K1 ²⁶	O1	K2 ²³	97.46(7)	O1 ¹⁷	K1	O1 ¹⁴	110.31(8)
K1 ⁵	O2	K1 ⁶	119.57(2)	O1 ¹⁸	K1	O1 ¹⁴	180.00(7)
K1 ⁵	O2	K1 ⁷	119.57(2)	O1 ¹⁵	K1	O1 ¹⁶	110.31(8)
K1 ⁶	O2	K1 ⁷	119.57(2)	O1 ¹⁷	K1	O1 ¹⁶	69.69(8)
K1 ⁶	Re1	K1 ⁵	105.324(5)	O1 ¹³	K1	O2 ¹⁹	127.52(9)
K1 ⁵	Re1	K1 ⁷	105.323(5)	O1 ¹⁴	K1	O2 ¹⁹	67.76(6)
K1 ⁶	Re1	K1 ⁷	105.323(5)	O1 ¹⁵	K1	O2 ¹⁹	67.76(6)
K1 ⁵	Re1	K2 ⁴	61.01(1)	O1 ¹⁶	K1	O2 ¹⁹	52.48(9)
K1 ⁶	Re1	K2 ⁴	127.273(2)	O1 ¹⁷	K1	O2 ¹⁹	112.24(6)
K1 ⁷	Re1	K2 ⁴	127.272(2)	O1 ¹⁸	K1	O2 ¹⁹	112.24(6)
K2 ²³	N1	K2 ²⁴	77.66(5)	O1 ⁹	K2	O1 ¹⁰	69.66(8)
K2 ²⁵	N1	K2 ²⁴	150.0(1)	O1 ¹⁰	K2	O1 ¹²	102.34(5)
K2 ²³	N1	K2 ²⁵	77.66(5)	O1 ¹¹	K2	O1 ¹²	68.34(9)
K2	N2	K1 ⁵	93.77(7)	O1 ⁹	K2	O1 ¹²	137.25(3)
K2	N2	K1 ⁶	93.77(7)	O2 ²⁰	K1	O2 ¹⁹	119.57(2)
K2	N2	K1 ⁷	93.77(7)	O2 ²¹	K1	O2 ¹⁹	60.43(2)
K2 ²³	O1	K2 ²⁴	77.66(5)	O2	K2	O1 ¹⁰	138.74(5)
K2 ²⁵	O1	K2 ²⁴	150.0(1)	O2	K2	O1 ¹²	75.12(5)
K2 ²³	O1	K2 ²⁵	77.66(5)	O2	Re1	O1 ⁸	109.78(8)
K2	O2	K1 ⁵	93.77(7)	Re1 ²²	N1	K2 ²³	151.0(1)
K2	O2	K1 ⁶	93.77(7)	Re1 ²²	N1	K2 ²⁴	96.68(5)
K2	O2	K1 ⁷	93.77(7)	Re1 ²²	N1	K2 ²⁵	96.68(5)
K2 ¹	Re1	K1 ⁵	73.80(1)	Re1 ²²	N1	K1 ²⁶	111.5(1)
K2 ²	Re1	K1 ⁵	178.44(2)	Re1	N2	K1 ⁵	86.23(7)
K2 ³	Re1	K1 ⁵	73.80(1)	Re1	N2	K1 ⁶	86.23(7)
K2 ¹	Re1	K1 ⁶	178.44(2)	Re1	N2	K1 ⁷	86.23(7)
K2 ²	Re1	K1 ⁶	73.80(1)	Re1	N2	K2	180
K2 ³	Re1	K1 ⁶	73.798(9)	Re1 ²²	O1	K2 ²³	151.0(1)
K2 ¹	Re1	K1 ⁷	73.798(9)	Re1 ²²	O1	K2 ²⁴	96.68(5)
K2 ²	Re1	K1 ⁷	73.80(1)	Re1 ²²	O1	K2 ²⁵	96.68(5)
K2 ³	Re1	K1 ⁷	178.44(2)	Re1 ²²	O1	K1 ²⁶	111.5(1)
K2 ¹	Re1	K2 ²	107.05(2)	Re1	O2	K1 ⁵	86.23(7)
K2 ¹	Re1	K2 ³	107.05(2)	Re1	O2	K1 ⁶	86.23(7)
K2 ²	Re1	K2 ³	107.05(2)	Re1	O2	K1 ⁷	86.23(7)
K2 ¹	Re1	K2 ⁴	53.531(8)	Re1	O2	K2	180

¹_{1/3-x,-2/3-y,4/3-z}; ²_{2/3-x,1/3-y,4/3-z}; ³_{1/3-x,1/3-y,4/3-z}; ⁴_{2/3+x,-1/3+y,-1/3+z}; ⁵_{2/3+x,-1/3+y,2/3+z}; ⁶_{1/3+x,2/3+y,2/3+z}; ⁷_{1/3+x,-1/3+y,2/3+z}; ⁸_{2/3+y-x,1/3-x,1/3+z}; ⁹_{2/3+x,2/3+y,2/3+z}; ¹⁰_{4/3+y-x,2/3-x,2/3+z}; ¹¹_{2/3-y,-4/3+x-y,2/3+z}; ¹²_{1-y+x,-1+x,1-z}; ¹³_{2/3-y,-4/3+x-y,-1/3+z}; ¹⁴_{4/3+y-x,2/3-x,-1/3+z}; ¹⁵_{2/3+x,2/3+y,-1/3+z}; ¹⁶_{2/3+y,4/3-x+y,1/3-z}; ¹⁷_{2/3-x,-2/3-y,1/3-z}; ¹⁸_{4/3-y+x,-2/3+x,1/3-z}; ¹⁹_{1/3-x,2/3-y,2/3-z}; ²⁰_{2/3-x,-1/3-y,2/3-z}; ²¹_{2/3+x,1/3+y,-2/3+z}; ²²_{1/3+x,-1/3+y,-1/3+z}; ²³_{2/3+x,-2/3+y,-2/3+z}; ²⁴_{1-x,-y,1-z}; ²⁵_{-x,-1-y,1-z}; ²⁶_{2/3+x,-2/3+y,1/3+z}

Table S10 Atomic occupancy for K₃[ReO₄][ReO₃N].

Atom	Occupancy	Atom	Occupancy
O1	0.875	N1	0.125
O2	0.875	N2	0.125

Table S11 Examples of coloring variants for $\text{Ba}_3[\text{PO}_4]_2$ / $\text{K}_2\text{Pb}[\text{SO}_4]_2$ type representatives (space group $R\bar{3}m$, Pearson code $hR39$ and Wyckoff sequence hc^3a).

Compound	3a	6c	6c	18h	6c	Ref.
$\text{Ba}_3[\text{PO}_4]_2$	Ba	Ba	P	O	O	[33a]
$\text{Eu}_3[\text{PO}_4]_2$	Ba	Ba	P	O	O	[33b]
$\text{K}_2\text{Pb}[\text{BeF}_4]_2$	Pb	K	Be	F	F	[33c]
$\text{K}_3[\text{Re}(\text{O}_{0.875}\text{N}_{0.125})_4]_2$	K	K	Re	O	O/N	this work
$\text{Ba}_3[(\text{Ti}/\text{Mo})\text{O}_4]_2$	Ba	Ba	Ti/Mo	O	O	[33d]
$\text{Ba}_3[\text{MoO}_3\text{N}]_2$	Ba	Ba	Mo	O/N	O/N	[17a]
$\text{Ba}_3[\text{WO}_3\text{N}]_2$	Ba	Ba	W	O/N	O/N	[17a]
$\text{Ba}_3\text{Mo}_2\text{O}_{6.04}\text{N}_{1.96}$	Ba	Ba	Mo	O/N	O/N	[17b]
$\text{Ba}_3\text{W}_2\text{O}_{6.27}\text{N}_{1.73}$	Ba	Ba	W	O/N	O/N	[17b]
$\text{SrRb}_2[\text{SO}_4]_2$	Sr	Rb	S	O	O	[33e]
$\text{SrRb}_2[\text{SeO}_4]_2$	Sr	Rb	Se	O	O	[33f]
$\text{SrTl}_2[\text{SO}_4]_2$	Sr	Tl	S	O	O	[33e]
$\text{SnTl}_2[\text{SO}_4]_2$	Sn	Tl	S	O	O	[33g]
$\text{PbRb}_2[\text{SO}_4]_2$	Pb	Rb	S	O	O	[33h]
$\text{Ba}_3[\text{VO}_4]_2$	Ba	Ba	V	O	O	[33i]
$\text{Pb}_3[\text{VO}_4]_2$	Pb	Pb	V	O	O	[33j]
$\text{K}_2\text{Pb}[\text{SO}_4]_2$	Pb	K	S	O	O	[33j]
$\text{NaBaLa}[\text{VO}_4]_2$	Na/Ba/La	Na/Ba/La	V	O	O	[33k]
$\text{Ba}_3[\text{CrO}_4]_2$	Ba	Ba	Cr	O	O	[33l]
$\text{K}_2\text{Pb}[\text{CrO}_4]_2$	Pb	K	Cr	O	O	[33l]
$\text{K}_2\text{Ba}[\text{MoO}_4]_2$	Ba	K	Mo	O	O	[33m]

B. Spectroscopic Methods

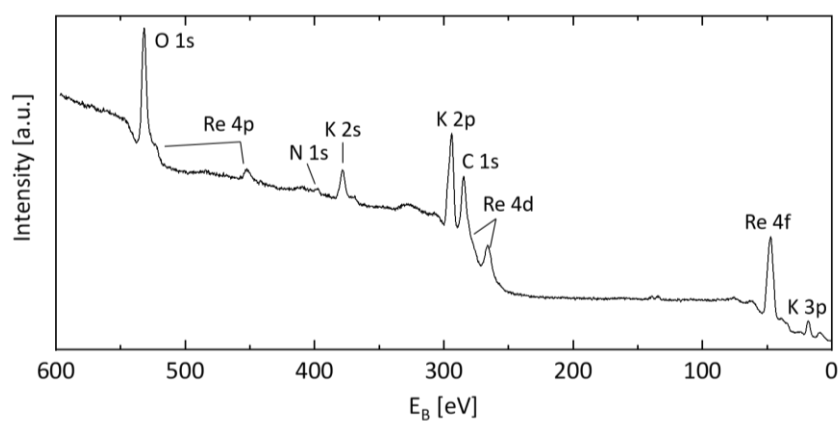


Figure S1 XPS core level spectrum of $K_3[ReO_4][ReO_3N]$ powder on a carbon coated Cu film.

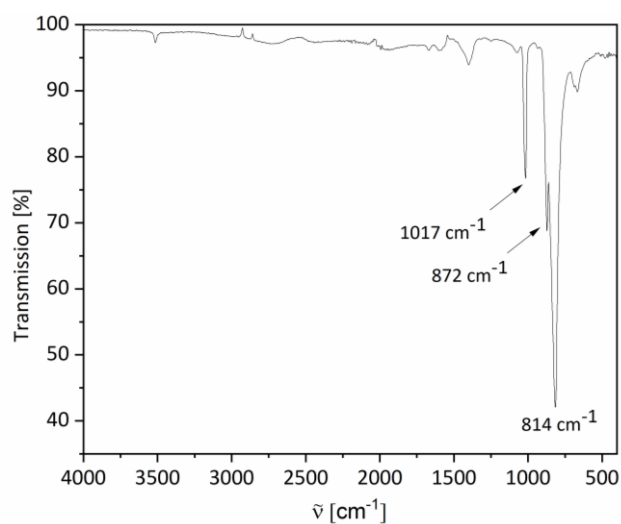


Figure S2 IR spectrum of $K_2[ReO_3N]$, synthesized according to the literature.^[12]

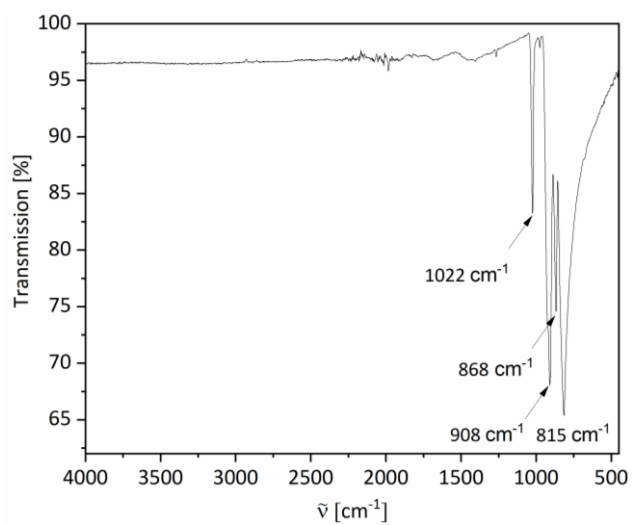


Figure S3 IR spectrum of $K_3[ReO_4][ReO_3N]$.

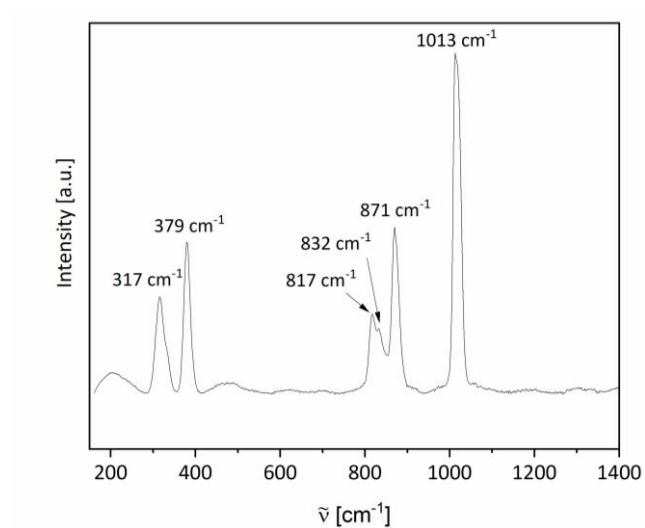


Figure S4 Raman spectrum of $K_2[ReO_3N]$, synthesized according to the literature. ^[12]

C. Powder X-ray diffraction and Rietveld refinement details

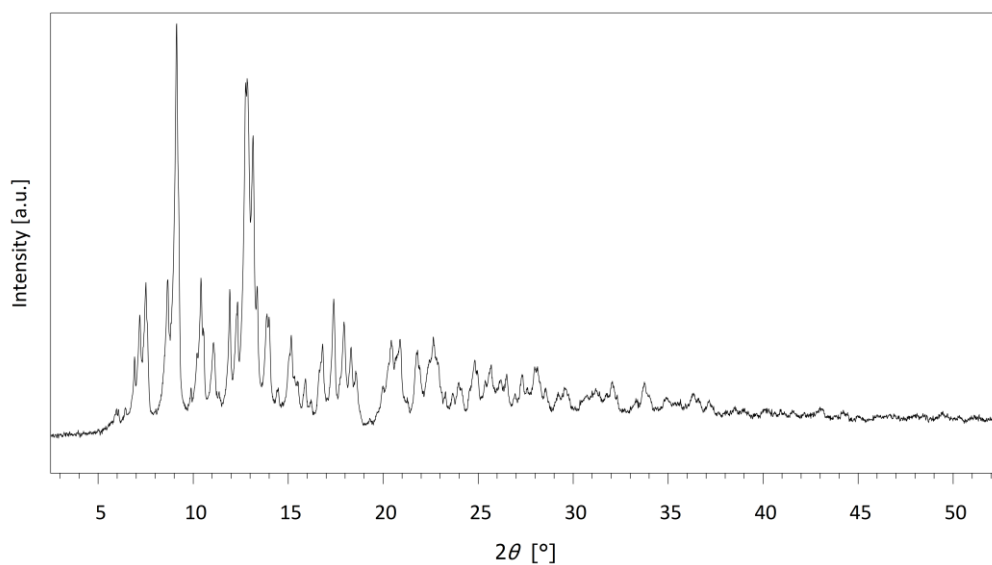


Figure S5 Powder X-ray diffraction pattern of $K_2[ReO_3N]$, synthesized according to the literature. ^[12]

Table S12 Lattice parameters and refinement factors for the Rietveld fit of the ambient temperature powder diffraction pattern of $K_3[ReO_4][ReO_3N]$.

Lattice parameters	$a = 6.0674(1) \text{ \AA}$	Refinement factors	$R_{wp} = 9.83$
	$c = 21.3109(8) \text{ \AA}$		$R_{exp} = 9.44$
	$V = 679.42(4) \text{ \AA}^3$		$R_p = 7.79$
			$gof = 1.04$

7.3 $A_3[\text{ReO}_4][\text{ReO}_3\text{N}]$ and $A'_2[\text{ReO}_3\text{N}]$ ($A = \text{Rb}, \text{Cs}$; $A' = \text{K}, \text{Cs}$)

Supporting Information

of

Publication 4

**Synthesis and Characterization of $A_3[\text{ReO}_4][\text{ReO}_3\text{N}]$ and $A'_2[\text{ReO}_3\text{N}]$
($A = \text{Rb}, \text{Cs}$; $A' = \text{K}, \text{Cs}$)**

D. Badea, C. Lenting, M. Hanrath and J. Bruns*

Eur. J. Inorg. Chem. **2025**, 28, e202500036.

Table of Contents

- A. Spectroscopic methods
- B. Powder X-ray diffraction and Rietveld refinement details
- C. Structure determination and crystallographic details
- D. Calculated Raman data

A. Spectroscopic methods

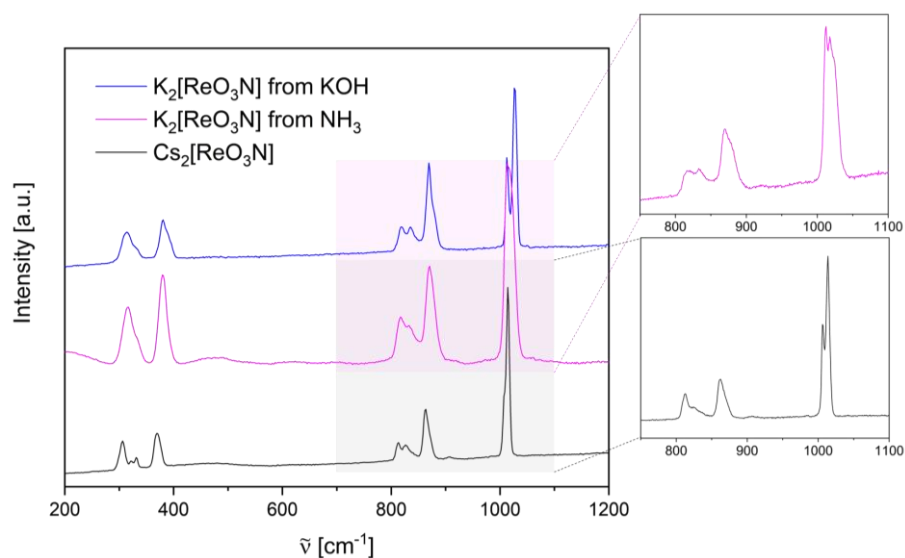


Figure S1. Raman spectra of $K_2[ReO_3N]$ synthesized from a KOH hydroflux, of $K_2[ReO_3N]$ synthesized in liquid NH_3 according to a literature procedure and of $Cs_2[ReO_3N]$ from a CsOH hydroflux.^[1] The cutouts of the spectra were measured using the same samples but at a higher resolution compared to the overall measurement range.

B. Powder X-ray diffraction and Rietveld refinement details

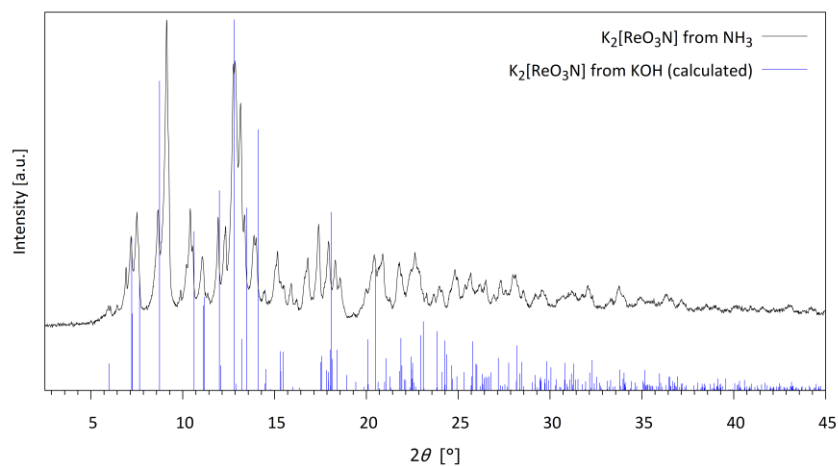


Figure S2. Powder X-ray diffraction pattern of $K_2[ReO_3N]$ synthesized in liquid NH_3 according to a literature procedure and calculated pattern of single crystal data of $K_2[ReO_3N]$ synthesized from a KOH hydroflux.^[1]

Table S1. Lattice parameters and refinement factors for the Rietveld fit of the ambient temperature powder diffraction pattern of $Rb_3[ReO_4][ReO_3N]$.

Lattice parameters	$a = 6.2208(2) \text{ \AA}$	Refinement factors	$R_{wp} = 5.87$
	$c = 22.2003(9) \text{ \AA}$		$R_{exp} = 6.63$
	$V = 744.02(6) \text{ \AA}^3$		$R_p = 4.61$
			$gof = 0.89$

Table S2. Lattice parameters and refinement factors for the Rietveld fit of the ambient temperature powder diffraction pattern of Cs₃[ReO₄][ReO₃N].

Lattice parameters	$a = 6.4468(3) \text{ \AA}$ $c = 23.284(2) \text{ \AA}$ $V = 838.1(1) \text{ \AA}^3$	Refinement factors	$R_{wp} = 18.05$ $R_{exp} = 18.68$ $R_p = 14.12$ $gof = 0.97$
--------------------	--	--------------------	--

C. Structure determination and crystallographic details

The structures of A₃[ReO₄][ReO₃N] (A = Rb, Cs) were refined with a 7 : 1 O/N ratio and the structures of A'₂[ReO₄] (A' = K, Cs) were refined with a 3 : 1 O/N ratio using EADP and EXYZ with ShelX in Olex2.^[2]

Rb₃[ReO₄][ReO₃N]

Table S3. Atomic coordinates ($\times 10^4$), equivalent isotropic displacement parameters ($\text{\AA}^2 \times 10^3$) and Wyckoff positions for Rb₃[ReO₄][ReO₃N]. $U(eq)$ is defined as one third of the trace of the orthogonalized U_{ij} tensor.

Atom	Wyckoff position	x	y	z	$U(eq)$
N1	18h	4866(4)	5134(4)	2343(2)	20.6(9)
N2	6c	0	0	6725(4)	36(2)
O1	18h	4866(4)	5134(4)	2343(2)	20.6(9)
O2	6c	0	0	6725(4)	36(2)
Rb1	3a	0	0	0	33.4(4)
Rb2	6c	0	0	8005.3(4)	16.8(2)
Re1	6c	0	0	5950.0(2)	12.9(1)

Table S4. Anisotropic displacement parameters ($\text{\AA}^2 \times 10^3$) for Rb₃[ReO₄][ReO₃N]. The anisotropic displacement factor exponent takes the form: $-2\pi^2 [h^2 a^{*2} U_{11} + 2 h k a^* b^* U_{12} + \dots]$.

Atom	U_{11}	U_{22}	U_{33}	U_{23}	U_{13}	U_{12}
N1	19(2)	19(2)	29(2)	-0.9(8)	0.9(8)	13(2)
N2	47(4)	47(4)	15(4)	0	0	23(2)
O1	19(2)	19(2)	29(2)	-0.9(8)	0.9(8)	13(2)
O2	47(4)	47(4)	15(4)	0	0	23(2)
Rb1	43.1(6)	43.1(6)	13.8(6)	0	0	21.6(3)
Rb2	17.1(3)	17.1(3)	16.3(4)	0	0	8.6(2)
Re1	11.3(2)	11.3(2)	16.1(2)	0	0	5.65(8)

Table S5. Bond lengths for Rb₃[ReO₄][ReO₃N].

Atom	Atom	Length [\AA]	Atom	Atom	Length [\AA]
Rb1	O1 ¹⁸	2.912(4)	Rb2	O1 ¹³	3.185(1)
Rb1	O1 ¹⁹	2.912(4)	Rb2	O1 ¹⁴	2.936(4)
Rb1	O1 ²⁰	2.912(4)	Rb2	O1 ¹⁵	3.185(1)
Rb1	O1 ²¹	2.912(4)	Rb2	O1 ¹⁶	3.185(1)
Rb1	O1 ²²	2.912(4)	Rb2	O1 ¹⁷	3.185(1)
Rb1	O1 ²³	2.912(4)	Rb2	O2	2.825(8)
Rb1	O2 ²⁴	3.5673(4)	Re1	N2	1.710(8)
Rb1	O2 ²⁵	3.5673(4)	Re1	O1 ⁷	1.747(4)
Rb1	O2 ²⁶	3.5673(4)	Re1	O1 ⁸	1.747(4)
Rb1	O2 ²⁷	3.5673(4)	Re1	O1 ⁹	1.747(4)
Rb1	O2 ²⁸	3.5673(4)	Re1	O2	1.710(8)
Rb1	O2 ²⁹	3.5673(4)	Re1	Rb1 ⁴	3.8998(2)
Rb2	N2	2.825(8)	Re1	Rb1 ⁵	3.8998(2)
Rb2	O1 ⁵	2.936(4)	Re1	Rb1 ⁶	3.8999(2)
Rb2	O1 ¹⁰	2.936(4)	Re1	Rb2 ¹	3.8199(4)
Rb2	O1 ¹¹	3.185(1)	Re1	Rb2 ²	3.8199(4)
Rb2	O1 ¹²	3.185(1)	Re1	Rb2 ³	3.8199(4)

¹-1/3-x,-2/3-y,4/3-z, ²2/3-x,1/3-y,4/3-z, ³-1/3-x,1/3-y,4/3-z, ⁴1/3+x,2/3+y,2/3+z, ⁵-2/3+x,-1/3+y,2/3+z, ⁶1/3+x,1/3+y,2/3+z, ⁷-1/3+y,-x,1/3-x,1/3+z, ⁸-1/3+x,2/3+y,1/3+z, ⁹2/3-y,1/3+x-y,1/3+z, ¹⁰1/3+y-x,2/3-x,2/3+z, ¹¹1-x,1-y,1-z, ¹²-1+y,-x+y,1-z, ¹³+y,-x+y,1-z, ¹⁴1/3-y,-1/3+x-y,2/3+z, ¹⁵-y+x,-1+x,1-z, ¹⁶-x,-y,1-z, ¹⁷-y+x,x,1-z, ¹⁸-1/3+y,1/3-x+y,1/3-z, ¹⁹1/3+y-x,2/3-x,1/3+z, ²⁰1/3-y,-1/3+x-y,-1/3+z, ²¹2/3-x,1/3-y,1/3-z, ²²-2/3+x,-1/3+y,-1/3+z, ²³-1/3-y+x,-2/3+x,1/3-z, ²⁴-2/3-x,-1/3-y,2/3-z, ²⁵-1/3+x,-2/3+y,-2/3+z, ²⁶-1/3+x,1/3+y,-2/3+z, ²⁷1/3-x,2/3-y,2/3-z, ²⁸2/3+x,1/3+y,-2/3+z, ²⁹1/3-x,-1/3-y,2/3-z.

Table S6. Bond angles for Rb₃[ReO₄][ReO₃N].

Atom	Atom	Atom	Angle [°]	Atom	Atom	Atom	Angle [°]
N2	Rb2	O1 ¹⁵	139.01(9)	O1 ⁹	Re1	Rb1 ⁴	124.68(4)
N2	Rb2	O1 ¹⁶	76.03(8)	O1 ⁷	Re1	Rb1 ⁵	124.68(4)
N2	Rb2	O1 ¹⁷	76.03(8)	O1 ⁸	Re1	Rb1 ⁵	124.68(4)
N2	Re1	O1 ⁷	110.2(2)	O1 ⁹	Re1	Rb1 ⁵	44.12(14)
O1 ¹⁸	Rb1	O1 ¹⁹	180.0(1)	O1 ⁷	Re1	Rb1 ⁶	124.68(4)
O1 ¹⁸	Rb1	O1 ²⁰	69.9(1)	O1 ⁸	Re1	Rb1 ⁶	44.1(1)
O1 ¹⁹	Rb1	O1 ²⁰	110.1(1)	O1 ⁹	Re1	Rb1 ⁶	124.68(4)
O1 ¹⁸	Rb1	O1 ²¹	110.1(1)	O1 ⁷	Re1	Rb2 ¹	55.81(3)
O1 ¹⁹	Rb1	O1 ²¹	69.9(1)	O1 ⁸	Re1	Rb2 ¹	138.8(2)
O1 ²⁰	Rb1	O1 ²¹	110.1(1)	O1 ⁹	Re1	Rb2 ¹	55.81(3)
O1 ²²	Rb1	O1 ²¹	180.0(1)	O1 ⁷	Re1	Rb2 ²	138.8(2)
O1 ²³	Rb1	O1 ²¹	69.9(1)	O1 ⁸	Re1	Rb2 ²	55.81(3)
O1 ¹⁸	Rb1	O1 ²²	69.9(1)	O1 ⁹	Re1	Rb2 ²	55.81(3)
O1 ¹⁹	Rb1	O1 ²²	110.1(1)	O1 ⁷	Re1	Rb2 ³	55.81(3)
O1 ²⁰	Rb1	O1 ²²	69.9(1)	O1 ⁸	Re1	Rb2 ³	55.81(3)
O1 ²³	Rb1	O1 ²²	110.1(1)	O1 ⁹	Re1	Rb2 ³	138.8(2)
O1 ¹⁸	Rb1	O1 ²³	110.1(1)	O2 ²⁴	Rb1	O2 ²⁵	60.13(2)
O1 ¹⁹	Rb1	O1 ²³	69.9(1)	O2 ²⁶	Rb1	O2 ²⁵	60.13(2)
O1 ²⁰	Rb1	O1 ²³	180.0(1)	O2 ²⁷	Rb1	O2 ²⁵	119.87(2)
O1 ¹⁸	Rb1	O2 ²⁴	111.0(1)	O2 ²⁸	Rb1	O2 ²⁵	180
O1 ¹⁹	Rb1	O2 ²⁴	69.1(1)	O2 ²⁹	Rb1	O2 ²⁵	119.87(2)
O1 ²⁰	Rb1	O2 ²⁴	111.0(1)	O2 ²⁴	Rb1	O2 ²⁶	119.87(2)
O1 ²¹	Rb1	O2 ²⁴	129.3(2)	O2 ²⁹	Rb1	O2 ²⁶	60.13(2)
O1 ²²	Rb1	O2 ²⁴	50.7(2)	O2 ²⁴	Rb1	O2 ²⁷	60.13(2)
O1 ²³	Rb1	O2 ²⁴	69.1(1)	O2 ²⁶	Rb1	O2 ²⁷	180
O1 ¹⁸	Rb1	O2 ²⁵	129.3(2)	O2 ²⁹	Rb1	O2 ²⁷	119.87(2)
O1 ¹⁹	Rb1	O2 ²⁵	50.7(2)	O2 ²⁴	Rb1	O2 ²⁸	119.87(2)
O1 ²⁰	Rb1	O2 ²⁵	69.1(1)	O2 ²⁶	Rb1	O2 ²⁸	119.87(2)
O1 ²¹	Rb1	O2 ²⁵	111.0(1)	O2 ²⁷	Rb1	O2 ²⁸	60.13(2)
O1 ²²	Rb1	O2 ²⁵	69.1(1)	O2 ²⁹	Rb1	O2 ²⁸	60.13(2)
O1 ²³	Rb1	O2 ²⁵	111.0(1)	O2 ²⁴	Rb1	O2 ²⁹	180
O1 ¹⁸	Rb1	O2 ²⁶	111.0(1)	O2	Rb2	O1 ⁴	139.02(9)
O1 ¹⁹	Rb1	O2 ²⁶	69.1(1)	O2	Rb2	O1 ¹⁰	76.03(8)
O1 ²⁰	Rb1	O2 ²⁶	50.7(2)	O2	Rb2	O1 ¹¹	139.01(9)
O1 ²¹	Rb1	O2 ²⁶	69.1(1)	O2	Rb2	O1 ¹²	76.03(8)
O1 ²²	Rb1	O2 ²⁶	111.0(1)	O2	Rb2	O1 ¹³	76.03(8)
O1 ²³	Rb1	O2 ²⁶	129.3(2)	O2	Rb2	O1 ¹⁴	76.03(8)
O1 ¹⁸	Rb1	O2 ²⁷	69.1(1)	O2	Rb2	O1 ¹⁵	139.01(9)
O1 ¹⁹	Rb1	O2 ²⁷	111.0(1)	O2	Rb2	O1 ¹⁶	76.03(8)
O1 ²⁰	Rb1	O2 ²⁷	129.3(2)	O2	Rb2	O1 ¹⁷	76.03(8)
O1 ²¹	Rb1	O2 ²⁷	111.0(1)	O2	Rb2	Re1 ¹	68.95(1)
O1 ²²	Rb1	O2 ²⁷	69.1(1)	O2	Re1	O1 ⁷	110.2(2)
O1 ²³	Rb1	O2 ²⁷	50.7(2)	O2	Re1	O1 ⁸	110.2(2)
O1 ¹⁸	Rb1	O2 ²⁸	50.7(2)	O2	Re1	O1 ⁹	110.2(1)
O1 ¹⁹	Rb1	O2 ²⁸	129.3(2)	O2	Re1	Rb1 ⁴	66.083(5)
O1 ²⁰	Rb1	O2 ²⁸	111.0(1)	O2	Re1	Rb1 ⁵	66.083(5)
O1 ²¹	Rb1	O2 ²⁸	69.1(1)	O2	Re1	Rb1 ⁶	66.083(6)
O1 ²²	Rb1	O2 ²⁸	111.0(1)	O2	Re1	Rb2 ¹	111.05(1)
O1 ²³	Rb1	O2 ²⁸	69.1(1)	O2	Re1	Rb2 ²	111.05(1)
O1 ¹⁸	Rb1	O2 ²⁹	69.1(1)	O2	Re1	Rb2 ³	111.05(1)
O1 ¹⁹	Rb1	O2 ²⁹	111.0(1)	Rb1 ³¹	N1	Rb2 ¹²	98.71(8)
O1 ²⁰	Rb1	O2 ²⁹	69.1(1)	Rb1 ³¹	N1	Rb2 ¹⁴	98.71(8)
O1 ²¹	Rb1	O2 ²⁹	50.7(2)	Rb1 ³¹	N1	Rb2 ²⁹	97.6(1)
O1 ²²	Rb1	O2 ²⁹	129.3(2)	Rb1 ⁴	N2	Rb1 ⁵	119.87(2)
O1 ²³	Rb1	O2 ²⁹	111.0(1)	Rb1 ⁶	N2	Rb1 ⁵	119.87(2)
O1 ¹¹	Rb2	O1 ¹⁰	102.22(8)	Rb1 ⁴	N2	Rb1 ⁶	119.87(2)
O1 ¹⁵	Rb2	O1 ¹⁰	67.5(2)	Rb1 ³¹	O1	Rb2 ¹²	98.71(8)
O1 ¹⁶	Rb2	O1 ¹⁰	63.1(2)	Rb1 ³¹	O1	Rb2 ¹⁴	98.71(8)
O1 ⁴	Rb2	O1 ¹⁰	135.90(3)	Rb1 ³¹	O1	Rb2 ²⁹	97.6(1)
O1 ¹⁵	Rb2	O1 ¹¹	69.2(1)	Rb1 ⁴	O2	Rb1 ⁵	119.87(2)

O1 ⁴	Rb2	O1 ¹¹	69.2(1)	Rb1 ⁶	O2	Rb1 ⁵	119.87(2)
O1 ¹⁰	Rb2	O1 ¹²	114.37(6)	Rb1 ⁴	O2	Rb1 ⁶	119.87(2)
O1 ¹¹	Rb2	O1 ¹²	67.5(2)	Rb1 ⁶	Re1	Rb1 ⁴	104.683(6)
O1 ¹⁵	Rb2	O1 ¹²	135.90(3)	Rb1 ⁴	Re1	Rb1 ⁵	104.682(6)
O1 ¹⁶	Rb2	O1 ¹²	53.0(2)	Rb1 ⁶	Re1	Rb1 ⁵	104.682(6)
O1 ⁴	Rb2	O1 ¹²	102.22(8)	Rb2	O2	Rb1 ⁴	92.1(1)
O1 ¹⁰	Rb2	O1 ¹³	151.6(2)	Rb2	O2	Rb1 ⁵	92.1(1)
O1 ¹¹	Rb2	O1 ¹³	102.22(8)	Rb2	O2	Rb1 ⁶	92.1(1)
O1 ¹²	Rb2	O1 ¹³	63.14(16)	Rb2	N2	Rb1 ⁴	92.1(1)
O1 ¹⁴	Rb2	O1 ¹³	114.37(6)	Rb2	N2	Rb1 ⁵	92.1(1)
O1 ¹⁵	Rb2	O1 ¹³	135.90(3)	Rb2	N2	Rb1 ⁶	92.1(1)
O1 ¹⁶	Rb2	O1 ¹³	114.37(6)	Rb2 ²⁹	N1	Rb2 ¹²	77.78(8)
O1 ⁴	Rb2	O1 ¹³	67.5(2)	Rb2 ¹²	N1	Rb2 ¹⁴	151.6(2)
O1 ¹⁰	Rb2	O1 ¹⁴	53.0(2)	Rb2 ²⁹	N1	Rb2 ¹⁴	77.78(8)
O1 ¹¹	Rb2	O1 ¹⁴	135.90(3)	Rb2 ²⁹	O1	Rb2 ¹²	77.78(8)
O1 ¹²	Rb2	O1 ¹⁴	151.6(2)	Rb2 ¹²	O1	Rb2 ¹⁴	151.6(2)
O1 ¹⁵	Rb2	O1 ¹⁴	67.5(2)	Rb2 ²⁹	O1	Rb2 ¹⁴	77.78(8)
O1 ¹⁶	Rb2	O1 ¹⁴	114.37(6)	Rb2 ¹	Re1	Rb1 ⁴	73.684(8)
O1 ⁴	Rb2	O1 ¹⁴	102.22(8)	Rb2 ²	Re1	Rb1 ⁴	177.14(2)
O1 ⁴	Rb2	O1 ¹⁵	69.22(14)	Rb2 ³	Re1	Rb1 ⁴	73.684(7)
O1 ¹¹	Rb2	O1 ¹⁶	67.5(2)	Rb2 ¹	Re1	Rb1 ⁵	73.685(7)
O1 ¹⁵	Rb2	O1 ¹⁶	102.22(8)	Rb2 ²	Re1	Rb1 ⁵	73.684(8)
O1 ⁴	Rb2	O1 ¹⁶	135.90(3)	Rb2 ³	Re1	Rb1 ⁵	177.14(2)
O1 ¹⁰	Rb2	O1 ¹⁷	114.37(6)	Rb2 ¹	Re1	Rb1 ⁶	177.14(2)
O1 ¹¹	Rb2	O1 ¹⁷	135.90(3)	Rb2 ²	Re1	Rb1 ⁶	73.684(8)
O1 ¹²	Rb2	O1 ¹⁷	114.37(6)	Rb2 ³	Re1	Rb1 ⁶	73.685(7)
O1 ¹³	Rb2	O1 ¹⁷	52.95(16)	Rb2 ¹	Re1	Rb2 ²	107.85(2)
O1 ¹⁴	Rb2	O1 ¹⁷	63.14(16)	Rb2 ¹	Re1	Rb2 ³	107.85(2)
O1 ¹⁵	Rb2	O1 ¹⁷	102.22(8)	Rb2 ²	Re1	Rb2 ³	107.85(2)
O1 ¹⁶	Rb2	O1 ¹⁷	151.6(2)	Re1 ³⁰	N1	Rb1 ³¹	111.2(2)
O1 ⁴	Rb2	O1 ¹⁷	67.5(2)	Re1 ³⁰	N1	Rb2 ¹²	97.21(8)
O1 ¹⁰	Rb2	Re1 ¹	87.43(8)	Re1 ³⁰	N1	Rb2 ¹⁴	97.21(9)
O1 ¹¹	Rb2	Re1 ¹	70.07(9)	Re1 ³⁰	N1	Rb2 ²⁹	151.2(2)
O1 ¹²	Rb2	Re1 ¹	26.98(8)	Re1	N2	Rb1 ⁴	87.9(1)
O1 ¹³	Rb2	Re1 ¹	87.43(8)	Re1	N2	Rb1 ⁵	87.9(1)
O1 ¹⁴	Rb2	Re1 ¹	132.52(8)	Re1	N2	Rb1 ⁶	87.9(1)
O1 ¹⁵	Rb2	Re1 ¹	125.25(2)	Re1	N2	Rb2	180
O1 ¹⁶	Rb2	Re1 ¹	26.98(8)	Re1 ³⁰	O1	Rb1 ³¹	111.2(2)
O1 ¹⁷	Rb2	Re1 ¹	132.52(8)	Re1 ³⁰	O1	Rb2 ¹²	97.21(8)
O1 ⁴	Rb2	Re1 ¹	125.25(2)	Re1 ³⁰	O1	Rb2 ¹⁴	97.21(9)
O1 ⁷	Re1	O1 ⁸	108.7(2)	Re1 ³⁰	O1	Rb2 ²⁹	151.2(2)
O1 ⁷	Re1	O1 ⁹	108.7(2)	Re1	O2	Rb1 ⁴	87.9(1)
O1 ⁸	Re1	O1 ⁹	108.7(2)	Re1	O2	Rb1 ⁵	87.9(1)
O1 ⁷	Re1	Rb1 ⁴	44.1(1)	Re1	O2	Rb1 ⁶	87.9(1)
O1 ⁸	Re1	Rb1 ⁴	124.68(4)	Re1	O2	Rb2	180

¹-1/3-x,-2/3-y,4/3-z, ²2/3-x,1/3-y,4/3-z, ³-1/3-x,1/3-y,4/3-z, ⁴-2/3+x, 1/3+y,2/3+z, ⁵1/3+x,-1/3+y,2/3+z, ⁶1/3+x,2/3+y,2/3+z, ⁷-1/3+y-x,1/3-x,1/3+z, ⁸2/3-y,1/3+x-y,1/3+z, ⁹-1/3+x,-2/3+y,1/3+z, ¹⁰+y,-x+y,1-z, ¹¹1/3-y,-1/3+x-y,2/3+z, ¹²-x,-y,1-z, ¹³-1+y,-x+y,1-z, ¹⁴1-x,1-y,1-z, ¹⁵1/3+y-x,2/3-x,2/3+z, ¹⁶-y+x,-1+x,1-z, ¹⁷-y+x,+x,1-z, ¹⁸2/3-x,1/3-y,1/3-z, ¹⁹-2/3+x,-1/3+y,-1/3+z, ²⁰-1/3+y,1/3-x+y,1/3-z, ²¹1/3+y-x,2/3-x,-1/3+z, ²²-1/3-y+x,-2/3+x,1/3-z, ²³1/3-y,-1/3+x-y,-1/3+z, ²⁴-2/3-x,-1/3-y,2/3-z, ²⁵-1/3+x,1/3+y,-2/3+z, ²⁶1/3-x,2/3-y,2/3-z, ²⁷-1/3+x,-2/3+y,-2/3+z, ²⁸1/3-x,-1/3-y,2/3-z, ²⁹2/3+x,1/3+y,-2/3+z, ³⁰1/3+x,2/3+y,-1/3+z, ³¹2/3+x,1/3+y,1/3+z

Table S7. Atomic occupancy for Rb₃[ReO₄][ReO₃N].

Atom	Occupancy	Atom	Occupancy
O1	0.875	O2	0.875
N1	0.125	N2	0.125

Cs₃[ReO₄][ReO₃N]

Table S8. Atomic coordinates ($\times 10^4$), equivalent isotropic displacement parameters ($\text{\AA}^2 \times 10^3$) and Wyckoff positions for Cs₃[ReO₄][ReO₃N]. $U(eq)$ is defined as one third of the trace of the orthogonalized U_{ij} tensor.

Atom	Wyckoff position	x	y	z	$U(eq)$
Cs1	3a	0	0	0	36.0(2)
Cs2	6c	0	0	7985.2(2)	15.33(13)
N1	18h	4816(3)	5184(3)	2343(1)	20.2(6)
N2	6c	0	0	6680(2)	38(2)
O1	18h	4816(3)	5184(3)	2343(1)	20.2(6)
O2	6c	0	0	6680(2)	38(2)
Re1	6c	0	0	5933.5(2)	13.9(1)

Table S9. Anisotropic displacement parameters ($\text{\AA}^2 \times 10^3$) for Cs₃[ReO₄][ReO₃N]. The anisotropic displacement factor exponent takes the form: $-2\pi^2 [h^2 a^{*2} U_{11} + 2 h k a^* b^* U_{12} + \dots]$.

Atom	U_{11}	U_{22}	U_{33}	U_{23}	U_{13}	U_{12}
Cs1	47.2(3)	47.2(3)	13.7(3)	0	0	23.6(2)
Cs2	14.1(2)	14.1(2)	17.9(2)	0	0	7.02(8)
N1	18(1)	18(1)	28(1)	0.6(6)	-0.6(6)	11(1)
N2	49(3)	49(3)	17(2)	0	0	25(1)
O1	18(1)	18(1)	28(1)	0.6(6)	-0.6(6)	11(1)
O2	49(3)	49(3)	17(2)	0	0	25(1)
Re1	12.1(1)	12.1(1)	17.4(2)	0	0	6.07(7)

Table S10. Bond lengths for Cs₃[ReO₄][ReO₃N].

Atom	Atom	Length [\AA]	Atom	Atom	Length [\AA]
Cs1	O1 ²⁴	3.076(3)	Cs2	O1 ¹³	3.2927(7)
Cs1	O1 ²⁵	3.076(3)	Cs2	O1 ¹⁴	3.2927(7)
Cs1	O1 ²⁶	3.076(3)	Cs2	O1 ¹⁵	3.2927(7)
Cs1	O1 ²⁷	3.076(3)	Cs2	O1 ¹⁶	3.2927(7)
Cs1	O1 ²⁸	3.076(3)	Cs2	O1 ¹⁷	3.135(3)
Cs1	O1 ²⁹	3.076(3)	Cs2	O2	3.023(6)
Cs1	O2 ¹⁸	3.6921(1)	Re1	Cs1 ⁴	4.0637(2)
Cs1	O2 ¹⁹	3.6921(1)	Re1	Cs1 ⁵	4.0637(2)
Cs1	O2 ²⁰	3.6921(1)	Re1	Cs1 ⁶	4.0637(2)
Cs1	O2 ²¹	3.6921(1)	Re1	Cs2 ¹	3.9331(2)
Cs1	O2 ²²	3.6921(1)	Re1	Cs2 ²	3.9331(2)
Cs1	O2 ²³	3.6921(1)	Re1	Cs2 ³	3.9331(2)
Cs2	N2	3.023(6)	Re1	N2	1.728(6)
Cs2	O1 ⁶	3.135(3)	Re1	O1 ⁷	1.747(3)
Cs2	O1 ¹⁰	3.2927(7)	Re1	O1 ⁸	1.747(3)
Cs2	O1 ¹¹	3.135(3)	Re1	O1 ⁹	1.747(3)
Cs2	O1 ¹²	3.2927(7)	Re1	O2	1.728(6)

¹-1/3-x,-2/3-y,4/3-z, ²2/3-x,1/3-y,4/3-z, ³-1/3-x,1/3-y,4/3-z, ⁴1/3+x,2/3+y,2/3+z, ⁵1/3+x,-1/3+y,2/3+z, ⁶-2/3+x,-1/3+y,2/3+z, ⁷2/3-y,1/3+x-y,1/3+z, ⁸-1/3+x,-2/3+y,1/3+z, ⁹-1/3+y-x,1/3-x,1/3+z, ¹⁰-1+y,-x+y,1-z, ¹¹1/3+y-x,2/3-x,2/3+z, ¹²-x,-y,1-z, ¹³+y,-x+y,1-z, ¹⁴-y+x,-1+x,1-z, ¹⁵-y+x,x,1-z, ¹⁶-x,1-y,1-z, ¹⁷1/3-y,-1/3+x-y,2/3+z, ¹⁸1/3-x,-1/3-y,2/3-z, ¹⁹-2/3-x,-1/3-y,2/3-z, ²⁰2/3+x,1/3+y,-2/3+z, ²¹1/3-x,2/3-y,2/3-z, ²²-1/3+x,-2/3+y,-2/3+z, ²³-1/3+x,1/3+y,-2/3+z, ²⁴-2/3+x,-1/3+y,-1/3+z, ²⁵-1/3-y+x,-2/3+x,1/3-z, ²⁶1/3-y,-1/3+x-y,-1/3+z, ²⁷1/3+y-x,2/3-x,-1/3+z, ²⁸-1/3+y,1/3-x+y,1/3-z, ²⁹2/3-x,1/3-y,1/3-z.

Table S11. Bond angles for Cs₃[ReO₄][ReO₃N].

Atom	Atom	Atom	Angle [$^\circ$]	Atom	Atom	Atom	Angle [$^\circ$]
Cs1 ³¹	N1	Cs2 ¹¹	97.53(5)	O1 ¹⁷	Cs2	O1 ¹⁴	114.84(4)
Cs1 ³¹	N1	Cs2 ¹⁷	97.53(5)	O1 ⁴	Cs2	O1 ¹⁴	66.72(9)
Cs1 ³¹	N1	Cs2 ¹⁹	97.40(8)	O1 ¹¹	Cs2	O1 ¹⁵	114.84(4)
Cs1 ⁴	N2	Cs1 ⁵	119.994(3)	O1 ¹³	Cs2	O1 ¹⁵	66.72(9)
Cs1 ⁴	N2	Cs1 ⁶	119.993(3)	O1 ¹⁶	Cs2	O1 ¹⁵	102.42(5)
Cs1 ⁵	N2	Cs1 ⁶	119.993(3)	O1 ¹⁷	Cs2	O1 ¹⁵	51.2(1)
Cs1 ³¹	O1	Cs2 ¹¹	97.53(5)	O1 ⁴	Cs2	O1 ¹⁵	134.77(2)

Cs1 ³¹	O1	Cs2 ¹⁷	97.53(5)	O1 ⁴	Cs2	O1 ¹⁶	68.96(8)
Cs1 ³¹	O1	Cs2 ¹⁹	97.40(8)	O1 ⁷	Re1	O1 ⁸	109.01(9)
Cs1 ⁴	O2	Cs1 ⁵	119.994(3)	O2 ¹⁸	Cs1	O2 ¹⁹	180
Cs1 ⁴	O2	Cs1 ⁶	119.993(3)	O2 ¹⁸	Cs1	O2 ²⁰	119.994(3)
Cs1 ⁵	O2	Cs1 ⁶	119.993(3)	O2 ¹⁹	Cs1	O2 ²⁰	60.006(3)
Cs1 ⁵	Re1	Cs1 ⁴	103.778(4)	O2 ¹⁸	Cs1	O2 ²¹	60.006(3)
Cs1 ⁴	Re1	Cs1 ⁶	103.777(5)	O2 ¹⁹	Cs1	O2 ²¹	119.994(3)
Cs1 ⁵	Re1	Cs1 ⁶	103.777(4)	O2 ²⁰	Cs1	O2 ²¹	180
Cs2 ¹⁷	N1	Cs2 ¹¹	152.4(1)	O2 ¹⁸	Cs1	O2 ²²	60.007(3)
Cs2 ¹⁹	N1	Cs2 ¹¹	77.58(5)	O2 ¹⁹	Cs1	O2 ²²	119.993(3)
Cs2 ¹⁹	N1	Cs2 ¹⁷	77.58(5)	O2 ²⁰	Cs1	O2 ²²	60.007(3)
Cs2	N2	Cs1 ⁴	90.47(9)	O2 ²¹	Cs1	O2 ²²	119.993(3)
Cs2	N2	Cs1 ⁵	90.47(9)	O2 ²³	Cs1	O2 ²²	180
Cs2	N2	Cs1 ⁶	90.47(9)	O2 ¹⁸	Cs1	O2 ²³	119.993(3)
Cs2 ¹⁷	O1	Cs2 ¹¹	152.4(1)	O2 ¹⁹	Cs1	O2 ²³	60.007(3)
Cs2 ¹⁹	O1	Cs2 ¹¹	77.58(5)	O2 ²⁰	Cs1	O2 ²³	119.993(3)
Cs2 ¹⁹	O1	Cs2 ¹⁷	77.58(5)	O2 ²¹	Cs1	O2 ²³	60.007(3)
Cs2	O2	Cs1 ⁴	90.47(9)	O2	Cs2	O1 ⁴	139.18(5)
Cs2	O2	Cs1 ⁵	90.47(9)	O2	Cs2	O1 ¹⁰	76.65(5)
Cs2	O2	Cs1 ⁶	90.47(9)	O2	Cs2	O1 ¹¹	76.65(5)
Cs2 ¹	Re1	Cs1 ⁴	73.596(3)	O2	Cs2	O1 ¹²	76.65(5)
Cs2 ²	Re1	Cs1 ⁴	175.469(9)	O2	Cs2	O1 ¹³	139.18(5)
Cs2 ³	Re1	Cs1 ⁴	73.597(3)	O2	Cs2	O1 ¹⁴	76.65(5)
Cs2 ¹	Re1	Cs1 ⁵	175.469(9)	O2	Cs2	O1 ¹⁵	76.65(5)
Cs2 ²	Re1	Cs1 ⁵	73.596(3)	O2	Cs2	O1 ¹⁶	139.18(5)
Cs2 ³	Re1	Cs1 ⁵	73.597(3)	O2	Cs2	O1 ¹⁷	76.65(5)
Cs2 ¹	Re1	Cs1 ⁶	73.597(3)	O2	Cs2	Re1 ¹	69.835(7)
Cs2 ²	Re1	Cs1 ⁶	73.597(3)	O2	Re1	Cs1 ⁴	65.304(4)
Cs2 ³	Re1	Cs1 ⁶	175.469(9)	O2	Re1	Cs1 ⁵	65.304(4)
Cs2 ¹	Re1	Cs2 ²	108.769(7)	O2	Re1	Cs1 ⁶	65.304(4)
Cs2 ¹	Re1	Cs2 ³	108.768(7)	O2	Re1	Cs2 ¹	110.165(7)
Cs2 ²	Re1	Cs2 ³	108.768(7)	O2	Re1	Cs2 ²	110.165(7)
N2	Cs2	O1 ¹⁴	76.65(5)	O2	Re1	Cs2 ³	110.165(7)
N2	Cs2	O1 ¹⁵	76.65(5)	O2	Re1	O1 ⁷	109.93(9)
N2	Cs2	O1 ¹⁶	139.18(5)	O2	Re1	O1 ⁸	109.93(9)
N2	Re1	O1 ⁸	109.93(9)	O2	Re1	O1 ⁹	109.93(9)
O1 ²⁴	Cs1	O1 ²⁵	109.52(8)	Re1 ³⁰	N1	Cs1 ³¹	111.8(1)
O1 ²⁶	Cs1	O1 ²⁵	70.48(8)	Re1 ³⁰	N1	Cs2 ¹¹	97.86(5)
O1 ²⁸	Cs1	O1 ²⁵	109.52(8)	Re1 ³⁰	N1	Cs2 ¹⁷	97.86(5)
O1 ²⁹	Cs1	O1 ²⁵	70.48(8)	Re1 ³⁰	N1	Cs2 ¹⁹	150.8(1)
O1 ²⁸	Cs1	O1 ²⁶	109.52(8)	Re1	N2	Cs1 ⁴	89.53(9)
O1 ²⁹	Cs1	O1 ²⁶	70.48(8)	Re1	N2	Cs1 ⁵	89.53(9)
O1 ²⁴	Cs1	O1 ²⁷	70.48(8)	Re1	N2	Cs1 ⁶	89.53(9)
O1 ²⁵	Cs1	O1 ²⁷	180.00(7)	Re1	N2	Cs2	180
O1 ²⁶	Cs1	O1 ²⁷	109.52(8)	Re1 ³⁰	O1	Cs1 ³¹	111.8(1)
O1 ²⁸	Cs1	O1 ²⁷	70.48(8)	Re1 ³⁰	O1	Cs2 ¹¹	97.86(5)
O1 ²⁹	Cs1	O1 ²⁷	109.52(8)	Re1 ³⁰	O1	Cs2 ¹⁷	97.86(5)
O1 ¹⁰	Cs2	O1 ¹⁴	51.2(1)	Re1 ³⁰	O1	Cs2 ¹⁹	150.8(1)
O1 ¹¹	Cs2	O1 ¹⁴	65.2(1)	Re1	O2	Cs1 ⁴	89.53(9)
O1 ¹³	Cs2	O1 ¹⁴	134.77(2)	Re1	O2	Cs1 ⁵	89.53(9)
O1 ¹⁵	Cs2	O1 ¹⁴	152.4(1)	Re1	O2	Cs1 ⁶	89.53(9)
O1 ¹⁶	Cs2	O1 ¹⁴	102.42(5)	Re1	O2	Cs2	180

¹-1/3-x,-2/3-y,4/3-z, ²2/3-x,1/3-y,4/3-z, ³-1/3-x,1/3-y,4/3-z, ⁴-2/3+x,-1/3+y,2/3+z, ⁵1/3+x,2/3+y,2/3+z, ⁶1/3+x,-1/3+y,2/3+z, ⁷-1/3+x,-2/3+y,1/3+z, ⁸-1/3+y-x,1/3-x,1/3+z, ⁹2/3-y,1/3+x-y,1/3+z, ¹⁰-1+y,-x+y,1-z, ¹¹1-x,1-y,1-z, ¹²+y,-x+y,1-z, ¹³1/3-y,-1/3+x-y,2/3+z, ¹⁴-y+x,x,1-z, ¹⁵-y+x,-1+x,1-z, ¹⁶1/3+y-x,2/3-x,2/3+z, ¹⁷-x,-y,1-z, ¹⁸-2/3-x,-1/3-y,2/3-z, ¹⁹2/3+x,1/3+y,-2/3+z, ²⁰1/3-x,2/3-y,2/3-z, ²¹-1/3+x,-2/3+y,-2/3+z, ²²-1/3+x,1/3+y,-2/3+z, ²³1/3-x,-1/3-y,2/3-z, ²⁴1/3-y,-1/3+x-y,-1/3+z, ²⁵-1/3-y+x,-2/3+x,1/3-z, ²⁶-1/3+y,1/3-x+y,1/3-z, ²⁷1/3+y-x,2/3-x,-1/3+z, ²⁸-2/3+x,-1/3+y,-1/3+z, ²⁹2/3-x,1/3-y,1/3-z, ³⁰1/3+x,2/3+y,-1/3+z, ³¹2/3+x,1/3+y,1/3+z.

Table S12. Atomic occupancy for Cs₃[ReO₄][ReO₃N].

Atom	Occupancy	Atom	Occupancy
O1	0.875	O2	0.875
N1	0.125	N2	0.125

K₂[ReO₃N]**Table S13.** Atomic coordinates ($\times 10^4$), equivalent isotropic displacement parameters ($\text{\AA}^2 \times 10^3$) and Wyckoff positions for K₂[ReO₃N]. $U(eq)$ is defined as one third of the trace of the orthogonalized U_{ij} tensor.

Atom	Wyckoff position	x	y	z	$U(eq)$
K1	4i	5068.6(9)	5000	2364(1)	10.2(2)
K2	4i	8396.1(9)	5000	2557(1)	11.0(2)
N1	8j	8583(2)	7389(4)	9253(4)	12.0(5)
N2	4i	9212(3)	5000	6460(5)	12.7(7)
N3	4i	6766(3)	5000	6168(5)	18.3(8)
O1	8j	8583(2)	7389(4)	9253(4)	12.0(5)
O2	4i	9212(3)	5000	6460(5)	12.7(7)
O3	4i	6766(3)	5000	6168(5)	18.3(8)
Re1	4i	8289.7(2)	5000	7762.6(2)	6.83(7)

Table S14. Anisotropic displacement parameters ($\text{\AA}^2 \times 10^3$) for K₂[ReO₃N]. The anisotropic displacement factor exponent takes the form: $-2\pi^2 [h^2 a^{*2} U_{11} + 2 h k a^* b^* U_{12} + \dots]$.

Atom	U_{11}	U_{22}	U_{33}	U_{23}	U_{13}	U_{12}
K1	8.8(5)	13.0(5)	8.8(5)	0	3.6(4)	0
K2	8.2(5)	14.3(5)	9.4(5)	0	2.6(4)	0
N1	10(1)	10(1)	14(1)	-1(1)	3(1)	-1(1)
N2	9(2)	20(2)	9(2)	0	5(1)	0
N3	16(2)	23(2)	13(2)	0	4(2)	0
O1	10(1)	10(1)	14(1)	-1(1)	3(1)	-1(1)
O2	9(2)	20(2)	9(2)	0	5(1)	0
O3	16(2)	23(2)	13(2)	0	4(2)	0
Re1	6.0(1)	7.7(1)	6.8(1)	0	2.60(7)	0

Table S15. Bond lengths for K₂[ReO₃N].

Atom	Atom	Length [\AA]	Atom	Atom	Length [\AA]
K1	K1 ⁵	3.463(2)	K2	O2 ¹²	2.727(4)
K1	N3	2.737(4)	K2	O3 ¹	3.196(1)
K1	O1 ¹	2.897(3)	K2	O3 ²	3.196(1)
K1	O1 ⁶	2.772(2)	Re1	K1 ¹	3.6578(6)
K1	O1 ⁷	2.772(2)	Re1	K1 ²	3.6578(6)
K1	O1 ⁸	2.897(3)	Re1	K2 ¹	3.6163(6)
K1	O2 ¹	3.165(1)	Re1	K2 ²	3.6163(6)
K1	O2 ²	3.165(1)	Re1	K2 ³	3.528(1)
K1	O3	2.737(4)	Re1	N1	1.765(2)
K1	O3 ⁹	2.898(4)	Re1	N2	1.780(3)
K2	N2	2.658(3)	Re1	N3	1.756(4)
K2	O1 ¹	2.741(3)	Re1	O1	1.765(2)
K2	O1 ¹⁰	2.949(3)	Re1	O1 ⁴	1.765(2)
K2	O1 ¹¹	2.949(3)	Re1	O2	1.780(3)
K2	O1 ⁸	2.741(3)	Re1	O3	1.756(4)
K2	O2	2.658(3)			

¹3/2-x,3/2-y,1-z ²3/2-x,1/2-y,1-z ³+x,+y,1+z ⁴+x,1-y,+z ⁵1-x,1-y,-z ⁶-1/2+x,-1/2+y,-1+z ⁷-1/2+x,3/2-y,-1+z ⁸3/2-x,-1/2+y,1-z ⁹1-x,1-y,1-z ¹⁰+x,1-y,-1+z ¹¹+x,+y,-1+z ¹²2-x,1-y,1-z.

Table S16. Bond angles for K₂[ReO₃N].

Atom	Atom	Atom	Angle [°]	Atom	Atom	Atom	Angle [°]
K1 ⁵	K1	Re1 ¹	76.44(2)	O1 ¹⁰	K2	Re1 ²	126.63(5)
K1 ⁵	K1	Re1 ²	76.44(2)	O1 ¹¹	K2	Re1 ²	77.32(5)
K1 ¹³	N1	K1 ¹	75.28(7)	O1 ⁷	K2	Re1 ²	28.17(5)
K1 ¹	N1	K2 ³	150.94(9)	O1	Re1	K1 ¹	51.12(8)
K1 ¹³	N1	K2 ³	80.34(7)	O1 ⁴	Re1	K1 ¹	136.13(8)
K1 ¹	N2	K1 ²	145.0(1)	O1	Re1	K1 ²	136.13(8)
K1	N3	K1 ⁹	90.8(1)	O1 ⁴	Re1	K1 ²	51.12(8)
K1	N3	K2 ¹	101.16(7)	O1	Re1	K2 ¹	47.17(8)
K1 ⁹	N3	K2 ¹	74.41(7)	O1 ⁴	Re1	K2 ¹	133.17(8)
K1	N3	K2 ²	101.16(7)	O1	Re1	K2 ²	133.17(8)
K1 ⁹	N3	K2 ²	74.41(7)	O1 ⁴	Re1	K2 ²	47.17(8)
K1 ¹³	O1	K1 ¹	75.28(7)	O1	Re1	K2 ³	56.53(8)
K1 ¹	O1	K2 ³	150.94(9)	O1 ⁴	Re1	K2 ³	56.53(8)
K1 ¹³	O1	K2 ³	80.34(7)	O1	Re1	O1 ⁴	109.6(2)
K1 ¹	O2	K1 ²	145.0(1)	O1	Re1	O2	109.6(1)
K1	O3	K1 ⁹	90.8(1)	O1 ⁴	Re1	O2	109.6(1)
K1	O3	K2 ¹	101.16(7)	O2 ¹	K1	K1 ⁵	99.89(6)
K1 ⁹	O3	K2 ¹	74.41(7)	O2 ²	K1	K1 ⁵	99.89(6)
K1	O3	K2 ²	101.16(7)	O2 ¹	K1	O2 ²	145.0(1)
K1 ⁹	O3	K2 ²	74.41(7)	O2 ¹	K1	Re1 ¹	29.11(6)
K1 ¹	Re1	K1 ²	111.20(3)	O2 ²	K1	Re1 ¹	134.43(7)
K2 ¹	N1	K1 ¹	91.72(7)	O2 ¹	K1	Re1 ²	134.43(7)
K2 ¹	N1	K1 ¹³	103.15(8)	O2 ²	K1	Re1 ²	29.11(6)
K2 ¹	N1	K2 ³	109.22(8)	O2	K2	O1 ¹	113.10(8)
K2	N2	K1 ¹	103.79(6)	O2 ¹²	K2	O1 ¹	140.66(6)
K2 ¹²	N2	K1 ¹	77.23(6)	O2	K2	O1 ⁷	113.10(8)
K2	N2	K1 ²	103.79(6)	O2 ¹²	K2	O1 ⁷	140.66(6)
K2 ¹²	N2	K1 ²	77.23(6)	O2	K2	O1 ¹⁰	142.36(7)
K2	N2	K2 ¹²	99.6(1)	O2 ¹²	K2	O1 ¹⁰	76.79(8)
K2 ¹	N3	K2 ²	141.6(1)	O2	K2	O1 ¹¹	142.36(7)
K2 ¹	O1	K1 ¹	91.72(7)	O2 ¹²	K2	O1 ¹¹	76.79(8)
K2 ¹	O1	K1 ¹³	103.15(8)	O2	K2	O2 ¹²	80.4(1)
K2 ¹	O1	K2 ³	109.22(8)	O2	K2	O3 ¹	73.45(7)
K2	O2	K1 ¹	103.79(6)	O2 ¹²	K2	O3 ¹	96.61(7)
K2 ¹²	O2	K1 ¹	77.23(6)	O2	K2	O3 ²	73.45(7)
K2	O2	K1 ²	103.79(6)	O2 ¹²	K2	O3 ²	96.61(7)
K2 ¹²	O2	K1 ²	77.23(6)	O2	K2	Re1 ¹	90.93(4)
K2	O2	K2 ¹²	99.6(1)	O2 ¹²	K2	Re1 ¹	123.07(2)
K2 ¹	O3	K2 ²	141.6(1)	O2	K2	Re1 ²	90.93(4)
K2 ¹	Re1	K1 ¹	67.61(2)	O2 ¹²	K2	Re1 ²	123.07(2)
K2 ²	Re1	K1 ¹	175.10(2)	O2	K2	Re1 ¹⁰	161.80(8)
K2 ³	Re1	K1 ¹	103.88(2)	O2 ¹²	K2	Re1 ¹⁰	81.42(7)
K2 ¹	Re1	K1 ²	175.10(2)	O2	Re1	K1 ¹	59.90(4)
K2 ²	Re1	K1 ²	67.61(2)	O2	Re1	K1 ²	59.90(4)
K2 ³	Re1	K1 ²	103.88(2)	O2	Re1	K2 ¹	116.46(4)
K2 ²	Re1	K2 ¹	113.14(3)	O2	Re1	K2 ²	116.46(4)
K2 ³	Re1	K2 ¹	81.00(2)	O2	Re1	K2 ³	142.5(1)
K2 ³	Re1	K2 ²	81.00(2)	O3	K1	K1 ⁵	138.50(9)
N1	Re1	N2	109.6(1)	O3 ⁹	K1	K1 ⁵	132.25(8)
N2	K2	O3 ¹	73.45(7)	O3	K1	O1 ¹	96.27(9)
N3	Re1	N1	107.9(1)	O3	K1	O1 ⁶	145.25(5)
N3	Re1	N2	112.2(2)	O3	K1	O1 ⁷	96.27(9)
O1 ¹	K1	K1 ⁵	50.73(5)	O3	K1	O1 ⁸	145.25(5)
O1 ⁶	K1	K1 ⁵	53.99(5)	O3	K1	O2 ¹	73.00(6)
O1 ⁷	K1	K1 ⁵	50.73(5)	O3 ⁹	K1	O2 ¹	93.87(7)
O1 ⁸	K1	K1 ⁵	53.99(5)	O3	K1	O2 ²	73.00(6)
O1 ⁶	K1	O1 ¹	104.72(7)	O3 ⁹	K1	O2 ²	93.87(7)
O1 ⁸	K1	O1 ¹	68.61(9)	O3	K1	O3 ⁹	89.2(1)
O1 ¹	K1	O1 ⁷	65.9(1)	O3	K1	Re1 ¹	80.50(5)
O1 ⁶	K1	O1 ⁷	68.61(9)	O3 ⁹	K1	Re1 ¹	122.55(2)

O1 ⁸	K1	O1 ⁷	104.72(7)	O3	K1	Re1 ²	80.50(5)
O1 ⁶	K1	O1 ⁸	69.3(1)	O3 ⁹	K1	Re1 ²	122.55(2)
O1 ¹	K1	O2 ¹	56.88(8)	O3 ¹	K2	O3 ²	141.6(1)
O1 ⁶	K1	O2 ¹	141.76(8)	O3 ¹	K2	Re1 ¹	29.04(7)
O1 ⁷	K1	O2 ¹	119.43(8)	O3 ²	K2	Re1 ¹	134.58(7)
O1 ⁸	K1	O2 ¹	72.61(8)	O3 ¹	K2	Re1 ¹⁰	108.79(6)
O1 ¹	K1	O2 ²	119.43(8)	O3 ²	K2	Re1 ¹⁰	108.79(6)
O1 ⁶	K1	O2 ²	72.61(8)	O3 ¹	K2	Re1 ²	134.58(7)
O1 ⁷	K1	O2 ²	56.88(8)	O3 ²	K2	Re1 ²	29.04(7)
O1 ⁸	K1	O2 ²	141.76(8)	O3	Re1	K1 ¹	115.48(5)
O1 ¹	K1	O3 ⁹	146.43(5)	O3	Re1	K1 ²	115.48(5)
O1 ⁶	K1	O3 ⁹	88.25(8)	O3	Re1	K2 ¹	62.08(4)
O1 ⁷	K1	O3 ⁹	146.43(5)	O3	Re1	K2 ²	62.08(4)
O1 ⁸	K1	O3 ⁹	88.25(8)	O3	Re1	K2 ³	105.3(1)
O1 ¹	K1	Re1 ¹	28.31(5)	O3	Re1	O1	107.9(1)
O1 ⁶	K1	Re1 ¹	128.83(6)	O3	Re1	O1 ⁴	107.9(1)
O1 ⁷	K1	Re1 ¹	91.00(5)	O3	Re1	O2	112.2(1)
O1 ⁸	K1	Re1 ¹	71.87(5)	Re1 ¹	K1	Re1 ²	111.20(3)
O1 ¹	K1	Re1 ²	91.00(5)	Re1 ¹⁰	K2	Re1 ¹	99.01(2)
O1 ⁶	K1	Re1 ²	71.87(5)	Re1 ²	K2	Re1 ¹	113.14(3)
O1 ⁷	K1	Re1 ²	28.31(5)	Re1 ¹⁰	K2	Re1 ²	99.01(2)
O1 ⁸	K1	Re1 ²	128.83(6)	Re1	N1	K1 ¹	100.6(1)
O1 ⁷	K2	O1 ¹	70.2(1)	Re1	N1	K1 ¹³	152.0(1)
O1 ¹	K2	O1 ¹⁰	70.78(8)	Re1	N1	K2 ¹	104.7(1)
O1 ¹¹	K2	O1 ¹⁰	58.55(9)	Re1	N1	K2 ³	93.52(9)
O1 ⁷	K2	O1 ¹⁰	103.48(5)	Re1	N2	K1 ¹	90.99(7)
O1 ¹	K2	O1 ¹¹	103.48(5)	Re1	N2	K1 ²	90.99(7)
O1 ⁷	K2	O1 ¹¹	70.78(8)	Re1	N2	K2	124.3(2)
O1 ¹	K2	O3 ¹	56.66(8)	Re1	N2	K2 ¹²	136.1(2)
O1 ¹⁰	K2	O3 ¹	79.87(8)	Re1	N3	K1	147.4(2)
O1 ¹¹	K2	O3 ¹	138.39(8)	Re1	N3	K1 ⁹	121.8(2)
O1 ⁷	K2	O3 ¹	122.43(9)	Re1	N3	K2 ¹	88.88(8)
O1 ¹	K2	O3 ²	122.43(9)	Re1	N3	K2 ²	88.88(8)
O1 ¹⁰	K2	O3 ²	138.39(8)	Re1	O1	K1 ¹	100.6(1)
O1 ¹¹	K2	O3 ²	79.87(8)	Re1	O1	K1 ¹³	152.0(1)
O1 ⁷	K2	O3 ²	56.66(8)	Re1	O1	K2 ¹	104.7(1)
O1 ¹	K2	Re1 ¹	28.17(5)	Re1	O1	K2 ³	93.52(9)
O1 ¹⁰	K2	Re1 ¹	77.32(5)	Re1	O2	K1 ¹	90.99(7)
O1 ¹¹	K2	Re1 ¹	126.63(5)	Re1	O2	K1 ²	90.99(7)
O1 ⁷	K2	Re1 ¹	94.48(6)	Re1	O2	K2	124.3(2)
O1 ¹	K2	Re1 ¹⁰	81.46(5)	Re1	O2	K2 ¹²	136.1(2)
O1 ¹⁰	K2	Re1 ¹⁰	29.95(5)	Re1	O3	K1	147.4(2)
O1 ¹¹	K2	Re1 ¹⁰	29.95(5)	Re1	O3	K1 ⁹	121.8(2)
O1 ⁷	K2	Re1 ¹⁰	81.46(5)	Re1	O3	K2 ¹	88.88(8)
O1 ¹	K2	Re1 ²	94.48(6)	Re1	O3	K2 ²	88.88(8)

¹3/2-x,3/2-y,1-z, ²3/2-x,1/2-y,1-z, ³+x,+y,1+z, ⁴+x,1-y,+z, ⁵1-x,1-y,-z, ⁶-1/2+x,-1/2+y,-1+z, ⁷3/2-x,-1/2+y,1-z, ⁸-1/2+x,3/2-y,-1+z, ⁹1-x,1-y,1-z, ¹⁰+x,+y,-1+z, ¹¹+x,1-y,-1+z, ¹²2-x,1-y,1-z, ¹³1/2+x,1/2+y,1+z.

Table S17. Atomic occupancy for K₂[ReO₃N].

Atom	Occupancy	Atom	Occupancy	Atom	Occupancy
O1	0.75	O2	0.75	O3	0.75
N1	0.25	N2	0.25	N3	0.25

Cs₂[ReO₃N]

Table S18. Atomic coordinates ($\times 10^4$), equivalent isotropic displacement parameters ($\text{\AA}^2 \times 10^3$) and Wyckoff positions for Cs₂[ReO₃N]. $U(eq)$ is defined as one third of the trace of the orthogonalized U_{ij} tensor.

Atom	Wyckoff position	x	y	z	$U(eq)$
Cs1	4c	5120.8(3)	7500	7025.7(2)	9.41(7)
Cs2	4c	1691.0(3)	2500	5854.4(2)	10.15(7)
N1	8d	7998(3)	4746(3)	6494(2)	15.3(4)
N2	4c	5247(5)	2500	5820(3)	20.5(8)
N3	4c	7927(4)	2500	4344(3)	13.8(6)
O1	8d	7998(3)	4746(3)	6494(2)	15.3(4)
O2	4c	5247(5)	2500	5820(3)	20.5(8)
O3	4c	7927(4)	2500	4344(3)	13.8(6)
Re1	4c	7281.2(2)	2500	5798.5(2)	6.45(6)

Table S19. Anisotropic displacement parameters ($\text{\AA}^2 \times 10^3$) for Cs₂[ReO₃N]. The anisotropic displacement factor exponent takes the form: $-2\pi^2 [h^2 a^{*2} U_{11} + 2 h k a^* b^* U_{12} + \dots]$.

Atom	U_{11}	U_{22}	U_{33}	U_{23}	U_{13}	U_{12}
Cs1	8.6(1)	12.8(1)	6.9(1)	0	0.02(8)	0
Cs2	8.9(1)	10.1(1)	11.4(1)	0	1.41(8)	0
N1	19(1)	11(1)	16(1)	-4.5(8)	-3.7(9)	-1.8(9)
N2	16(2)	24(2)	22(2)	0	4(1)	0
N3	12(1)	18(2)	12(1)	0	4(1)	0
O1	19(1)	11(1)	16(1)	-4.5(8)	-3.7(9)	-1.8(9)
O2	16(2)	24(2)	22(2)	0	4(1)	0
O3	12(1)	18(2)	12(1)	0	4(1)	0
Re1	7.55(9)	6.76(8)	5.05(8)	0	0.09(5)	0

Table S20. Bond lengths for Cs₂[ReO₃N].

Atom	Atom	Length [\AA]	Atom	Atom	Length [\AA]
Cs1	N1	3.097(3)	Cs2	O1 ¹⁴	3.550(3)
Cs1	N2	3.527(2)	Cs2	O2	3.036(4)
Cs1	O1	3.097(3)	Cs2	O3 ¹	3.2651(4)
Cs1	O1 ⁶	3.097(3)	Cs2	O3 ⁴	3.2651(4)
Cs1	O1 ⁷	3.061(2)	Cs2	O3 ¹³	3.653(4)
Cs1	O1 ⁸	3.061(2)	Re1	Cs1 ¹	3.8422(3)
Cs1	O2	3.527(2)	Re1	Cs2 ¹	3.8585(2)
Cs1	O2 ¹	3.289(4)	Re1	Cs2 ²	3.7654(3)
Cs1	O2 ¹⁰	3.527(2)	Re1	Cs2 ³	3.8837(3)
Cs1	O3 ¹	3.042(4)	Re1	Cs2 ⁴	3.8585(2)
Cs1	O3 ⁹	3.146(3)	Re1	N1	1.771(2)
Cs2	N2	3.036(4)	Re1	N2	1.737(4)
Cs2	O1 ¹	3.249(2)	Re1	N3	1.761(3)
Cs2	O1 ⁸	3.559(2)	Re1	O1	1.771(2)
Cs2	O1 ¹¹	3.249(2)	Re1	O1 ⁵	1.771(2)
Cs2	O1 ¹²	3.559(2)	Re1	O2	1.737(4)
Cs2	O1 ¹³	3.550(3)	Re1	O3	1.761(3)

¹1-x,1-y,1-z, ²1+x,y,z, ³1/2+x,y,3/2-z, ⁴1-x,-y,1-z, ⁵x,1/2-y,z, ⁶x,3/2-y,z, ⁷-1/2+x,3/2-y,3/2-z, ⁸-1/2+x,y,3/2-z, ⁹3/2-x,1-y,1/2+z, ¹⁰x,1+y,z, ¹¹1-x,-1/2+y,1-z, ¹²-1/2+x,1/2-y,3/2-z, ¹³-1+x,y,z, ¹⁴-1+x,1/2-y,z.

Table S21. Bond angles for Cs₂[ReO₃N].

Atom	Atom	Atom	Angle [°]	Atom	Atom	Atom	Angle [°]
Cs1 ³	N1	Cs1	91.37(6)	O2	Cs2	O1 ¹	84.69(8)
Cs1	N1	Cs2 ¹	84.98(6)	O2	Cs2	O1 ⁷	72.41(8)
Cs1 ³	N1	Cs2 ¹	95.39(6)	O2	Cs2	O1 ¹¹	152.97(5)
Cs1	N1	Cs2 ³	79.51(6)	O2	Cs2	O1 ¹²	72.41(8)
Cs1 ³	N1	Cs2 ³	86.99(6)	O2	Cs2	O1 ¹³	152.97(5)
Cs1	N1	Cs2 ⁴	169.00(8)	O2	Cs2	O1 ¹⁴	84.69(8)
Cs1 ³	N1	Cs2 ⁴	80.13(6)	O2	Cs2	O3 ¹	84.21(7)
Cs1 ¹	N2	Cs1	112.87(6)	O2	Cs2	O3 ²	84.21(7)
Cs1 ¹⁶	N2	Cs1	133.5(1)	O2	Cs2	O3 ¹¹	150.86(9)
Cs1 ¹	N2	Cs1 ¹⁶	112.87(6)	O2	Cs2	Re1 ¹¹	178.28(8)
Cs1 ¹	N3	Cs1 ¹⁵	90.79(9)	O2	Re1	Cs1 ¹	58.56(13)
Cs1 ¹	N3	Cs2 ¹	92.82(7)	O2	Re1	Cs2 ¹	103.56(7)
Cs1 ¹⁵	N3	Cs2 ¹	83.55(6)	O2	Re1	Cs2 ²	103.56(7)
Cs1 ¹	N3	Cs2 ²	92.82(7)	O2	Re1	Cs2 ³	81.7(1)
Cs1 ¹⁵	N3	Cs2 ²	83.55(6)	O2	Re1	Cs2 ⁴	178.2(1)
Cs1 ¹	N3	Cs2 ⁴	177.2(1)	O2	Re1	O1 ⁵	109.8(1)
Cs1 ¹⁵	N3	Cs2 ⁴	86.39(8)	O2	Re1	O3	109.1(2)
Cs1 ³	O1	Cs1	91.37(6)	O3 ¹	Cs1	Re1 ¹	26.53(6)
Cs1	O1	Cs2 ¹	84.98(6)	O3 ¹	Cs1	O1 ⁶	77.39(7)
Cs1 ³	O1	Cs2 ¹	95.39(6)	O3 ¹	Cs1	O1 ⁷	77.39(7)
Cs1	O1	Cs2 ³	79.51(6)	O3 ¹	Cs1	O1 ⁸	125.17(6)
Cs1 ³	O1	Cs2 ³	86.99(6)	O3 ¹	Cs1	O2	79.76(7)
Cs1	O1	Cs2 ⁴	169.00(8)	O3 ⁹	Cs1	O2	108.51(7)
Cs1 ³	O1	Cs2 ⁴	80.13(6)	O3 ¹	Cs1	O2 ¹	53.3(1)
Cs1 ¹	O2	Cs1	112.87(6)	O3 ⁹	Cs1	O2 ¹	153.5(1)
Cs1 ¹⁶	O2	Cs1	133.5(1)	O3 ¹	Cs1	O2 ¹⁰	79.76(7)
Cs1 ¹	O2	Cs1 ¹⁶	112.87(6)	O3 ⁹	Cs1	O2 ¹⁰	108.51(7)
Cs1 ¹	O3	Cs1 ¹⁵	90.79(9)	O3 ¹	Cs1	O3 ⁹	153.21(9)
Cs1 ¹	O3	Cs2 ¹	92.82(7)	O3 ⁹	Cs1	Re1 ¹	179.74(7)
Cs1 ¹⁵	O3	Cs2 ¹	83.55(6)	O3 ¹	Cs2	O1 ⁷	67.83(7)
Cs1 ¹	O3	Cs2 ²	92.82(7)	O3 ²	Cs2	O1 ⁷	115.77(7)
Cs1 ¹⁵	O3	Cs2 ²	83.55(6)	O3 ¹	Cs2	O1 ¹¹	72.32(7)
Cs1 ¹	O3	Cs2 ⁴	177.2(1)	O3 ²	Cs2	O1 ¹¹	120.69(7)
Cs1 ¹⁵	O3	Cs2 ⁴	86.39(8)	O3 ¹	Cs2	O1 ¹²	115.77(7)
Cs1 ¹	Re1	Cs2 ¹	72.820(5)	O3 ²	Cs2	O1 ¹²	67.83(7)
Cs1 ¹	Re1	Cs2 ²	72.820(5)	O3 ¹	Cs2	O1 ¹³	120.69(7)
Cs1 ¹	Re1	Cs2 ³	140.287(7)	O3 ²	Cs2	O1 ¹³	72.32(7)
Cs2 ¹	N1	Cs2 ³	164.37(9)	O3 ¹	Cs2	O3 ²	166.0(1)
Cs2 ⁴	N1	Cs2 ³	106.76(6)	O3 ¹	Cs2	O3 ¹¹	93.13(7)
Cs2 ¹	N1	Cs2 ⁴	88.86(6)	O3 ²	Cs2	O3 ¹¹	93.13(7)
Cs2	N2	Cs1	87.96(7)	O3 ¹	Cs2	Re1 ¹¹	95.67(7)
Cs2	N2	Cs1 ¹	85.27(11)	O3 ¹¹	Cs2	Re1 ¹¹	27.41(5)
Cs2	N2	Cs1 ¹⁶	87.96(7)	O3 ²	Cs2	Re1 ¹¹	95.67(7)
Cs2 ¹	N3	Cs2 ²	166.0(1)	O3	Re1	Cs1 ¹	50.5(1)
Cs2 ¹	N3	Cs2 ⁴	86.87(7)	O3	Re1	Cs2 ¹	57.37(1)
Cs2 ²	N3	Cs2 ⁴	86.87(7)	O3	Re1	Cs2 ²	57.37(1)
Cs2 ¹	O1	Cs2 ³	164.37(9)	O3	Re1	Cs2 ³	169.2(1)
Cs2 ⁴	O1	Cs2 ³	106.76(6)	O3	Re1	Cs2 ⁴	72.8(1)
Cs2 ¹	O1	Cs2 ⁴	88.86(6)	O3	Re1	O1 ⁵	108.8(1)
Cs2	O2	Cs1	87.96(7)	Re1	N1	Cs1	106.8(1)
Cs2	O2	Cs1 ¹	85.3(1)	Re1	N1	Cs1 ³	159.3(1)
Cs2	O2	Cs1 ¹⁶	87.96(7)	Re1	N1	Cs2 ¹	95.96(9)
Cs2 ¹	O3	Cs2 ²	166.0(1)	Re1	N1	Cs2 ³	86.72(8)
Cs2 ¹	O3	Cs2 ⁴	86.87(7)	Re1	N1	Cs2 ⁴	82.87(8)
Cs2 ²	O3	Cs2 ⁴	86.87(7)	Re1	N2	Cs1	92.07(9)
Cs2 ⁴	Re1	Cs1 ¹	123.238(6)	Re1	N2	Cs1 ¹	94.7(1)
Cs2 ²	Re1	Cs2 ¹	114.255(8)	Re1	N2	Cs1 ¹⁶	92.07(9)
Cs2 ⁴	Re1	Cs2 ¹	77.352(5)	Re1	N2	Cs2	179.9(2)
Cs2 ⁴	Re1	Cs2 ²	77.352(5)	Re1	N3	Cs1 ¹	103.0(2)
Cs2 ¹	Re1	Cs2 ³	121.210(4)	Re1	N3	Cs1 ¹⁵	166.2(2)

Cs2 ²	Re1	Cs2 ³	121.210(4)	Re1	N3	Cs2 ¹	95.61(6)
Cs2 ⁴	Re1	Cs2 ³	96.476(6)	Re1	N3	Cs2 ²	95.61(6)
N1	Cs1	O2 ¹	83.06(8)	Re1	N3	Cs2 ⁴	79.8(1)
N2	Re1	N3	109.1(2)	Re1	O1	Cs1	106.8(1)
O1 ⁶	Cs1	O1	156.26(5)	Re1	O1	Cs1 ³	159.3(1)
O1 ⁷	Cs1	O1	104.09(7)	Re1	O1	Cs2 ¹	95.96(9)
O1	Cs1	O2 ¹	83.06(8)	Re1	O1	Cs2 ³	86.72(8)
O1 ⁶	Cs1	O2 ¹	119.81(7)	Re1	O1	Cs2 ⁴	82.87(8)
O1 ⁷	Cs1	O2 ¹	119.81(7)	Re1	O2	Cs1	92.07(9)
O1 ⁸	Cs1	O2 ¹	83.06(8)	Re1	O2	Cs1 ¹	94.7(2)
O1 ⁵	Re1	O1	110.6(2)	Re1	O2	Cs1 ¹⁶	92.07(9)
O2 ¹	Cs1	O2	67.13(6)	Re1	O2	Cs2	179.9(2)
O2 ¹⁰	Cs1	O2	133.5(1)	Re1	O3	Cs1 ¹	103.0(2)
O2 ¹	Cs1	O2 ¹⁰	67.13(6)	Re1	O3	Cs1 ¹⁵	166.2(2)
O2	Cs1	Re1 ¹	71.56(7)	Re1	O3	Cs2 ¹	95.61(6)
O2 ¹	Cs1	Re1 ¹	26.78(8)	Re1	O3	Cs2 ²	95.61(6)
O2 ¹⁰	Cs1	Re1 ¹	71.56(7)	Re1	O3	Cs2 ⁴	79.8(1)

¹1-x,1-y,1-z, ²1-x,-y,1-z, ³1/2+x,y,3/2-z, ⁴1+x,y,z, ⁵+x,1/2-y,z, ⁶-1/2+x,3/2-y,3/2-z, ⁷-1/2+x,y,3/2-z, ⁸+x,3/2-y,z, ⁹3/2-x,1-y,1/2+z, ¹⁰+x,1+y,z, ¹¹-1+x,y,z, ¹²-1/2+x,1/2-y,3/2-z, ¹³-1+x,1/2-y,z, ¹⁴1-x,-1/2+y,1-z, ¹⁵3/2-x,1-y,-1/2+z, ¹⁶+x,-1+y,z.

Table S22. Atomic occupancy for Cs₂[ReO₃N].

Atom	Occupancy	Atom	Occupancy	Atom	Occupancy
O1	0.75	O2	0.75	O3	0.75
N1	0.25	N2	0.25	N3	0.25

D. Calculated Raman data

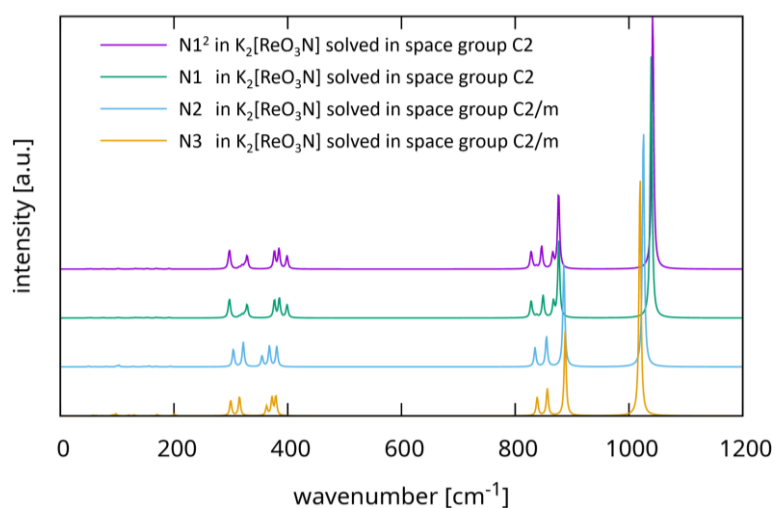


Figure S3. Calculated Raman spectra for $K_2[ReO_3N]$ solved in the space group $C2/m$ with nitrogen on oxygen position O3 (yellow), solved in the space group $C2/m$ with nitrogen on oxygen position O2 (blue), solved in the space group $C2$ (to make the two positions 1 crystallographically independent) with nitrogen on oxygen position O1 (green) and solved in the space group $C2$ with nitrogen on oxygen position O1² (purple). For naming details see Figure S4.

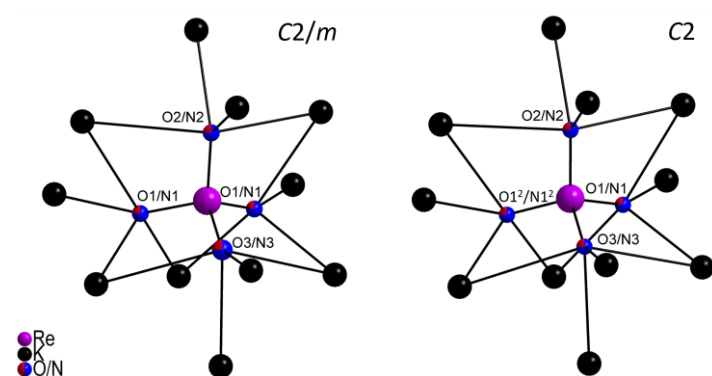


Figure S4. Structure of the coordination of O/N atoms by K in $K_2[ReO_3N]$ solved in the space group $C2/m$ (left) and $C2$ (right) with different position naming.

Table S23. Calculated Raman frequencies, irreducible representation and intensities for $K_2[ReO_3N]$ solved in the space group $C2/m$ with nitrogen on position O3, see Figure S4. ω wagging, δ bending, ν stretching, as asymmetric, s symmetric, lattice.

#	Irreducible Representation	Wavenumber [cm ⁻¹]	Intensity			Mode
			Total	Parallel	Perpendicular	
1	B _g	40.08	0.14	0.08	0.06	lattice
2	A _g	57.8	2.45	1.69	0.75	lattice
3	A _g	62.97	1.07	0.7	0.37	lattice
4	B _g	73.96	0.67	0.38	0.29	lattice
5	A _g	92.22	3.18	2.14	1.05	lattice
6	B _g	97.83	8.14	4.65	3.49	lattice
7	B _g	120.77	2.96	1.69	1.27	lattice
8	A _g	130.06	3.76	2.15	1.61	lattice
9	A _g	159.7	0.54	0.31	0.23	lattice
10	B _g	170.01	1.65	0.94	0.71	lattice
11	A _g	170.61	3.55	3.15	0.4	lattice
12	A _g	200.91	7.07	4.52	2.55	lattice
13	B _g	299.74	63.91	36.52	27.39	$\delta(O-Re-O)$
14	A _g	315.14	80.11	46.89	33.22	$\delta(O-Re-O)$
15	A _g	362.83	37.24	22.97	14.27	$\delta(O-Re-O)$
16	B _g	372.36	73.69	42.11	31.58	$\delta(O-Re-N)$
17	A _g	379.07	80.07	46.53	33.53	$\omega(O-Re-N)$
18	B _g	838.62	76.05	43.46	32.59	$\nu_{as}(O-Re-O)$
19	A _g	856.45	110.11	65.3	44.81	$\nu_{as}(O-Re-O)$
20	A _g	887.82	347.89	301.01	46.88	$\nu_s(O-Re-O)$
21	A _g	1019.42	1000	956.77	43.23	$\nu_s(Re-N)$

Table S24. Calculated Raman frequencies, irreducible representation and intensities for $K_2[ReO_3N]$ solved in the space group $C2/m$ with nitrogen on position O2, see Figure S4. ω wagging, δ bending, ν stretching, as asymmetric, s symmetric, lattice.

#	Irreducible Representation	Wavenumber [cm ⁻¹]	Intensity			Mode
			Total	Parallel	Perpendicular	
1	B _g	41.32	0.01	0	0	lattice
2	A _g	49.89	2.96	2.01	0.95	lattice
3	A _g	62.34	0.71	0.47	0.24	lattice
4	B _g	81.2	1.98	1.13	0.85	lattice
5	A _g	98.32	2.67	1.53	1.14	lattice
6	B _g	103.01	6.6	3.77	2.83	lattice
7	B _g	128.18	2.39	1.37	1.03	lattice
8	A _g	146.61	1.49	0.85	0.63	lattice
9	B _g	148.84	0.85	0.49	0.37	lattice
10	A _g	155.8	3.9	2.51	1.39	lattice
11	A _g	168.74	2.58	2.41	0.17	lattice
12	A _g	193.75	2.85	1.66	1.19	lattice
13	B _g	304.42	73.01	41.72	31.29	$\delta(O-Re-O)$
14	A _g	321.82	101.63	58.53	43.1	$\delta(O-Re-O)$
15	A _g	354.86	44.92	26.69	18.22	$\delta(O-Re-O)$
16	B _g	367.77	86.45	49.4	37.05	$\delta(O-Re-N)$
17	A _g	380.72	83.66	48.78	34.88	$\omega(O-Re-N)$
18	B _g	834.86	79.16	45.23	33.92	$\nu_{as}(O-Re-O)$
19	A _g	854.98	125.12	76.1	49.02	$\nu_{as}(O-Re-O)$
20	A _g	885.52	425.9	374.14	51.77	$\nu_s(O-Re-O)$
21	A _g	1025.38	1000	958.14	41.86	$\nu_s(Re-N)$

Table S25. Calculated Raman frequencies, irreducible representation and intensities for $K_2[ReO_3N]$ solved in the space group C2 with nitrogen on position O1, see Figure S4. ω wagging, δ bending, ν stretching, as asymmetric, s symmetric, lattice.

#	Irreducible Representation	Wavenumber [cm ⁻¹]	Intensity			Mode
			Total	Parallel	Perpendicular	
1	B	46.06	0.22	0.13	0.1	lattice
2	A	48.19	0.48	0.28	0.2	lattice
3	A	53.56	1.21	0.71	0.49	lattice
4	A	73.58	0.72	0.42	0.31	lattice
5	B	76.9	1.01	0.57	0.43	lattice
6	B	88.03	0.42	0.24	0.18	lattice
7	A	101.45	1.95	1.16	0.79	lattice
8	A	104.94	0.67	0.62	0.06	lattice
9	B	111.52	0.15	0.09	0.07	lattice
10	B	125.12	0.62	0.35	0.26	lattice
11	B	132.18	2.07	1.18	0.89	lattice
12	A	137.07	0.85	0.49	0.36	lattice
13	B	140.24	0.41	0.24	0.18	lattice
14	A	142.6	0.84	0.51	0.33	lattice
15	A	151.86	1.56	0.91	0.66	lattice
16	B	154.58	1.01	0.58	0.43	lattice
17	A	169.01	2.56	2.21	0.36	lattice
18	B	175.05	0.1	0.06	0.04	lattice
19	A	176	0.92	0.7	0.22	lattice
20	A	191.24	2.28	1.34	0.94	lattice
21	A	296.3	23.7	13.57	10.13	$\delta(O-Re-O)$
22	B	297.86	62.38	35.65	26.73	$\delta(O-Re-O)$
23	B	314.91	6.47	3.7	2.77	$\delta(O-Re-O)$
24	A	319.62	12.16	7.07	5.09	$\delta(O-Re-O)$
25	B	324.3	13.09	7.48	5.61	$\omega(O-Re-O)$
26	A	328.5	54.39	33.85	20.54	$\omega(O-Re-O)$
27	B	376.61	73.31	41.89	31.42	$\delta(O-Re-N)$
28	A	385.2	82.18	47.06	35.12	$\delta(O-Re-N)$
29	B	395.08	0.41	0.23	0.18	$\delta(O-Re-N)$
30	A	398.85	54.45	31.41	23.05	$\delta(O-Re-N)$
31	A	828	70.47	40.62	29.85	$\nu_{as}(O-Re-O)$
32	B	831.77	5.65	3.23	2.42	$\nu_{as}(O-Re-O)$
33	B	837.9	9.08	5.19	3.89	$\nu_{as}(O-Re-O)$
34	A	849.02	92.94	57.67	35.27	$\nu_{as}(O-Re-O)$
35	B	867.28	63.57	36.32	27.24	$\nu_s(O-Re-O)$
36	A	876.61	317.91	302.4	15.52	$\nu_s(O-Re-O)$
37	B	1038.6	73.42	41.95	31.46	$\nu_s(Re-N)$
38	A	1039.11	1000	969.4	30.6	$\nu_s(Re-N)$

Table S26. Calculated Raman frequencies, irreducible representation and intensities for $K_2[ReO_3N]$ solved in the space group C2 with nitrogen on position O1², see Figure S4. ω wagging, δ bending, ν stretching, as asymmetric, s symmetric, lattice.

#	Irreducible Representation	Wavenumber [cm ⁻¹]	Intensity			Mode
			Total	Parallel	Perpendicular	
1	B	46.05	0.22	0.13	0.1	lattice
2	A	48.15	0.47	0.28	0.19	lattice
3	A	53.34	1.25	0.74	0.51	lattice
4	A	73.46	0.72	0.42	0.31	lattice
5	B	76.75	0.99	0.57	0.42	lattice
6	B	87.77	0.44	0.25	0.19	lattice
7	A	101.35	1.97	1.17	0.8	lattice
8	A	104.93	0.69	0.63	0.06	lattice
9	B	111.57	0.15	0.08	0.06	lattice
10	B	124.73	0.62	0.35	0.26	lattice
11	B	132.09	2.11	1.21	0.9	lattice
12	A	136.86	0.87	0.5	0.37	lattice
13	B	140.34	0.4	0.23	0.17	lattice
14	A	142.77	0.82	0.5	0.32	lattice
15	A	151.8	1.6	0.93	0.67	lattice
16	B	154.57	1.01	0.58	0.43	lattice
17	A	168.99	2.63	2.26	0.36	lattice
18	B	175.02	0.1	0.06	0.04	lattice
19	A	175.9	0.89	0.68	0.21	lattice
20	A	191.24	2.29	1.35	0.94	lattice
21	A	296.35	23.52	13.47	10.05	$\delta(O-Re-O)$
22	B	297.84	62.73	35.85	26.89	$\delta(O-Re-O)$
23	B	314.9	6.51	3.72	2.79	$\delta(O-Re-O)$
24	A	319.64	12.47	7.25	5.23	$\delta(O-Re-O)$
25	B	324.34	13.12	7.5	5.62	$\omega(O-Re-O)$
26	A	328.5	54.55	33.94	20.61	$\omega(O-Re-O)$
27	B	376.57	73.63	42.07	31.56	$\delta(O-Re-N)$
28	A	384.66	83.17	47.62	35.55	$\delta(O-Re-N)$
29	B	394.58	0.44	0.25	0.19	$\delta(O-Re-N)$
30	A	398.77	54.3	31.32	22.97	$\delta(O-Re-N)$
31	A	827.96	70.76	40.69	30.07	$\nu_{as}(O-Re-O)$
32	B	830.73	9.16	5.24	3.93	$\nu_{as}(O-Re-O)$
33	B	837.21	8.4	4.8	3.6	$\nu_{as}(O-Re-O)$
34	A	846.53	94.8	60.97	33.83	$\nu_{as}(O-Re-O)$
35	B	866.07	60.3	34.46	25.84	$\nu_s(O-Re-O)$
36	A	876.26	323.64	306.57	17.07	$\nu_s(O-Re-O)$
37	B	1041.35	74.67	42.67	32	$\nu_s(Re-N)$
38	A	1041.86	1000	969.17	30.83	$\nu_s(Re-N)$

- [1] a) A. F. Clifford, R. R. Olsen, *Inorg. Synth.* **1960**, 6, 167; b) D. Badea, S. Olthof, J. Neudörfel, R. Glaum, R. Pöttgen, M. Reimann, K. Meerholz, M. Reimer, C. Logemann, E. Strub, J. Bruns, *Eur. J. Inorg. Chem.* **2023**, 26, e202300160.
- [2] a) O. V. Dolomanov, L. J. Bourhis, R. J. Gildea, J. A. K. Howard, H. Puschmann, *J. Appl. Crystallogr.* **2009**, 42, 339-341; b) G. Sheldrick, *Acta Crystallogr.* **2015**, C71, 3-8.

7.4 $\text{Ba}_2[\text{Ir}(\text{OH})_6](\text{OH})_2$

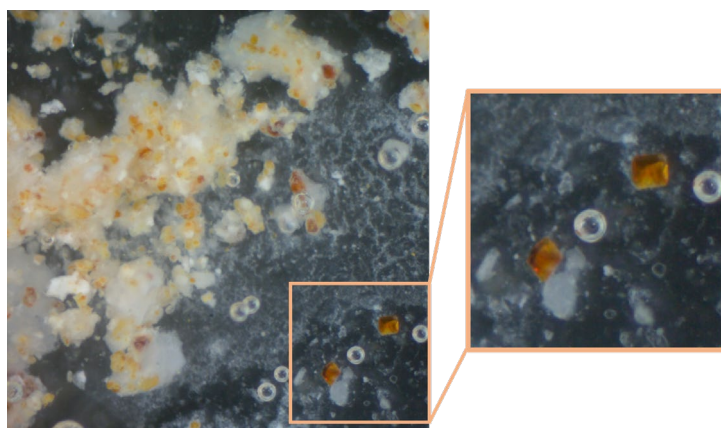


Figure 29. Microscopic image of brown single crystals of $\text{Ba}_2[\text{Ir}(\text{OH})_6](\text{OH})_2$ in a $\text{Ba}(\text{OH})_2$ hydroflux (left) and enlarged section (right).

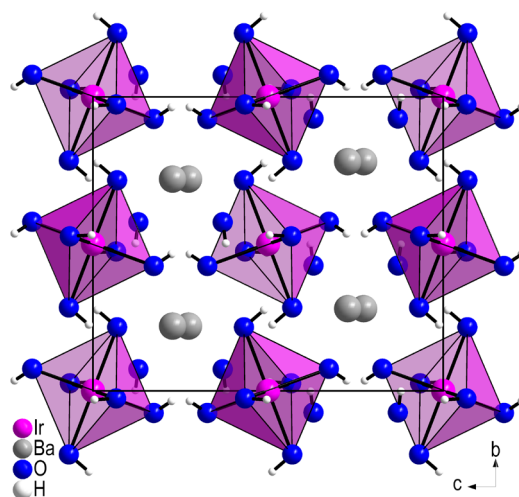


Figure 30. Unit cell of the crystal structure of $\text{Ba}_2[\text{Ir}(\text{OH})_6](\text{OH})_2$ viewed along the a -axis with pink $\text{Ir}(\text{OH})_6$ octahedra.^[78]

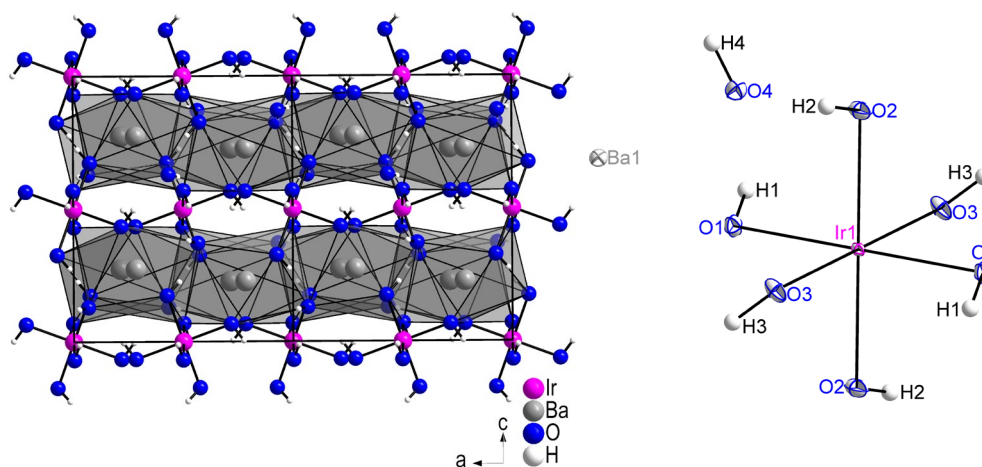


Figure 31. 3D stacking of layers with grey $\text{Ba}(\text{OH})_9$ polyhedra (left) and extended asymmetric unit of $\text{Ba}_2[\text{Ir}(\text{OH})_6](\text{OH})_2$ with thermal ellipsoids with a probability of 70% (right).^[78]

7.5 Ba_{2.4}Sr_{1.6}[Ir(OH)₆](OH)₆Table 13. Crystallographic data of Ba_{2.4}Sr_{1.6}[Ir(OH)₆](OH)₆.

Empirical formula	Ba _{2.4} Sr _{1.6} [Ir(OH) ₆](OH) ₆
Formula weight	866.10 g/mol
Temperature	100(2) K
Wavelength	0.71073 Å
Crystal system	trigonal
Space group	$R\bar{3}$ (no. 148)
Unit cell dimensions	$a = 6.3403(2)$ Å $c = 26.430(1)$ Å
Volume	920.12(7) Å ³
Z	3
Density (calculated)	4.69 g·cm ⁻³
$F(000)$	1141
Crystal size	0.10 × 0.10 × 0.05 mm ³
2 θ range for data collection	4.62° to 59.78°
Index ranges	$-8 \leq h \leq 8$, $-8 \leq k \leq 8$, $-36 \leq l \leq 36$
Reflections collected	21067
Independent reflections	598 [$R_{\text{int}} = 0.0395$, $R_{\sigma} = 0.0123$]
Completeness to θ	100%
Absorption correction	multi-scan
Maximum / minimum transmission	0.7474 / 0.4157
Data / parameters	598 / 35
Goodness-of-fit on F^2	1.049
Final R indices [$I_o > 2\sigma(I_o)$]	$R_1 = 0.0158$, $wR_2 = 0.0334$
Final R indices (all data)	$R_1 = 0.0159$, $wR_2 = 0.0334$
Largest diff. peak and hole	1.77/−1.05 e·Å ⁻³

Table 14. Atomic coordinates ($\times 10^4$) and equivalent isotropic displacement parameters ($\text{\AA}^2 \times 10^3$) for Ba_{2.4}Sr_{1.6}[Ir(OH)₆](OH)₆. $U(eq)$ is defined as one third of the trace of the orthogonalized U_{ij} tensor.

Atom	x	y	z	$U(eq)$
Ba1	6666.67	3333.33	5408.4(2)	5.04(8)
Ba2	0	0	6451.8(2)	7.69(9)
Ir1	0	0	5000	4.33(8)
O1	2187(4)	3028(4)	5398.9(9)	7.1(4)
O2	-210(4)	3681(4)	6193.1(8)	8.2(4)
Sr1	0	0	6451.8(2)	7.69(9)

Appendix

Table 15. Anisotropic displacement parameters ($\text{\AA}^2 \times 10^3$) for $\text{Ba}_{2.4}\text{Sr}_{1.6}[\text{Ir}(\text{OH})_6](\text{OH})_6$. The anisotropic displacement factor exponent takes the form: $-2\pi^2 [h^2 a^{*2} U_{11} + 2 h k a^* b^* U_{12} + \dots]$.

Atom	U_{11}	U_{22}	U_{33}	U_{23}	U_{13}	U_{12}
Ba1	4.7(1)	4.7(1)	5.7(1)	0	0	2.36(5)
Ba2	5.6(1)	5.6(1)	11.9(2)	0	0	2.79(6)
Ir1	3.97(9)	3.97(9)	5.0(1)	0	0	1.99(4)
O1	6.5(9)	8.1(9)	6.2(9)	-3.3(8)	-0.3(8)	3.1(8)
O2	10(1)	9(1)	6.1(9)	0.1(8)	1.1(8)	4.7(9)
Sr1	5.6(1)	5.6(1)	11.9(2)	0	0	2.79(6)

Table 16. Bond lengths for $\text{Ba}_{2.4}\text{Sr}_{1.6}[\text{Ir}(\text{OH})_6](\text{OH})_6$.

Atom	Atom	Length [\AA]	Atom	Atom	Length [\AA]
Ba1	O1	2.748(2)	Ir1	O1 ⁷	2.014(2)
Ba1	O1 ⁴	2.954(2)	Ir1	O1 ⁸	2.014(2)
Ba1	O1 ⁹	2.954(2)	Ir1	O1 ⁹	2.014(2)
Ba1	O1 ¹⁰	2.748(2)	O1	Ba2	3.270(2)
Ba1	O1 ¹¹	2.954(2)	O2	Ba2	2.499(2)
Ba1	O1 ¹²	2.748(2)	Sr1	O1	3.270(2)
Ba1	O2 ⁶	2.799(2)	Sr1	O1 ⁶	3.270(2)
Ba1	O2 ¹³	2.799(2)	Sr1	O1 ⁷	3.270(2)
Ba1	O2 ¹⁴	2.799(2)	Sr1	O2	2.499(2)
Ir1	Ba1	3.8164(1)	Sr1	O2 ⁶	2.499(2)
Ir1	Ba1 ¹	3.8164(1)	Sr1	O2 ⁷	2.499(2)
Ir1	Ba1 ²	3.8164(1)	Sr1	O2 ¹⁵	2.616(2)
Ir1	Ba1 ³	3.8164(1)	Sr1	O2 ¹⁸	2.616(2)
Ir1	Ba1 ⁴	3.8164(1)	Sr1	O2 ¹⁹	2.616(2)
Ir1	Ba1 ⁵	3.8164(1)	Sr1	Sr1 ¹⁵	3.8328(3)
Ir1	O1	2.014(2)	Sr1	Sr1 ¹⁶	3.8328(3)
Ir1	O1 ²	2.014(2)	Sr1	Sr1 ¹⁷	3.8328(3)
Ir1	O1 ⁶	2.014(2)			

¹-1+x,+y,+z; ²-x,-y,1-z; ³1-x,-y,1-z; ⁴1-x,1-y,1-z; ⁵-1+x,-1+y,+z; ⁶+y-x,-x,+z; ⁷-y,+x-y,+z; ⁸-y+x,+x,1-z; ⁹+y,-x+y,1-z; ¹⁰1-y,+x-y,+z; ¹¹1-y+x,+x,1-z; ¹²1+y-x,1-x,+z; ¹³1+x,+y,+z; ¹⁴1-y,1+x-y,+z; ¹⁵-1/3-x,1/3-y,4/3-z; ¹⁶-1/3-x,-2/3-y,4/3-z; ¹⁷2/3-x,1/3-y,4/3-z; ¹⁸2/3-y+x,1/3+x,4/3-z; ¹⁹-1/3+y,-2/3-x+y,4/3-z.

Table 17. Bond angles for $\text{Ba}_{2.4}\text{Sr}_{1.6}[\text{Ir}(\text{OH})_6](\text{OH})_6$.

Atom	Atom	Atom	Angle [$^\circ$]	Atom	Atom	Atom	Angle [$^\circ$]
Ba1 ¹⁶	Ba2	Ba1 ¹	126.992(6)	O1	Sr1	Sr1 ¹⁷	137.55(4)
Ba1	Ir1	Ba1 ³	112.335(4)	O1	Sr1	Sr1 ¹⁸	96.75(4)
Ba1	Ir1	Ba1 ⁴	67.665(4)	O1 ⁷	Sr1	O1 ⁹	54.08(6)
Ba1	Ir1	Ba1 ⁵	180	O1 ⁷	Sr1	Sr1 ¹⁶	137.55(4)

Appendix

Ba1 ¹	Ir1	Ba1 ²	180	O1 ⁷	Sr1	Sr1 ¹⁷	96.75(4)
Ba1 ¹	Ir1	Ba1 ⁴	67.665(4)	O1 ⁷	Sr1	Sr1 ¹⁸	84.34(4)
Ba1 ¹	Ir1	Ba1	112.335(4)	O1 ⁹	Sr1	Sr1 ¹⁶	96.75(4)
Ba1 ¹	Ir1	Ba1 ⁵	67.665(4)	O1 ⁹	Sr1	Sr1 ¹⁷	84.34(4)
Ba1 ¹	Ir1	Ba1 ³	112.335(4)	O1 ⁹	Sr1	Sr1 ¹⁸	137.55(4)
Ba1 ²	Ir1	Ba1 ³	67.665(4)	O2 ¹⁰	Ba1	Ir1	142.87(5)
Ba1 ²	Ir1	Ba1 ⁴	112.335(4)	O2 ¹⁵	Ba1	Ir1	98.28(5)
Ba1 ²	Ir1	Ba1 ⁵	112.335(4)	O2 ⁹	Ba1	Ir1	71.78(5)
Ba1 ²	Ir1	Ba1	67.665(4)	O2 ¹⁰	Ba1	Ir1 ¹⁰	71.78(5)
Ba1 ³	Ir1	Ba1 ⁴	180	O2 ¹⁵	Ba1	Ir1 ¹⁰	142.87(5)
Ba1 ⁵	Ir1	Ba1 ⁴	112.334(4)	O2 ⁹	Ba1	Ir1 ¹⁰	98.28(5)
Ba1 ⁵	Ir1	Ba1 ³	67.666(4)	O2 ¹⁰	Ba1	Ir1 ¹¹	98.28(5)
Ba1	O1	Ba1 ⁴	96.29(7)	O2 ¹⁵	Ba1	Ir1 ¹¹	71.78(5)
Ba1	O1	Ba2	98.84(7)	O2 ⁹	Ba1	Ir1 ¹¹	142.87(5)
Ba1 ⁴	O1	Ba2	160.01(8)	O2 ¹⁰	Ba1	O1 ⁴	125.84(7)
Ba1	O1	Sr1	98.84(7)	O2 ¹⁵	Ba1	O1 ⁴	96.32(6)
Ba1 ⁴	O1	Sr1	160.01(8)	O2 ⁹	Ba1	O1 ⁴	155.48(7)
Ir1	Ba1	Ir1 ¹¹	112.336(4)	O2 ¹⁰	Ba1	O1 ⁶	155.48(7)
Ir1 ¹⁰	Ba1	Ir1 ¹¹	112.336(4)	O2 ¹⁵	Ba1	O1 ⁶	125.84(7)
Ir1 ¹⁰	Ba1	Ir1	112.336(4)	O2 ⁹	Ba1	O1 ⁶	96.32(7)
Ir1	Ba2	Ba1 ¹	53.007(6)	O2 ¹⁰	Ba1	O1 ¹⁴	96.32(6)
Ir1	Ba2	Ba1 ¹⁶	180	O2 ¹⁵	Ba1	O1 ¹⁴	155.48(7)
Ir1	O1	Ba1	105.47(9)	O2 ⁹	Ba1	O1 ¹⁴	125.84(7)
Ir1	O1	Ba1 ⁴	98.61(8)	O2 ¹⁰	Ba1	O2 ⁹	71.13(7)
Ir1	O1	Ba2	89.89(8)	O2 ¹⁰	Ba1	O2 ¹⁵	71.13(7)
Ir1	O1	Sr1	89.89(8)	O2 ⁹	Ba1	O2 ¹⁵	71.13(7)
O1	Ba1	Ir1	30.58(5)	O2	Ba2	Ba1 ¹	32.05(5)
O1 ¹²	Ba1	Ir1	93.21(5)	O2 ¹⁸	Ba2	Ba1 ¹	87.32(5)
O1 ¹³	Ba1	Ir1	142.87(5)	O2 ¹⁹	Ba2	Ba1 ¹	160.41(5)
O1 ¹⁴	Ba1	Ir1	103.90(5)	O2 ²⁰	Ba2	Ba1 ¹	111.11(5)
O1 ⁴	Ba1	Ir1	90.00(4)	O2 ⁷	Ba2	Ba1 ¹	82.66(5)
O1 ⁶	Ba1	Ir1	31.46(4)	O2 ⁹	Ba2	Ba1 ¹	118.78(5)
O1	Ba1	Ir1 ¹⁰	142.87(5)	O2	Ba2	Ba1 ¹⁶	105.88(5)
O1 ¹²	Ba1	Ir1 ¹⁰	30.58(5)	O2 ¹⁸	Ba2	Ba1 ¹⁶	45.93(5)
O1 ¹³	Ba1	Ir1 ¹⁰	93.21(5)	O2 ¹⁹	Ba2	Ba1 ¹⁶	45.93(5)
O1 ¹⁴	Ba1	Ir1 ¹⁰	31.46(4)	O2 ²⁰	Ba2	Ba1 ¹⁶	45.93(5)
O1 ⁴	Ba1	Ir1 ¹⁰	103.90(4)	O2 ⁷	Ba2	Ba1 ¹⁶	105.88(5)
O1 ⁶	Ba1	Ir1 ¹⁰	90.00(4)	O2 ⁹	Ba2	Ba1 ¹⁶	105.88(5)
O1	Ba1	Ir1 ¹¹	93.21(5)	O2	Ba2	Ir1	74.12(5)
O1 ¹²	Ba1	Ir1 ¹¹	142.87(5)	O2 ¹⁸	Ba2	Ir1	134.07(5)
O1 ¹³	Ba1	Ir1 ¹¹	30.58(5)	O2 ¹⁹	Ba2	Ir1	134.07(5)

Appendix

O1 ¹⁴	Ba1	Ir1 ¹¹	90.00(4)	O2 ²⁰	Ba2	Ir1	134.07(5)
O1 ⁴	Ba1	Ir1 ¹¹	31.46(4)	O2 ⁷	Ba2	Ir1	74.12(5)
O1 ⁶	Ba1	Ir1 ¹¹	103.90(4)	O2 ⁹	Ba2	Ir1	74.12(5)
O1 ¹²	Ba1	O1	119.991(2)	O2	Ba2	O1	54.81(7)
O1 ¹³	Ba1	O1	119.992(2)	O2 ¹⁸	Ba2	O1	136.26(6)
O1	Ba1	O1 ⁴	83.71(7)	O2 ¹⁹	Ba2	O1	146.43(7)
O1 ¹²	Ba1	O1 ⁴	129.58(3)	O2 ²⁰	Ba2	O1	102.72(6)
O1 ¹³	Ba1	O1 ⁴	56.81(8)	O2 ⁷	Ba2	O1	105.03(6)
O1 ¹⁴	Ba1	O1 ⁴	73.60(7)	O2 ⁹	Ba2	O1	67.55(7)
O1 ⁶	Ba1	O1 ⁴	73.60(7)	O2	Ba2	O1 ⁷	67.55(7)
O1	Ba1	O1 ⁶	56.81(8)	O2 ¹⁸	Ba2	O1 ⁷	102.72(6)
O1 ¹²	Ba1	O1 ⁶	83.71(7)	O2 ¹⁹	Ba2	O1 ⁷	136.26(7)
O1 ¹³	Ba1	O1 ⁶	129.58(3)	O2 ²⁰	Ba2	O1 ⁷	146.43(7)
O1 ¹⁴	Ba1	O1 ⁶	73.60(7)	O2 ⁷	Ba2	O1 ⁷	54.81(7)
O1 ¹²	Ba1	O1 ¹³	119.992(2)	O2 ⁹	Ba2	O1 ⁷	105.03(6)
O1	Ba1	O1 ¹⁴	129.58(3)	O2	Ba2	O1 ⁹	105.03(6)
O1 ¹²	Ba1	O1 ¹⁴	56.81(8)	O2 ¹⁸	Ba2	O1 ⁹	146.43(7)
O1 ¹³	Ba1	O1 ¹⁴	83.71(7)	O2 ¹⁹	Ba2	O1 ⁹	102.73(6)
O1	Ba1	O2 ⁹	72.24(7)	O2 ²⁰	Ba2	O1 ⁹	136.26(7)
O1 ¹²	Ba1	O2 ⁹	69.36(7)	O2 ⁷	Ba2	O1 ⁹	67.55(7)
O1 ¹³	Ba1	O2 ⁹	132.67(7)	O2 ⁹	Ba2	O1 ⁹	54.81(7)
O1	Ba1	O2 ¹⁰	132.67(7)	O2	Ba2	O2 ⁷	112.81(5)
O1 ¹²	Ba1	O2 ¹⁰	72.24(7)	O2	Ba2	O2 ⁹	112.81(5)
O1 ¹³	Ba1	O2 ¹⁰	69.36(7)	O2 ⁷	Ba2	O2 ⁹	112.81(4)
O1	Ba1	O2 ¹⁵	69.36(7)	O2	Ba2	O2 ¹⁸	82.97(8)
O1 ¹²	Ba1	O2 ¹⁵	132.67(7)	O2 ¹⁹	Ba2	O2 ¹⁸	76.96(8)
O1 ¹³	Ba1	O2 ¹⁵	72.24(7)	O2 ²⁰	Ba2	O2 ¹⁸	76.96(8)
O1	Ba2	Ba1 ¹	51.33(4)	O2 ⁷	Ba2	O2 ¹⁸	79.2(1)
O1 ⁷	Ba2	Ba1 ¹	36.34(4)	O2 ⁹	Ba2	O2 ¹⁸	151.69(5)
O1 ⁹	Ba2	Ba1 ¹	83.91(4)	O2	Ba2	O2 ¹⁹	151.69(5)
O1	Ba2	Ba1 ¹⁶	148.33(4)	O2 ⁷	Ba2	O2 ¹⁹	82.97(8)
O1 ⁷	Ba2	Ba1 ¹⁶	148.33(4)	O2 ⁹	Ba2	O2 ¹⁹	79.2(1)
O1 ⁹	Ba2	Ba1 ¹⁶	148.33(4)	O2	Ba2	O2 ²⁰	79.2(1)
O1	Ba2	Ir1	31.67(4)	O2 ¹⁹	Ba2	O2 ²⁰	76.96(8)
O1 ⁷	Ba2	Ir1	31.67(4)	O2 ⁷	Ba2	O2 ²⁰	151.69(5)
O1 ⁹	Ba2	Ir1	31.67(4)	O2 ⁹	Ba2	O2 ²⁰	82.97(8)
O1	Ba2	O1 ⁷	54.08(6)	O2	Sr1	O1	54.81(7)
O1	Ba2	O1 ⁹	54.08(6)	O2 ¹⁸	Sr1	O1	136.26(6)
O1 ⁷	Ba2	O1 ⁹	54.08(6)	O2 ¹⁹	Sr1	O1	146.43(7)
O1	Ir1	Ba1	43.95(6)	O2 ²⁰	Sr1	O1	102.72(6)
O1 ⁵	Ir1	Ba1	136.05(6)	O2 ⁷	Sr1	O1	105.03(6)

Appendix

O1 ⁶	Ir1	Ba1	49.93(7)	O2 ⁹	Sr1	O1	67.55(7)
O1 ⁷	Ir1	Ba1	130.07(7)	O2	Sr1	O1 ⁷	67.55(7)
O1 ⁸	Ir1	Ba1	111.58(7)	O2 ¹⁸	Sr1	O1 ⁷	102.72(6)
O1 ⁹	Ir1	Ba1	68.42(7)	O2 ¹⁹	Sr1	O1 ⁷	136.26(7)
O1	Ir1	Ba1 ¹	68.42(6)	O2 ²⁰	Sr1	O1 ⁷	146.43(7)
O1 ⁵	Ir1	Ba1 ¹	111.58(6)	O2 ⁷	Sr1	O1 ⁷	54.81(7)
O1 ⁶	Ir1	Ba1 ¹	136.05(6)	O2 ⁹	Sr1	O1 ⁷	105.03(6)
O1 ⁷	Ir1	Ba1 ¹	43.95(6)	O2	Sr1	O1 ⁹	105.03(6)
O1 ⁸	Ir1	Ba1 ¹	49.93(6)	O2 ¹⁸	Sr1	O1 ⁹	146.43(7)
O1 ⁹	Ir1	Ba1 ¹	130.07(6)	O2 ¹⁹	Sr1	O1 ⁹	102.73(6)
O1	Ir1	Ba1 ²	111.58(6)	O2 ²⁰	Sr1	O1 ⁹	136.26(7)
O1 ⁵	Ir1	Ba1 ²	68.42(6)	O2 ⁷	Sr1	O1 ⁹	67.55(7)
O1 ⁶	Ir1	Ba1 ²	43.95(6)	O2 ⁹	Sr1	O1 ⁹	54.81(7)
O1 ⁷	Ir1	Ba1 ²	136.05(6)	O2	Sr1	O2 ⁷	112.81(5)
O1 ⁸	Ir1	Ba1 ²	130.07(6)	O2	Sr1	O2 ⁹	112.81(5)
O1 ⁹	Ir1	Ba1 ²	49.93(6)	O2 ⁷	Sr1	O2 ⁹	112.81(4)
O1	Ir1	Ba1 ³	130.06(6)	O2	Sr1	O2 ¹⁸	82.97(8)
O1 ⁵	Ir1	Ba1 ³	49.93(6)	O2 ¹⁹	Sr1	O2 ¹⁸	76.96(8)
O1 ⁶	Ir1	Ba1 ³	111.58(6)	O2 ²⁰	Sr1	O2 ¹⁸	76.96(8)
O1 ⁷	Ir1	Ba1 ³	68.42(6)	O2 ⁷	Sr1	O2 ¹⁸	79.23(10)
O1 ⁸	Ir1	Ba1 ³	136.05(7)	O2 ⁹	Sr1	O2 ¹⁸	151.69(5)
O1 ⁹	Ir1	Ba1 ³	43.95(7)	O2	Sr1	O2 ¹⁹	151.69(5)
O1	Ir1	Ba1 ⁴	49.94(6)	O2 ⁷	Sr1	O2 ¹⁹	82.97(8)
O1 ⁵	Ir1	Ba1 ⁴	130.07(6)	O2 ⁹	Sr1	O2 ¹⁹	79.23(10)
O1 ⁶	Ir1	Ba1 ⁴	68.42(6)	O2	Sr1	O2 ²⁰	79.2(1)
O1 ⁷	Ir1	Ba1 ⁴	111.58(6)	O2 ¹⁹	Sr1	O2 ²⁰	76.96(8)
O1 ⁸	Ir1	Ba1 ⁴	43.95(7)	O2 ⁷	Sr1	O2 ²⁰	151.69(5)
O1 ⁹	Ir1	Ba1 ⁴	136.05(7)	O2 ⁹	Sr1	O2 ²⁰	82.97(8)
O1	Ir1	Ba1 ⁵	136.05(6)	O2	Sr1	Sr1 ¹⁶	97.19(6)
O1 ⁵	Ir1	Ba1 ⁵	43.95(6)	O2 ¹⁸	Sr1	Sr1 ¹⁶	114.83(6)
O1 ⁶	Ir1	Ba1 ⁵	130.07(7)	O2 ¹⁹	Sr1	Sr1 ¹⁶	73.98(6)
O1 ⁷	Ir1	Ba1 ⁵	49.93(7)	O2 ²⁰	Sr1	Sr1 ¹⁶	40.32(5)
O1 ⁸	Ir1	Ba1 ⁵	68.42(7)	O2 ⁷	Sr1	Sr1 ¹⁶	148.62(5)
O1 ⁹	Ir1	Ba1 ⁵	111.58(7)	O2 ⁹	Sr1	Sr1 ¹⁶	42.65(5)
O1 ⁵	Ir1	O1	180	O2	Sr1	Sr1 ¹⁷	148.62(6)
O1 ⁶	Ir1	O1	84.88(9)	O2 ¹⁸	Sr1	Sr1 ¹⁷	73.98(5)
O1 ⁷	Ir1	O1	95.12(9)	O2 ¹⁹	Sr1	Sr1 ¹⁷	40.32(5)
O1 ⁸	Ir1	O1	84.88(9)	O2 ²⁰	Sr1	Sr1 ¹⁷	114.83(6)
O1 ⁹	Ir1	O1	95.12(9)	O2 ⁷	Sr1	Sr1 ¹⁷	42.65(5)
O1 ⁵	Ir1	O1 ⁶	95.12(9)	O2 ⁹	Sr1	Sr1 ¹⁷	97.19(5)
O1 ⁵	Ir1	O1 ⁷	84.88(9)	O2	Sr1	Sr1 ¹⁸	42.65(5)

Appendix

O1 ⁶	Ir1	O1 ⁷	180.00(8)	O2 ¹⁸	Sr1	Sr1 ¹⁸	40.32(5)
O1 ⁵	Ir1	O1 ⁸	95.12(9)	O2 ¹⁹	Sr1	Sr1 ¹⁸	114.83(6)
O1 ⁶	Ir1	O1 ⁸	95.12(9)	O2 ²⁰	Sr1	Sr1 ¹⁸	73.98(5)
O1 ⁷	Ir1	O1 ⁸	84.88(9)	O2 ⁷	Sr1	Sr1 ¹⁸	97.19(5)
O1 ⁵	Ir1	O1 ⁹	84.88(9)	O2 ⁹	Sr1	Sr1 ¹⁸	148.62(5)
O1 ⁶	Ir1	O1 ⁹	84.88(9)	Sr1	O2	Ba1 ¹	119.68(9)
O1 ⁷	Ir1	O1 ⁹	95.12(9)	Sr1 ¹⁸	O2	Ba1 ¹	91.88(7)
O1 ⁸	Ir1	O1 ⁹	180.0(1)	Sr1	O2	Sr1 ¹⁸	97.03(8)
O1	Sr1	O1 ⁷	54.08(6)	Sr1 ¹⁶	Sr1	Sr1 ¹⁷	111.61(1)
O1	Sr1	O1 ⁹	54.08(6)	Sr1 ¹⁶	Sr1	Sr1 ¹⁸	111.61(1)
O1	Sr1	Sr1 ¹⁶	84.34(4)	Sr1 ¹⁷	Sr1	Sr1 ¹⁸	111.61(1)

¹-1+x,+y,+z; ²1-x,-y,1-z; ³-1+x,-1+y,+z; ⁴1-x,1-y,1-z; ⁵-x,-y,1-z; ⁶+y,-x+y,1-z; ⁷-y,+x-y,+z; ⁸-y+x,+x,1-z; ⁹+y-x,-x,+z; ¹⁰1+x,+y,+z; ¹¹1+x,1+y,+z; ¹²1-y,+x-y,+z; ¹³1+y-x,1-x,+z; ¹⁴1-y+x,+x,1-z; ¹⁵1-y,1+x-y,+z; ¹⁶2/3-x,1/3-y,4/3-z; ¹⁷-1/3-x,-2/3-y,4/3-z; ¹⁸-1/3-x,1/3-y,4/3-z; ¹⁹-1/3+y,-2/3-x+y,4/3-z; ²⁰2/3-y+x,1/3+x,4/3-z.

Table 18. Hydrogen atom coordinates ($\times 10^4$) and equivalent isotropic displacement parameters ($\text{\AA}^2 \times 10^3$) for $\text{Ba}_{2.4}\text{Sr}_{1.6}[\text{Ir}(\text{OH})_6](\text{OH})_6$. $U(eq)$ is defined as one third of the trace of the orthogonalized U_{ij} tensor $\text{Ba}_{2.4}\text{Sr}_{1.6}[\text{Ir}(\text{OH})_6](\text{OH})_6$.

Atom	x	y	z	$U(eq)$
H1	1560(100)	3290(90)	5630(20)	18(12)
H2	610(100)	4970(110)	6240(20)	20(13)

Table 19. Atomic occupancy for $\text{Ba}_{2.4}\text{Sr}_{1.6}[\text{Ir}(\text{OH})_6](\text{OH})_6$.

Atom	Occupancy	Atom	Occupancy
Sr1	0.8	Ba2	0.2

7.6 Ag₂PbO₃Table 20. Crystallographic data of Ag₂PbO₃.

Empirical formula	Ag ₂ PbO ₃
Formula weight	470.93 g/mol
Temperature	100(2) K
Wavelength	0.71073 Å
Crystal system	orthorhombic
Space group	<i>Fddd</i> (no. 70)
Unit cell dimensions	$a = 7.0352(5)$ Å $b = 9.4729(6)$ Å $c = 20.126(1)$ Å
Volume	1341.3(2) Å ³
<i>Z</i>	16
Density (calculated)	9.33 g·cm ⁻³
<i>F</i> (000)	3200
Crystal size	0.05 × 0.04 × 0.03 mm ³
2 θ range for data collection	7.49° to 62.97°
Index ranges	-10 ≤ <i>h</i> ≤ 10, -13 ≤ <i>k</i> ≤ 13, -29 ≤ <i>l</i> ≤ 29
Reflections collected	9111
Independent reflections	565 [<i>R</i> _{int} = 0.0437, <i>R</i> _σ = 0.0199]
Completeness to θ	100%
Absorption correction	multi-scan
Maximum / minimum transmission	0.7470 / 0.4547
Data / parameters	565 / 31
Goodness-of-fit on <i>F</i> ²	1.117
Final <i>R</i> indices [<i>I</i> _o > 2σ (<i>I</i> _o)]	<i>R</i> ₁ = 0.0268, <i>wR</i> ₂ = 0.0639
Final <i>R</i> indices (all data)	<i>R</i> ₁ = 0.0326, <i>wR</i> ₂ = 0.0675
Largest diff. peak and hole	3.09/-2.77 e·Å ⁻³

Table 21. Atomic coordinates (×10⁴) and equivalent isotropic displacement parameters (Å²×10³) for Ag₂PbO₃. *U*(eq) is defined as one third of the trace of the orthogonalized *U*_{ij} tensor.

Atom	<i>x</i>	<i>y</i>	<i>z</i>	<i>U</i> (eq)
Ag1	8750	-1250	6192.2(6)	22.9(3)
Ag2	8750	3750	8024.4(5)	6.8(2)
O1	8243(13)	1250	6250	12(2)
O2	6171(10)	3559(7)	7202(3)	12(1)
Pb1	6250	1250	7100.3(2)	6.6(2)

Appendix

Table 22. Anisotropic displacement parameters ($\text{\AA}^2 \times 10^3$) for Ag_2PbO_3 . The anisotropic displacement factor exponent takes the form: $-2\pi^2 [h^2 a^{*2} U_{11} + 2 h k a^* b^* U_{12} + \dots]$.

Atom	U_{11}	U_{22}	U_{33}	U_{23}	U_{13}	U_{12}
Ag1	42.0(7)	17.3(5)	9.3(5)	0	0	16.5(5)
Ag2	5.1(4)	9.1(4)	6.3(4)	0	0	-1.7(3)
O1	10(4)	12(4)	12(4)	0(3)	0	0
O2	11(3)	10(3)	14(3)	-2(2)	4(2)	0(3)
Pb1	7.6(2)	6.6(2)	5.8(2)	0	0	0.4(2)

Table 23. Bond lengths for Ag_2PbO_3 .

Atom	Atom	Length [\AA]	Atom	Atom	Length [\AA]
Ag2	Ag1 ¹⁰	3.3449(7)	Ag2	O2 ⁶	2.590(7)
Ag2	Ag1 ¹¹	3.2416(6)	O1	Ag1	2.398(1)
Ag2	Ag1 ⁷	3.3449(7)	O1	Ag1 ¹²	2.398(1)
Ag2	Ag1 ⁹	3.2416(6)	O2	Ag1 ¹²	2.562(7)
Ag2	Ag2 ⁴	2.921(2)	Pb1	O1	2.212(6)
Ag2	O1 ⁷	2.571(8)	Pb1	O1 ¹	2.212(6)
Ag2	O1 ⁸	2.571(8)	Pb1	O2	2.198(7)
Ag2	O2	2.462(7)	Pb1	O2 ¹	2.198(7)
Ag2	O2 ³	2.590(7)	Pb1	O2 ²	2.214(7)
Ag2	O2 ⁵	2.462(7)	Pb1	O2 ³	2.214(7)

¹5/4-x,1/4-y,+z; ²1-x,1/2-y,3/2-z; ³1/4+x,-1/4+y,3/2-z; ⁴7/4-x,+y,7/4-z; ⁵7/4-x,3/4-y,+z; ⁶3/2-x,1-y,3/2-z; ⁷2-x,1/2-y,3/2-z; ⁸-1/4+x,1/4+y,3/2-z; ⁹1/4+x,-y,1/4+z; ¹⁰3/2-x,-y,3/2-z; ¹¹-1/4+x,1/2-y,1/4+z; ¹²7/4-x,1/2+y,5/4-z.

Table 24. Bond angles for Ag_2PbO_3 .

Atom	Atom	Atom	Angle [$^\circ$]	Atom	Atom	Atom	Angle [$^\circ$]
Ag1 ⁵	Ag2	Ag1 ⁶	64.70(1)	O1 ¹	Pb1	O2 ²	167.9(3)
Ag1 ⁷	Ag2	Ag1 ⁶	92.09(2)	O1	Pb1	O2 ³	167.9(3)
Ag1 ⁵	Ag2	Ag1 ⁷	131.01(5)	O1 ¹	Pb1	O2 ³	90.2(3)
Ag1 ⁵	Ag2	Ag1 ⁸	92.09(2)	O2 ¹⁵	Ag1	Ag2 ⁶	90.5(2)
Ag1 ⁶	Ag2	Ag1 ⁸	123.75(5)	O2 ¹⁸	Ag1	Ag2 ⁶	130.8(2)
Ag1 ⁷	Ag2	Ag1 ⁸	64.70(1)	O2 ¹⁵	Ag1	Ag2 ⁸	130.8(2)
Ag1 ⁵	Ag2	Pb1	116.33(1)	O2 ¹⁸	Ag1	Ag2 ⁸	90.5(2)
Ag1 ⁶	Ag2	Pb1	175.90(4)	O2 ¹⁵	Ag1	Ag2 ¹⁴	51.4(2)
Ag1 ⁷	Ag2	Pb1	89.92(1)	O2 ¹⁸	Ag1	Ag2 ¹⁴	92.4(2)
Ag1 ⁸	Ag2	Pb1	60.36(2)	O2 ¹⁵	Ag1	Ag2 ¹⁷	92.4(2)
Ag1	O1	Ag1 ¹²	162.9(4)	O2 ¹⁸	Ag1	Ag2 ¹⁷	51.4(2)
Ag1	O1	Ag2 ⁶	84.6(2)	O2 ¹⁸	Ag1	O2 ¹⁵	90.7(3)
Ag1 ¹²	O1	Ag2 ⁶	81.4(2)	O2 ¹⁵	Ag1	Pb1 ⁸	134.6(2)

Appendix

Ag1	O1	Ag2 ¹⁴	81.4(2)	O2 ¹⁸	Ag1	Pb1 ⁸	134.6(2)
Ag1 ¹²	O1	Ag2 ¹⁴	84.6(2)	O2 ¹⁵	Ag1	Pb1 ¹³	95.0(2)
Ag1 ¹²	O2	Ag2 ⁹	78.0(2)	O2 ¹⁸	Ag1	Pb1 ¹³	41.0(2)
Ag2 ¹⁴	Ag1	Ag2 ⁶	52.62(3)	O2 ¹⁵	Ag1	Pb1 ¹⁵	41.0(2)
Ag2 ¹⁷	Ag1	Ag2 ⁶	176.37(4)	O2 ¹⁸	Ag1	Pb1 ¹⁵	95.0(2)
Ag2 ¹⁴	Ag1	Ag2 ⁸	176.37(4)	O2 ¹⁵	Ag1	Pb1 ¹⁶	87.9(2)
Ag2 ¹⁷	Ag1	Ag2 ⁸	52.62(3)	O2 ¹⁸	Ag1	Pb1 ¹⁶	141.0(2)
Ag2 ⁶	Ag1	Ag2 ⁸	123.75(5)	O2	Ag2	Ag1 ⁵	86.1(2)
Ag2 ¹⁷	Ag1	Ag2 ¹⁴	131.01(4)	O2 ¹⁰	Ag2	Ag1 ⁵	128.7(2)
Ag2 ¹⁴	Ag1	Pb1 ⁸	114.49(2)	O2 ²	Ag2	Ag1 ⁵	141.3(2)
Ag2 ¹⁷	Ag1	Pb1 ⁸	114.50(2)	O2 ⁹	Ag2	Ag1 ⁵	50.6(2)
Ag2 ⁶	Ag1	Pb1 ⁸	61.87(2)	O2	Ag2	Ag1 ⁶	139.1(2)
Ag2 ⁸	Ag1	Pb1 ⁸	61.87(2)	O2 ¹⁰	Ag2	Ag1 ⁶	83.0(2)
Ag2 ¹⁴	Ag1	Pb1 ¹³	64.62(1)	O2 ²	Ag2	Ag1 ⁶	142.3(2)
Ag2 ¹⁷	Ag1	Pb1 ¹³	91.96(2)	O2 ⁹	Ag2	Ag1 ⁶	51.3(2)
Ag2 ⁶	Ag1	Pb1 ¹³	90.00(1)	O2	Ag2	Ag1 ⁷	128.7(2)
Ag2 ⁸	Ag1	Pb1 ¹³	116.643(7)	O2 ¹⁰	Ag2	Ag1 ⁷	86.1(2)
Ag2 ¹⁴	Ag1	Pb1 ¹⁵	91.96(2)	O2 ²	Ag2	Ag1 ⁷	50.6(2)
Ag2 ¹⁷	Ag1	Pb1 ¹⁵	64.62(1)	O2 ⁹	Ag2	Ag1 ⁷	141.3(2)
Ag2 ⁶	Ag1	Pb1 ¹⁵	116.643(7)	O2	Ag2	Ag1 ⁸	83.0(2)
Ag2 ⁸	Ag1	Pb1 ¹⁵	90.00(1)	O2 ¹⁰	Ag2	Ag1 ⁸	139.1(2)
Ag2 ¹⁴	Ag1	Pb1 ¹⁶	116.228(8)	O2 ²	Ag2	Ag1 ⁸	51.3(2)
Ag2 ¹⁷	Ag1	Pb1 ¹⁶	89.70(1)	O2 ⁹	Ag2	Ag1 ⁸	142.3(2)
Ag2 ⁶	Ag1	Pb1 ¹⁶	88.19(2)	O2	Ag2	Ag2 ⁴	132.2(2)
Ag2 ⁸	Ag1	Pb1 ¹⁶	62.29(2)	O2 ¹⁰	Ag2	Ag2 ⁴	132.2(2)
Ag2 ⁴	Ag2	Ag1 ⁵	65.51(2)	O2 ²	Ag2	Ag2 ⁴	100.2(2)
Ag2 ⁴	Ag2	Ag1 ⁶	61.87(2)	O2 ⁹	Ag2	Ag2 ⁴	100.2(2)
Ag2 ⁴	Ag2	Ag1 ⁷	65.51(2)	O2	Ag2	O1 ⁶	171.2(2)
Ag2 ⁴	Ag2	Ag1 ⁸	61.87(2)	O2 ¹⁰	Ag2	O1 ⁶	77.0(2)
Ag2 ⁴	Ag2	Pb1	122.23(2)	O2	Ag2	O1 ¹¹	77.0(2)
Ag2 ⁶	O1	Ag2 ¹⁴	69.2(2)	O2 ¹⁰	Ag2	O1 ¹¹	171.2(2)
Ag2	O2	Ag1 ¹²	86.8(2)	O2	Ag2	O2 ²	78.1(2)
Ag2	O2	Ag2 ⁹	91.7(2)	O2 ¹⁰	Ag2	O2 ²	88.3(2)
O1	Ag1	Ag2 ⁶	49.9(2)	O2	Ag2	O2 ⁹	88.3(2)
O1 ¹⁹	Ag1	Ag2 ⁶	126.7(2)	O2 ¹⁰	Ag2	O2 ⁹	78.1(2)
O1	Ag1	Ag2 ⁸	126.7(2)	O2 ²	Ag2	O2 ⁹	159.7(3)
O1 ¹⁹	Ag1	Ag2 ⁸	49.9(2)	O2	Ag2	O2 ¹⁰	95.6(3)
O1	Ag1	Ag2 ¹⁴	51.6(2)	O2	Ag2	Pb1	38.8(2)
O1 ¹⁹	Ag1	Ag2 ¹⁴	131.4(2)	O2 ¹⁰	Ag2	Pb1	93.6(2)
O1	Ag1	Ag2 ¹⁷	131.4(2)	O2 ²	Ag2	Pb1	39.4(2)
O1 ¹⁹	Ag1	Ag2 ¹⁷	51.6(2)	O2 ⁹	Ag2	Pb1	125.8(2)

Appendix

O1 ¹⁹	Ag1	O1	174.44(5)	O2	Pb1	O1	95.1(2)
O1	Ag1	O2 ¹⁵	102.1(2)	O2 ¹	Pb1	O1	93.2(2)
O1 ¹⁹	Ag1	O2 ¹⁵	81.9(2)	O2	Pb1	O1 ¹	93.2(2)
O1	Ag1	O2 ¹⁸	81.9(2)	O2 ¹	Pb1	O1 ¹	95.1(2)
O1 ¹⁹	Ag1	O2 ¹⁸	102.1(2)	O2	Pb1	O2 ¹	169.3(4)
O1	Ag1	Pb1 ⁸	87.22(3)	O2	Pb1	O2 ²	92.4(2)
O1 ¹⁹	Ag1	Pb1 ⁸	87.22(3)	O2 ¹	Pb1	O2 ²	80.8(3)
O1	Ag1	Pb1 ¹³	41.2(1)	O2	Pb1	O2 ³	80.8(3)
O1 ¹⁹	Ag1	Pb1 ¹³	143.0(2)	O2 ¹	Pb1	O2 ³	92.4(2)
O1	Ag1	Pb1 ¹⁵	143.0(2)	O2 ²	Pb1	O2 ³	101.3(4)
O1 ¹⁹	Ag1	Pb1 ¹⁵	41.2(1)	Pb1 ¹³	Ag1	Pb1 ⁸	118.40(2)
O1	Ag1	Pb1 ¹⁶	136.4(1)	Pb1 ¹⁵	Ag1	Pb1 ⁸	118.40(2)
O1 ¹⁹	Ag1	Pb1 ¹⁶	39.2(1)	Pb1 ¹⁵	Ag1	Pb1 ¹³	123.20(3)
O1 ¹¹	Ag2	Ag1 ⁵	47.00(1)	Pb1 ¹³	Ag1	Pb1 ¹⁶	176.62(3)
O1 ⁶	Ag2	Ag1 ⁵	102.18(8)	Pb1 ¹⁵	Ag1	Pb1 ¹⁶	60.18(1)
O1 ¹¹	Ag2	Ag1 ⁶	99.49(9)	Pb1 ⁸	Ag1	Pb1 ¹⁶	58.22(2)
O1 ⁶	Ag2	Ag1 ⁶	45.53(2)	Pb1	O1	Ag1	97.6(1)
O1 ¹¹	Ag2	Ag1 ⁷	102.18(8)	Pb1 ¹³	O1	Ag1	93.3(1)
O1 ⁶	Ag2	Ag1 ⁷	47.00(1)	Pb1	O1	Ag1 ¹²	93.3(1)
O1 ¹¹	Ag2	Ag1 ⁸	45.53(2)	Pb1 ¹³	O1	Ag1 ¹²	97.6(1)
O1 ⁶	Ag2	Ag1 ⁸	99.49(9)	Pb1	O1	Ag2 ⁶	94.71(7)
O1 ¹¹	Ag2	Ag2 ⁴	55.4(1)	Pb1 ¹³	O1	Ag2 ⁶	164.0(3)
O1 ⁶	Ag2	Ag2 ⁴	55.4(1)	Pb1	O1	Ag2 ¹⁴	164.0(3)
O1 ⁶	Ag2	O1 ¹¹	110.8(2)	Pb1 ¹³	O1	Ag2 ¹⁴	94.71(7)
O1 ¹¹	Ag2	O2 ²	94.7(2)	Pb1 ¹³	O1	Pb1	101.3(4)
O1 ⁶	Ag2	O2 ²	94.7(2)	Pb1	O2	Ag1 ¹²	89.2(2)
O1 ¹¹	Ag2	O2 ⁹	96.8(2)	Pb1 ³	O2	Ag1 ¹²	169.8(3)
O1 ⁶	Ag2	O2 ⁹	94.7(2)	Pb1	O2	Ag2	96.7(3)
O1 ¹¹	Ag2	Pb1	83.57(9)	Pb1 ³	O2	Ag2	97.7(2)
O1 ⁶	Ag2	Pb1	135.89(3)	Pb1	O2	Ag2 ⁹	164.3(3)
O1	Pb1	O1 ¹	78.7(4)	Pb1 ³	O2	Ag2 ⁹	92.8(2)
O1	Pb1	O2 ²	90.2(3)	Pb1	O2	Pb1 ³	99.2(3)

¹5/4-x,1/4-y,+z; ²1/4+x,-1/4+y,3/2-z; ³1-x,1/2-y,3/2-z; ⁴7/4-x,+y,7/4-z; ⁵-1/4+x,1/2-y,1/4+z; ⁶2-x,1/2-y,3/2-z; ⁷1/4+x,-y,1/4+z; ⁸3/2-x,-y,3/2-z; ⁹3/2-x,1-y,3/2-z; ¹⁰7/4-x,3/4-y,+z; ¹¹-1/4+x,1/4+y,3/2-z; ¹²7/4-x,1/2+y,5/4-z; ¹³5/4-x,+y,5/4-z; ¹⁴1/4+x,1/2-y,-1/4+z; ¹⁵7/4-x,-1/2+y,5/4-z; ¹⁶1/2+x,-1/2+y,+z; ¹⁷-1/4+x,-y,-1/4+z; ¹⁸+x,1/4-y,5/4-z; ¹⁹7/4-x,-1/4-y,+z.

Table 25. Lattice parameters and refinement factors for the *Rietveld* fit of the ambient temperature powder diffraction pattern of Ag_2PbO_3 .

Lattice parameters	$a = 6.9760(5) \text{ \AA}$	Refinement factors	$R_{\text{wp}} = 2.73$
	$b = 9.6095(7) \text{ \AA}$		$R_{\text{exp}} = 1.74$
	$c = 20.065(1) \text{ \AA}$		$R_p = 2.07$
	$V = 1345.1(2) \text{ \AA}^3$		$goof = 1.57$

7.7 Further Synthesis Attempts in the Multi Anvil Press

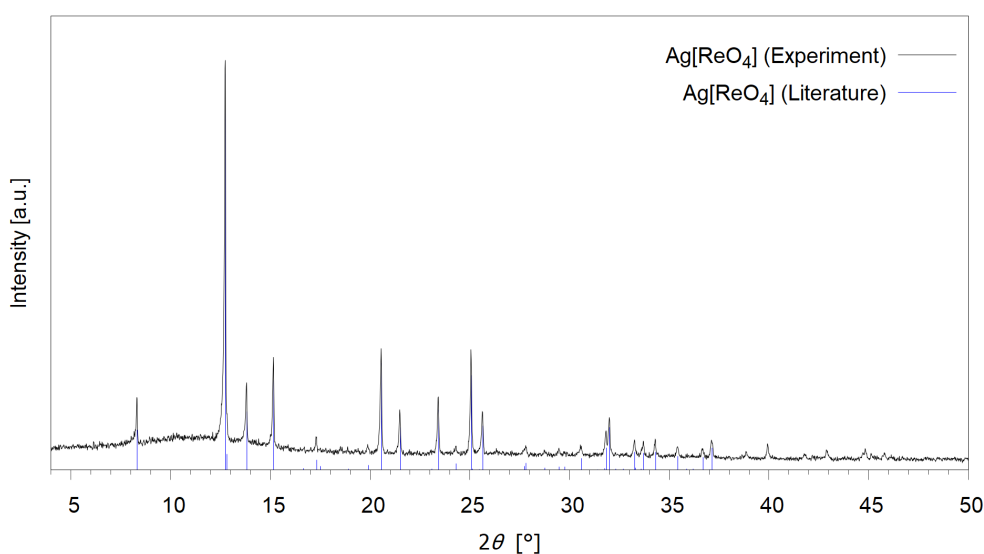


Figure 32. Powder X-ray data of the experiment of heating $\text{Ag}[\text{ReO}_4]$ in the multi anvil press measured with $\text{Mo-K}\alpha_1$ radiation and literature data.^[96]

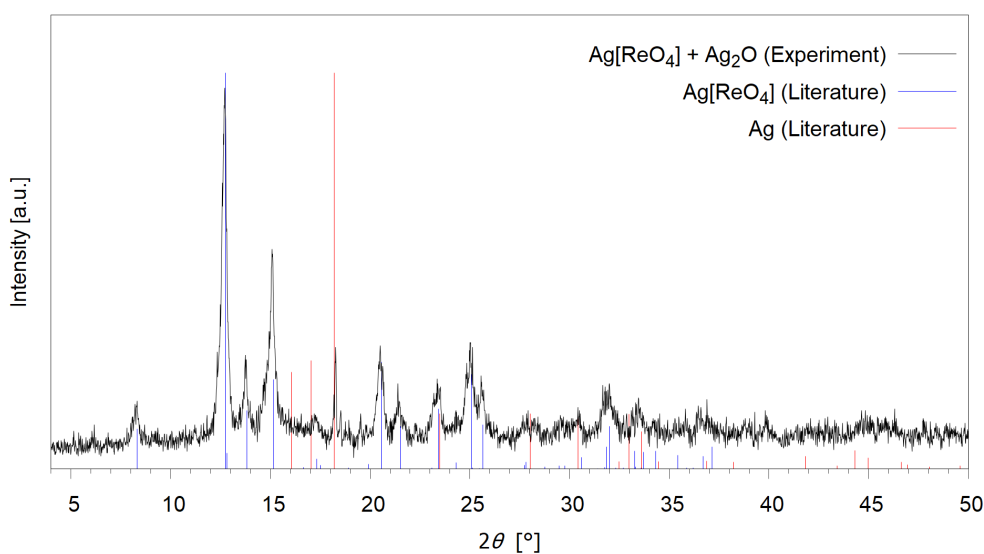


Figure 33. Powder X-ray data of the experiment of heating $\text{Ag}[\text{ReO}_4]$ and Ag_2O in the multi anvil press measured with $\text{Mo-K}\alpha_1$ radiation and literature data.^[96, 130]

Appendix

Table 26. Lattice parameters and refinement factors for the *Rietveld* fit of the ambient temperature powder diffraction pattern of the product mixture from the multi anvil experiment with H_3BO_3 and $\text{K}_2\text{S}_2\text{O}_7$.

Lattice parameters	$a = 8.989(3) \text{ \AA}$	Refinement factors	$R_{\text{wp}} = 11.37$
for $\text{K}[\text{B}(\text{SO}_4)_2]$	$c = 7.410(3) \text{ \AA}$		$R_{\text{exp}} = 7.30$
	$V = 598(4) \text{ \AA}^3$		$R_p = 8.78$
			$goof = 1.56$

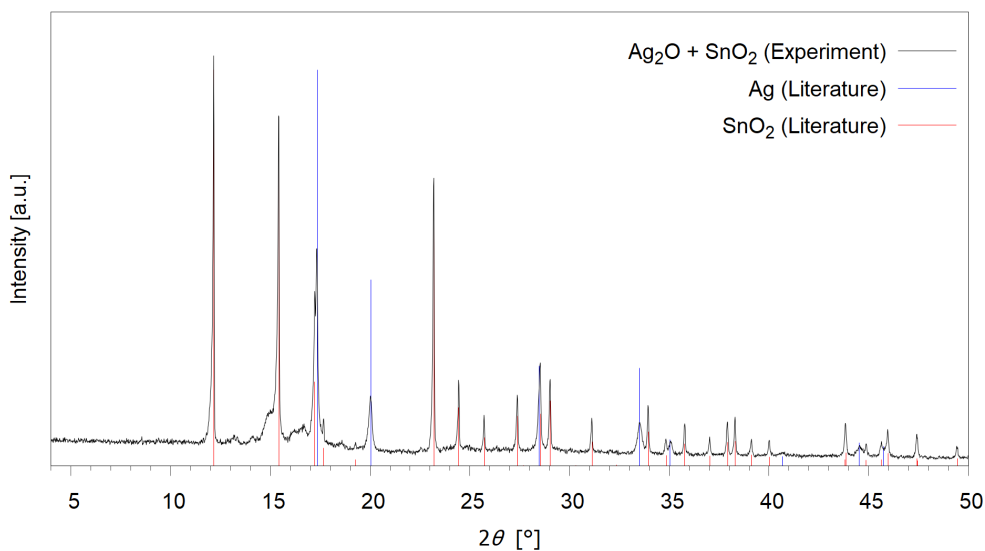


Figure 34. Powder X-ray data of the experiment of heating Ag_2O and SnO_2 in the multi anvil press measured with Mo- $\text{K}\alpha_1$ radiation and literature data.^[95, 131]

7.8 Characterization of the EO Catalyst

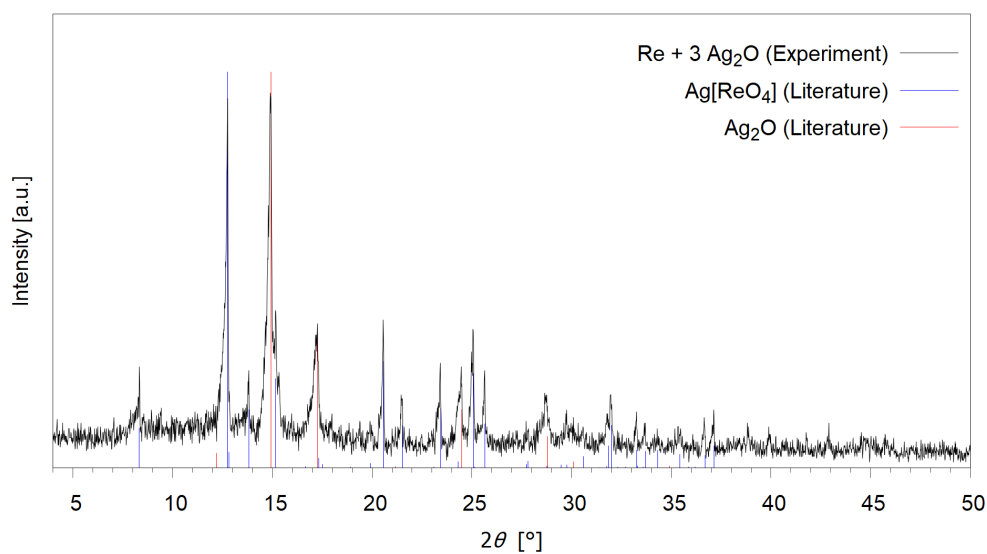


Figure 35. Powder X-ray data of the O₂ high pressure experiment No. 1 of combining 1 eq elemental Re with 3 eq Ag₂O measured with Mo-K α_1 radiation and literature data.^[96, 105]

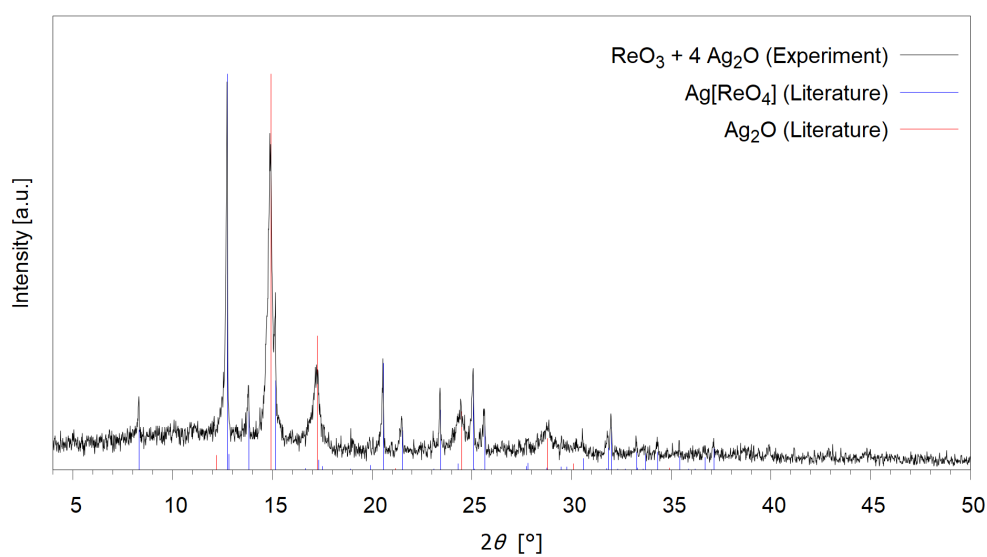


Figure 36. Powder X-ray data of the O₂ high pressure experiment No. 3 of combining 1 eq ReO₃ with 4 eq Ag₂O at 600°C measured with Mo-K α_1 radiation and literature data.^[96, 105]

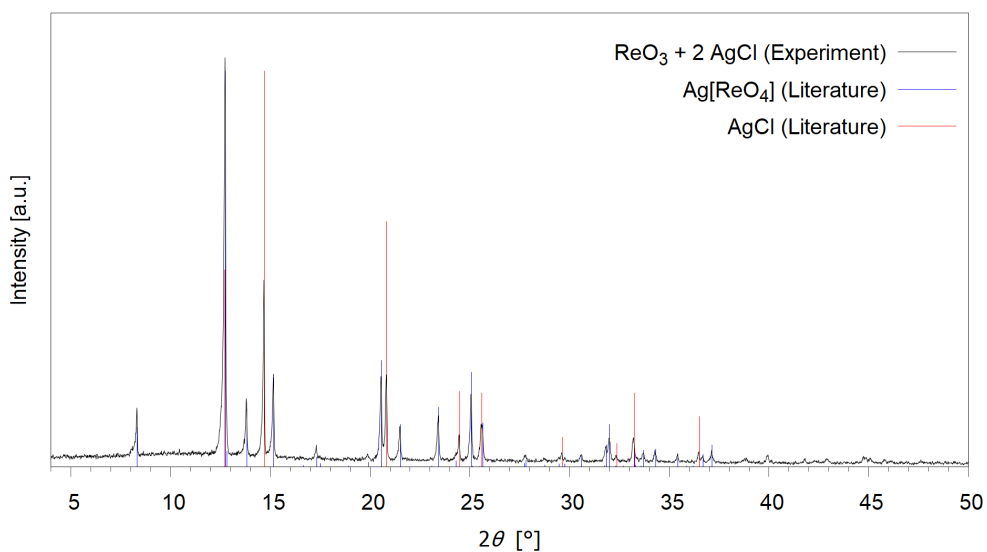


Figure 37. Powder X-ray data of the O_2 high pressure experiment No. 4 of combining ReO_3 with 2 eq AgCl measured with $\text{Mo-K}\alpha_1$ radiation and literature data.^[96, 98]

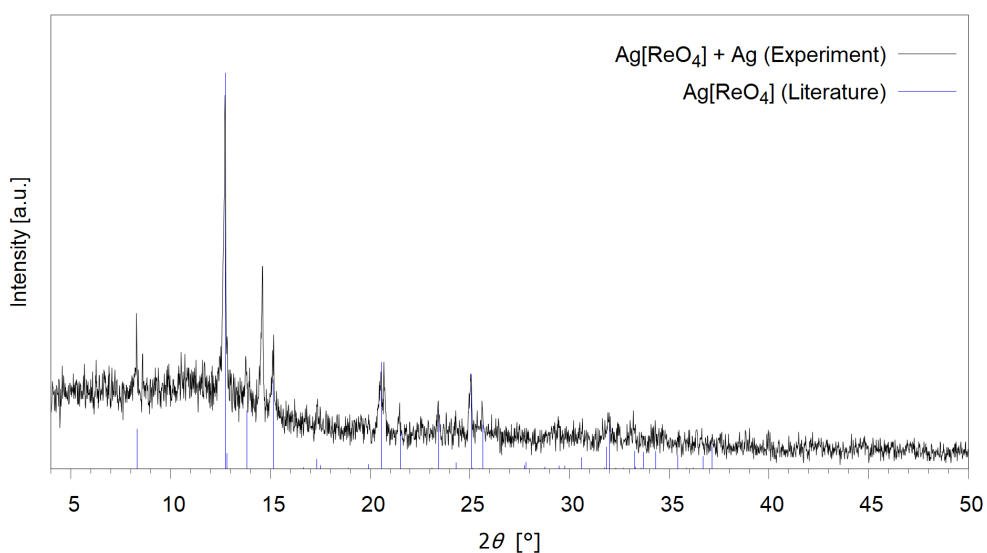


Figure 38. Powder X-ray data of the O_2 high pressure experiment No. 5 of combining $\text{Ag}[\text{ReO}_4]$ with 1 eq elemental Ag measured with $\text{Mo-K}\alpha_1$ radiation and literature data.^[96]

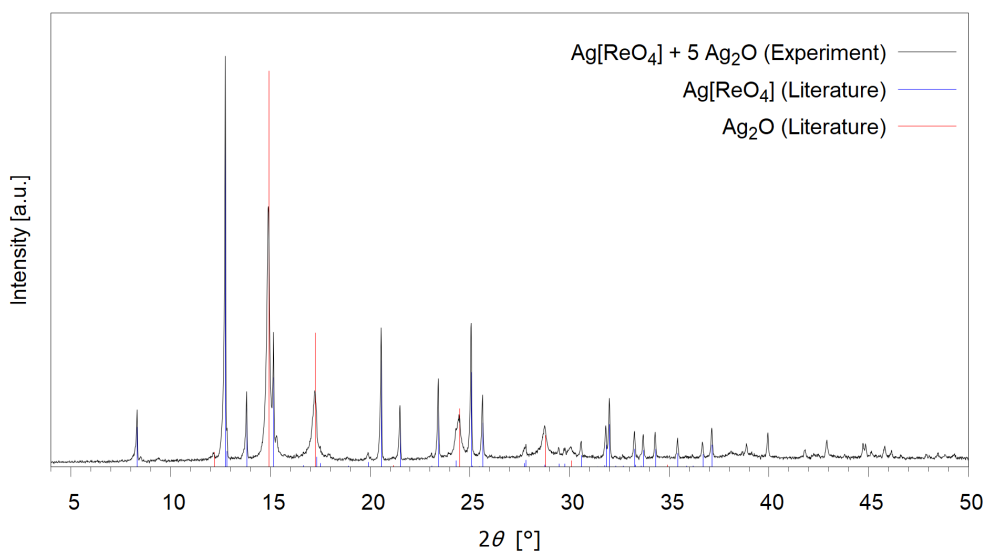


Figure 39. Powder X-ray data of the O_2 high pressure experiment No. 6 of combining $\text{Ag}[\text{ReO}_4]$ with 5 eq Ag_2O measured with $\text{Mo-K}\alpha_1$ radiation and literature data.^[96, 105]

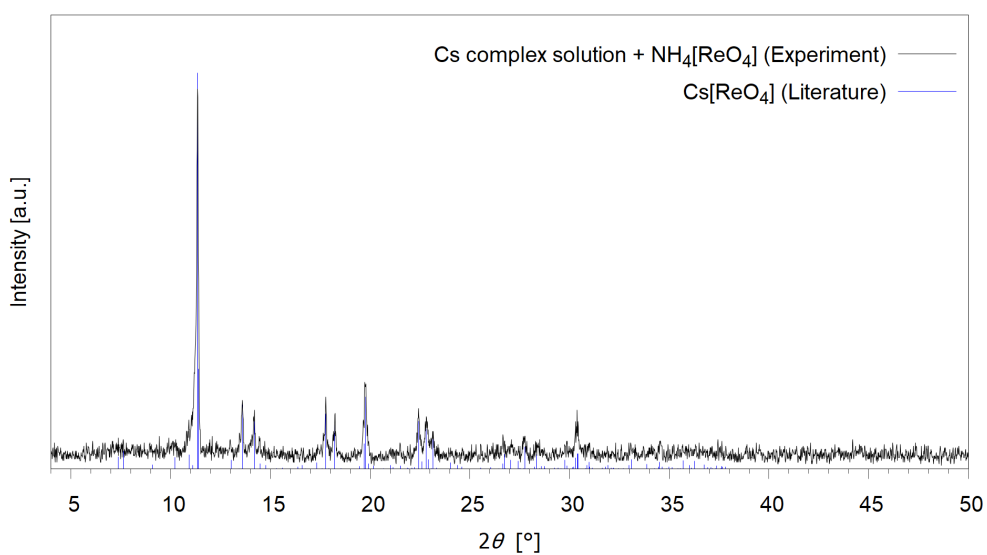


Figure 40. Powder X-ray data of the experiment of combining Cs complex solution with $\text{NH}_4[\text{ReO}_4]$ measured with $\text{Mo-K}\alpha_1$ radiation and literature data.^[96]

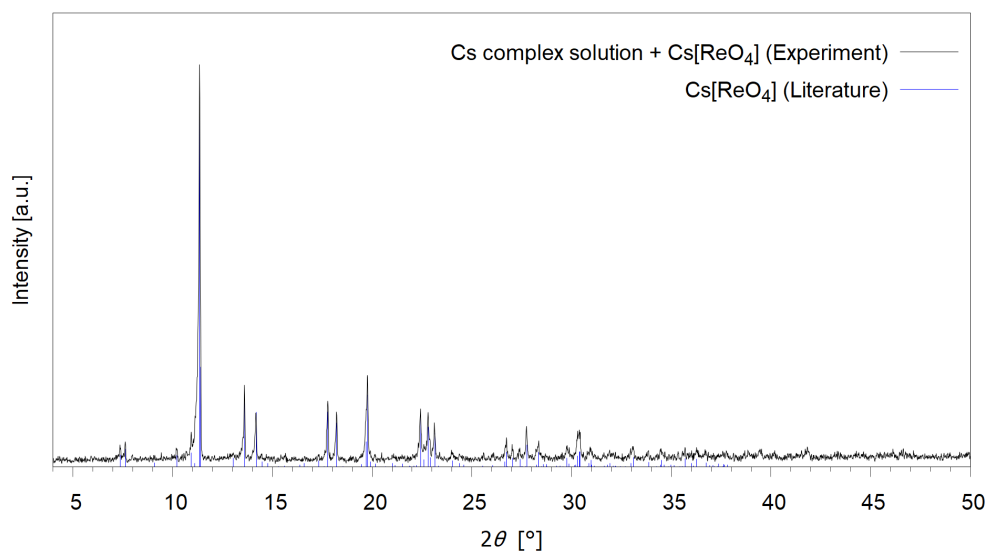


Figure 41. Powder X-ray data of the experiment of combining Cs complex solution with Cs[ReO₄] measured with Mo-K α_1 radiation and literature data.^[96]

7.9 [Ag(μ -en)][ReO₄]

Supporting Information

of

Publication 6

[Ag(μ -en)][ReO₄]: An Intermediate during Preparation of the Ethylene Epoxidation Catalyst

D. Badea, A. Karpov, M. Jansen and J. Bruns*

Z. Anorg. Allg. Chem. **2022**, e202200267.

doi.org/10.1002/zaac.202200267

Supporting Information

[Ag(μ -en)][ReO₄]: An Intermediate during Production of the Ethylene Epoxidation Catalyst

Désirée Badea, Andrey Karpov*, Martin Jansen*, and Jörn Bruns*

Table of Contents

- A. Structure determination, crystallographic details and Rietveld data
- B. Data for decomposition of [Ag(μ -en)][ReO₄] in argon
- C. Data for decomposition of [Ag(μ -en)][ReO₄] in synthetic air
- D. IR spectroscopy of [Ag(μ -en)][ReO₄]

A. Structure determination, crystallographic details and Rietveld data

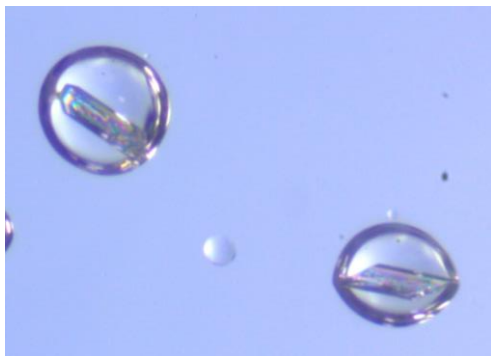


Figure S1. Microscopic picture of [Ag(en)][ReO₄] single crystals in drops of the crystallization solution.

Table S1. Fractional atomic coordinates ($\times 10^4$) and equivalent isotropic displacement parameters ($\text{\AA}^2 \times 10^3$) for [Ag(en)][ReO₄]. U_{eq} is defined as 1/3 of the trace of the orthogonalised U_{ij} tensor.

Atom	x	y	z	$U(\text{eq})$
Ag1	6575.6(4)	1048.1(4)	7564.7(4)	11.87(8)
C1	10240(6)	4423(6)	9122(6)	10.9(7)
C2	4046(6)	215(6)	9380(6)	11.4(7)
N1	9648(5)	2332(5)	8376(6)	11.2(6)
N2	3826(5)	-247(5)	7308(5)	11.8(6)
O1	1315(4)	1951(4)	5518(4)	15.6(6)
O2	5182(5)	3551(4)	6163(5)	19.8(6)
O3	2372(5)	5722(4)	6228(5)	18.9(6)
O4	1462(5)	2345(4)	2329(5)	20.3(6)
Re1	2569.6(2)	3409.4(2)	5057.0(2)	9.16(6)

Table S2. Anisotropic displacement parameters ($\text{\AA}^2 \times 10^3$) for [Ag(en)][ReO₄]. The anisotropic displacement factor exponent takes the form: $-2\pi^2[h^2a^{*2}U_{11}+2hka^*b^*U_{12}+\dots]$.

Atom	U_{11}	U_{22}	U_{33}	U_{23}	U_{13}	U_{12}
Ag1	12.8(2)	11.2(2)	12.5(2)	2.5(1)	7.1(1)	6.5(1)
C1	10(2)	10(2)	10(2)	0(2)	6(2)	3(2)
C2	14(2)	7(2)	14(2)	4(2)	7(2)	6(2)
N1	14(2)	13(2)	11(2)	6(1)	7(1)	9(1)
N2	11(2)	10(2)	13(2)	3(1)	5(1)	7(1)
O1	18(2)	16(1)	19(1)	7(1)	12(1)	11(1)
O2	12(1)	23(2)	27(2)	6(1)	8(1)	18(1)
O3	21(2)	12(1)	25(2)	4(1)	13(1)	9(1)
O4	28(2)	18(2)	13(1)	4(1)	9(1)	8(1)
Re1	9.63(9)	8.49(9)	9.62(9)	2.58(6)	4.36(6)	5.54(6)

Table S3. Bond lengths for [Ag(en)][ReO₄].

Atom	Atom	Length [Å]	Atom	Atom	Length [Å]
Ag1	Ag1 ¹	3.2484(6)	N2	C2	1.483(5)
Ag1	N1	2.141(3)	Re1	O1	1.735(3)
Ag1	N2	2.134(3)	Re1	O2	1.732(3)
C1	C1 ³	1.518(7)	Re1	O3	1.723(3)
C2	C2 ²	1.522(8)	Re1	O4	1.723(3)
N1	C1	1.481(5)			

¹1-x,-y,1-z, ²1-x,-y,2-z, ³2-x,1-y,2-zTable S4. Bond angles for [Ag(en)][ReO₄].

Atom	Atom	Atom	Angle [°]	Atom	Atom	Atom	Angle [°]
C1	N1	Ag1	116.7(2)	O2	Re1	O1	108.8(1)
C1 ²	C1	N1	109.7(4)	O2	Re1	O3	109.1(1)
C2 ¹	C2	N2	110.3(4)	O4	Re1	O1	108.6(1)
C2	N2	Ag1	114.6(2)	O4	Re1	O2	109.0(2)
N2	Ag1	N1	168.8(1)	O4	Re1	O3	110.9(1)
O1	Re1	O3	110.4(1)				

¹1-x,-y,2-z, ²2-x,1-y,2-zTable S5. Lattice parameters and refinement factors for the Rietveld fit of the ambient temperature powder diffraction pattern of [Ag(μ-en)][ReO₄].

Lattice parameters	$a = 7.5396(2) \text{ Å}$ $b = 8.2046(2) \text{ Å}$ $c = 8.2128(2) \text{ Å}$ $V = 387.36(3) \text{ Å}^3$	$\alpha = 116.902(2)^\circ$ $\beta = 115.557(2)^\circ$ $\gamma = 93.529(2)^\circ$	Refinement factors	$R_{\text{wp}} = 5.95$ $R_{\text{exp}} = 5.97$ $R_p = 4.68$ Goof = 1.00
--------------------	--	---	--------------------	--

Table S6. Fractional atomic coordinates obtained from the Rietveld refinement of [Ag(μ-en)][ReO₄].

Atom	x	y	z
Ag1	0.6628(8)	0.1080(7)	0.7658(8)
C1	1.061(9)	0.442(8)	0.925(8)
C2	0.42(1)	0.06(1)	0.98(1)
H1	0.29(6)	-0.23(6)	0.75(7)
H2	0.47(9)	0.14(7)	1.06(7)
H3	0.26(8)	0.22(7)	0.43(8)
H4	0.55(7)	0.00(7)	0.89(7)
H5	1.16(6)	0.21(5)	0.97(6)
H6	0.86(7)	0.31(7)	0.80(7)
H7	1.27(7)	0.76(5)	1.10(6)
H8	0.74(7)	0.39(6)	0.72(6)
N1	0.960(8)	0.214(7)	0.823(7)
N2	0.394(7)	-0.025(7)	0.728(8)
O1	0.124(5)	0.197(5)	0.529(6)
O2	0.472(6)	0.348(5)	0.6133(6)
O3	0.254(5)	0.547(6)	0.611(6)
O4	0.158(7)	0.268(5)	0.284(5)
Re1	0.2568(6)	0.3394(5)	0.5086(6)

B. Data for decomposition of $[\text{Ag}(\mu\text{-en})][\text{ReO}_4]$ in argon

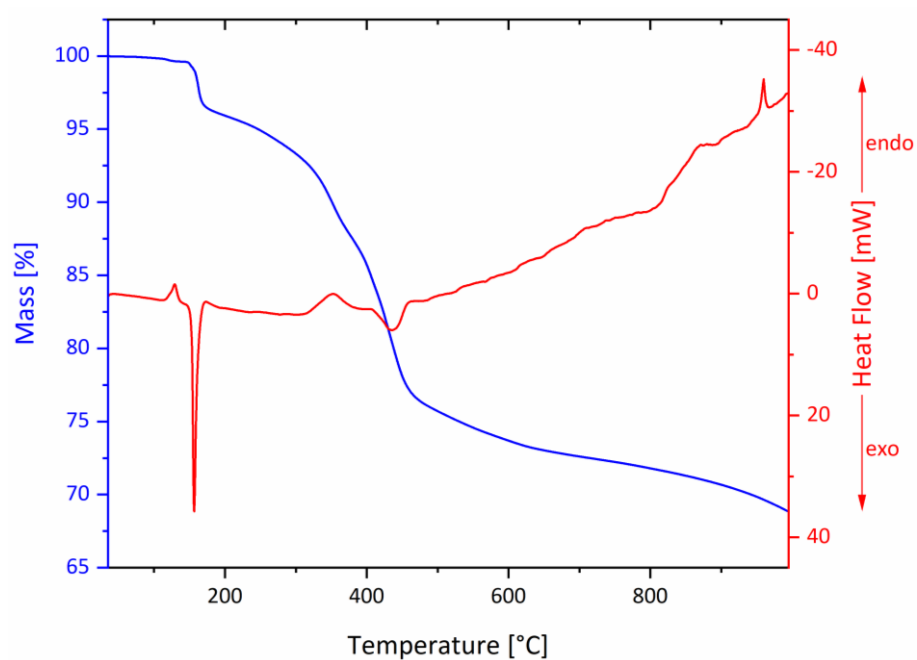


Figure S2. TG-DSC plot of $[\text{Ag}(\mu\text{-en})][\text{ReO}_4]$ in argon.

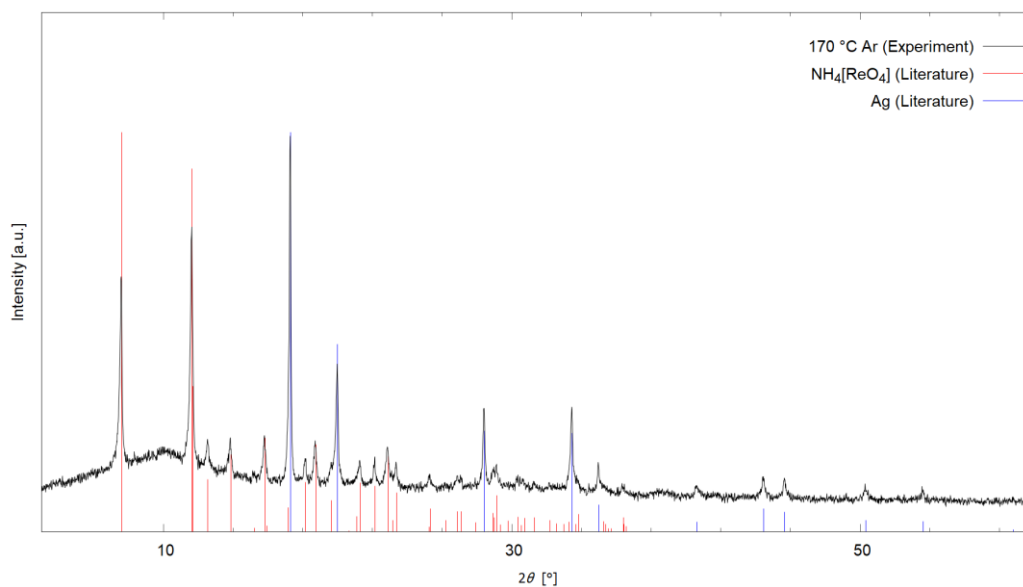


Figure S3. X-ray diffraction pattern of TG-DSC residue after heating at 170 °C in Ar steam with $\text{Mo-K}\alpha_1$ radiation. The data of $\text{NH}_4[\text{ReO}_4]$ and elemental Ag were calculated from literature.^[1]

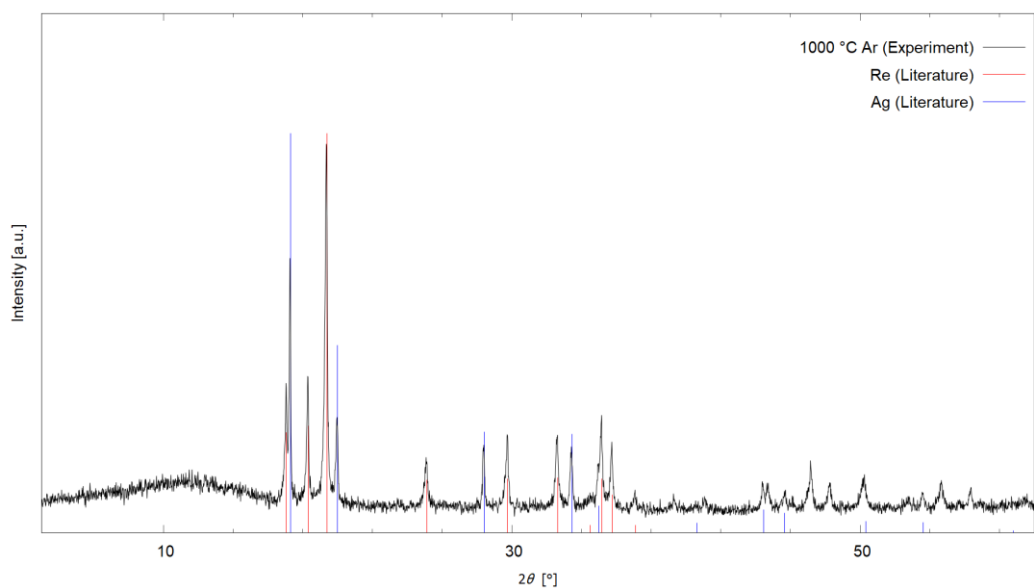


Figure S4. X-ray diffraction pattern of TG-DSC residue after heating at 1000 °C in Ar steam with Cu-K α radiation. The data of elemental Re and elemental Ag were calculated from literature.^[1a, 2]

C. Data for decomposition of [Ag(μ -en)][ReO $_4$] in synthetic air

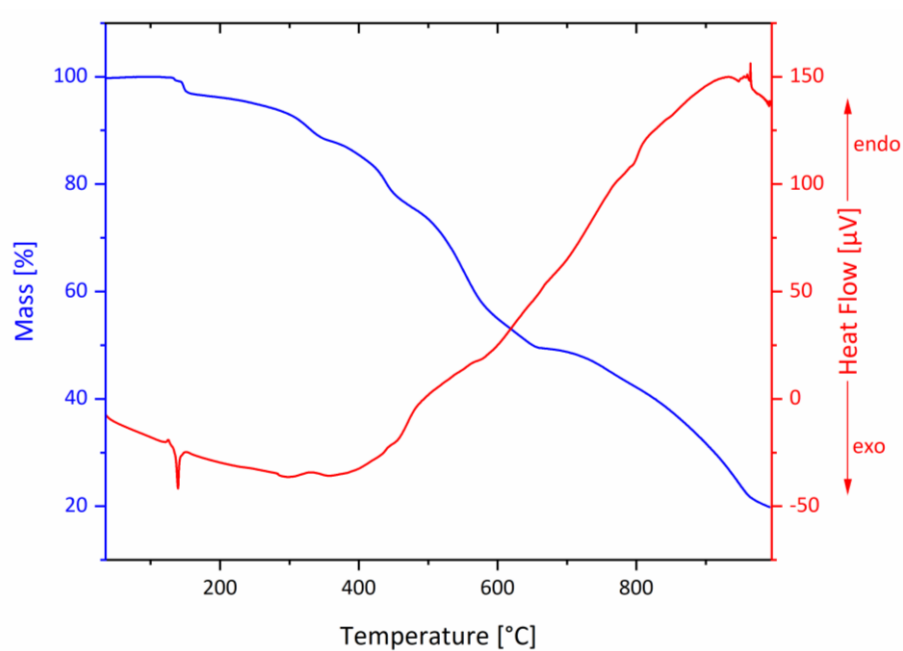


Figure S5. TG-DSC plot of [Ag(μ -en)][ReO $_4$] in synthetic air.

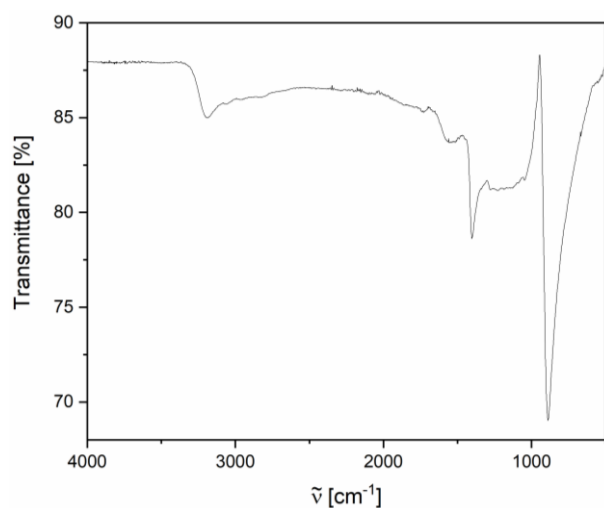


Figure S6. Infrared spectrum of the decomposition product of $[\text{Ag}(\mu\text{-en})][\text{ReO}_4]$ at 170 °C with background correction.

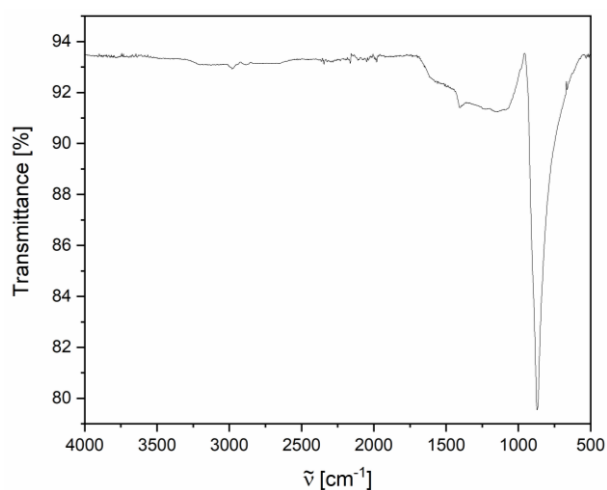


Figure S7. Infrared spectrum of the decomposition product of $[\text{Ag}(\mu\text{-en})][\text{ReO}_4]$ at 300 °C with background correction.

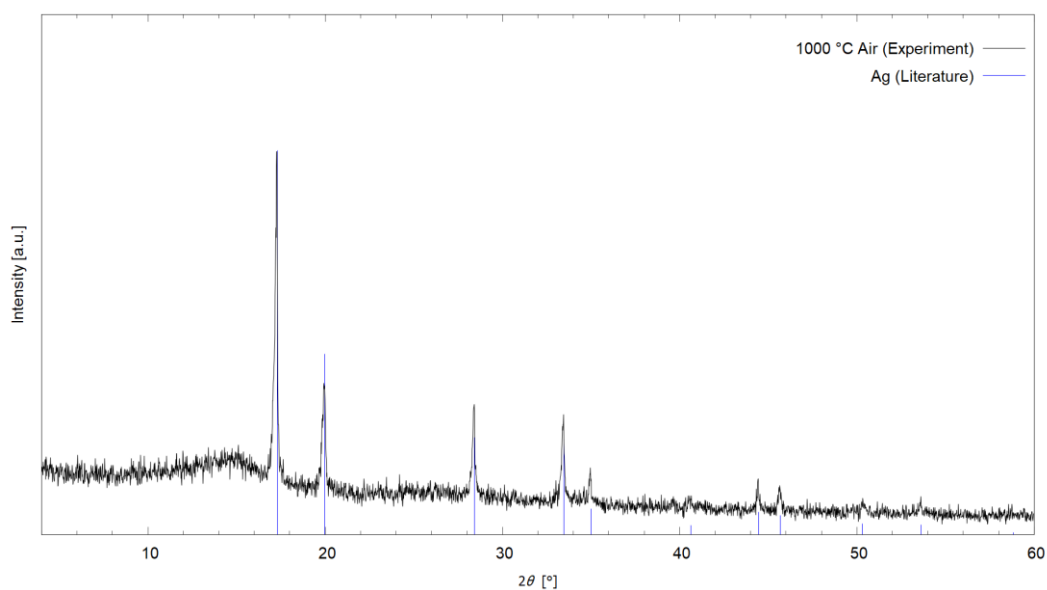


Figure S8. X-ray diffraction pattern of TG-DSC residue after heating at 995 °C in synthetic air steam with $\text{Cu-K}\alpha$ radiation. The data of elemental Ag was calculated from literature.^[1a]

D. IR spectroscopy of [Ag(μ -en)][ReO₄]

Table S7. Wavenumbers, vibrational modes and assignment from spectrum of [Ag(μ -en)][ReO₄].^[3]

Wavenumber [cm ⁻¹]	Vibrational mode	Assignment
3298	V _{as}	NH ₂
3245	V _{as}	NH ₂
3145	V _s	NH ₂
2918	V _{as}	CH ₂
2868	V _s	CH ₂
1613	δ	NH ₂
1588	δ	NH ₂
1460	δ	CH ₂
1373	ω	CH ₂
1290	ω	NH ₂
1149	τ	NH ₂
1083	τ	NH ₂
1014	V _s	C-N
964	ρ	NH ₂
890	V _{as}	ReO ₄
870	V _{as}	ReO ₄
802	ρ	CH ₂
656	ρ	NH ₂
614	v	Ag-N

Abbreviations: v, stretching; δ , scissoring; ρ , rocking; ω , wagging; τ , twisting; s, symmetric; as, anti-symmetric.

- [1] a) H. E. Swanson, E. Tatge, *Natl. Bur. Stand. Circ.* **1953**, 359, 1-95; b) E. M. Reynolds, M. Yu, G. J. Thorogood, H. E. A. Brand, F. Poineau, B. J. Kennedy, *J. Solid State Chem.* **2019**, 274, 64-68.
- [2] V. A. Finkel, M. I. Palatnik, G. P. Kovtun, *Phys. Met. Metallogr.* **1971**, 32, 231-235.
- [3] a) K. Ulbricht, H. Kriegsmann, *Z. Anorg. Allg. Chem.* **1968**, 358, 193-209; b) Y.-I. Lam, H. H. Huang, *J. Mol. Struct.* **1997**, 412, 141-152.

7.10 [Ag₂(DHPP)](C₂O₄)Table 27. Crystallographic data of [Ag₂(DHPP)](C₂O₄).

Empirical formula	C ₈ H ₁₄ Ag ₂ N ₄ O ₄
Formula weight	445.97 g/mol
Temperature	100(2) K
Wavelength	0.71073 Å
Crystal system	monoclinic
Space group	<i>C2/m</i> (no. 12)
Unit cell dimensions	<i>a</i> = 10.485(2) Å <i>b</i> = 9.339(2) Å <i>c</i> = 6.162(1) Å β = 103.495(7) °
Volume	586.8(2) Å ³
<i>Z</i>	2
Density (calculated)	2.52 g·cm ⁻³
<i>F</i> (000)	432
Crystal size	0.02 × 0.02 × 0.10 mm ³
2 θ range for data collection	5.92° to 54.72°
Index ranges	-13 ≤ <i>h</i> ≤ 13, -12 ≤ <i>k</i> ≤ 11, -7 ≤ <i>l</i> ≤ 7
Reflections collected	3339
Independent reflections	699 [<i>R</i> _{int} = 0.0839, <i>R</i> _σ = 0.0592]
Completeness to θ	100%
Absorption correction	multi-scan
Maximum / minimum transmission	0.607 / 0.746
Data / parameters	699 / 48
Goodness-of-fit on <i>F</i> ²	1.049
Final <i>R</i> indices [<i>I</i> _o > 2σ (<i>I</i> _o)]	<i>R</i> ₁ = 0.0429, <i>wR</i> ₂ = 0.0903
<i>R</i> indices (all data)	<i>R</i> ₁ = 0.0521, <i>wR</i> ₂ = 0.0941
Largest diff. peak and hole	1.77/-1.05 e·Å ⁻³

Appendix

Table 28. Atomic coordinates ($\times 10^4$) and equivalent isotropic displacement parameters ($\text{\AA}^2 \times 10^3$) for $[\text{Ag}_2(\text{DHPP})](\text{C}_2\text{O}_4)$. $U(eq)$ is defined as one third of the trace of the orthogonalized U_{ij} tensor.

Atom	<i>x</i>	<i>y</i>	<i>z</i>	<i>U(eq)</i>
Ag1	5000	6526.7(7)	5000	20.6(2)
C1	5701(5)	7574(6)	667(10)	21(1)
C2	5708(8)	5000	694(15)	22(2)
C3	5758(7)	10000	5568(14)	19(2)
N1	5938(5)	6289(5)	2105(9)	22(1)
O1	6303(4)	8811(4)	5970(8)	23(1)

Table 29. Anisotropic displacement parameters ($\text{\AA}^2 \times 10^3$) for $[\text{Ag}_2(\text{DHPP})](\text{C}_2\text{O}_4)$. The anisotropic displacement factor exponent takes the form: $-2\pi^2 [h^2 a^{*2} U_{11} + 2 h k a^* b^* U_{12} + \dots]$.

Atom	U_{11}	U_{22}	U_{33}	U_{23}	U_{13}	U_{12}
Ag1	26.6(4)	11.9(3)	20.7(4)	0	0.6(2)	0
C1	28(3)	16(3)	15(3)	-3(3)	-2(2)	-4(3)
C2	25(4)	17(4)	18(4)	0	-3(3)	0
C3	19(4)	17(4)	15(4)	0	-9(3)	0
N1	25(2)	17(3)	20(3)	1(2)	-1(2)	1(2)
O1	28(2)	9(2)	28(3)	1(2)	-3(2)	1(2)

Table 30. Bond lengths for $[\text{Ag}_2(\text{DHPP})](\text{C}_2\text{O}_4)$.

Atom	Atom	Length [\AA]	Atom	Atom	Length [\AA]
Ag1	Ag1 ¹	2.852(1)	C2	C2 ⁵	1.53(2)
Ag1	N1	2.240(6)	C3	C3 ³	1.58(1)
Ag1	N1 ²	2.240(6)	N1	C1	1.479(8)
Ag1	O1	2.528(4)	N1	C2	1.471(7)
Ag1	O1 ²	2.528(4)	O1	C3	1.247(5)
C1	C1 ⁴	1.51(1)			

¹1-*x*,1-*y*,1-*z*; ²1-*x*,+*y*,1-*z*; ³1-*x*,2-*y*,1-*z*; ⁴1-*x*,+*y*,*z*; ⁵1-*x*,1-*y*,*z*.

Appendix

Table 31. Bond angles for [Ag₂(DHPP)](C₂O₄).

Atom	Atom	Atom	Angle [°]	Atom	Atom	Atom	Angle [°]
C1	N1	Ag1	110.7(4)	N1	C1	C1 ⁵	109.4(4)
C2	N1	Ag1	120.7(5)	N1	C2	C2 ⁷	109.5(5)
C2	N1	C1	109.2(5)	N1 ⁶	C2	C2 ⁷	109.5(5)
C3	O1	Ag1	120.5(4)	N1	C2	N1 ⁶	109.7(7)
N1	Ag1	Ag1 ¹	84.3(1)	O1	Ag1	Ag1 ¹	147.53(9)
N1 ²	Ag1	Ag1 ¹	84.3(1)	O1 ²	Ag1	Ag1 ¹	147.53(9)
N1	Ag1	N1 ²	168.6(3)	O1	Ag1	O1 ²	64.9(2)
N1	Ag1	O1	87.6(2)	O1	C3	C3 ⁴	117.1(3)
N1 ²	Ag1	O1	102.1(2)	O1 ³	C3	C3 ⁴	117.1(3)
N1	Ag1	O1 ²	102.1(2)	O1 ³	C3	O1	125.9(7)
N1 ²	Ag1	O1 ²	87.6(2)				

¹1-x,1-y,1-z; ²1-x,+y,1-z; ³+x,2-y,+z; ⁴1-x,2-y,1-z; ⁵1-x,+y,-z; ⁶+x,1-y,+z; ⁷1-x,1-y,-z.

Table 32. Hydrogen atom coordinates ($\times 10^4$) and equivalent isotropic displacement parameters ($\text{\AA}^2 \times 10^3$) for [Ag₂(DHPP)](C₂O₄). $U(eq)$ is defined as one third of the trace of the orthogonalized U_{ij} tensor [Ag₂(DHPP)](C₂O₄).

Atom	x	y	z	$U(eq)$
H1	6660(70)	6220(70)	2730(130)	26
H1A	6302.84	7574.39	-355.5	25
H1B	5872.88	8447.79	1599.65	25
H2	6322.3	5000	-327.49	26

8 References

- [1] J. Bruns, M. Bykov, G. Heymann, G. Thiele, *Front. Chem.* **2024**, *12*, 1-2.
- [2] T. Sörgel, M. Jansen, *J. Solid State Chem.* **2007**, *180*, 8-15.
- [3] V. P. Prakapenka, G. Shen, L. S. Dubrovinsky, M. L. Rivers, S. R. Sutton, *J. Phys. Chem. Solids* **2004**, *65*, 1537-1545.
- [4] A. P. Drozdov, P. P. Kong, V. S. Minkov, S. P. Besedin, M. A. Kuzovnikov, S. Mozaffari, L. Balicas, F. F. Balakirev, D. E. Graf, V. B. Prakapenka, E. Greenberg, D. A. Knyazev, M. Tkacz, M. I. Erements, *Nature* **2019**, *569*, 528-531.
- [5] A. P. Drozdov, M. I. Erements, I. A. Troyan, V. Ksenofontov, S. I. Shylin, *Nature* **2015**, *525*, 73-76.
- [6] F. Haber, *Nobel Lecture* **1920**.
- [7] A. P. Steynberg, R. L. Espinoza, B. Jager, A. C. Vosloo, *Appl. Catal., A* **1999**, *186*, 41-54.
- [8] U. Betke, M. S. Wickleder, *Eur. J. Inorg. Chem.* **2012**, *2012*, 306-317.
- [9] A. Mertens, D. van Gerven, I. Kunert, M. S. Wickleder, *Chem. - Eur. J.* **2023**, *29*, e202302128.
- [10] P. L. Smallwood, M. D. Smith, H.-C. zur Loye, *J. Cryst. Growth* **2000**, *216*, 299-303.
- [11] W. M. Chance, D. E. Bugaris, A. S. Sefat, H.-C. zur Loye, *Inorg. Chem.* **2013**, *52*, 11723-11733.
- [12] D. Elwell, H. J. Scheel, *Crystal Growth from High-Temperature Solutions*, Academic Press, New York, **1975**.
- [13] D. E. Bugaris, M. D. Smith, H.-C. zur Loye, *Inorg. Chem.* **2013**, *52*, 3836-3844.
- [14] R. Albrecht, T. Doert, M. Ruck, *Z. Anorg. Allg. Chem.* **2020**, *646*, 1517-1524.
- [15] H. Flood, T. Förland, *Acta Chem. Scand.* **1947**, *1*, 592-604.
- [16] J. N. Brønsted, *Recl. Trav. Chim. Pays-Bas* **1923**, *42*, 718-728.
- [17] N. Pienack, W. Bensch, *Angew. Chem., Int. Ed.* **2011**, *50*, 2014-2034.
- [18] W. M. Chance, *Hydroflux Synthesis: A New and Effective Technique for Exploratory Crystal Growth, Doctoral dissertation*, University South Carolina, USA, **2014**.
- [19] C. Hérold, A. Hérold, P. Lagrange, *J. Phys. Chem. Solids* **1996**, *6*, 655-662.
- [20] W. M. Vogel, K. J. Routsis, V. J. Kehrler, D. A. Landsman, J. G. Tschinkel, *J. Chem. Eng. Data* **1967**, *12*, 465-472.
- [21] S. J. Mugavero, W. R. Gemmill, I. P. Roof, H.-C. zur Loye, *J. Solid State Chem.* **2009**, *182*, 1950-1963.
- [22] G. J. Harms, W. Gunßer, *Ber. Bunsenges. Phys. Chem.* **1986**, *90*, 764-767.
- [23] D. S. Cook, G. J. Clarkson, D. M. Dawson, S. E. Ashbrook, J. M. Fisher, D. Thompsett, D. M. Pickup, A. V. Chadwick, R. I. Walton, *Inorg. Chem.* **2018**, *57*, 11217-11224.
- [24] W. M. Chance, H.-C. zur Loye, *Solid State Sci.* **2014**, *28*, 90-94.

- [25] H. He, R. Albrecht, M. Ruck, *Z. Anorg. Allg. Chem.* **2022**, 648, e202200041.
- [26] R. Albrecht, M. Ruck, *Angew. Chem., Int. Ed.* **2021**, 60, 22570-22577.
- [27] H. Huppertz, *Z. Kristallogr. Cryst. Mater.* **2004**, 219, 330-338.
- [28] D. Walker, M. A. Carpenter, C. M. Hitch, *Am. Mineral.* **1990**, 75, 1020-1028.
- [29] F. P. Bundy, H. T. Hall, H. M. Strong, R. H. Wentorfjun, *Nature* **1955**, 176, 51-55.
- [30] E. Selb, T. Buttlar, O. Janka, M. Tribus, S. G. Ebbinghaus, G. Heymann, *J. Mater. Chem. C* **2021**, 9, 5486-5496.
- [31] J. S. Knyrim, P. Becker, D. Johrendt, H. Huppertz, *Angew. Chem., Int. Ed.* **2006**, 45, 8239-8241.
- [32] H. Emme, T. Nikelski, T. Schleid, R. Pöttgen, M. H. Möller, H. Huppertz, *Z. Naturforsch., B* **2004**, 59, 202-215.
- [33] H. Huppertz, *Z. Naturforsch., B* **2003**, 58, 278-290.
- [34] H. Hellwig, J. Liebertz, L. Bohatý, *Solid State Commun.* **1998**, 109, 249-251.
- [35] L. Li, G. Li, Y. Wang, F. Liao, J. Lin, *Inorg. Chem.* **2005**, 44, 8243-8248.
- [36] J. S. Knyrim, F. Roeßner, S. Jakob, D. Johrendt, I. Kinski, R. Glaum, H. Huppertz, *Angew. Chem., Int. Ed.* **2007**, 46, 9097-9100.
- [37] C. Linke, M. Jansen, *Z. Anorg. Allg. Chem.* **1997**, 623, 1441-1446.
- [38] V. Dietrich, M. Jansen, *Z. Naturforsch., B* **2011**, 66, 227-229.
- [39] W. Klein, M. Jansen, *Z. Anorg. Allg. Chem.* **2008**, 634, 1077-1081.
- [40] G. S. Thakur, H. Reuter, H. Rosner, G. H. Fecher, C. Felser, M. Jansen, *Dalton Trans.* **2019**, 48, 5058-5063.
- [41] M. W. Roberts, *Catal. Lett.* **2000**, 67, 1-4.
- [42] G. Ertl, H. Knözinger, F. Schüth, J. Weitkamp, *Handbook of Heterogeneous Catalysis*, 2nd Edition, Wiley-VCH Verlag GmbH & Co, Weinheim, **2008**.
- [43] M. O. Özbek, R. A. van Santen, *Catal. Lett.* **2013**, 143, 131-141.
- [44] I. I. Yukelson, *Khimiya* **1968**, 554-559.
- [45] E. T. Lefort, Patent US 1998878A, **1935**.
- [46] B. Leach, in *Applied Industrial Catalysis, Vol. 1*, Elsevier, **2012**, pp. 207-238.
- [47] G. H. Law, H. C. Chitwood, Patent US2279470A, **1942**.
- [48] J. M. Kobe, W. E. Evans, R. L. June, M. F. Lemanski, in *Encyclopedia of Catalysis*, **2002**.
- [49] R. P. Nielsen, Patent US3702259A, **1972**.
- [50] R. P. Nielsen, Patent US US3702259A, **1972**.
- [51] Shell, Patent GB 434011 A, **1935**.
- [52] A. J. van Peski, Patent US 2040782 A, **1936**.
- [53] P. Hayden, R. W. Clayton, J. R. Bamforth, A. F. G. Cope, Patent Europe EP0003642B1, **1984**.
- [54] A. M. Lauritzen, Patent US US4766105A, **1988**.

- [55] W. E. Evans, P. M. Mcallister, R. C. Yeates, J. M. Kobe, Patent US US8546592B2, **2013**.
- [56] W. E. Evans, P. M. Mcallister, R. C. Yeates, J. M. Kobe, Patent US US8859792B2, **2014**.
- [57] T. L. Lohr, J. R. Lockemeyer, S. D. Bishopp, A. H. Motagamwala, G. J. Wells, T. Wermink, *Ind. Eng. Chem. Res.* **2024**, *63*, 18221-18240.
- [58] A. Karpov, C. Walsdorff, M. Kraemer, A. Lange de Oliveira, G. Krennrich, C. Bartosch, J. Zuehlke, Patent WO2019/154832, **2019**.
- [59] M. O. Ozbek, I. Onal, R. A. van Santen, *J. Catal.* **2011**, *284*, 230-235.
- [60] W. Diao, C. D. DiGiulio, M. T. Schaal, S. Ma, J. R. Monnier, *J. Catal.* **2015**, *322*, 14-23.
- [61] J. T. Jankowiak, M. A. Barteau, *J. Catal.* **2005**, *236*, 379-386.
- [62] P. Christopher, S. Linic, *J. Am. Chem. Soc.* **2008**, *130*, 11264-11265.
- [63] C.-J. Chen, J. W. Harris, A. Bhan, *Chem. - Eur. J.* **2018**, *24*, 12405-12415.
- [64] L. Cao, A. Rokicki, Patent US 10,300,462, **2019**.
- [65] C. Kunz, C. Walsdorff, M. Viertelhaus, C. Adam, A. Karpov, J. Nuss, M. Jansen, *Z. Anorg. Allg. Chem.* **2021**, *647*, 1348-1353.
- [66] R. Albrecht, H. Poddig, J. Hunger, M. Ruck, P. Benrath, A. Möller, T. Doert, *Z. Anorg. Allg. Chem.* **2021**, *647*, 667-672.
- [67] A. M. Latshaw, M. D. Smith, W. M. Chance, H.-C. zur Loye, *Solid State Sci.* **2015**, *42*, 14-19.
- [68] K. D. zur Loye, W. M. Chance, J. Yeon, H.-C. zur Loye, *Solid State Sci.* **2014**, *37*, 86-90.
- [69] S. C. Neumair, H. Huppertz, *Z. Naturforsch. B* **2009**, *64*, 1339-1344.
- [70] T. A. Teichtmeister, C. Paulsen, S. J. Ambach, K. Wurst, L. Bayarjargal, W. Schnick, H. Huppertz, *J. Solid State Chem.* **2023**, *325*, 124170.
- [71] E. Strub, U. Otto, *Strahlenschutzanweisung 23.01.2014*, Department of Nuclear Chemistry, Cologne, Germany, **2014**.
- [72] D. Papagiannopoulou, *J. Labelled Compd. Radiopharm.* **2017**, *60*, 502-520.
- [73] K. H. Lieser, *Radiochim. Acta* **1993**, *63*, 5-8.
- [74] C. I. Pearce, J. P. Icenhower, R. M. Asmussen, P. G. Tratnyek, K. M. Rosso, W. W. Lukens, N. P. Qafoku, *ACS Earth Space Chem.* **2018**, *2*, 532-547.
- [75] R. Alberto, *Inorg. Chem.* **2023**, *62*, 20539-20548.
- [76] M. Riondato, D. Rigamonti, P. Martini, C. Cittanti, A. Boschi, L. Urso, L. Uccelli, *J. Med. Chem.* **2023**, *66*, 4532-4547.
- [77] D. Badea, C. Lenting, M. Hanrath, J. Bruns, *Eur. J. Inorg. Chem.* **2025**, *28*, e202500036.
- [78] D. Badea, J. Bruns, *Z. Kristallogr. N. Cryst. Struct.* **2025**, *240*, 255-256.

- [79] D. Badea, S. Olthof, J. Neudörfl, R. Glaum, R. Pöttgen, M. Reimann, K. Meerholz, M. Reimer, C. Logemann, E. Strub, J. Bruns, *Eur. J. Inorg. Chem.* **2023**, 26, e202300160.
- [80] D. Badea, K. Dardenne, R. Polly, J. Rothe, K. Meerholz, M. Hanrath, M. Reimer, J. Neudörfl, E. Strub, J. Bruns, *Chem. Eur. J.* **2022**, 28, e202201738.
- [81] L. Link, R. Niewa, *J. Appl. Crystallogr.* **2023**, 56.
- [82] G. Sheldrick, *Acta Crystallogr.* **2015**, C71, 3-8.
- [83] G. Sheldrick, *Acta Crystallogr.* **2015**, A71, 3-8.
- [84] O. V. Dolomanov, L. J. Bourhis, R. J. Gildea, J. A. K. Howard, H. Puschmann, *J. Appl. Crystallogr.* **2009**, 42, 339-341.
- [85] K. E. Bullen, *Geophys. J. Int.* **1949**, 5, 335-368.
- [86] M. Jansen, M. Bortz, *Z. Anorg. Allg. Chem.* **1989**, 579, 123-128.
- [87] A. Byström, L. Evers, L. G. Sillén, M. Rottenberg, *Acta Chem. Scand.* **1950**, 4, 613-627.
- [88] F. Bullnheimer, *Ber. Dtsch. Chem. Ges.* **1898**, 31, 1287-1289.
- [89] J. R. Gavarri, D. Weigel, A. W. Hewat, *J. Solid State Chem.* **1978**, 23, 327-339.
- [90] P. M. Skarstad, S. Geller, *Mater. Res. Bull.* **1975**, 10, 791-799.
- [91] W. Urland, R. Hoppe, *Z. Anorg. Allg. Chem.* **1972**, 392, 23-36.
- [92] J. Stoch, J. Gablankowska-Kukucz, *Surf. Interface Anal.* **1991**, 17, 165-167.
- [93] A. R. Gonzalez-Elipe, J. P. Espinos, A. Fernandez, G. Munuera, *Surf. Interface Anal.* **1990**, 45, 103-108.
- [94] F. M. Chang, M. Jansen, *Z. Anorg. Allg. Chem.* **1983**, 507, 59-65.
- [95] H. E. Swanson, E. Tatge, *Natl. Bur. Stand. Circ.* **1953**, 359, 1-95.
- [96] C. Chay, M. Avdeev, H. E. A. Brand, S. Injac, T. A. Whittle, B. J. Kennedy, *Dalton Trans.* **2019**, 48, 17524-17532.
- [97] A. Magnéli, S. Siitonen, B. Skrifvars, J. Schliack, L. Reio, *Acta Chem. Scand.* **1957**, 11, 28-33.
- [98] S. Hull, D. A. Keen, *Phys. Rev. B* **1999**, 59, 750-761.
- [99] S. Sutorius, D. van Gerven, S. Olthof, B. Rasche, J. Bruns, *Chem. Eur. J.* **2022**, 28, e202200004.
- [100] S. Sutorius, M. Hanrath, J. Bruns, *Eur. J. Inorg. Chem.* **2022**, 2022, e202200009.
- [101] M. Daub, H. A. Höppe, H. Hillebrecht, *Z. Anorg. Allg. Chem.* **2014**, 640, 2914-2921.
- [102] J. E. Yoon, K. B. Lee, C.-J. Yoo, B. K. Min, D. K. Lee, D. H. Won, S. Kim, J.-H. Moon, C. Kim, U. Lee, *J. Clean. Prod.* **2024**, 475, 143539.
- [103] S. Ahlert, K. Friese, M. Jansen, *Z. Anorg. Allg. Chem.* **2002**, 628, 1525-1531.
- [104] D. Lu, J. Zhang, H. Zhao, M. Pi, X. Ye, Z. Liu, X. Wang, X. Zhang, Z. Pan, S.-Y. Hsu, C.-K. Chang, J.-M. Chen, Z. Hu, Y. Long, *Inorg. Chem.* **2024**, 63, 3191-3198.
- [105] P. Norby, R. Dinnebier, A. N. Fitch, *Inorg. Synth.* **2002**, 41, 3628-3637.
- [106] D. Badea, A. Karpov, M. Jansen, J. Bruns, *Z. Anorg. Allg. Chem.* **2022**, e202200267.

- [107] M. Jansen, *Angew. Chem., Int. Ed. Engl.* **1987**, 26, 1098-1110.
- [108] L. Vegard, *London, Edinburgh Dublin Philos. Mag. J. Sci.* **1916**, 31, 83-87.
- [109] I. G. Dance, L. J. Fitzpatrick, A. D. Rae, M. L. Scudder, *Inorg. Chem.* **1983**, 22, 3785-3788.
- [110] M. R. Udupa, B. Krebs, *Inorg. Chim. Acta* **1973**, 7, 271-276.
- [111] U. Schubert, D. Neugebauer, A. A. M. Aly, *Z. Anorg. Allg. Chem.* **1980**, 464, 217-232.
- [112] D. Y. Naumov, A. V. Virovets, N. V. Podberezskaya, E. V. Boldyreva, *Acta Crystallogr.* **1995**, C51, 60-62.
- [113] P. Böttcher, H. Buchkremer-Hermanns, W. Höhle, H. G. v. Schnering, *Z. Kristallog.* **1987**, 181, 223-226.
- [114] J. Chen, Z.-X. Zeng, W.-L. Xue, D. Wang, Y. Huang, *Ind. Eng. Chem. Res.* **2011**, 50, 11755-11762.
- [115] E. Strub, D. Badea, J. Bruns, A. Frontera, N. Mayordomo, A. Sakhonenkova, M. Roca Jungfer, M. Wickleder, C. Yong, M. Zegke, *Eur. J. Inorg. Chem.* **2025**, e202400780.
- [116] R. C. L. Mooney, *J. Chem. Phys.* **1948**, 16, 1003-1003.
- [117] K. Brandenburg, *Diamond 4, Crystal and Molecular Structure Visualization*, Crystal Impact GbR, Bonn, Germany, **2019**.
- [118] WinXPow, *version 3.12*, Stoe & Cie GmbH, Darmstadt, Germany, **2018**.
- [119] T. Williams, C. Kelley, R. Lang, *Gnuplot, version 5.2*, **2019**.
- [120] A. A. Coelho, *J. Appl. Crystallogr.* **2018**, 51, 210-218.
- [121] Topas-Academic, *version V6*, Brisbane, Australia, **2016**.
- [122] OriginPro 2019b, *version 9.6.5.169*, OriginLab Corporation, Northampton, MA, USA, **2019**.
- [123] N. Fairley, *CasaXPS Manual 2.3. 15: Introduction to XPS and AES*, Casa Software, **2009**.
- [124] D. Casanova, J. Cirera, M. Llunell, P. Alemany, D. Avnir, S. Alvarez, *J. Am. Chem. Soc.* **2004**, 126, 1755-1763.
- [125] M. Llunell, D. Casanova, J. Cirera, P. Alemany, S. Alvarez, *SHAPE, version 2.1*, Universitat de Barcelona, Barcelona, Spain, **2013**.
- [126] M. Nespolo, B. Guillot, *J. Appl. Crystallogr.* **2016**, 49, 317-321.
- [127] M. Nespolo, *Acta Crystallogr., Sect. B* **2016**, 72, 51-66.
- [128] D. Y. Curtin, R. J. Harder, *J. Am. Chem. Soc.* **1960**, 82, 2357-2368.
- [129] Y. V. Kokunov, Y. E. Gorbunova, V. V. Kovalev, *Russ. J. Inorg. Chem.* **2011**, 56, 1733-1738.
- [130] D. Novgorodova, A. Gorshkov, A. Mokhov, *Zap. Vses. Mineral. O-va.* **1979**, 108, 552-554.
- [131] W. H. Baur, A. A. Khan, *Acta Crystallogr., Sect. B* **1971**, 27, 2133-2139.